

Additive Manufacturing of Ceramics and Ceramic Composites via Robocasting

Ezra Feilden

Supervisors:

Finn Giuliani, Luc Vandeperre, Eduardo Saiz

Centre for Advanced Structural Ceramics

Department of Materials

Imperial College London

Submitted for the degree of

Doctor of *Philosophy* (PhD)

'Blank' Page

Declaration

This is all my own work, except for the bits which are someone else's, all of which have been properly referenced and acknowledged.

Ezra Feilden

The copyright of this thesis *rests* with the author and is made available under a Creative Commons Attribution Non-Commercial No Derivatives licence. Researchers are free to copy, distribute or transmit the thesis on the condition that they attribute it, that they do not use it for commercial *purposes* and that they do not alter, transform or build upon it. For any reuse or redistribution, *researchers* must make clear to others the licence terms of this *work*.



Abstract

In the last two decades additive manufacturing (AM) has emerged as a highly important and influential technology. A large range of approaches to AM have been developed which give rise to hundreds of distinct techniques. Many of these are specific to one material system, and only a handful have been successful at producing ceramic parts. Robocasting is one such technique, having been used to produce complex ceramic parts with reasonable mechanical properties. In this thesis robocasting is investigated further, firstly by characterising the rheology of the robocasting paste, and then by measuring the strength and reliability of ceramic parts produced by robocasting. The critical defects associated with the process are identified, and efforts have been made to eliminate them. Furthermore, it was possible to produce a new class of ceramic composites consisting of alumina platelets aligned by the shear forces that arise during printing. These platelets themselves and the composites were extensively characterised. A new *in-situ* double cantilever test was developed in order to study the fracture behaviour of the composites. Lastly, the principle of using the printing process to align platelets was applied to fibres in order to create printed fibre reinforced ceramic matrix composites, and printed carbon fibre reinforced epoxy.

Selected Acknowledgements

3 years is a long time to work on one project. A lot of people helped me out along the way, and I'm very grateful to them all.

Firstly, I would like to thank the CASC industrial consortium and EPSRC for providing the funding for this work, and all of the technical staff and colleagues who helped out with my experiments: Na, Cati, Mahmoud, and Garry.

Eduardo, Luc, and Finn – three fantastic supervisors. I've seen how much of a difference good supervision can make, and I know I've been very lucky to be your PhD student.

Of course, family. Mo, Andrew, Luke, Jack. I know you'd be there anytime, anywhere.

Justine, in no uncertain terms you've changed my life in just a few months, not least by proof reading this whole thesis. Thank you for everything.

Some marvellous people keeping the sesh in their hearts: Abbas, Amy, Gil, Alan, Eugenio. Were it not for you, these last 3 years would have been quiet, boring, and much better for my health. Thank you for making London the most fun city in the world to live in.

Some friends and fellow CASCites: Claudio, Tommaso, Ele, Chiara, Annalisa, Esther (ft. the legendary yoga sessions), Giorgio, Na, Victoria, Dan, Dimitri, Claudia, Tessa. You've all been smashing.

All the organisations that gave me awards for pretty pictures I made with SEMs, which is not just a nice ego boost, but also some very welcome cash for a 'destitute' PhD student living in a very expensive city.

And last but certainly not least, I'd like to thank all of the techno for getting me through the long hours of data crunching and other activities.

Publications

- **Robocasting of Structural Ceramic Parts with Hydrogel Inks**
Ezra Feilden, Esther Garcia Tunon Blanca, Finn Giuliani, Eduardo Saiz, Luc Vandeperre
Journal of the European Ceramic Society, **36**, 2525-2533 (2016)
- **3D Printing Bioinspired Ceramic Composites**
Ezra Feilden, Claudio Ferraro, Qinghua Zhang, Eleonora D'Elia, Esther Garcia Tunon Blanca, Finn Giuliani, Luc Vandeperre, Eduardo Saiz
Scientific Reports, **7**, 13759 (2017)
- **Micromechanical Properties of Al₂O₃ Platelets**
Ezra Feilden, Tommaso Giovannini, Claudio Ferraro, Luc Vandeperre, Eduardo Saiz, Finn Giuliani
Scripta Materialia, **131**, 55-58 (2017)
- **Progress in Novel and Unexpected Areas**
Ezra Feilden, Claudio Ferraro, Finn Giuliani, Luc Vandeperre, Eduardo Saiz
Materials Today, **19**, 9 (2016)
- **Graphene Oxide: An All-in-One Processing Additive for 3D Printing**
Esther García-Tuñón, Ezra Feilden, Eleonora D'Elia, Alan Leong, Eduardo Saiz
ACS applied materials & interfaces, **9**, 38, 32977-32989 (2017)
- **Multi-material 3D printing of Graphene-based electrodes for Electrochemical Energy Storage using Thermo-Responsive Inks**
Victoria G. Rocha, Esther García-Tuñón, Foivos Markoulidis, Ezra Feilden, Eleonora D'Elia, Na Ni, Milo Shaffer and Eduardo Saiz
ACS applied materials & interfaces, **9**, 42, 37136-37145 (2017)
- **A Review of the Role of Rheology in Robocasting - A Quantitative Definition of Printability**
Ezra Feilden, Luc Vandeperre, Eduardo Saiz ([in preparation](#))
- **Robocasting Dense UHTC Parts**
Ezra Feilden / Daniel Glymond, Eduardo Saiz, Luc Vandeperre ([in preparation](#))
- **Electrically-responsive Graphene-based Shape-memory Composites**
Eleonora D'Elia, Hanaë Ahmed, Ezra Feilden, Eduardo Saiz ([in preparation](#))

Conference Attendance

- International Conference on Additive Manufacturing & 3D Printing, **UK**, 2015
- EuropeMakes AM Kick-off Meeting, **Belgium**, 2015
- Biobone Conference, **Spain**, 2015
- Printing for the Future Conference, Institute of Physics, **UK**, 2016
- International Conference on Ceramic Processing Science, **Japan**, 2016
- 1DRAC Conference, **UK**, 2017
- International Conference and Expo on Advanced Ceramics and Composites, **USA**, 2017
- yCAM Conference, **Germany**, 2017
- CASC Industry Day, Imperial College London, **UK**, 2015, 2016, 2017

Table of Contents

INTRODUCTION.....	12
CHAPTER I – LITERATURE REVIEW	13
TAXONOMY OF AM OF CERAMIC MATERIALS	14
DIRECTED ENERGY DEPOSITION	16
SELECTIVE LASER SINTERING/SELECTIVE LASER MELTING.....	18
STEREOLITHOGRAPHY	20
LAMINATED OBJECT MANUFACTURE.....	22
INK-JET PRINTING.....	23
FUSED DEPOSITION	25
ROBOCASTING.....	26
<i>Paste Formulations.....</i>	<i>27</i>
<i>Rheology and Extrusion</i>	<i>29</i>
<i>Structures of Individual Robocast Filaments</i>	<i>31</i>
<i>Structures of Robocast Parts</i>	<i>34</i>
<i>Applications.....</i>	<i>35</i>
<i>Robocast Materials</i>	<i>36</i>
CONCLUSIONS	42
AIMS AND OBJECTIVES OF THIS THESIS.....	43
CHAPTER II – METHODS.....	44
POWDER PROCESSING	45
<i>Powder Pastes.....</i>	<i>45</i>
<i>Platelet Composite Pastes.....</i>	<i>48</i>
<i>Fibre Composite Pastes</i>	<i>49</i>
RHEOLOGY.....	50
PRINTING.....	53
POST-PROCESSING	57
<i>Drying</i>	<i>57</i>
<i>Burn-out and Sintering</i>	<i>57</i>
<i>Infiltration.....</i>	<i>57</i>
CHARACTERISATION AND TESTING	58
<i>In-situ DCB Testing</i>	<i>59</i>
<i>Micromechanical Testing</i>	<i>61</i>
CHAPTER III – RHEOLOGY AND ROBOCASTING: THE NEBULOUS CONCEPT OF ‘PRINTABILITY’.....	63
INTRODUCTION.....	64

BASIC RHEOLOGICAL PROPERTIES	65
PLURONIC F-127 HYDROGELS	67
<i>Gelation</i>	67
<i>Yielding</i>	70
<i>Flow</i>	73
POWDER PASTES	75
<i>Powder Characterisation</i>	75
<i>Effect of Ceramic Powder on Rheology</i>	76
<i>Effect of Ceramic Volume Fraction</i>	78
<i>Effect of Surface Chemistry</i>	80
PLATELET PASTES	82
<i>Rheology of Platelet Pastes verses Powder Pastes</i>	86
FIBRE PASTES	89
<i>SiC Whisker Pastes</i>	89
<i>Carbon Fibre Pastes</i>	90
GENERAL DISCUSSION	92
<i>A New Meaning of 'Printability'</i>	92
<i>Optimising Pluronic Hydrogels and Pastes using Φ</i>	96
<i>A Brief Comparison to Other Paste Systems for Robocasting</i>	97
CONCLUSIONS	99
CHAPTER IV – MONOLITHIC CERAMIC PARTS	100
INTRODUCTION	101
PRINTING PARAMETERS	102
<i>Paste Selection</i>	102
<i>Print Speed</i>	102
<i>Raster Pattern</i>	104
<i>Substrate Material</i>	108
<i>Nozzle Selection</i>	108
DRYING	109
<i>Oil Bath</i>	109
<i>Air Drying</i>	110
CHARACTERISATION AND MECHANICAL PROPERTIES	113
SOME EXAMPLE PARTS	119
GENERAL DISCUSSION	122
<i>Comparison to Other AM Techniques</i>	123
CONCLUSIONS	125
CHAPTER V – CERAMIC PLATELET COMPOSITES	126
INTRODUCTION	127

PLATELET CHARACTERISATION.....	128
<i>Defect Analysis</i>	132
<i>Comparison to other alumina particles</i>	137
PLATELET ALIGNMENT DURING EXTRUSION.....	138
<i>A Mechanistic Look at the Processes behind Platelet Alignment</i>	141
MICROSTRUCTURAL DESIGN	143
<i>Post Processing</i>	143
<i>Characterisation and Mechanical Properties</i>	144
<i>The 'Novel' in-situ DCB Setup</i>	146
<i>Application of DCB to the Platelet Composites</i>	147
CONCLUSIONS	154
CHAPTER VI – CERAMIC FIBRE COMPOSITES.....	155
INTRODUCTION.....	156
FIBRE REINFORCED POLYMER MATRIX COMPOSITES	157
<i>Paste Selection</i>	157
<i>Printing and Fibre Alignment</i>	157
<i>Post Processing</i>	159
<i>Microstructure</i>	160
<i>Mechanical Properties</i>	162
FIBRE REINFORCED CERAMIC MATRIX COMPOSITES (CMC)	165
<i>Paste Selection and Printing</i>	165
<i>Post Processing</i>	168
GENERAL DISCUSSION & FUTURE WORK	175
<i>Fibre Reinforced Polymer Matrix Composites</i>	175
<i>Fibre Reinforced Ceramic Matrix Composites</i>	177
CONCLUSIONS	179
REFERENCES.....	180
APPENDICES	193
APPENDIX I – ANOTHER APPROACH TO DEFINE Φ	194
APPENDIX II – A CASE STUDY.....	195
APPENDIX III – A SIMPLE BIT OF G-CODE TO PRINT LARGE NUMBERS OF TEST BARS.....	198
APPENDIX IV – CORRECTING WEIBULL MODULUS FOR IRREGULAR SIZED SAMPLES.....	199
<i>Volume correction for Weibull analysis</i>	199
<i>Area correction for Weibull analysis</i>	200

Abbreviations

<i>Acronym</i>	Meaning
<i>AM</i>	Additive Manufacturing
<i>CLIP</i>	Continuous Liquid Interface Production
<i>CMC</i>	Ceramic Matrix Composite
<i>CODE</i>	Ceramic On-Demand Extrusion
<i>CVI</i>	Chemical Vapour Infiltration
<i>DCB</i>	Double Cantilever Beam
<i>DIW</i>	Direct Ink Writing
<i>DWF</i>	Direct Write Fabrication
<i>EDX</i>	Energy Dispersive X-ray Spectroscopy
<i>EFF</i>	Extrusion Freeform Fabrication
<i>FDC</i>	Fused Deposition of Ceramics
<i>FDM</i>	Fused Deposition Modelling
<i>FEF</i>	Freezeform Extrusion Fabrication
<i>LCM</i>	Lithography-based Ceramic Manufacturing
<i>LENS</i>	Laser Engineered Net Shaping
<i>LOM</i>	Laminated Object Manufacturing
<i>MMC</i>	Metal Matrix Composite
<i>PAA</i>	Polyacrylic Acid
<i>PAN</i>	Polyacrylonitrile
<i>PEI</i>	Polyethylenimine
<i>PEO</i>	Polyethylene Oxide
<i>PIP</i>	Polymer Infiltration and Pyrolysis
<i>PMC</i>	Polymer Matrix Composite
<i>PPO</i>	Polypropylene Oxide
<i>RC</i>	Robocasting
<i>SENB</i>	Single Edge Notched Beam
<i>SLM</i>	Selective Laser Melting
<i>SLS</i>	Selective Laser Sintering
<i>STL</i>	Stereolithography
<i>WRT</i>	With Respect To
<i>YAG</i>	Yttrium Aluminium Garnet
<i>YAM</i>	Yttrium Aluminate Monoclinic

Introduction

Additive manufacturing – also known as 3D printing – is a diverse group of manufacturing techniques that build objects by adding material in a layer-by-layer fashion. Implementation of this simple idea makes a myriad of applications possible, and opens up opportunities for far-reaching change to society. It is therefore unsurprising that additive manufacturing has received a significant amount of interest, speculation, and investment from industry and academia, and in recent years it has entered the public consciousness. This has resulted in rapid development of the technology, which has progressed well beyond sensationalised press articles and preliminary prototypes, and is already a disruptive technology in the real world.

Most work on additive manufacturing has focused on metals and polymers, both of which are currently being embraced in industry. On the other hand, additive manufacturing of ceramic materials is less well developed. Most ceramic 3D printers produce a green body which is subsequently sintered to obtain a dense part. Robocasting is one such ceramic additive manufacturing technique that works by this principle, precisely extruding a ceramic paste into the shape of a layer of the desired part.

While robocasting has shown much promise in producing a range of ceramic materials with relatively good mechanical properties, significant gaps in the literature remain – the mechanical properties of printed parts has not been fully characterised and defects coming from the printing process have yet to be identified. Furthermore, the flexibility of robocasting opens up a number of possibilities of new microstructures and materials that have yet to be explored.

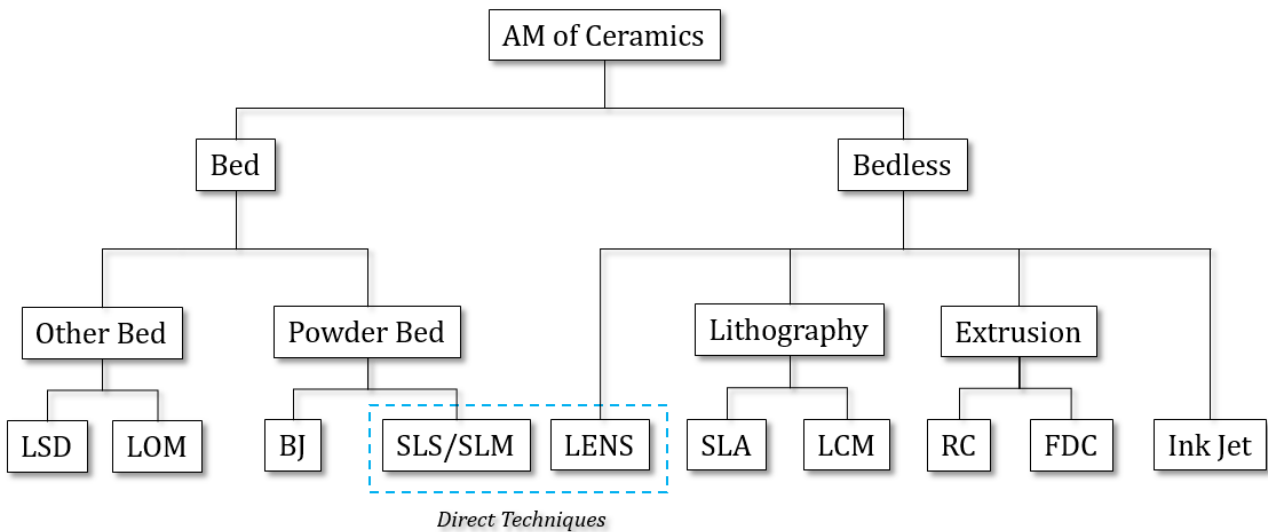
This thesis begins with a literature review, Chapter I, which evaluates the current state of the art of ceramic additive manufacturing in order to assess robocasting's place in this field. The methods used throughout the work are presented in Chapter II. Next, the first results chapter, Chapter III, looks at the underpinning science of the robocasting process – rheology. Results Chapters IV, V, and VI examine monolithic ceramics, platelet composites, and fibre composites produced by robocasting, with an emphasis on optimisation of mechanical properties. Chapter V also features a detailed analysis of the platelets used throughout the chapter, as well as a new *in-situ* mechanical test which was developed to probe the mechanical properties of the composites. Lastly, the appendices present supplementary information and a case study illustrating robocasting's present utility, which may be of interest to the reader.

Chapter I – Literature Review

Taxonomy of AM of Ceramic Materials

Ceramic additive manufacturing techniques are extraordinarily varied and diverse, to the extent that on the surface it often seems nonsensical for two technologies to both appear under the same heading. However, when one looks deeper a clear thread connecting all the techniques can be found; the fact that parts are always produced by adding material (as suggested by the name) in a manner prescribed from a CAD model, layer by layer. A *brief* overview of each of the major techniques is presented below, followed by a more detailed look at robocasting, the principle technique used experimentally throughout this thesis. The final parts of the literature review cover the range of materials produced using robocasting, including various composite systems.

There are many ways of dividing the diverse family of ceramic AM techniques into sensible categories. None of these are perfect, but in terms of capabilities, limitations, and the underlying technology, it makes sense to divide them between printing processes that use a bed (powder or otherwise) and processes that do not. This categorisation is presented in Figure 1.



LSD- Layerwise Slurry Deposition
 LOM- Layered Object Manufacture
 BJ- Binder jetting
 SLS- Selective Laser Sintering
 SLM- Selective Laser Melting

LENS- Laser Engineered Net Shaping
 SLA- Stereolithography
 LCM- Lithography Ceramic Manufacturing
 RC- Robocasting
 FDC- Fused Deposition of Ceramics

Figure 1. One approach to categorise the most prominent ceramic AM techniques.

Similarly, different parts can be categorised by their fundamental features. All parts, no matter how complex, can be broken down into a series of the following structures: space filling features, spanning features, overhanging features, floating features, and cavities, all illustrated in Figure 2. This classification builds upon work by Lewis et al.[1] Each technique has demonstrated varying abilities at producing each feature, which will be discussed individually. This is summarised in Table 1.

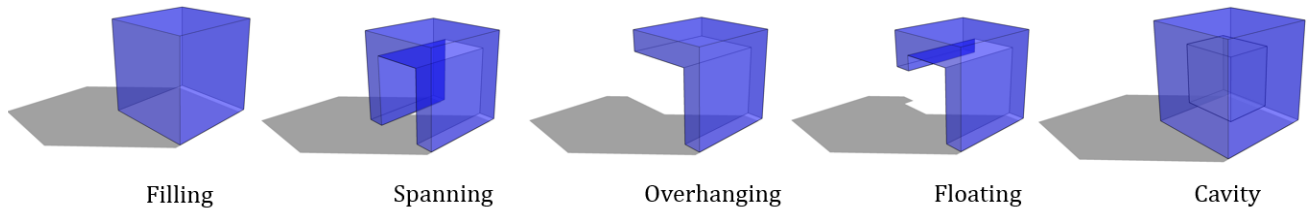


Figure 2- The fundamental features any part.

Table 1. Comparison of the abilities of each main ceramic AM technology.

Technique	Features				
	Filling	Spanning	Overhanging	Floating	Closed Cavity
Directed Energy Deposition	Green	Red	Yellow	Red	Green
Selective Laser Sintering	Green	Green	Green	Green	Red
Stereolithography	Green	Red	Green	Red	Green
Layered Object Manufacturing	Green	Green	Green	Green	Red
Binder Jetting	Green	Green	Green	Green	Red
Direct Ink Jet Printing	Green	Red	Yellow	Red	Green
Fused Deposition	Green	Yellow	Yellow	Red	Green
Robocasting	Green	Yellow	Yellow	Red	Green

Generally possible	Notable limitations	Generally impossible

Directed Energy Deposition

The foundations of Directed Energy Deposition (DED), also known by the proprietary term laser engineered net shaping (LENS™), were laid at Sandia National Laboratories in the early 1990s.[2] Like all AM processes, the first step of DED is the slicing of a CAD model into equally spaced cross-sections. Deposition then begins by focusing a high-power laser (typically a YAG laser) onto a spot on a substrate, generating a molten pool of substrate material. Feedstock powder is then continuously added into the melt pool via a powder delivery nozzle where it melts upon contact. The laser spot and powder delivery nozzle are translated relative to the substrate, creating a quickly solidifying line of deposited material. The spot and nozzle are moved across the substrate in a pattern defined by the CAD model slice until all the material constituting the first layer of the part has been deposited, whereupon the substrate moves down by one layer/slice height and the process is completed for the second layer. Fabrication is typically carried out in an inert atmosphere to avoid oxidation of the melt pool.

As with many AM techniques, most of the initial work with DED was for AM of metallic materials. Full melting of the ceramic feedstock powder is required to achieve parts with acceptable properties, thus for high melting point materials the thermal gradients encountered during printing are extremely high. Only oxides with relatively modest melting points such as Al_2O_3 , [3] $\text{Al}_2\text{O}_3\text{-ZrO}_2\text{-Y}_2\text{O}_3$ [4,5] and lead zirconate titanate [6] can presently be produced, and even for these materials very careful control of the process parameters is required to avoid cracking from thermal stresses. [7] Two big advantages to the technique are the lack of powder bed (which makes the process more efficient in terms of waste, and makes larger objects more feasible) and the fact that it is a direct AM process, not necessarily requiring any post processing – an attribute that is very rare amongst ceramic AM techniques. Despite this, the use of DED to print of large, geometrically complex ceramic parts with acceptable mechanical properties has yet to be demonstrated, and ceramics with very high melting points may never be directly produced. Due to the nature of the process it is unable to produce spanning and floating features, and has limitations on the angle of overhanging features. These issues, alongside the high setup cost and complexity of the equipment have severely limited the study and industrial uptake of this technique.

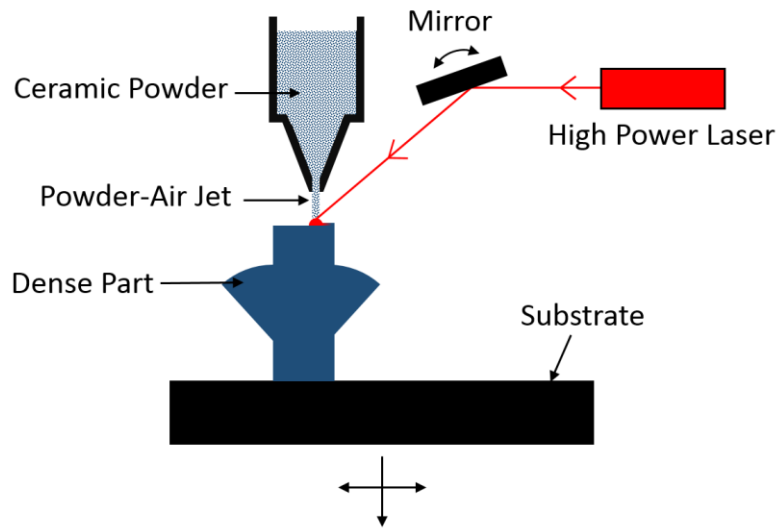


Figure 3. Schematic illustrating the DED process.

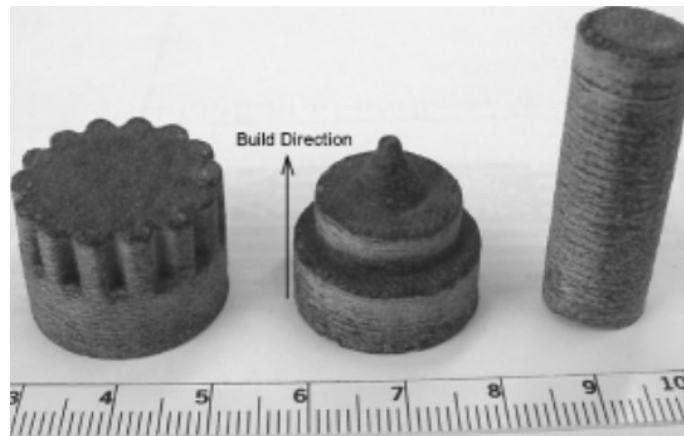


Figure 4. Three simple Al_2O_3 components produced by DED. Reproduced with permission from [3].

Selective Laser Sintering/Selective Laser Melting

Selective laser sintering (SLS) was developed in the 1980s, at the University of Texas[8]. The process directs a high power laser at a powder bed of material, using the thermal energy of the laser beam to sinter selected areas. The pattern that the laser traces defines the geometry of a slice of the part. Once the layer is complete, the part is lowered and a fresh layer of powder is rolled on top of it, as shown in Figure 5. This process is repeated layer by layer until the part is complete. A wide range of powder materials have been demonstrated, with most work focusing on polymers[9] and alloys[10]. The basic requirement for a material's eligibility for SLS is that it readily densifies when sufficiently heated. Selective laser melting (SLM) is identical to SLS except for the fact that the laser delivers enough energy to the spot to melt the material there, not just sinter it.

SLS/SLM present some benefits over other AM techniques, principally the fact that it is a "one step process", requiring no post processing steps. Again, this is a very unusual attribute in additive manufacturing of ceramics. As it is a powder bed process there are virtually no limitations on the type of features that can be printed. However, in reality the benefits are far outweighed by some serious challenges which have yet to be overcome. As with all powder bed techniques, closed hollow cavities are not possible (as the powder cannot be removed from these), and delicate structures are difficult as they can easily be damaged when removing the powder bed. The laser scan speed is usually reasonably fast (50 - 500mm/s),[11] so the time for which each spot of the powder bed is heated is very short. For solid state sintering of ceramics this is insufficient to allow full densification, so the produced parts are usually very porous and have inadequate mechanical properties for most applications.[12-14] Also, while the laser scan speed is fast, the spot size is typically ~50 μm , so even small parts can take days to complete. Furthermore, the whole system experiences extreme thermal gradients due to the local heating from the laser beam. This is a serious issue for ceramic materials due to their low thermal shock resistance, and subsequently the parts are often badly damaged by thermal stress. This issue has recently been partially overcome in an alumina-zirconia system by preheating the whole powder bed to >1500°C with a second laser before scanning across the bed and inducing melting in the required areas of each layer.[11] Using this method along with careful control of powder morphology resulted in near maximum theoretical density and acceptable mechanical properties, showing flexural strengths of around 500 MPa. However it is not clear whether this concept would be suitable for other ceramic systems or for larger ceramic parts.

A further problem is that the complexity of the system can lead to irregular parts. This is because the temperature profile a given area experiences cannot be accurately known without extensive simulations, as the scan speed, road width, laser power, the thermal conductivity and emissivity of the

part and bed all contribute to the speed at which thermal energy is accumulated under irradiation and is dissipated after the beam moves on. This can have effects on the local microstructure of the material[11] and make structures and properties less reproducible when changing geometries. In general the microstructural control is poor, and depending on the powder bed material it is sometimes necessary to add another material (such as C) to assist the absorbance of the laser. This further influences the final microstructure.

Some work has been done to avoid the aforementioned issues by using SLS to simply form a green body by adding a binder element to the powder bed and using much lower laser powers.[13,15,16] This helps mitigate the problems caused by large thermal gradients and allows the part to be sintered in a separate step in a furnace, however the green densities achieved by this method are also fairly poor and so densities after sintering post-processing are typically <90%, leading to mechanical properties which are generally insufficient for load bearing applications.

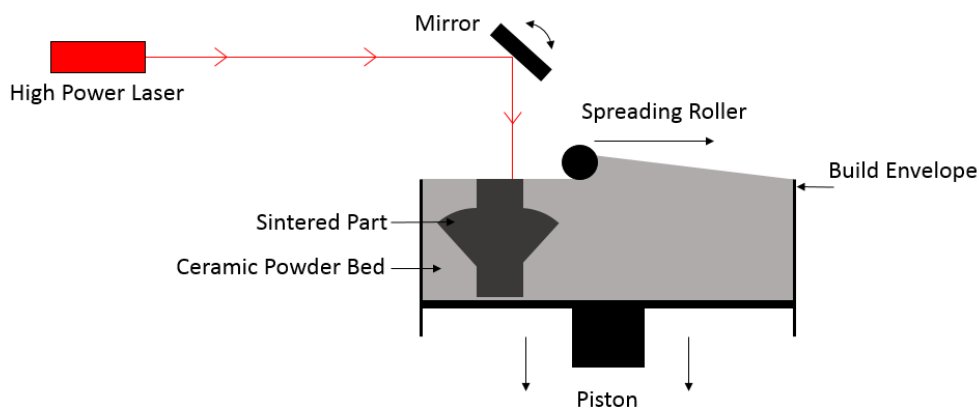


Figure 5. Schematic illustrating the SLS process.



Figure 6. Al_2O_3 parts produced by SLM. Reproduced with permission from [16].

Stereolithography

Stereolithography (STL) is another technique which uses a light source to form each layer of an object in the pattern specified by a CAD file. However, unlike SLS, the source material is a vat of liquid ceramic slurry mixed with a photocurable monomer. A directed UV light source, most often a UV laser, is translated across the surface of this vat, curing the monomer and selectively solidifying this material. The base of the vat is then lowered by a small distance (typically $<200\ \mu\text{m}$), allowing fresh slurry to flow or be wiped over the top of the cured part. The process is then repeated until the object is completed,[17] as illustrated in Figure 7.

This process was initially developed for additive manufacturing of polymer parts from photomonomers, however by loading the photomonomer with a large volume fraction of ceramic powder ($>40\ \text{vol}\%$), the technique can be used to create green bodies. The polymer can then be burnt out and post processing can proceed in the same manner as with traditional green bodies.

STL is capable of producing precise, high resolution ceramic parts. Technically it cannot produce spanning or floating features, although parts with overhanging features at very large angles have been demonstrated. Mechanical properties comparable to parts made by traditional manufacturing have been demonstrated, such as alumina with flexural strength $>400\ \text{MPa}$.[18] This is indeed very promising, however there are a number of limitations to STL. The monomer-ceramic powder suspension has to have a very low viscosity to allow it to flow evenly when the bottom of the vat is lowered. It has to have a high solids loading, and it has to have appropriate optical properties in the UV range to allow curing to a specific depth below the surface, typically tens of microns.[17] This puts constraints on material selection, favouring translucent ceramics such as alumina and zirconia. Despite this, there has been great interest in producing highly opaque ceramics such as SiC and Si₃N₄ via this method with promising preliminary results. As with many processes there are also restraints on the maximum size of parts that can be printed, due to cracking caused by the shrinkage of the part, and issues related to debinding of large pieces.[19] This is a particularly poignant issue for parts with large monolithic sections; the time required to achieve debinding without delamination/cracking becomes prohibitively long, and even for a 10 mm x 10 mm x 10 mm piece debinding requires several days. This is however not a big issue for parts with short diffusion pathways such as lattices or thin-walled objects.[20] Another problem is adhesion between the layers during printing – each time a layer is cured it shrinks, leading to residual shear stresses between the printed layers.

The technology is still in rapid development, and recently there have been a number of significant innovations. One example of this is “continuous liquid interface production” (CLIP), which eliminates

the stepwise nature of the process by inverting the printing platform and exposing layers continuously as the part is pulled out of the monomer vat. This greatly improves printing speed and surface finish.[21] Similarly, “Lithography-based Ceramic Manufacturing” (LCM) inverts the build platform to allow smaller volumes of slurry to be used at a given time,[18] and models based on this setup are among the first commercially available, batch scale ceramic AM equipment available.

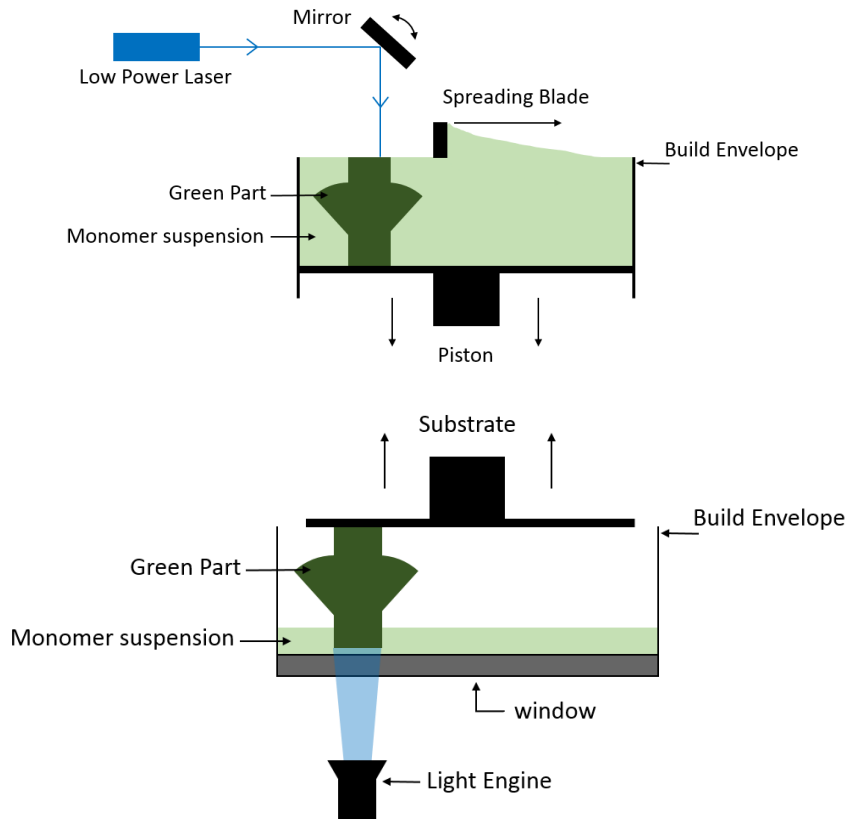


Figure 7. Schematic illustrating the typical SLA process (top) and the inverted process found in CLIP and LCM (bottom).

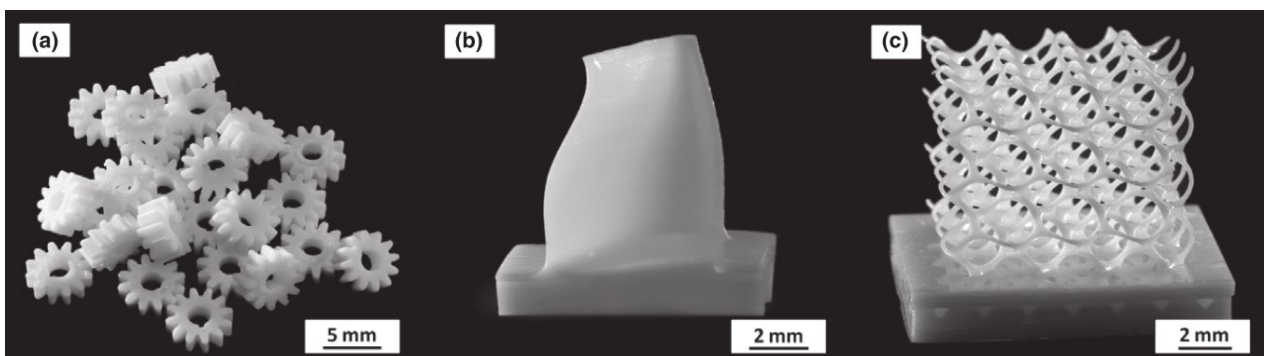


Figure 8. Sintered Al_2O_3 parts fabricated using the LCM technique. Reproduced with permission from [18].

Laminated Object Manufacture

Laminated object manufacture (LOM) is a technique which was originally developed for additive manufacturing using sheets of polymer or paper. In this somewhat unusual process, a sheet of material is cut using a laser into the shape of a 2D slice of the desired object. This shape is then lowered by one layer height, a fresh sheet of material is pressed on top with a heated roller, and again cut with the laser, forming the next slice.[22] This process is repeated until all the layers of the part have been added. As with other techniques, the part is then separated from the unused waste material (the areas of the sheets that have been cut away), and post processing can proceed.

There are no limitations of the type of feature that can be printed (except for closed cavities), and the process lends itself to layers of materials, such as paper. Its application to ceramics has been limited. Most work occurred in the late 1990s and early 2000s, and preliminary studies yielded low green densities, necessitating further pressing/infiltration steps.[23,24] Mechanical strength of ceramic parts made by this method are seldom reported. For bulk ceramic parts, it is unclear whether there are any significant advantages over other methods, and there are certainly disadvantages, including the extra processing step to produce the sheet material, and the large amount of waste material which is difficult to reuse or recycle.

There has been a recent resurgence of interest in LOM for applications in ceramic composites,[25] where the structure is naturally layered. The concept of making composite sheets to be stacked into a shape (prepregs) is well established for other composite systems, however CMCs produced by LOM have yet to demonstrate acceptable mechanical performance due to the aforementioned issues with densification.

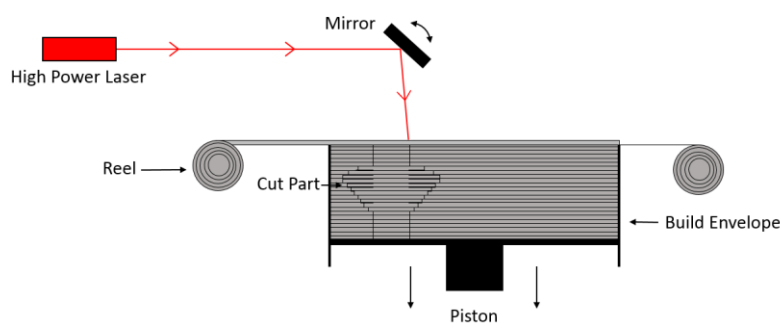


Figure 9. Schematic illustrating the LOM process.



Figure 10. Si_3N_4 objects fabricated by means of LOM. Reprinted with permission from [26].

Ink-Jet Printing

Some of the first 3D printers developed were based on existing ink-jet printers loaded with binder material. In this family of techniques, piezoelectric nozzles atomise a binder material while the print head is translated across the surface of a powder bed, depositing micro-droplets of binder which infiltrate the powder bed, selectively binding the material together. Once the layer is complete the build area is moved down and a roller spreads new powder on top. This process is repeated until the part is complete, then the excess powder is carefully removed, leaving the green part. Post processing can then be carried out. This technique is a particular variety of ink-jet printing known as “binder jetting”, [27] and sometimes confusingly as “3D printing” (referring to this technique and not the overarching group), and is illustrated in Figure 11. It is appropriate for a range of different powder beds including polymers, [28] alloys, [29] and ceramics, [30] and has no limitations of the type of feature that can be printed. The key process parameters are defined by the powder flowability when spreading a new layer, the droplet formation of binder when exiting the print head and the binder infiltration into the powder bed. As with many powder bed techniques, good densification presents a big challenge. The green densities achieved are typically too low to allow full densification of ceramics after post processing, and the powders used need to be large to allow for good flowability, which hinders sintering. [31] As a result, mechanical properties are severely limited. [32] Additionally, the use of coarse powders also gives rise to poor surface finish (large surface roughness), giving rise to the characteristic appearance of parts made by binder jetting. This also limits the resolution of the technique.

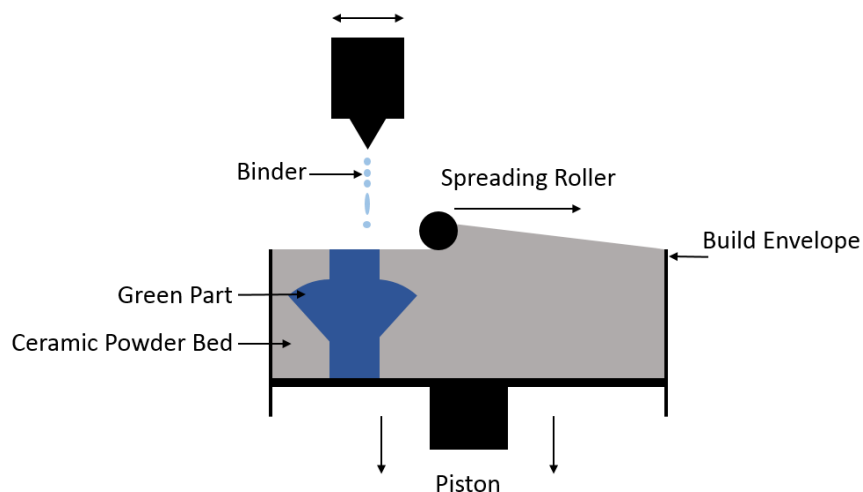


Figure 11. Schematic illustrating the binder jetting technique.

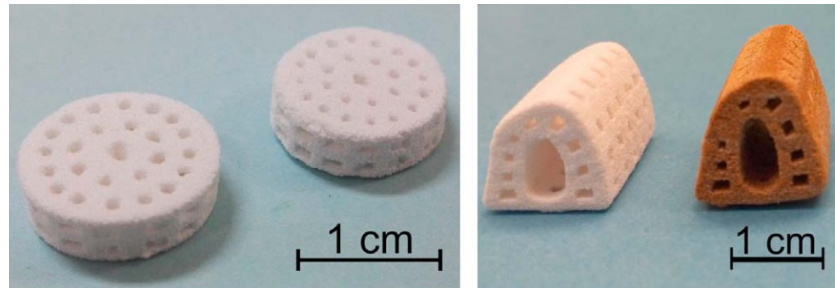


Figure 12. Glass-ceramic components produce by binder jetting. Reproduced with permission from [32].

More recently some work has focused on another approach in which the binder material is replaced by a ceramic slurry which is printed onto a substrate. This is termed “direct inkjet printing” as illustrated in Figure 13. The advantage to this approach is that it avoids all of the difficulties associated with powder beds, and the complex process of binder infiltration. Fully dense technical ceramic parts have been produced with properties comparable to conventionally produced ceramics.[33] However, the surface quality is usually quite poor and parts become increasingly more difficult to print as they become taller, limiting most pieces to <1cm in height. Furthermore, support material is required to build all spanning, floating, and most overhanging structures.

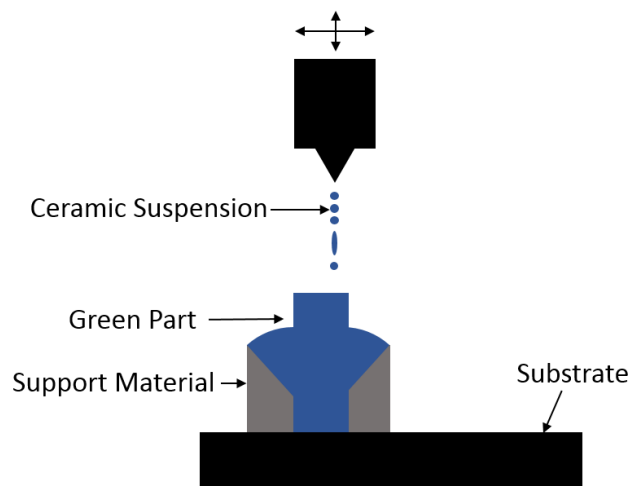


Figure 13. Schematic illustrating the direct inkjet printing technique.

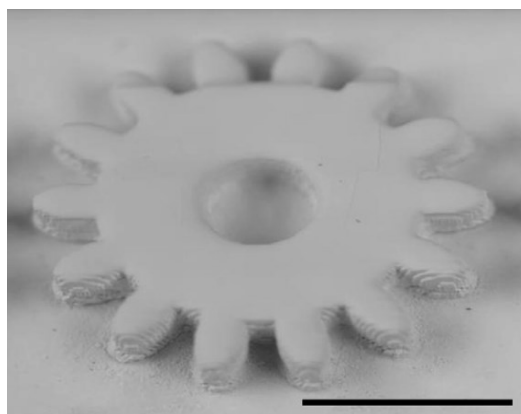


Figure 14. Si_3N_4 gearwheel produced via direct inkjet printing. Scale bar 5 mm. Reproduced with permission from [33].

Fused Deposition

Fused Deposition of Ceramics (FDC) is a rapid prototyping technique which is a modification of an older technique known as Fused Deposition Modelling (FDM).[34] FDM operates by depositing a filament of molten polymer in a pattern set from each slice of a CAD model. The molten polymer is extruded from a long, flexible, solid filament using a hot die and electric motors. The newly extruded material is continuously cooled via conduction from the substrate, and occasionally via a built-in fan. Solidification usually takes place very shortly after deposition, maintaining the part's desired shape. FDM has become the most common AM technique for use in commercial off-the-shelf instruments, largely due to its simple operation principle and its low start up and operating costs. FDC is simply FDM which uses a filament containing a moderate concentration of ceramic particles (20 - 45 vol%). Once the printing is complete, the polymer is burnt out and sintering can proceed. With careful control of the printing conditions and post processing steps, near full density has been achieved for ceramics.[35] The main drawbacks of FDC are the need for support structures for many spanning, overhanging and all floating features, the poor part resolution and the large volume of polymer in the green part which can require extremely slow burn-out schedules and limited densification.

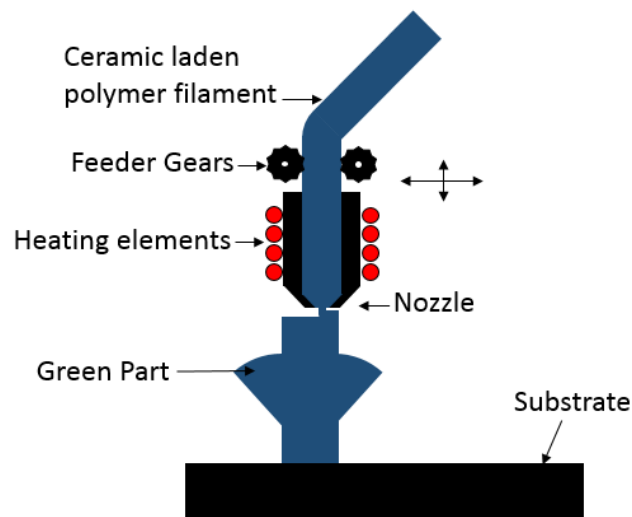


Figure 15. Schematic illustrating the FDC technique.

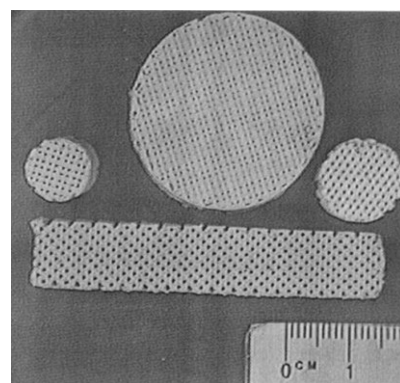


Figure 16. Mullite parts produced by FDC. Reprinted with permission from [36].

Robocasting

Robocasting (also known as “Direct Ink Writing”, “Direct Write Fabrication” or “Robot Assisted Deposition”) is a process that emerged in the mid-1990s at Sandia National Laboratories.[37,38] Objects are built by extruding a filament of pseudoplastic paste (often known confusingly as an “ink” due to the facetious analogy with 2D printers) containing ceramic particles through a nozzle while its position is controlled by a computer taking instruction from a CAD model. Objects are built up in a layer-by-layer fashion, with the nozzle extruding paste in an appropriate pattern for each “slice” of the CAD model. In this respect it shares many similarities with FDC, but it generally relies on pseudoplasticity, rather than solidification, to maintain the part’s shape after the material has been extruded through the nozzle. Nozzles as fine as 30 μm have been used with ceramic pastes,[39] and 1 μm with polymer pastes.[40] Larger nozzles (> 1mm) are also compatible with the process so parts can be built considerably faster than other AM processes. As with FDC, there are difficulties with certain spanning and overhanging features, and all floating features.

There are a number of very closely related AM technologies to robocasting, and the distinction of what distinguishes a separate technique from an adaption to an existing one is not clear. Some examples include “freezeform extrusion fabrication” (FEF),[41] “extrusion freeform fabrication” (EFF),[42] and “ceramic on-demand extrusion” (CODE).[43] In FEF the substrate is cooled below the freezing point of the paste such that the water in the printed part freezes during printing, adding strength to the green part. In EFF the paste incorporates a monomer, and the substrate is heated such that the monomer polymerises on contact, again adding strength to the green part. In CODE each layer is dried before the next layer is deposited while the sides of the part are kept submerged in oil to prevent uneven drying.

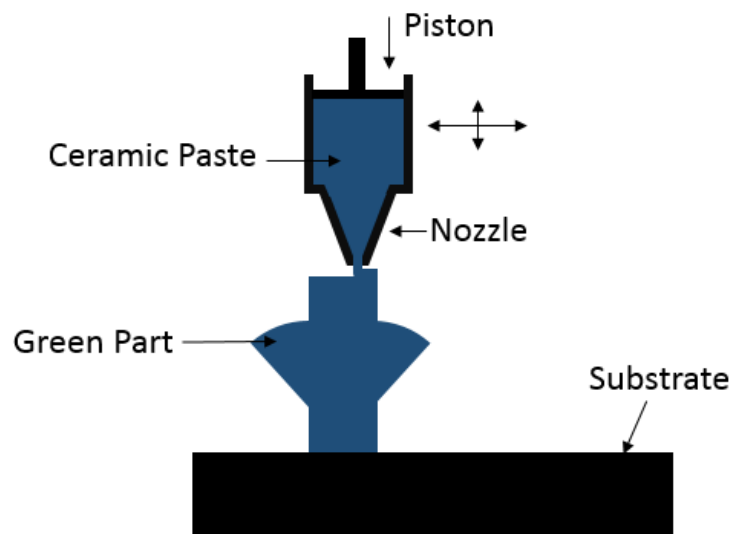


Figure 17. Schematic illustrating the robocasting technique.

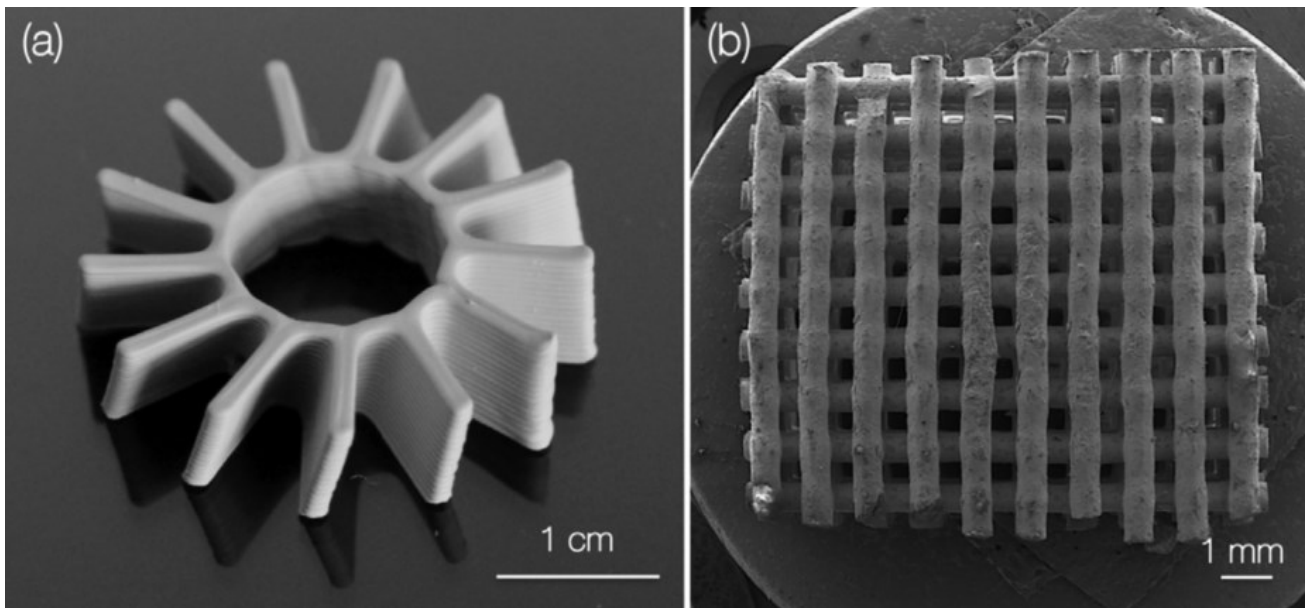


Figure 18. SiC scaffolds produced by robocasting. Reprinted with permission from [44].

Paste Formulations

The properties of the paste are not only crucial, but absolutely central to the robocasting technique. The basic requirements of the paste have been laid out qualitatively in the literature as[45]:

- They must be suitably homogenous (free of air bubbles and agglomerates).
- Their viscosity must be low enough to allow extrusion through a fine nozzle at relatively low pressures.
- They must have an adequate yield stress and storage modulus (stiffness).
- The volume fraction of ceramic powder must be high, to give high green densities which reduce drying shrinkage and allow complete sintering.

Aqueous pastes with low organic content are also preferred, although this is not a necessity. Also, shear thinning behaviour is preferable as it allows the paste to be extruded through smaller nozzles at a lower pressure. Since the advent of robocasting several approaches have been explored to meet each of these criteria. The first pastes were developed by Cesarano et al. and were simply high solids loading (>60 vol%) aqueous suspensions of alumina with <1% organic dispersants.[37,38] They relied on inter-particle forces and surface interactions in the slurry to attain some of the required pseudoplastic properties. They also utilised drying of the filament after deposition to maintain the part's shape; the paste undergoing a pseudoplastic to dilatant transition to give strength to the underlying layers, supporting the layers deposited on top of them.[38] One big advantage of this approach is the very high solids loading possible, which allows for easier densification in post processing and lower drying stresses. However, relying on drying to give strength while printing adds significant environmental

variability to the process and adds limitations, such as reduced potential for overhangs and issues with small nozzles being blocked by highly loaded pastes. Furthermore, homogenisation and preventing agglomerates in these pastes can be difficult. For these reasons, most work has moved away from this primitive, rudimentary paste design.

Recent work has focused on developing pastes by coagulating moderately high solids loading (40 - 50 vol%) slurries. While a range of coagulation methods have been attempted, such as with $\text{Pb}(\text{NO}_3)_2$ and cellulose as coagulation agents,[45,46] by far the most commonly used method has been tailoring functionalised surface interactions of colloidal solutions.[39] For example, ceramic particles can be functionalised with a polyelectrolyte such as polyacrylic acid (PAA), electrosterically stabilising the suspension (as the modified particles repel each other), allowing for good homogenisation. The electrostatic repulsion of these groups can then be decreased and reversed by carefully adjusting the pH[47] or by addition of salts.[39] Lewis et al. have developed a system which has become very commonly used for robocasting, consisting of ceramic particles stabilised by polyethylenimine (PEI). This system allows for the paste to be homogenised in a fluid like state, and then the pH to be brought to the isoelectric point, gelling the paste, giving it the desired rheological properties for robocasting.[1] While this approach is capable of giving desirable flow properties and high solids loading while using a low proportion of organic additives, it is very sensitive to small variations in surface chemistry and pH, which complicates paste production and limits the variety of materials that can be printed with current formulations.

More recent work has explored a different approach to the problem; rather than relying on the surface chemistry and adsorbed species to give the desired rheological properties, the ceramic powder is mixed with a weak hydrogel which acts as a “carrier” for the powder.[48] The inter-particle interactions are therefore less important, and so the paste system is in theory compatible with virtually any powder regardless of surface chemistry.[48] Also, the pastes formed are typically very stable, and can be stored in a gelled state without aggregation for months. Thus far the hydrogel that has received most attention for robocasting pastes is the commercially available Pluronic® F127. F127 is a copolymer of polyethylene oxide (PEO) and polypropylene oxide (PPO) segments in a rough 2:1 ratio. Its chemical structure is shown in Figure 19. It is water soluble and non-toxic. In 20 - 30 wt% solutions with water it forms a hydrogel near room temperature, but counterintuitively acts as a liquid at low temperature. This is due to the adsorption of water to the hydrophobic PPO groups at low temperature, allowing them to slide across each other and flow. At room temperature, however, this adsorption is entropically unfavourable, so the PPO groups are left bare and interact with each other via hydrophobic association, forming a load bearing network of micelles.[49] This behaviour allows pastes to be homogenised at low

temperature, then gelled once mixed to give highly printable pastes.[50] Despite some promising results in the literature, the use of hydrogels for robocasting have only seen limited use thus far.

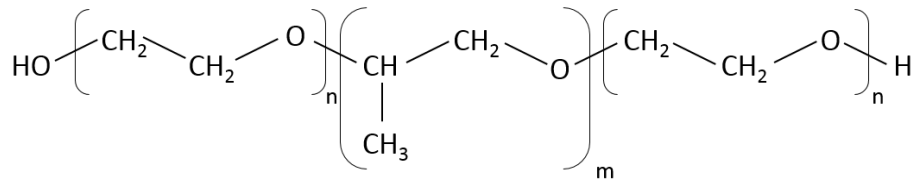


Figure 19. Chemical structure of the Pluronic F-127 polymer, where $n = 100$ (PEO segments) and $m = 65$ (PPO segments), giving an $M_w \sim 12,500$.

Rheology and Extrusion

The rheological behaviour of the paste in robocasting is one of the most important aspects for achieving successful prints. The flow behaviour of these pastes can often be approximated by the Herschel-Bulkley model.[45,51] This model describes ideal non-newtonian fluids which do not flow below a certain stress (the yield stress). When they are stressed above their yield stress, they exhibit shear thinning behaviour, such that their viscosity decreases greatly as shear rate increases. They can be mathematically described by the Herschel-Bulkley equation;

$$\tau = \tau_y + K\dot{\gamma}^n \quad (1.1)$$

where τ is the applied shear stress, τ_y is the yield stress, $\dot{\gamma}$ is the shear rate, n is the shear thinning exponent and K is the viscosity parameter. For robocasting, a low value of n is desirable such that extrusion pressures are reasonably low and to aid mixing. A low K is also desirable for the same reasons, while a high τ_y is needed to prevent collapse of the part after printing, to resist capillary forces pulling the part into a sphere, and to allow the part to support the weight of layers printed on top of it. Unfortunately most of these parameters are strongly dependent on one another; it is very difficult control any one in isolation. Typical pastes possess an n of 0.15 - 0.7, G' of 20 - 1000 kPa, τ_y of 3 - 1000 Pa and K of 50 - 100 Pa.[44,45,50,52] While these are guideline values for common pastes, the true quantitative *requirements* for robocasting have yet to be laid out. This is due to the fact that no such universal requirements exist – the requirements of G' , τ_y , n and K depend entirely on the geometry and scale of the part being printed, the size and shape of the nozzle, the density of the paste, and many other factors. The closest attempt at this level of quantification is that based on calculating the minimum G' required to prevent excessive sagging from first principles, as shown in Figure 20.

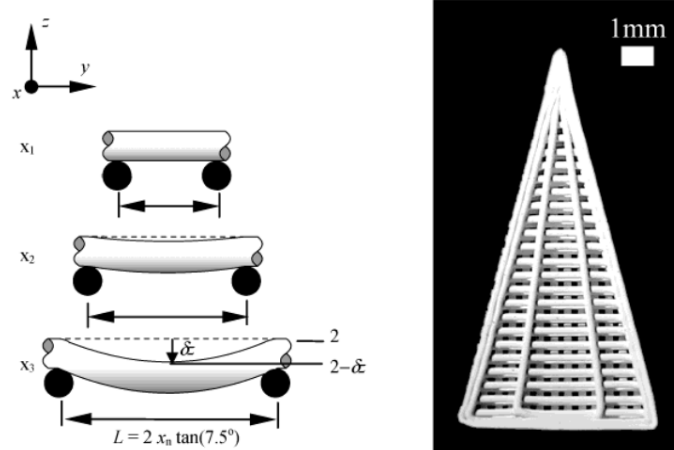


Figure 20. Deflection of spanning structures under gravity and a part used to probe the maximum spanning distance. In this work the pastes possessed a G' of 1 MPa. Reproduced with permission from [45].

The shear thinning behaviour of pastes can come from a number of different mechanisms. The most commonly cited is the alignment of particles with the direction of flow to form preferential flow structures, decreasing the system's viscosity at higher flow rates. This effect is experienced by all systems except for those involving perfectly spherical particles.[53] Colloidal pastes experience additional shear thinning due to the dynamic break-up of particle-particle bonds when sheared, while hydrogel pastes experience shear thinning due to the reversible disruption and breakdown of the hydrogel network under stress. A low value for K ensures the paste can be mixed and homogenised with relative ease.[50]

As the paste flows through a cylindrical nozzle, the material never all flows at one uniform velocity; a velocity profile develops. For a Newtonian fluid the profile will be a simple parabola, with the fluid furthest from the nozzle wall travelling fastest, and the fluid touching the nozzle wall being stationary. However, for Herschel-Bulkley fluids, the velocity profile is less simple;

$$V(r) = \frac{2nL}{\Delta P (n+1)} \left(\frac{1}{K}\right)^{\frac{1}{n}} \left[\left(\frac{\Delta P R}{2L} - \tau_y\right)^{\frac{n+1}{n}} - \left(\frac{\Delta P r}{2L} - \tau_y\right)^{\frac{n+1}{n}} \right] \quad (1.2)$$

where ΔP is the pressure drop over the nozzle, n is the shear thinning exponent, τ_y is the yield stress L is the nozzle length, K is the viscosity parameter, R is the nozzle radius and r is any point between the nozzle centre and R .[54] This can be readily differentiated, giving:

$$\frac{dV}{dr} = \left(\frac{1}{K}\right)^{\frac{1}{n}} \left(\frac{\tau_w r}{R} - \tau_y\right)^{\frac{1}{n}} \quad (1.3)$$

The added complexity for Herschel-Bulkley fluids is due to the presence of a yield stress, and the fact that the material nearer the wall has a lower viscosity than the material in the centre of the nozzle (due to its shear thinning nature).

In order to choose appropriate volume fractions in any paste, the maximum possible packing fraction must be considered. This provides the upper limit to the volume fraction, the point where particles are randomly packed in the closest configuration allowable, however the selected volume fraction will typically be substantially below this, as the suspension's viscosity increases exponentially as the maximum packing fraction is approached. This behaviour can be empirically fitted to the Krieger-Dougherty model;

$$\eta_r = \left(1 - \frac{\varphi}{\varphi_m}\right)^{-[\eta]\varphi_m} \quad (1.4)$$

relating relative viscosity η_r to volume fraction φ , maximum theoretical volume fraction φ_m and intrinsic viscosity $[\eta]$. Depending on the paste formulation, the volume fraction of the ceramic phase ranges from 0.07 - 0.65.[55,56]

Printability

One key concept in robocasting is 'printability'. Printability is a measure of how suitable a paste's properties are for robocasting. There has only been two attempts to formally define printability in the literature. The first simply considers the minimum G' required to print spanning structures.[45] The second attempt determines the yield stress required to withstand the forces of gravity and surface tension, compiling each factor into a figure of merit:[57]

$$\mathcal{E} = \frac{\sigma_y}{\rho g h + \gamma_s R^{-1}} \quad (1.5)$$

where \mathcal{E} is a figure of merit, σ_y is the paste's yield stress, ρ is the density of the paste, γ_s is the surface tension, h is the height of the part, g is gravitational acceleration, and R^{-1} is the radius of curvature of the smallest printed feature (in most cases the radius of a single filament). This goes further than any previous attempt to define printability, however \mathcal{E} is not a paste-specific figure of merit, as it depends on both paste parameters and part parameters.

Structures of Individual Robocast Filaments

During standard robocasting, a continuous, monolithic filament of material with a circular cross section is extruded. This is the simplest repeat unit, and arguably the most versatile for the majority of applications of robocasting, however a number of alternative filament structures have been investigated. Filaments with a foamed structure have been printed recently by Minas et al.[58] and Muth et al.,[59] and earlier by Moon et al.[60] Foamed filaments can be achieved by introducing stable

bubbles or droplets into the paste to form an emulsion. Micron-scale bubbles/droplets can be stabilised by functionalising the surface of the ceramic powder with amphiphilic molecules which cause the ceramic particles to cluster on the liquid-gas (or liquid-oil) interface, known as a Pickering emulsion. Following sintering, these features are retained. When these foams are printed into scaffold geometries, a part with porosity on multiple length scales is obtained, see Figure 21, with large pores between each printed filament and smaller stochastic porosity within each filament. It is claimed that this hierarchical structuring results in improved strength to weight ratios and may find uses in catalyst support, thermal insulation, electrode and tissue scaffold applications.

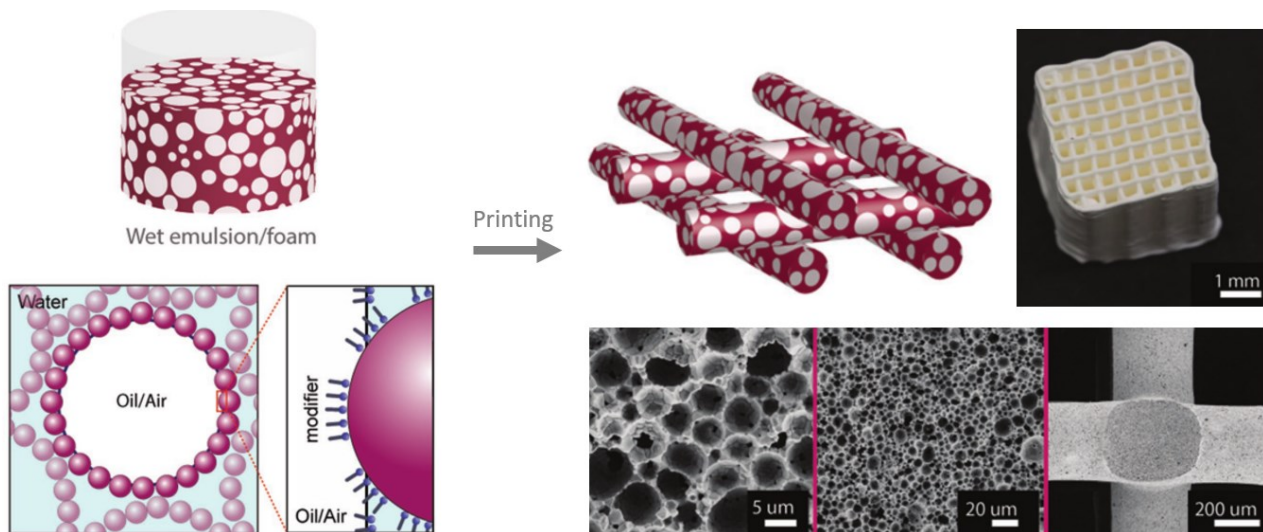


Figure 21. Simplified explanation of the robocasting of foamed materials. Adapted with permission from [58].

The production of scaffolds with hollow struts (filaments) has also received attention,[60–62] again due to the increased controlled porosity and surface area that this geometry brings, as seen in Figure 22. This has been achieved by either modifying the nozzle with a mandrel,[61] or by coextruding a sacrificial material through the nozzle alongside the material to be printed.[60] The latter method has been more successful in creating complex, detailed parts due to the fact that it is difficult to fabricate functional mandrel nozzles on micron scales. Additionally, the hollow filaments are more stable when they are filled with a sacrificial material which can be removed following drying, when the part has a higher green strength.

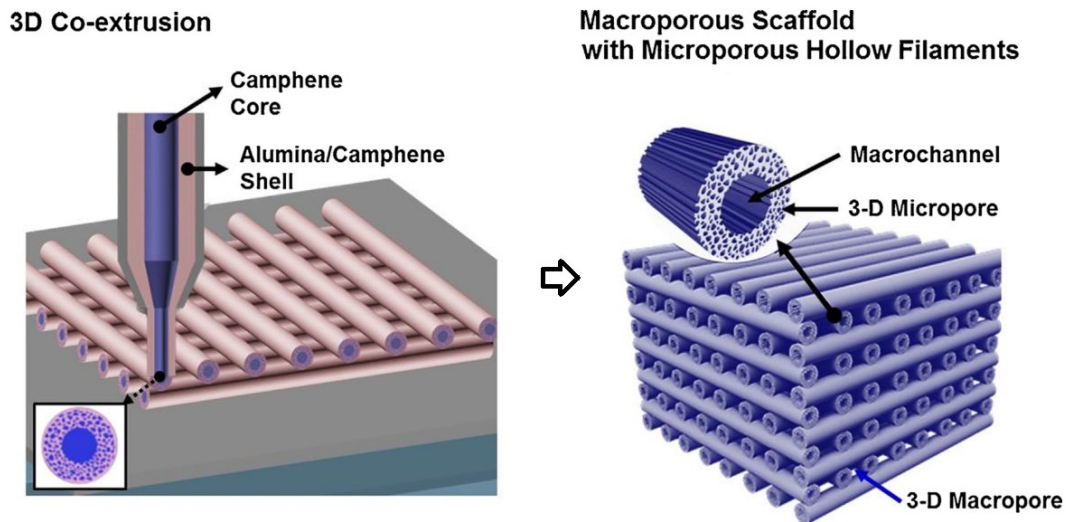


Figure 22. Schematics representing the robocasting of hollow filament lattices via coextrusion. Reproduced with permission from [60].

Robocasting of filaments with a non-circular cross section has also been explored briefly.[63] In order to achieve this, microscopic dies were fabricated using lithography methods, and extrusion of the filament took place through these dies. While the structures produced are undoubtedly aesthetically pleasing, see Figure 23 and 24, no explicit application is mentioned in this work, and the utility of this research is unclear.***

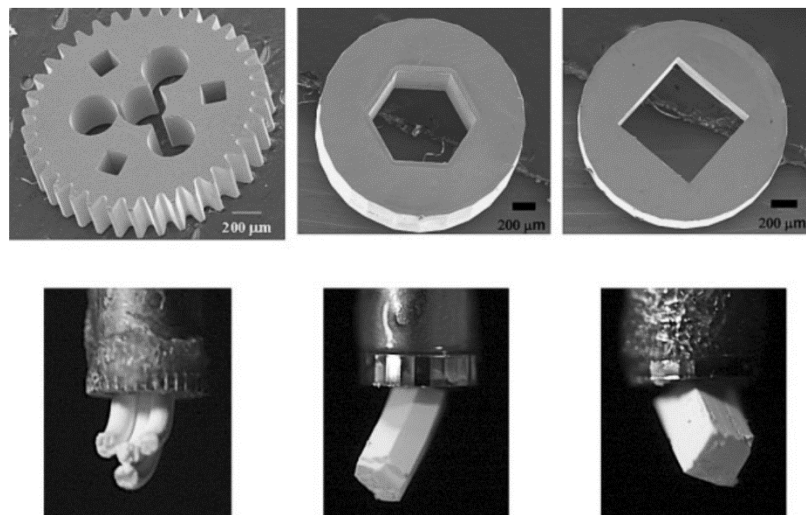


Figure 23. A range of micro-extrusion dies fabricated via stereolithography. Reproduced with permission from [63].

***One could argue that square and hexagonal filaments should aid their packing when fabricating monolithic parts, however this would require control of the orientation of the filament (I.e. by rotating the die). This capability that has not been attempted.

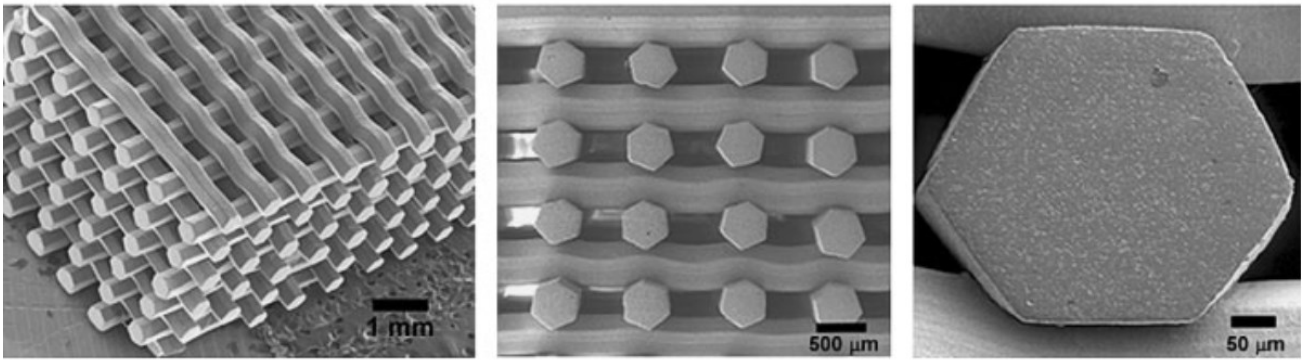


Figure 24. Lattice structures produced using a die from Figure 23. Reproduced with permission from [63].

Structures of Robocast Parts

The largest limitation of robocasting is the level of detail (resolution) and complexity possible in printed parts. “Resolution” can be defined in a number of ways, but it is usually closely related to the size of the nozzle. Thus to improve resolution, smaller diameter nozzles must be used, however this increases the build time and the extrusion pressure exponentially. For this reason, it is uncommon for nozzles with diameters smaller than 200 μm to be used with typical ceramic pastes.[55] Thus with current approaches the smallest addressable feature that can be printed is limited to a length scale of $\sim 200 \mu\text{m}$, and surface roughness will be of a similar order of magnitude due to step-edges. For comparison, LCM has demonstrated resolutions of 40 μm in the x-y build plane, 25 μm in the vertical build direction, and surface roughness of 0.36 μm . Very large overhangs and spanning features are also possible in LCM due to the high green strength of the part, while these features are difficult in robocasting as the viscoelastic properties of the paste must be relied upon to give strength during printing. For these reasons, robocast parts are usually very crude, rarely venturing beyond basic shapes such as grids, cubes, cylinders and single-walled vases. The parts presented in Figures 25 and 26 are among the most complex ever produced by robocasting. This is undoubtedly the biggest drawback of robocasting compared to other AM methods, and must be addressed before the technique can be even considered as a viable general ceramic AM method.

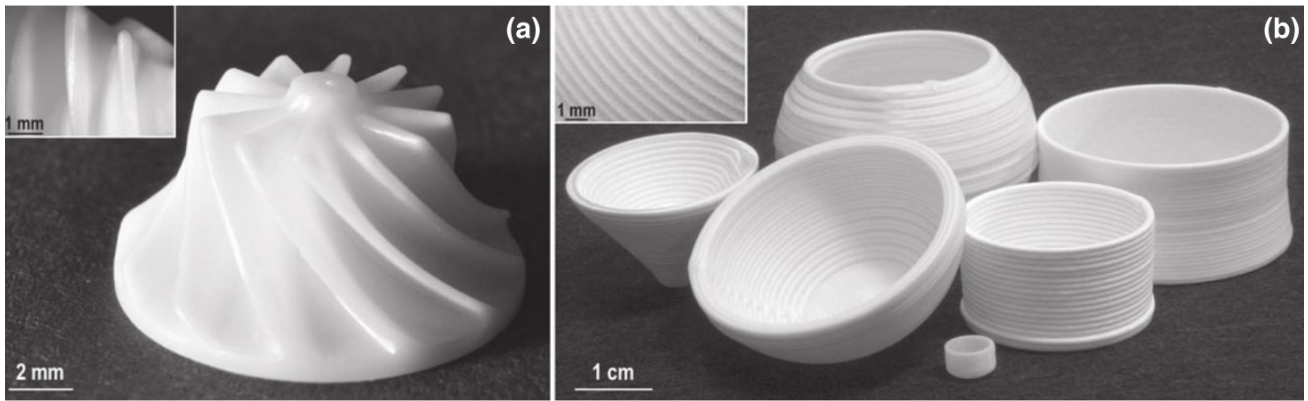


Figure 25. Photographs of: (a) A ZrO_2 part produced by LCM and (b) Al_2O_3 labware produced by Robocasting. This starkly illustrates the difference between the resolution and complexity capabilities of these two techniques. Reproduced with permission from [64].

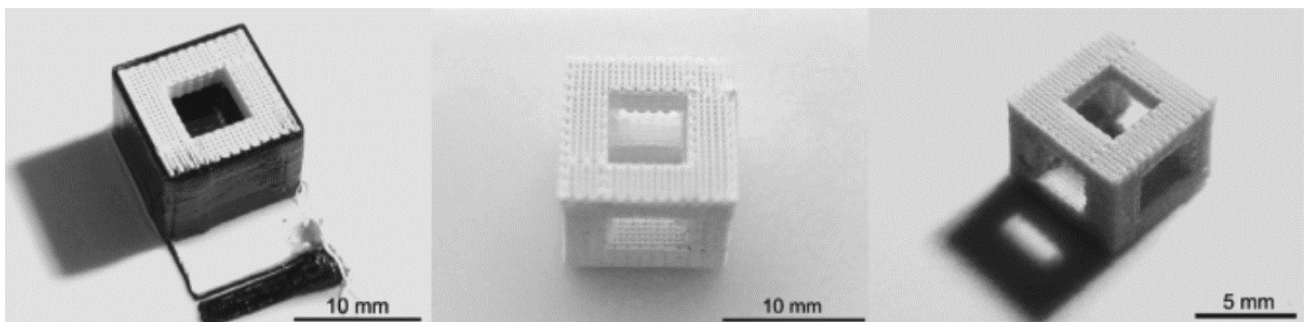


Figure 26. A rare example of a robocast part with overhanging features, utilising a multimaterial robocasting instrument to print sacrificial support material (a paste based on carbon black in this case). Reproduced with permission from [1].

Applications

At this time robocasting has been relatively limited in the scope of its commercial applications. By far the most common application is in the production of woodpile style scaffolds.[30,48,50,65–72] Robocasting is particularly well suited to manufacture this geometry compared to other additive manufacturing techniques, and allows load bearing 3D architectures with precisely controlled porosity to be fabricated quickly and relatively cheaply, and is presently seeing commercial use in this area.[73] These scaffolds are thought to have great potential in tissue engineering, particularly for the production of bio-compatible bone grafts, and tend to exhibit much greater compressive strength than stochastic foams of the same porosity, allowing inflow and ingrowth of blood and tissues which assists in the recovery of the injury. Other work has looked at using scaffolds for filtration where high temperature resistance is required,[74] as a catalyst support to maximise surface area,[43] and as the reinforcing phase in interpenetrating phase composites (following infiltration with polymers or alloys[75]). Simple alumina labware produced by robocasting is also presently commercially available.

Robocast Materials

Monolithic Ceramics via Robocasting

In the field of AM of ceramics, the majority of work has focussed on printing well studied, monolithic parts using common, well studied ceramics such as alumina,[76] zirconia,[42] or silicon carbide.[77] Many techniques are quite flexible with regards to composition and can print most common ceramic powders. However there are often a number of restrictions, unique to each printing technique, most prominently with SLA and SLS/SLM. In SLA the optical properties of the photomonomer slurry have to be carefully tuned to allow adequate curing of the monomer slurry by the light source, thus the size and refractive index of the ceramic particles in the slurry need to be taken into account. In SLS/SLM the sinterability of the powder bed is crucial; SLM is simply not possible for ceramics which do not readily melt (such as SiC).

As mentioned above, being able to print the material is only the beginning of an engineer's trials and tribulations; the material properties of "successfully" printed parts can vary greatly between techniques. For load bearing parts the first property to consider is always density, as a high residual porosity must be avoided in order to preserve mechanical performance. In cases of porosity >10%, the literature typically quotes compressive strength rather than bending strength. Looking beyond residual porosity, even parts above 95% theoretical density can exhibit poor mechanical properties. Printed parts suffer from all of the usual ceramic processing defects, such as agglomerates, bubbles, contaminates/inclusions, and large grains. Additionally, there are a number of defects that are fairly unique to AM: surface defects due to poor finish/step edges, defects between printed layers,[19] and thermal shock defects.[6,11] For most techniques the printing defects remain the strength limiting defects, and the end goal is for the strength limiting defects to be microstructural. In other words the goal is to get to the point where the material is no more defective than material produced using traditional processing.

Robocasting is perhaps the most versatile AM technique when it comes to composition. The literature has so far shown that any powder that can be made into a slurry can be printed in the right conditions. The principal restriction is on particle size – nano powders result in prohibitively viscous slurries,[78] while coarse powders can cause blocking of the nozzle.[45] Strength and density of robocast parts are typically high compared to other methods. This is mainly because robocasting is a "wet" process, resulting in high green densities, and thus sintering can proceed to completion. The reliability of robocast material is less well studied – the Weibull moduli for dense parts produced by robocasting or related processes has only been reported once.[79] This is an important gap in the literature. Other mechanical properties such as hardness and elastic modulus are generally in the expected range for

traditionally produced material of the given density, while toughness has not been notably studied as it is expected to be comparable to conventionally produced material. Some basic mechanical properties have been demonstrated for a range of robocast ceramic materials, as shown in Table 1. As sintering is performed separately from printing, it can be done using conventional conditions using conventional furnaces. Given a printed part with a high green density and no large printing defects, it is reasonable to state that the mechanical properties of any robocast material should be comparable to that material produced by traditional manufacturing methods. This is why robocasting is considered such a flexible technique when it comes to material choice, however these conjectures have yet to be fully demonstrated in the literature.

Table 2. Range of ceramic materials printed by robocasting, with bending strength where applicable. (*) Indicates most available work has been on scaffolds, which are typically tested in compression rather than bending.

Material Family	Material	Density (%)	Strength (MPa)
<i>Oxides</i>	Al ₂ O ₃ [76]	97	310
	Ca ₃ (PO ₄) ₂ [67]	99	*
	Hydroxyapatite [67]	97	*
	Bioglass (various) [80]	98	*
	Mullite [81]	96	-
<i>Carbides</i>	C (carbon black) [1]	-	-
	SiC [77]	98	-
	ZrC [82]	62	73
<i>Nitrides</i>	Si ₃ N ₄ [83]	99	740
<i>Borides</i>	ZrB ₂ [84]	96	-
	B ₄ C [85]	82	-

Polymer Matrix Composites and Metal Matrix Composites via Robocasting

Despite showing very attractive thermomechanical properties, low density, and excellent corrosion resistance, ceramic materials are notorious for their prohibitively low toughness, typically exhibiting a $K_{IC} < 10 \text{ MPa}\sqrt{\text{m}}$. Even the most basic engineering alloys put this toughness to shame, exhibiting toughness values an order of magnitude greater than this.[86] This stark fact has greatly limited the use of ceramics in load bearing components due to the inherent reliability issues that come with the fact that they fail catastrophically, rather than via gradual plastic deformation that can be monitored over time.[87] For decades, industry and academia have attempted to increase the toughness of structural ceramics using a wide range of mechanisms and approaches. One approach of promise is ceramic composites, where a ceramic material's properties can be combined with another material's, for example to give acceptable toughness without greatly compromising strength.[88] An enormous number of materials systems are possible, each generally falling into the categories of "polymer matrix

composite" (PMC), "ceramic matrix composite" (CMC) or "metal matrix composite" (MMC). Within each category, the reinforcing material may take the form of fibres (long and short), platelets, flakes, particles or an interpenetrating network. Fibres and whiskers usually bring the greatest proportional benefits to mechanical properties, but are often expensive, hazardous to handle,[89] and agglomerate at low volume fractions,[90] while platelets[91] and powders[92] are not as effective at reinforcing but are generally safer, cheaper, and easier to handle.

Composite materials have garnered an increasing level of attention for many decades, with the archetypal PMC "carbon fibre reinforced polymer" spearheading the class of materials, with specific strengths greatly exceeding that of high strength steel or advanced titanium alloys. In the aerospace sector for example, major engine manufacturers are currently developing or producing jet engines with PMC and MMC fan blades,[93] CFRP nacelles and CMC combustion chambers.[94] The latest generation of commercial aircraft now often constitute >50% by weight composite materials, with entirely PMC wing sections and fuselages.[95] Benefits such as high specific strength and stiffness, corrosion resistance and high temperature properties (in the case of CMCs and MMCs) often greatly offset drawbacks such as unclear fatigue properties, high costs incurred in manufacture, reasonably poor impact resistance and issues with recycling.[96]

To date robocasting of ceramic composites is a relatively scant area of research, and represents a sizeable gap in the literature. Current production methods can either be considered "direct", where the matrix and reinforcing material are deposited in the same AM step, or "indirect", where a preform is printed and the matrix material is infiltrated in a later process.

Most work has looked at the indirect approach, printing the reinforcing material followed by pressured or pressureless infiltration of a liquid metal, liquid polymer, or ceramic slurry. Some of these systems include $\text{Al}_2\text{O}_3\text{-Al}$, [97] Mullite-Al, [34,98] $\text{Al}_2\text{O}_3\text{-Al}_2\text{O}_3$, [99] and Glass-Polymer. [70] In each case a macroporous ceramic preform is fabricated by an AM step and sintered to partial density. This can either take the form of a porous solid piece, or a dense scaffold. The matrix material is then infiltrated into the pores and spaces in the preform. The resulting structures are usually quite crude. A sceptical reader might suggest that in some cases the true motivation for production of such composites is not due to any interest in the composite system, but simply to offset the poor densification inherent to many ceramic AM techniques, filling the pores with another material as a way to eliminate them.

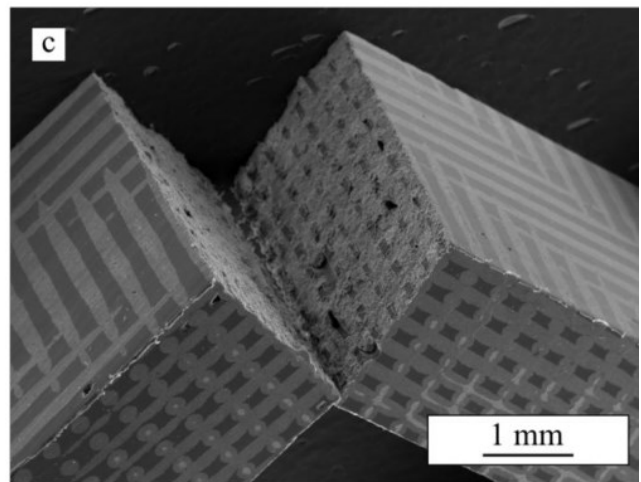
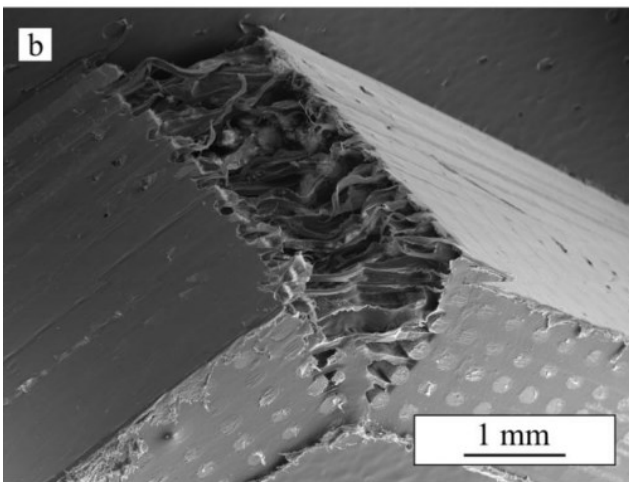
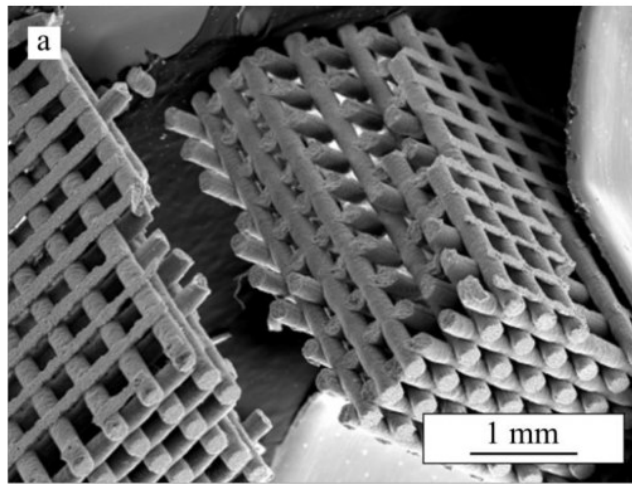


Figure 27. SEM images of: (a) fracture of a tricalcium phosphate scaffold (b,c) fracture of scaffolds infiltrated with two different polymers, forming an interpenetrating phase composite. Reprinted with permission from [71].

There has been some research into the potential for composites to be additively manufactured more directly, mostly on PMCs such as epoxy-SiC,[100] epoxy-carbon fibre,[101,102] epoxy-glass fibre,[103] and ABS-carbon fibre[104] systems. One advantage of this method is that anisotropic reinforcement particles tend to align in the direction of printing/extrusion, see Figure 28. This allows the exciting prospect of unprecedented control of a part's anisotropic properties at the CAD stage, fully exploiting toughening mechanisms such as fibre pull-out and crack deflection in the areas of the part that they are most needed. Furthermore, a large amount of work has reported on the unusual rheology and flow properties of platelet[105] and fibre[106,107] slurries, alone as well as mixed with powders. It is not farfetched to consider that this work could be applied to directly fabricate a range of CMC systems by flow based AM techniques such as robocasting or FDM. In terms of tensile strength these robocast PMCs offer improvements compared to the matrix material in the range 20 - 120%, however reported strengths have still not exceeded 100 MPa.[100] This is far below typical values for traditional CFRP, which typically demonstrate tensile strength in excess of 1 GPa, however these values are for long fibre composites, while most composites produced by AM are usually short fibre composites.

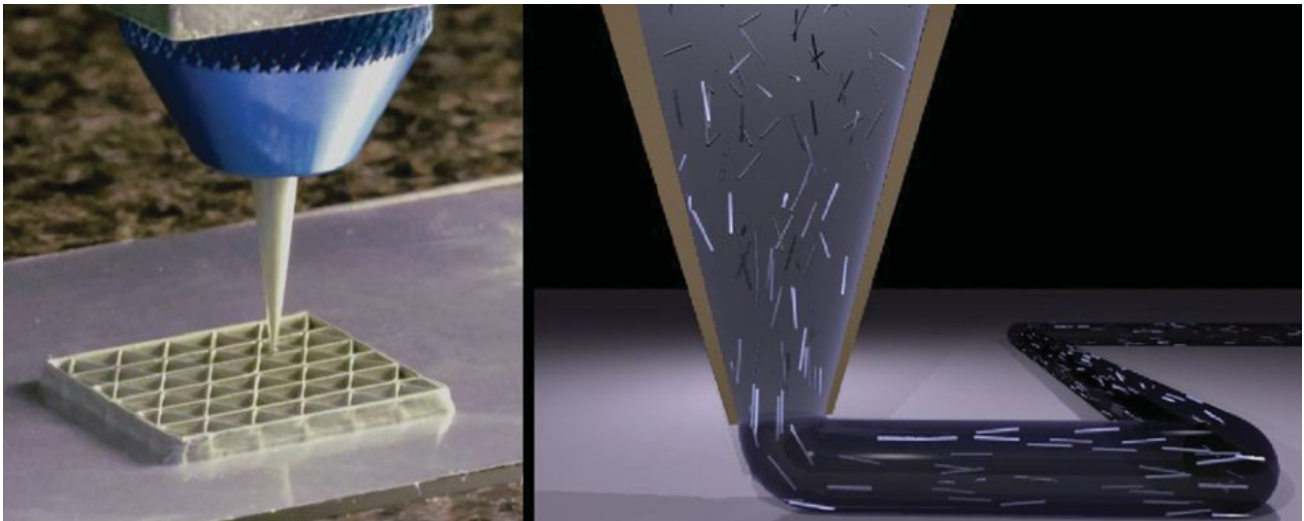


Figure 28. Robocasting of an aligned Cf-Epoxy composite. Reproduced with permission from [100].

Ceramic Matrix Composites via Robocasting

CMCs are a class of composites that have been developed primarily to improve upon the toughness of monolithic ceramics while maintaining their inherent thermomechanical properties. Most CMCs achieve this by incorporating strong reinforcing particles such as fibres into a ceramic matrix during processing. The largest application of this class of materials is in disc brakes in the automotive field, specifically carbon-carbon composites,[108] however they are increasingly being used in the aerospace sector for hot areas in jet engines, and are being used and developed as the choice materials for heat shields of space vehicles during atmospheric re-entry. All of these applications arise from the need of materials that can withstand mechanical loads at elevated temperatures, and not suffer from brittle failure due to thermal shock.

Processing of CMCs is typically much more complex and expensive than processing monolithic ceramic parts, and almost any other engineering material. This is often due difficulties densifying the matrix phase without damaging the reinforcing phase and the laborious layup processes required to build complex shapes. While the individual reinforcing particles are often spectacularly strong (e.g. 3 GPa SiC whiskers[109]), these properties are rarely approached in CMCs utilising them. In fact, most CMCs exhibit lower strength than the monolithic matrix material, mainly due to higher residual porosity, damage from the infiltration process, and weak fibre-matrix interfaces. Thus, the motivation for the production of CMCs is not to increase strength, but to increase toughness, usually to facilitate higher thermal shock resistance and promote graceful failure over catastrophic failure.

Given the difficulties of AM of simple ceramic materials, there has been little work attempting AM of CMCs. One study has produced SiC/SiC via LOM,[24] an appealing prospect due to the analogy with the

layup process of prepregs in the manufacture of CFRP. However, the mechanical properties were not studied, and are unlikely to compare favourably to CMCs produced by traditional methods such as chemical vapour infiltration (CVI) or polymer infiltration and pyrolysis (PIP).

In another study, Cf-SiC was produced via robocasting by printing pastes consisting of a preceramic polymer and carbon fibres.[110] While this approach may hold promise for certain parts, the shrinkage of the preceramic polymer during pyrolysis makes monolithic parts near impossible.

Despite this, successful AM of CMCs remains a much coveted goal. The applications that CMCs address tend to require small production runs, or entirely bespoke components, using manufacturing lines that are likely to incorporate AM as the technology matures further. This is one area that is ripe for further research and development.

Conclusions

AM of ceramics is an especially broad and fast developing field. No single technique has yet to demonstrate universal superiority overall, although SLA and robocasting show noteworthy promise for dense, strong components. It is entirely possible, and in fact very likely, that no single technique will be appropriate for all part designs and materials, thus a number of distinct techniques will be developed in tandem. For example, even after hundreds of years of development there is no single optimal way to produce all steel parts; depending on the specification of properties and geometry, forging, rolling, or casting may be appropriate. The same reasoning applies to AM of ceramics.

In terms of mechanical properties, parts produced by SLS/SLM, inkjet printing, DED and LOM all suffer serious shortcomings, while parts produced by STL, fused deposition, and robocasting have demonstrated adequate strength for many ceramic engineering applications. All of the techniques except for fused deposition and robocasting are significantly hindered by printing speed and sample volume. Meanwhile, robocasting, LOM, inkjet printing, and fused deposition all exhibit serious failings at producing high resolution, complex parts.

Hydrogel paste systems for robocasting have been tentatively studied in the literature, but the rheology of these pastes have not been investigated in depth. The mechanical properties of parts produced by robocasting have yet to be fully examined, and there have not been any attempts to identify how the printing process may introduce strength limiting defects. The flexibility of materials selection that robocasting affords makes it ideal for direct AM of complex composite systems, but many of these possibilities have yet to be explored.

Aims and Objectives of this Thesis

The aim of this thesis is to further develop the robocasting technique and to examine its place among the diverse family of ceramic AM techniques, exploring the range of printable ceramic composites and structures. It also aims to characterise printability, mechanical properties, and other physical properties of printed material in order to attempt to solve some of the issues it experiences when printing complex, high resolution parts.

The following six objectives are set out in order to tackle this rather broad goal:

- Study the relationship between rheological properties and paste characteristics (such as ceramic volume fraction, binder content, powder type, powder surface chemistry and dispersant use) in order to determine best-practice for paste design.
- Develop a further understanding of the role of rheology in the printing process, identifying the rheological properties that allow a paste to be successfully printed, and set out the range of values that these properties can take for optimal printability.
- Identify the optimal printing parameters for the production of dense, monolithic ceramic parts, and study the effect of these parameters on density, mechanical properties and reliability of simple test bars.
- Investigate the range of particle types (such as fibres, platelets) that can be successfully printed, and identify the key particle features (size, morphology, surface chemistry) affecting the rheological behaviour of pastes utilising these particles, and how this affects printability.
- Investigate a number of promising composite systems based on these particles, and interrogate the microstructures obtained from printing, the factors affecting post processing, and the mechanical properties of a range of printed composites.

Chapter II – Methods

Powder Processing

Powder Pastes

Alumina powder (SMA6, Baikowski, FR) was sieved using a vibratory sieve to below 100 μm to remove large agglomerates. Alumina milling media were placed in the top of the sieve to speed up the process, typically taking 5 - 10 hours. α -Silicon carbide powder (UF-25, H.C. Starck, DE) was mixed with 6 wt% alumina (SMA6, Baikowski, FR) and 4 wt% yttria (Grade-C, H.C. Starck, DE) as liquid phase sintering aids[111] in methylethylketone for 24 hours with Si_3N_4 milling media in a roll mill, followed by drying in a rotary evaporator and sieving to below 100 μm . The Al_2O_3 powder used in this work was produced by spray drying, and so consisted of large ~ 0.5 mm granules. These were not found to break up easily during mixing and paste production, giving rise to pastes with visible agglomerates which printed poorly and blocked nozzles. In order to solve this issue, sieving was employed. Alumina milling media in the top sieve assisted in breaking the granules down into sizes that could be dealt with by the Thinky mixer. For very long sieving times it was observed that the powder started to agglomerate again, forming large pieces in the bottom pan. These pieces broke up easily during paste production so they were not considered to be a problem. In the case of the SiC pastes, the Al_2O_3 and Y_2O_3 additives were not found to disperse homogeneously throughout the paste, instead forming oxide rich agglomerates which did not disperse during mixing. The wet mixing in the roll mill and sieving was found to overcome this issue.

For powders, particle size distributions were measured by the Laser Scattering technique in a Mastersizer 2000 using 2 minute scans. The results reported are the average over 3 scans. For platelets the dimensions (average diameter and thickness) were measured using SEM. For fibres the diameter was measured using SEM while the length distribution was measured by scattering fibres on a glass slide and measuring the lengths of >100 fibres via optical microscopy.

A Pluronic stock solution was made by adding 50g of Pluronic F-127 powder (Sigma-Aldrich, UK) into a flask of 150g of deionised water at low temperature (0 - 5 $^\circ\text{C}$) and leaving to rest at this temperature in a refrigerator until a homogenous solution is obtained (typically within 48 hours). The desired volume of this stock solution can then be added to a cooled 150ml PTFE jar (Thinky, USA), along with any dispersants. Pre-weighed ceramic powders were then added to this jar in a stepwise manner, stirring constantly with a spatula, to prepare roughly mixed pastes. This process takes place in an ice bath to ensure the pluronic is in a liquid state to facilitate mixing. It is important that material is not left stuck to the inside sides of the jar, and this material can fall in later and act as agglomerates in the paste.

It is also possible to complete this process without making the stock solution; in this case, water and dispersant are added to the ceramic powder first to obtain a slurry, and then dry Pluronic F-127

powder is added to the slurry. This approach tends to be beneficial when a homogenous initial slurry is required, for example when using powders with hard agglomerates which need to be sonicated in the slurry form first. When sonication was required, it was performed for 1 minute at maximum power, with a 1 second interval, using a SciMED 200 W horn sonicator. Next the paste is mixed in the Thinky ARE-250 mixer at 2000 RPM for 1 minute followed by cooling to 0 °C in the ice bath. The mixing speed can be reduced to 1000 RPM and the mixing time increased to 10 minutes if the paste is becoming excessively hot, or if agglomerates are persisting. Alternatively if the paste is not becoming excessively hot during mixing then it may be mixed for 10 minutes at 2000 RPM. This is repeated until a visually smooth paste is obtained, typically 3 - 6 mixes are required depending on the total mass of paste and the powder used. Furthermore, when using coarser powders/particles ($>5 \mu\text{m}$), the paste may never appear visually smooth, and can possess a “grainy” texture, whilst still being printable through large ($>200 \mu\text{m}$) nozzles. Care needs to be taken to identify whether the paste possesses agglomerates at this stage, doing so will save a great deal of time and frustration with blocked nozzles later on.



Figure 29. The Thinky ARE-250 planetary mixer. Courtesy of Intertronics Ltd.

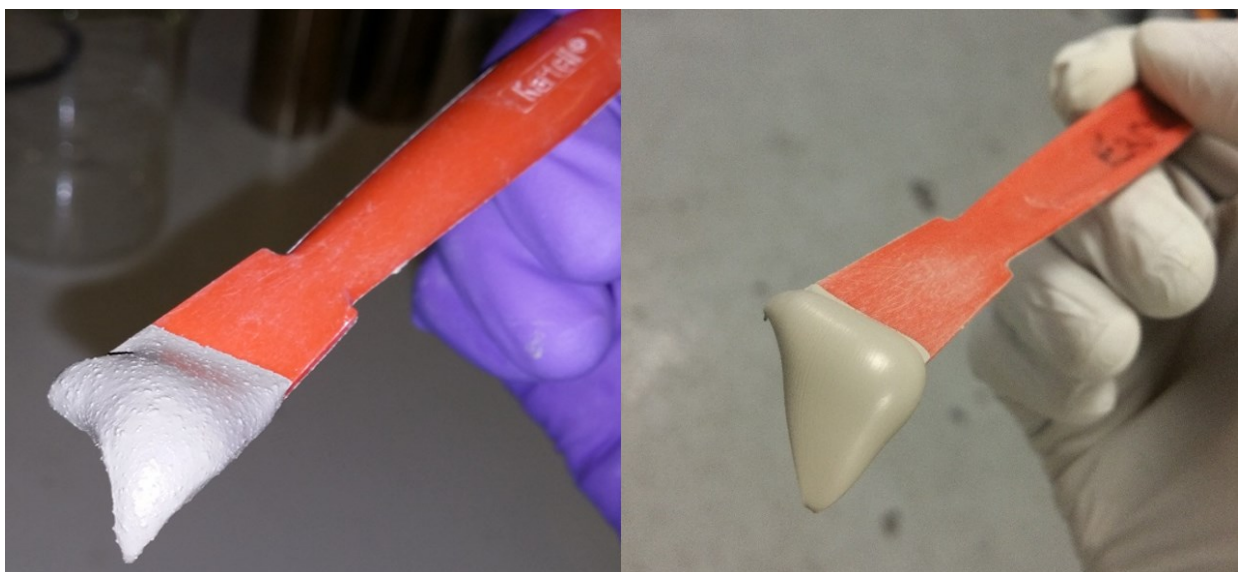


Figure 30. A 36 vol% SiC after 2 rounds of mixing (left) and 8 rounds of mixing (right). The paste on the left blocked nozzles smaller than $610 \mu\text{m}$.

The pastes were then defoamed at room temperature for 10 minutes at 2200 RPM in the Thinky mixer (defoaming when cold can cause segregation of the powder and liquid). As above, the required defoaming time depends upon the total volume of paste, with larger volumes requiring longer defoaming time (as the trapped bubbles have further to travel to be removed). The pastes can then be stored for up to 3 weeks at room temperature in these containers. If stored for substantially longer than this, then they often begin to reject water, resulting in condensation on the sides and top of the jar and a cracked, dry paste.

The pastes can then be loaded into either 3 or 12 cm³ syringe barrels (Nordson EFD) for printing. This is achieved by scooping the paste out of the mixing jar with a flat spatula, and spreading it over the top mouth of a 12 cm³ syringe, being careful to ensure no air bubbles get trapped between successive scoops. This process becomes more difficult as more paste is loaded, and typically only ~8 cm³ is possible. For lower volume fraction pastes which turn to a low viscosity liquid at low temperature, the paste can simply be sucked up with the syringe (avoiding the scooping process described above). This syringe can then be connected to a 3 cm³ syringe barrel using a female-female luer lock connector, and extruded from one to the other, leaving a ~1cm³ gap to allow for the piston and top cap to be inserted. Highly loaded pastes may require cooling to allow this to take place easily. Once loaded into the desired syringe barrel, syringe caps can be attached to prevent drying, and they have a pot life of months if they are stored in the gelled state above 18 °C, as long as the powder isn't reactive with water.

Platelet Composite Pastes

In order to produce platelet pastes, a similar method to the one presented above is used. The sieved alumina powder from above was mixed with alumina platelets provided by Advanced Nano Technologies Ltd., AU, at a mass ratio of 3:7. 20 g of this powder mixture was then added to the mixing jar with 8 g deionised water and 0.1 g of the dispersant Dolapix CA (Zschimmer & Schwarz, DE). This was mixed by hand followed by sonication with a SciMED 200 W horn sonicator for 60 seconds to break agglomerates. 2.75 g Pluronic copolymer (F-127, BASF, DE) was then added, followed by four rounds of mixing in a Thinky ARE-250 planetary mixer at 2000 RPM for 2 minutes, cooling the container in an ice bath between steps. Finally the paste is defoamed in the Thinky mixer at 2200 RPM for 15 minutes. This step is critical to remove bubbles, which are particularly pervasive in pastes involving platelets. Pastes were then cooled again and transferred to 3 cm³ syringe barrels ready for printing in the same manner as above. Overall the optimised pastes are 65 wt% (31 vol%) ceramic material.

Fibre Composite Pastes

Likewise, a very similar procedure to those presented above is used to produce fibre pastes. The fibres used in this work are 7 μm diameter PAN derived carbon fibres, supplied by EasyComposites UK, which have been chopped/milled. When handling this material in the dry state it was important to work in a fume hood with particle filter to avoid inhalation hazards. Once they are in a paste-like state this risk is mostly eliminated. The principle difference between producing powder pastes and fibre pastes is the maximum achievable volume fraction and issues with forming bubbles, discussed later. These issues were overcome by using significantly lower solids loadings, and by increasing the defoaming time to 30 minutes at 2200 RPM.

Rheology

The majority of the literature uses parallel/cone plate rheometry to study the rheological properties of robocasting pastes.[45,83,100] This involves placing a volume of paste between two metal plates and applying a torque to the plates, measuring the resulting angular displacement. This method has generally been favoured as it only requires a small amount of paste, is reasonably quick, and is well suited to highly viscous pastes. Despite this, other rheometry techniques have been used, such as capillary rheometry[50,112] and concentric cylinder rheometry,[52] illustrated in Figure 31.

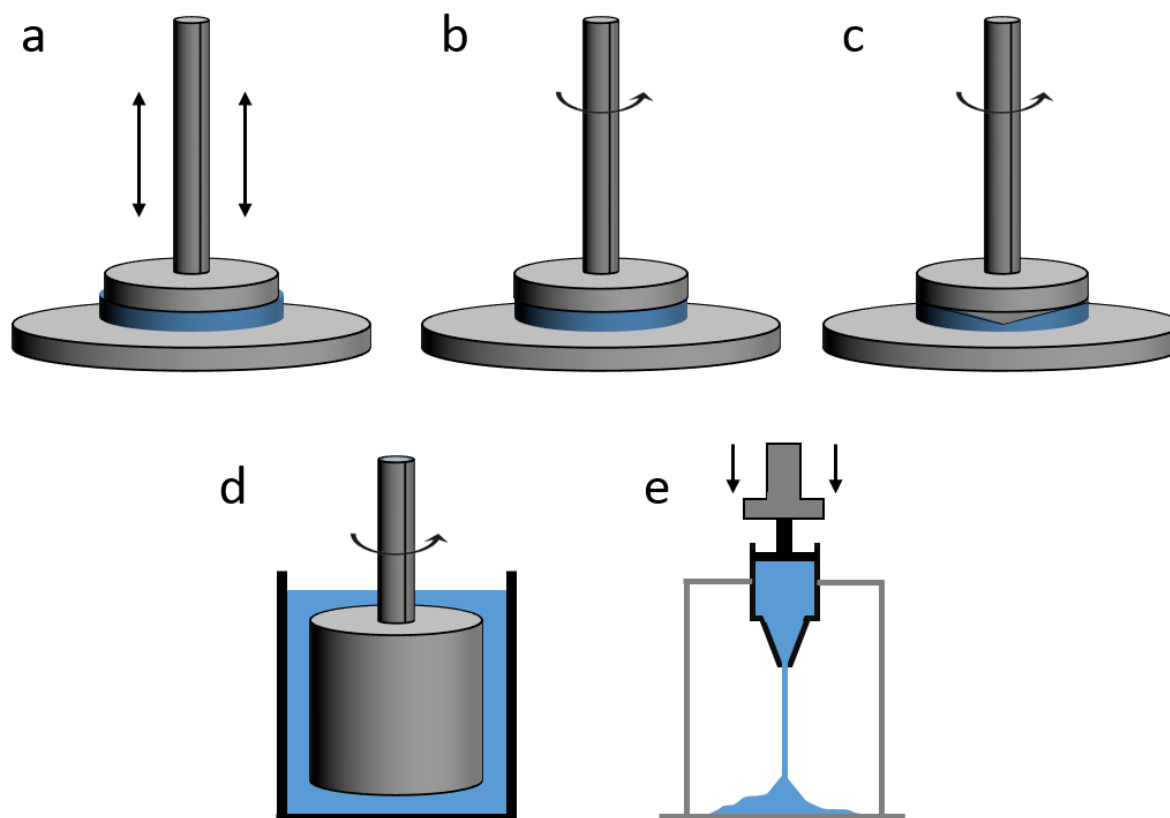


Figure 31. Schematics illustrating several major rheometry techniques: (a) Tension/compression parallel plate. (b) Torsion parallel plate. (c) Torsion cone. (d) Concentric cylinder. (e) Capillary rheometry.

Rheological measurements of all pastes were carried out on a TA Instruments Discovery HR-1 rheometer with a 40 mm parallel plate geometry, a 1 mm gap and a solvent trap to prevent drying. The 40 mm parallel plate geometry was chosen as it was found to be much better suited than other available geometries such as an 8 mm plate (which is designed for testing of solid pellets of material, for example rubber) and a 60 mm cone geometry (which is designed for testing low viscosity fluids, for example soy milk). A 1 mm gap was chosen arbitrarily, simply to remove it as a variable, allowing all tests to be compared directly. Roughly 3 cm³ of the material to be tested was placed on the bottom plate of the rheometer (either with a pipette or a spatula), and the geometry was then lowered to a 1 mm gap,

compressing the material, causing it to flow outwards ensuring it covered the whole area of the bottom the geometry and that no air pockets were trapped. Care was taken to trim excess material at the edges of the geometry as this interfered with the sensitive measurements during flow ramps. Oscillatory measurements were carried out first, as they tended to be less destructive to the sample. All were carried out at 1 Hz, varying the oscillation stress logarithmically from 0.1 to 3000 Pa depending on the loading of the paste. The phase lag (δ) between peak shear stress and peak shear strain was determined automatically by the equipment's software averaging over 10 oscillations. Yield stresses were measured by observing the stress at which the storage modulus (G') is equal to the loss modulus (G'') during amplitude ramps. Flow ramps were conducted at strain rates of 0.02 - 200 s⁻¹ and in the temperature range 0 - 45 °C. At higher strain rates (>10 s⁻¹) for higher loading pastes the plates were observed to slip, smearing material from under the geometry. This could potentially be prevented by using roughened plates. A stable temperature (usually 23°C) was ensured before beginning to gather any data for each test.



Figure 32. TA Discovery rheometer, courtesy of TA Instruments®.

Flow curves were generated by extruding syringes of paste using a Zwick iLine mechanical testing machine. A custom steel frame (Figure 33) was made to allow the machine to apply a constant displacement rate to the plunger of the syringe of paste while allowing the extrudate to flow freely. The displacement rate was chosen such that the paste is extruded at 2.5 - 30 mm/s, determined by the extrusion ratio, while the force is measured. This setup is essentially a rudimentary capillary rheometer which gives empirical data for the chosen nozzle.

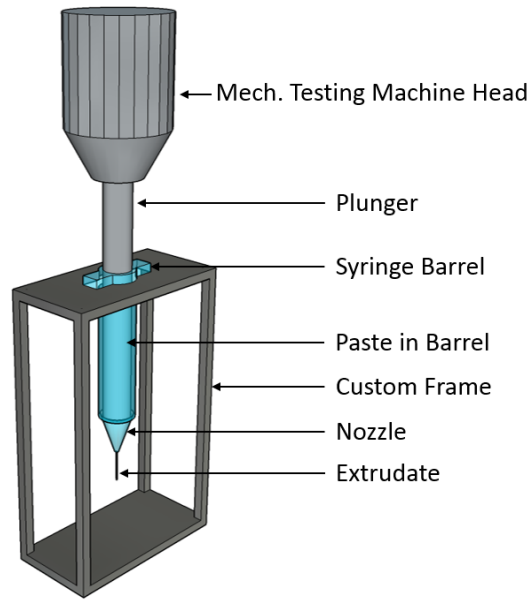


Figure 33. Schematic illustrating the "capillary rheometry" setup.

Printing

Aerobasic G-code (coded in the A3200 Motion Composer, Aerotech, UK) was used to design the tool paths for simple objects such as bars (see Appendix III) as this afforded the greatest flexibility, as discussed later. This flexibility comes from the fact that by using simple variables defined in the program header, parameters such as extrusion rate, printing speed, filament spacing, back-off distance, and basic dimensions can be set and adjusted just by changing these variables. This is not the case without a grasp of G-code; the only way to change most of these parameters is to reslice/redraw the whole part. For more complex tool paths, such as those of the Bouligard structures, RoboCAD 4.1 was used. Similarly, the STL tool in RoboCAD 4.1 was used to slice arbitrary .stl CAD models for production of complex geometries. When custom .stl files were required, Sketchup 2016 and Solidworks 2015 were used.

The first step to the practical side of the printing process is to load the syringe filled with paste into the collar of the robocaster and bring the robocaster's plunger into contact with the paste/piston. Two setups are possible at this stage, illustrated in Figure 34. Setup 1 is generally easier, but there can be difficulties with paste escaping through the top when the viscosity is very high, so Setup 2 should be used for highly loaded pastes. Also, Setup 2 is capable of applying a "back pressure" as well as a "forwards pressure" to the paste, so it generally gives better results for parts that require the machine to start and stop multiple times, such as during non-print travel moves. Either way, care must be taken to ensure there is no play in the setup, and that when the plunger begins to move, the force will be applied directly to the paste. If there is an air gap between the piston and the paste, or there are bubbles (large and visible or small and unapparent) in the paste, then this will be detectable as increased compliance when pressing the plunger. This greatly exacerbates issues with starting and stopping extrusion on demand, as the compressed air pockets and bubbles store energy and force extrusion to continue after the plunger has stopped.

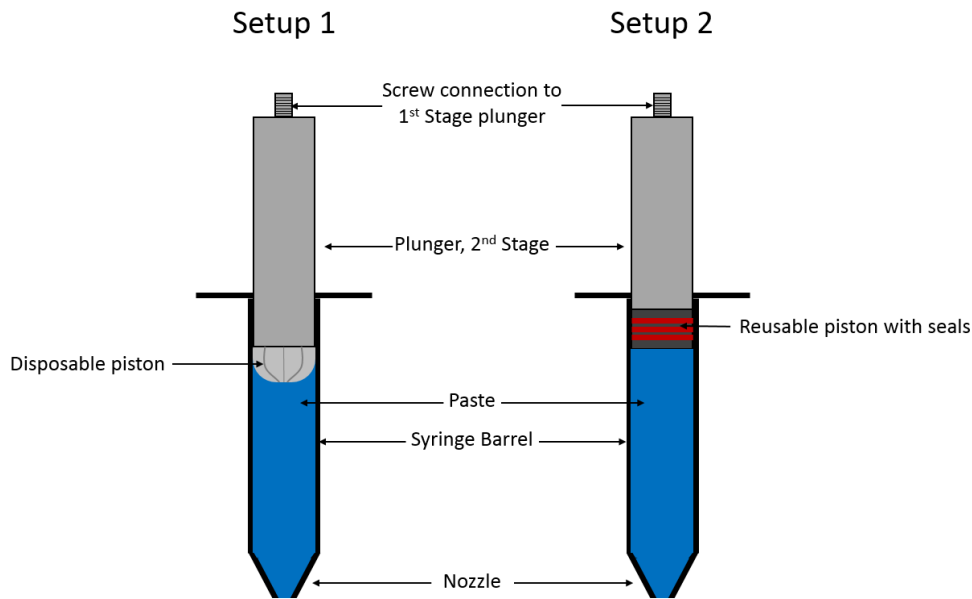


Figure 34. Schematic illustrating the two piston setups.

A large variety of nozzles were used throughout this work. The sizes range from 30 μm to 1.56 mm, and the shapes range from conical to straight (see Figure 36). All nozzles except for the microcapillary nozzles were supplied by Nordson EFD, UK. The microcapillary nozzles were supplied by World Precision Instruments Ltd, UK. Printing was carried out on a robocasting instrument (3DInks, USA) equipped with 3 extrusion heads, with extrusion pressure applied by 3 independent plungers powered by stepper motors. The heads are mounted to a gantry controlled by linear motors with a nominal precision of $\sim 1 \mu\text{m}$. When not immediately in use, the tip of the nozzles were left dipped in a cap filled with sunflower oil to prevent them blocking from drying. Materials were printed onto polished non-stick polytetrafluoroethylene substrates roughly 100 x 150 mm in size and 5 mm thick, or any flat surface with a thin coating of oleic acid applied to make it non-stick. The “zero height” was set by slowly lowering the nozzle until it is just in contact with the substrate, then moving up by one nozzle diameter. Finding the correct zero height is very important as an incorrect height will cause a defective first few layers, as well as exacerbating issues with drying. Immediately before printing each part, a dummy line (known as the “lead-in”) was printed to ensure flow is homogenous before the part is printed. The required length of the lead-in ranged from 5 mm for large nozzles to 100 mm for the smallest. The “back-off distance” (the distance that the plunger initially moves to initiate flow) was set to 0.05 - 1 mm, depending on the viscosity of the paste and the size of the nozzle (larger nozzles and higher viscosity pastes require larger back-off distances, the correct value is chosen by trial and error).

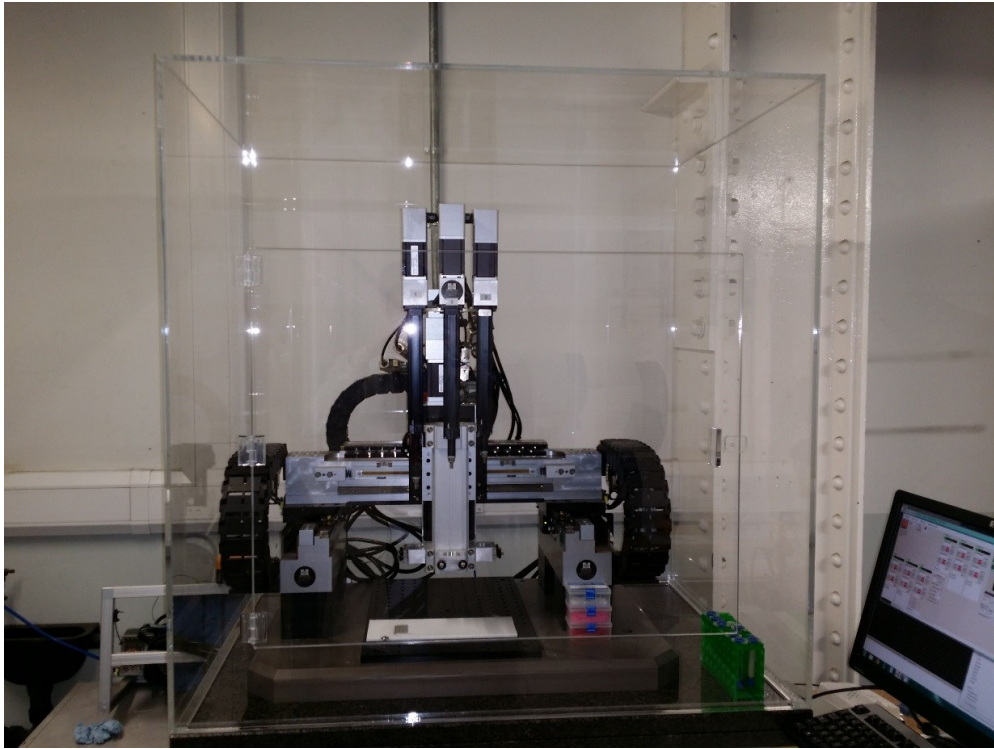


Figure 35. The robocaster used throughout this work.

For ram extrusion robocasting equipment (such as the one used in this work), the user controls the entire printing process via 4 actuators: the motors controlling the X, Y and Z position and velocity, and the motor controlling the plunger position and velocity. On a less fundamental (and more practical level), the main printing parameters under the control of the user are:

- Print speed (up to 30 mm/s)
- Raster pattern (spacing and direction between printing lines)
- Nozzle selection, including:
 - Diameter (100 – 1540 μm)
 - Shape (Conical or Straight)
 - Length (6.35 – 25.4 mm)
- Start/Stop Parameters (such as back off distance)

These are all controlled either by raw G-code, or through RoboCAD (which generates raw G-code for the user). The temperature and humidity of the whole system was controlled by a custom built enclosure housing a convection heater set to 23 °C and a consumer level ultrasonic humidifier. Humidity was manually maintained from 65 - 95% by keeping the door closed. 100% humidity was avoided to prevent condensation on the electrical components of the printer.

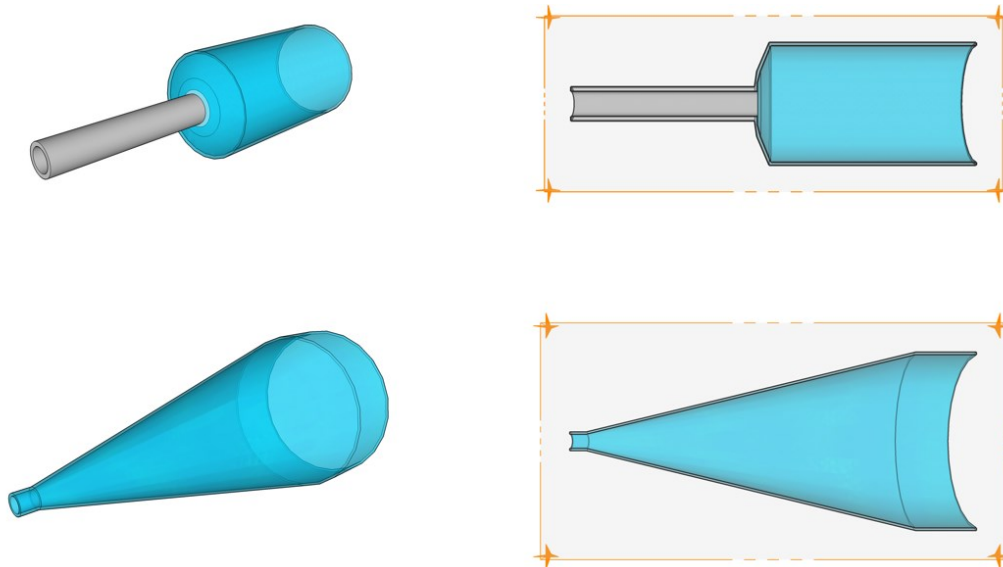


Figure 36. Schematics of the two main types of nozzle used: straight (top) and conical (bottom).

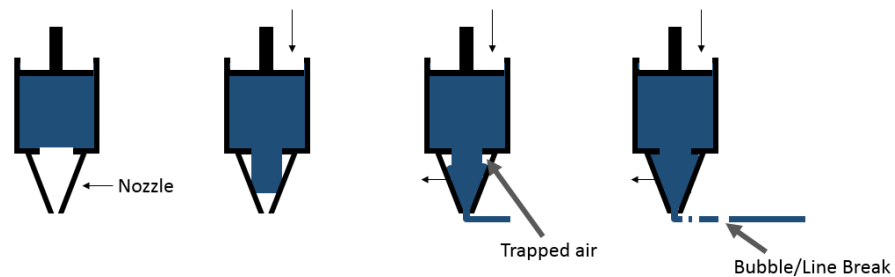


Figure 37. Schematic demonstrating how initial nozzle filling can cause bubbles during printing.

Multimaterial printing is very similar to monomaterial printing as RoboCAD controls the material switchover. The user can simply draw one area of a model in one material in RoboCAD, then draw another in a second, or third material. The only additional considerations are:

- The need to very accurately set the zero point for each nozzle in the Jog Controls before printing.
- The need to manually adjust the height of each nozzle to ensure their height is close enough that they won't be forced inside the substrate during printing.
- The need to ensure the other nozzles do not block from drying while they are not being used for printing.
- The need to very carefully optimise the back-off distances for all syringes, as generally lead-ins are not possible for multiple materials, so the material must start and stop precisely where required.

Besides these aspects, the printing process is identical to single material printing (the real issues typically arise during post-processing).

Post-processing

Drying

Larger printed parts were generally dried on the substrate at room temperature for 24 hours in the enclosure to avoid cracking from fast drying, followed by another drying step in a convection oven at 37°C for 24 hours. Following this, parts were removed from the substrates carefully. Where sticking occurred, the substrate was flexed and bent slightly to detach them. The drying step was generally where the parts failed (very few broke during burn-out or sintering). Larger parts were more prone to drying cracks and warping than smaller ones. This failure can be avoided by drying slowly (as prescribed above) and ensuring that the part is not attached to the substrate (allowing it to shrink homogeneously).

Where isostatic pressing was required, it was applied at 300 MPa for 1 minute with the sample in an evacuated balloon (or glove for larger parts) using a Stanstead Fluid Power isostatic press.

Burn-out and Sintering

De-binding of all samples was achieved by heating at a rate of 5 °C per minute to 600 °C and holding for 1 hour, in air for oxide parts and in argon for non-oxides. This temperature was chosen based on TGA analysis. Alumina and platelet parts were pressureless sintered at 1550 °C for one hour in air. Silicon carbide parts were pressureless sintered at 2050 °C for one hour in a graphite hot press (FTC Systeme, DE) under an argon atmosphere at 1 bar ambient pressure. A powder bed of the same composition as the parts was used to reduce the evaporative loss of sintering additives for the SiC. All heating and cooling rates were 5 °C per minute.[113]

Infiltration

For the production of platelet-epoxy and Cf-epoxy, infiltration of Aralidte resin (LY556, Huntsman, USA) was achieved by thoroughly mixing the resin with XB 3473 hardener (Huntsman, USA) at a ratio of 100:23 by weight, as suggested by the manufacturer, and then pouring this mixture over the preforms and holding for >12 hours under vacuum until no bubbles were visible emerging from the preforms. The part can then be taken out of the resin and the excess resin on the surface scraped away with a spatula. Special care needs to be taken with the Cf samples as they tended to be very fragile, so it was necessary to cure the samples before taking them out of the resin and cut off the excess epoxy. Curing took place sitting on a piece of aluminium foil at 180°C for 1 hour in a convection oven followed by post-curing at 200 °C for 2 hours.

Characterisation and Testing

Densities were measured by the Archimedes method. Average grain size was calculated by thermal etching (polishing followed by heating to 1575 °C). The grain structure was then analysed using SEM images of etched surfaces with the cell counter plugin in ImageJ. Microstructures were examined after careful grinding and polishing with diamond suspension down to 1 µm, ensuring minimal pull-out, followed by coating with gold and imaging with secondary electrons in a JEOL JSM-6010 SEM at 20 kV. Mechanical testing consisted of 4 point bending in accordance with ASTM C1161-13 on samples measuring 30 x 3 x 2 mm polished to 1 µm on one side. A displacement rate of 0.2 mm min⁻¹ was used and the polished surface was in tension.[114] A 20 mm bottom span and a 10 mm top span was used on a Zwick iLine universal testing machine. The same instrument was used with flat plates to test compression strength on 5 mm × 5 mm × 5 mm cubes at a rate of 1.3 mm min⁻¹. The elastic modulus of these bars were measured using the impulse excitation technique with an RFDA instrument produced by IMCE, BE, taking care to use the minimum impulse power necessary. For SENB toughness measurements, a notch was made using a 0.84 mm thickness diamond wafering blade followed by sharpening with a razor blade and 3 µm diamond suspension. For the composite parts this could be done by hand, and took ~30 seconds. For ceramic parts a custom built rig was used to sharpen for 10 - 30 minutes. The 4 point bending setup was also used for this test, but with a displacement rate of 0.01 mm min⁻¹. Hardness was measured using a diamond Vickers tip on an Indentec 6030LKV with a loads of 1 - 10 Kg (9.8 - 98 N). Indent sizes were measured by reflection optical microscopy.

Raman spectroscopy was carried out using a Renishaw inVia raman spectrometer, taking 5 minute scans focussed on individual fibre fracture surfaces.



Figure 38. A composite sample with a sharpened notch being measured in 4 point bending.

***In-situ* DCB Testing**

A new technique was developed in order to perform the double cantilever beam (DCB) fracture experiment inside an SEM and generate R-curves for various materials. For these measurements, samples were machined into double cantilever geometries, see Figure 39, using a diamond wafering saw. The groove and the notch can be cut using the same saw without removing the sample from the grips, as illustrated in Figure 40. This ensured that the groove and the notch align. The top surface was then polished as described above. Notches were then sharpened using the procedure described previously. The samples were then coated with gold and placed in a 2 kN Gatan *in-situ* mechanical testing stage equipped with a custom machined steel wedge of an angle of 70°, inside an FEI Quanta FEGSEM. Care must be taken to ensure the wedge is correctly placed between the arms, and touching (but not applying any force). Spacers (as seen in Figure 41) can be used if the range of motion of the stage is not sufficient to put the wedge in contact with the sample arms. A small amount of silver paint was applied between the back of the sample and the Gatan frame to reduce charging, as the sample is otherwise isolated from ground. Tests were carried out under displacement control with the displacement rate of the wedge as slow as the system allowed ($33 \mu\text{m min}^{-1}$). Before loading, a high resolution image of the arms was taken. High resolution was needed when imaging the tip due to the fact that the arm displacement is very small for stiff materials. This means that generally the arms and the crack cannot be tracked simultaneously at sufficient resolution. The tip of the sharpened notch was then monitored closely as the load increased, until crack initiation was observed and the stage was

immediately stopped. At this point, another high resolution image of the arms was taken (to compare to the first, to measure the arm displacement and thus to calculate G). The crack length is then measured, and the loading restarted. The measurement of the crack and arms was carried out in ImageJ. It was found that the calculated G was very sensitive to the initial measurement of the arms; a single pixel either way could result in a significant variation. For this reason the maximum resolution of the SEM was used ($\sim 6000 \times 4000$ pixel). The procedure is repeated until a sufficient number of points are collected to generate an R-curve, or until the crack nears the end of the sample.

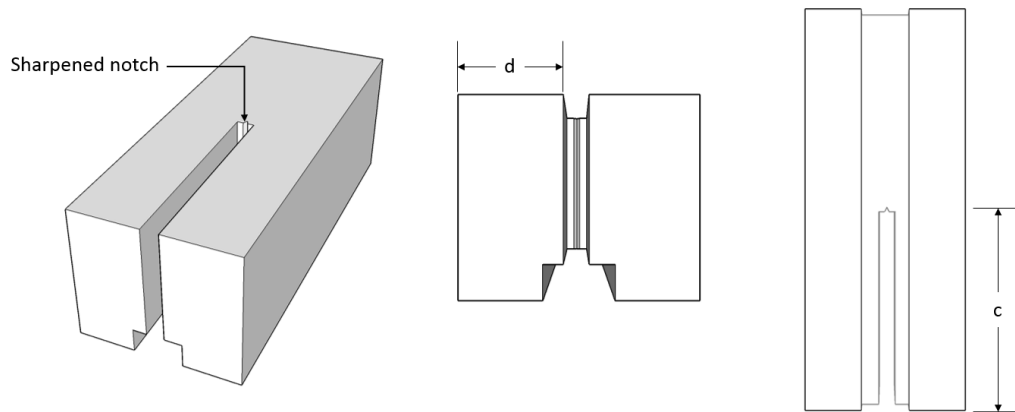


Figure 39. Schematic showing the geometry of the samples for in-situ DCB testing. d was ~ 2 mm and c was 5-10 mm. The thickness of the part was ~ 4 mm and the groove was ~ 2 mm deep.

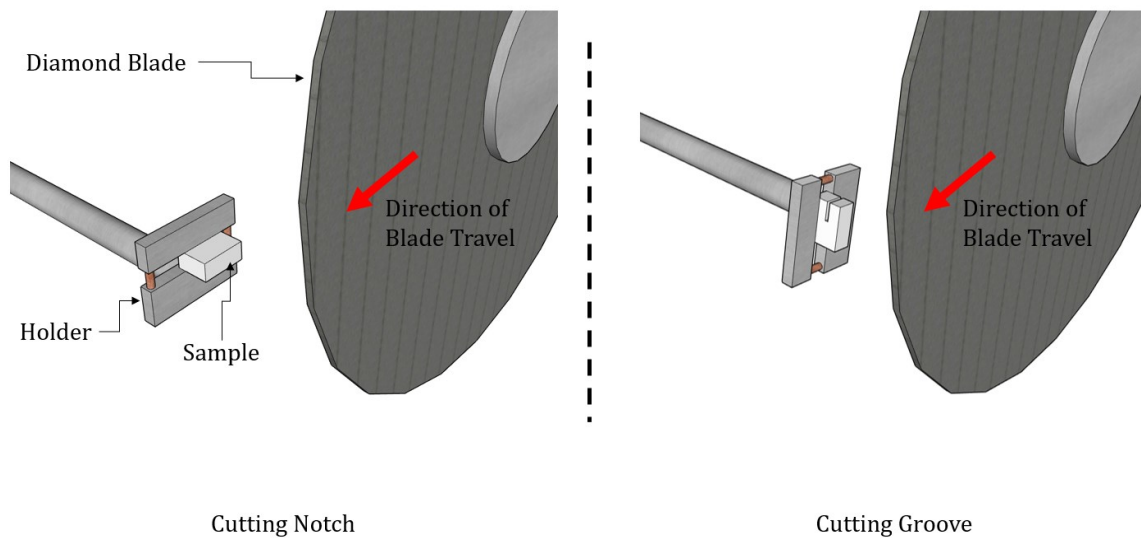


Figure 40. Schematic showing the procedure for machining the notch and groove of the DCB samples.

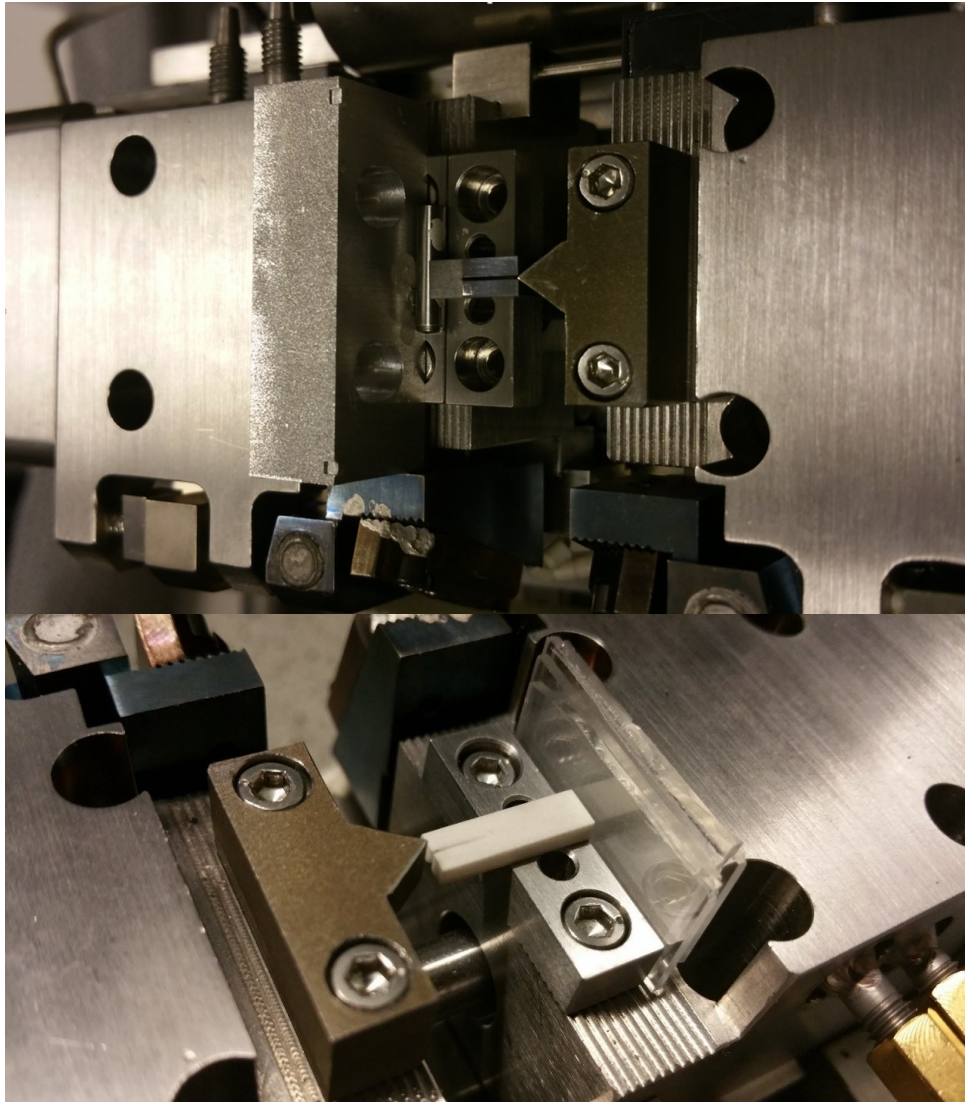


Figure 41. The Gatan compression rig, equipped with a steel wedge for in-situ DCB testing, with a sample in place (before coating).

Micromechanical Testing

In order to measure the mechanical properties and reliability of individual alumina platelets, micro 3 point bending was used. Firstly, $\sim 0.01\text{g}$ of the alumina platelets (obtained in bulk from Advanced Nano Technologies Ltd) were scattered on a silicon wafer attached to a SEM stub with silver paint (carbon tape was avoided in order to reduce unwanted compliance). Individual platelets were then selected (only selecting platelets that are large enough and clean enough for testing), carefully welded to a tungsten OmniProbe 200 micromanipulator in an SEM, and elevated away from the substrate. The platelets were milled into regular rectangles using a focused ion beam, using progressively lower currents for the final milling step to avoid sample damage. All sample preparation was performed using a Helios NanoLab FIB/SEM equipped with a Pt gas injection system for welding and a Ga source for milling. Each platelet was then placed across $5.5 \times 20 \times 5 \mu\text{m}$ trenches which had been milled in the silicon, welded at one or both edges of the trench, and the probe tip removed by milling. All milling was carried out with a current below 0.92 nA and all welding with a current below 0.28 nA . Although it is

performed on a smaller length scale, this technique bears some resemblance to previous work.[9–11] Mechanical testing of the samples was performed by using a nano-indentation rig (Alemnis GmbH, CH) designed for *in-situ* testing inside an SEM. The load was applied by means of a 60° diamond wedge with a radius of 100 nm. To allow for alignment of the tip perpendicular to the sample length, samples were mounted on top of a rotational stage. An indent was made with the tip in the substrate to verify correct alignment. All specimens were loaded in displacement control using a displacement rate of 5 nm s⁻¹ to the point of failure. To gain further insight on the defects causing failure, selected platelets were prepared for observation under TEM by FIB milling (2–30 keV Ga⁺ incident beam energy with currents of 16 pA – 21 nA). TEM and energy-dispersive x-ray spectroscopy was carried out on a FEI Titan 80 - 300 S/TEM at 300 kV equipped with a windowless EDX detector (Bruker QUANTAX 400-STEM). Focal series micrographs were acquired using a spherical aberration coefficient $C_s \sim -2 \mu\text{m}$ and exit-wave reconstruction was performed using TrueImage software (FEI, USA).**

** All TEM work was kindly carried out by Dr. Na Ni.

Chapter III – Rheology and Robocasting: The Nebulous Concept of 'Printability'

Introduction

In no uncertain terms, robocasting is inseparable from rheology. One cannot begin robocasting without first asking about the rheological properties of the paste. These properties determine the range of structures that can be printed, the optimal printing parameters, and ultimately the quality of the printed part. Despite this, the manner in which rheology ties in with these considerations has to date not been specified well in the literature. Some work has been done to identify some of the important rheological requirements of a paste and to suggest a range of values that these properties should take for a successful print. Many gaps remain however, and the role each property plays in the printing process is often ill-defined. This chapter aims to advance the understanding of how each key rheological property affects different aspects of the printing process, and to begin to refine the quantitative requirements of these properties.

Basic Rheological Properties

Perhaps the most basic rheological property is viscosity. Viscosity, μ ,** is defined as:

$$\mu = \frac{\tau}{\dot{\gamma}} \quad (3.1)$$

where τ is the shear stress applied to the fluid and $\dot{\gamma}$ is the shear strain rate it experiences under this stress. It is thus a measure of a fluid's resistance to flow; a fluid with a higher viscosity will require a greater force to flow at a given rate than a fluid with a lower viscosity. μ is known as the 'dynamic viscosity' and the 'absolute viscosity', and is distinct from 'kinematic viscosity', ν , which is defined as:

$$\nu = \frac{\mu}{\rho} \quad (3.2)$$

where ρ is the density of the fluid. Kinematic viscosity is typically used when considering the flow of a fluid due to the force of gravity. Throughout this work μ is the more relevant of the two, and thus is used exclusively as the measure of viscosity.

The most relevant rheological properties to robocasting are the storage modulus at low stress (G'_{eq}), the yield stress (τ_y), the yield strain (γ_y), the shear thinning coefficient (n), and the viscosity parameter (K). Table 3 summarises what each of these properties represents and how they are measured. Many of these properties appear in the Herschel-Bulkely model,[51]

$$\tau = \tau_y + K\dot{\gamma}^n \quad (3.3)$$

which has been found to be useful for describing the flow of robocasting pastes. This model describes materials with viscosity that varies with shear rate, and exhibit a yield stress ($\tau_y > 0$). When $n < 1$ viscosity will decrease with shear rate. This phenomenon is known as 'shear thinning' or 'psuedoplasticity', and is a very common rheological behaviour. Materials where $n = 1$ and $\tau_y = 0$ and are Newtonian fluids (no dependence of viscosity on shear rate), while materials where $n > 1$ are 'shear thickening', meaning their viscosity increases with shear rate. This is summarised in Table 4.

** μ , μ , is typically used by engineers, while η , η , is typically used by scientists to denote viscosity.

Table 3. List of rheological properties and conditions pertaining to robocasting pastes.

Property/ Quantity	Units	Rheological Test	Physical Meaning
G'_{eq}	Pa	Oscillation	Equivalent to the elastic modulus for viscoelastic materials. It is a material property when measured at stress far below the yield stress (although it can also weakly depend upon oscillation frequency).
τ	Pa	-	The shear stress applied to the paste.
τ_y	Pa	Flow/Oscillation	The minimum shear stress required to cause yielding of the paste (flow/plastic deformation).
γ_y	-	Flow/Oscillation	The minimum shear strain required to cause yielding of the paste (flow/plastic deformation)
$\dot{\gamma}$	s ⁻¹	-	The applied shear strain rate.
n	-	Flow	A measure of how shear thinning the paste is (1 indicates Newtonian, 0 indicates infinitely shear thinning, >1 indicates shear thickening).
K	Pa s ⁿ	Flow	A shear rate invariant measure of the viscosity of the paste.
μ	Pa s	Flow	The apparent viscosity of the paste, equal to $\tau/\dot{\gamma}$.

Table 4. Categories of fluids that can be described by the Herschel-Bulkley Equation.

	$0 < n < 1$	$n = 1$	$n > 1$
$\tau_y = 0$	Power Law Fluid (shear thinning)	Newtonian Fluid	Power Law Fluid (shear thickening)
$\tau_y > 0$	Herschel-Bulkley Fluid (shear thinning)	Bingham Plastic	Herschel-Bulkley Fluid (shear thickening)

Pluronic F-127 Hydrogels

Pluronic hydrogels were used as the base of all of the pastes used for robocasting in this work. For this reason, special attention was paid to measuring their rheological behaviour on their own, so the paste's behaviour could be more fully understood.

Gelation

Like many hydrogels, Pluronic hydrogels can adopt a low viscosity state with liquid-like behaviour at temperatures below their gelation temperature (T_{gel}). This is counterintuitive, as many other gel systems operate in the opposite manner (forming gels at low temperatures and 'melting' at higher temperatures). By measuring the viscosity of Pluronic samples across a range of temperatures the effects of gelation can be observed, as seen in Figure 42. For this typical gel (consisting of 75 wt% water, 25 wt% Pluronic), the viscosity can be seen to gently decrease by $\sim 30\%$ with increasing temperature from 0 – 10 °C. This behaviour is also seen in pure water, which experiences a relative fall in viscosity of a similar magnitude in this temperature range.[115] One can therefore stipulate that this fall is simply due to the decreased viscosity of the free water that makes up the majority of the gel. Previous work has suggested that micelles are formed in this temperature range,[49] but their concentration is too low to allow them to link to form a percolating network, so this process was not observed to have an effect on the rheology of the material. From 10 – 18 °C the downward trend is reversed; viscosity increases in an exponential manner by over three orders of magnitude. This corresponds to the formation of the percolating micelle gel network. Water groups continue to dissociate from the PPO segments of the polymer which causes the PPO segments to join via hydrophobic association,[49] allowing the micelles to grow and overlap. Above $\sim 19^\circ\text{C}$ the viscosity sharply levels off. At this point the network is fully percolating. Increasing the temperature beyond this increases the number and size of the micelles (and thus the number of percolating bonds), however this effect has a linear dependence, and is not as dramatic as the transition from a non-percolating to a percolating network.

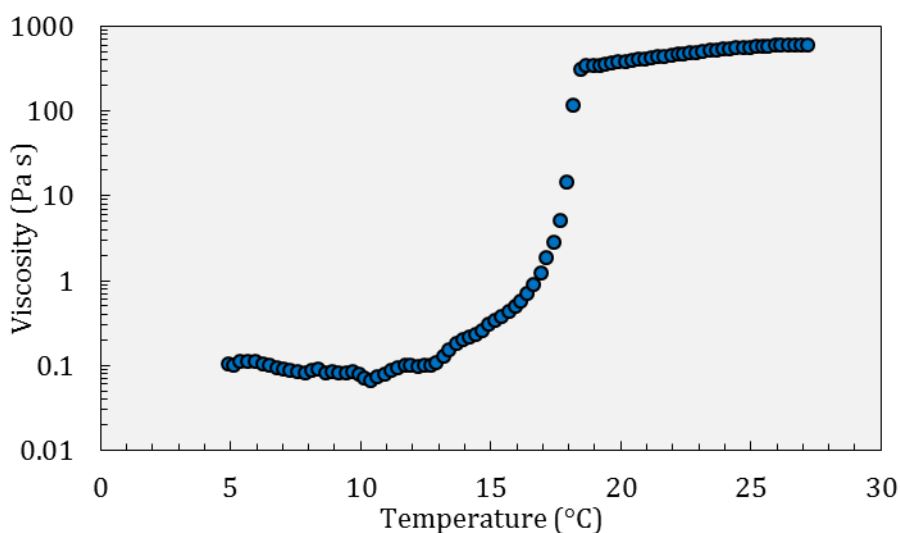


Figure 42. The temperature dependence of the viscosity of a 25 wt% Pluronic gel at a constant shear rate of 1 s^{-1} .

The behaviour described above was seen in all gels within the concentration range of 20 - 35 wt% Pluronic, as shown in Figure 43. The shape of the gelation curves is similar for all the concentrations in this range, however the temperature at which this process occurs decreases linearly with increasing concentration. In other words, concentrated gels remain 'solid-like' until lower temperatures. This trend is followed to extremes, such that 40 wt% Pluronic gels were never observed in a 'liquid-like' state, even at $0 \text{ }^\circ\text{C}$, and below this temperature ice crystal formation was observed. At the other end of the spectrum, 15 wt% Pluronic gels did not exhibit 'solid-like' behaviour at any temperature tested (up to $50 \text{ }^\circ\text{C}$). Figure 43 shows that these dilute gels do experience an increase in their viscosity as temperature is increased, however this occurs over a wider range of temperatures and starts to fall off at high temperatures. Pluronic gels are known to transform into less rigid "soft gels" at high temperatures.[116] This phenomenon is commonly encountered with thermally reversible hydrogels and is attributed to a change in the structure of the micelles. For 15 wt% Pluronic solutions this transformation has been reported to occur from $35 - 45 \text{ }^\circ\text{C}$, [116] consistent with the fall off in viscosity at higher temperatures for this concentration. The same effect was not observed in the other concentrations tested because it occurs at higher temperatures for higher concentrations (for example, the transition occurs at $60 \text{ }^\circ\text{C}$ for 20 wt% Pluronic gels).[116]

The dependence of T_{gel} on concentration, see Figure 43, is due to the fact that lower concentration gels have more readily available free water, which is likely to make the association of water around the PPO groups more favourable. Higher entropy (and thus higher temperatures) would be required to dissociate larger amounts of water from the PPO groups, and thus more dilute solutions are more difficult to gel.

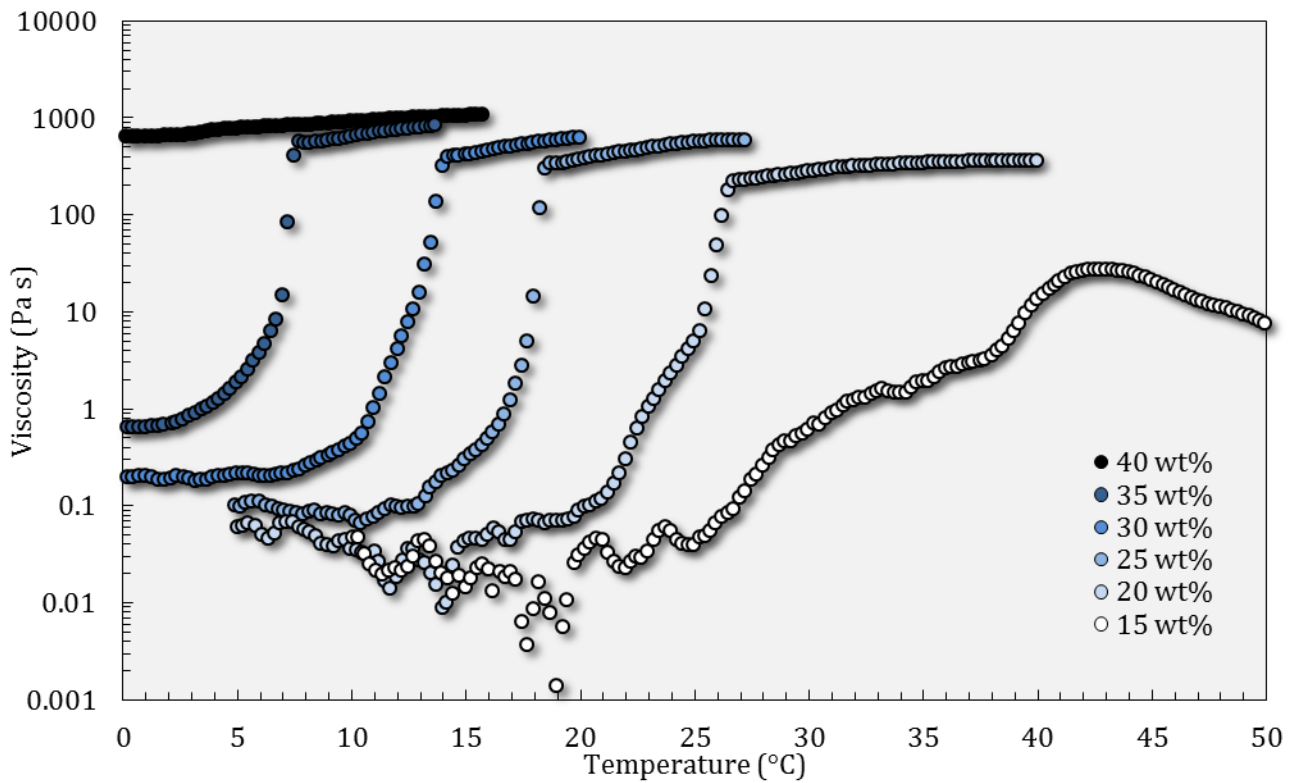


Figure 43. Viscosity-temperature curves for six different concentration Pluronic hydrogels. Note that the noise at lower temperatures for the lower concentration gels is due to the 40 mm plate geometry being unsuitable for measuring such low viscosities. The cone geometry could be used for these gels, but this would make it difficult to compare with the other data. For reference, water has a viscosity of 0.001 Pa s at 20 °C.

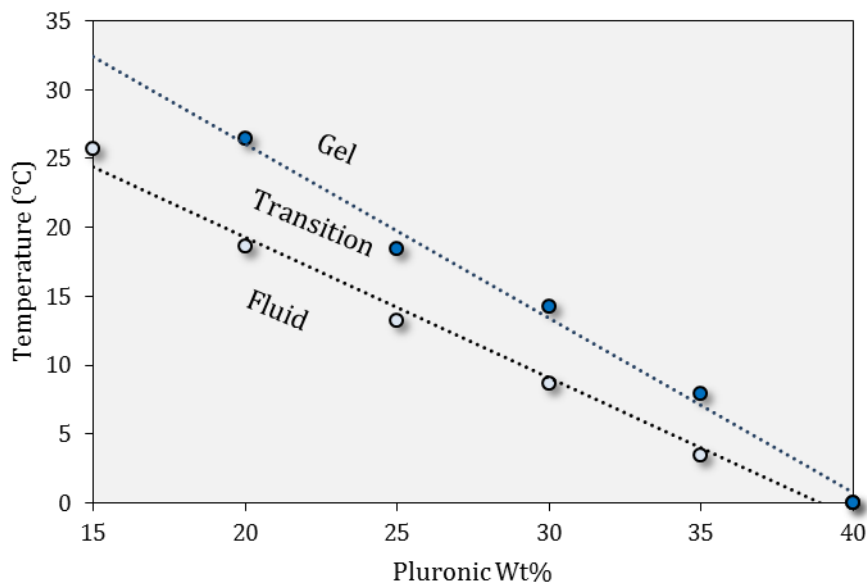


Figure 44. Map of the gelation of Pluronic gels of varying concentration. For convenience the transition region is defined by when the viscosity deviates off its trend line by 50%.

Yielding

The gel network of micelles that constitutes the Pluronic hydrogels gives rise to a material with a yield stress. This is because a minimum stress is required to break the bonds of the network. Figure 45 presents a clear example of this; at low stress the hydrogel behaves almost entirely as an elastic solid. G' is far greater than G'' , meaning most of the strain energy put into the gel can be recovered. We can define the stiffness of the gel/paste as the value that G' takes at these low stresses; the 'equilibrium storage modulus', G'_{eq} . At stresses from 100 - 300 Pa G' drops dramatically, while G'' steadily rises. This is due to plastic deformation mechanisms being activated; the gel network is beginning to be broken. The breakup is reversible; the network will reform in its new shape when the stress is removed. The fact that it is a reversible process, however, does not mean that the strain energy put into breaking the network can be recovered as it could in the elastic region. This constitutes 'internal friction', converting strain energy into minute amounts of thermal energy. Hence, G'' rises as losses rise, while G' falls as the network is broken, since there are fewer bonds to withstand the applied stress. The shear stress at which $G' = G''$ is one definition of the apparent** yield stress, as it represents the point at which the material transitions from 'solid-like' to 'liquid-like' behaviour, or from predominantly elastic to predominantly plastic deformation.[45] This is used as the definition of the yield stress throughout this work.*** When determining the yield stress directly using a measurement such as the one shown in Figure 46, it is not clear where the material begins to behave plastically, thus it was not possible to determine the yield strength in this case. Creep can further complicate the situation, bringing difficulties in defining the yield point from traditional stress-strain measurements. Thus, oscillatory measurements are used instead. These are particularly useful for highly loaded pastes, which can present practical difficulties such as slippage between the geometry and the sample during direct measurements of the yield stress. At stresses above the yield stress we see that G'' begins to fall, albeit less rapidly than G' . This is due to the fact that the network is mostly broken, so the internal friction is lower, resulting in less energy dissipated during each oscillation.

If G' were constant, then the yield strain could be calculated simply from;

$$\gamma_y = \frac{\tau_y}{G'} \quad (3.4)$$

however this is not sufficient in the case of the hydrogel, where yielding is preceded by a significant fall in G' . Thus γ_y should be calculated using:

** The yield stress varies depending on the technique used to measure it, hence the qualifier 'apparent'.

*** Using this measurement the yield stress is sometimes defined as the maximum of the product of G' and γ , the elastic stress.[189] This definition gives a yield stress close to the $G'=G''$ definition.

$$\gamma_y = \int_0^{\tau_y} \frac{1}{G'(\tau)} d\tau \quad (3.5)$$

In cases where G' is constant with respect to shear stress, this expression simplifies to Equation 3.4.

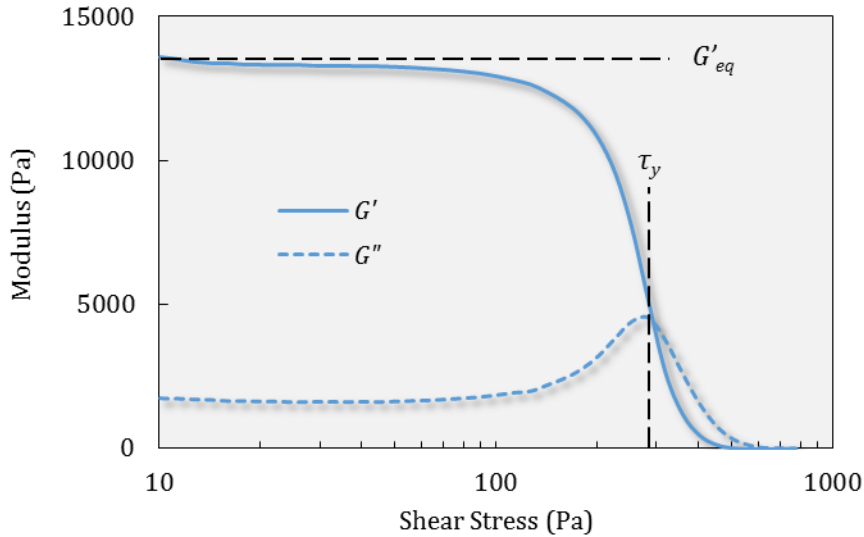


Figure 45. Example oscillation amplitude ramp of a 25 wt% Pluronic gel at a temperature of 23 °C and a frequency of 1 Hz.

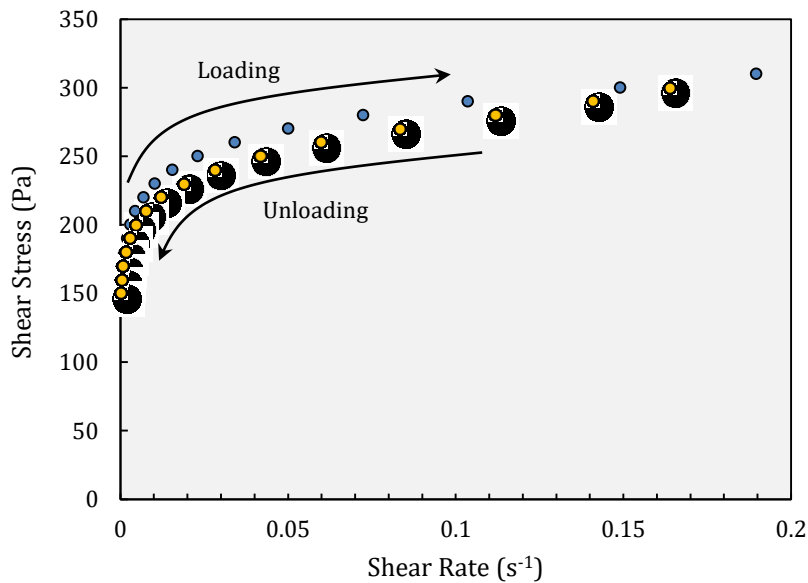


Figure 46. Controlled Stress Flow ramp of a 25 wt% Pluronic hydrogel at 23 °C, attempting to obtain a direct measurement of the yield stress.

Oscillation amplitude ramp tests were performed on Pluronic gels of varying concentration, from 20 - 35 wt%. This range was chosen using the prior gelation study. As seen in Figures 47 and 48, both the τ_y and the G'_{eq} were found to increase linearly with concentration in the range studied. This means

stronger and stiffer gels can be produced simply by increasing the concentration of Pluronic. The x-intercept is not zero because there exists a minimum concentration below which no gel forms.

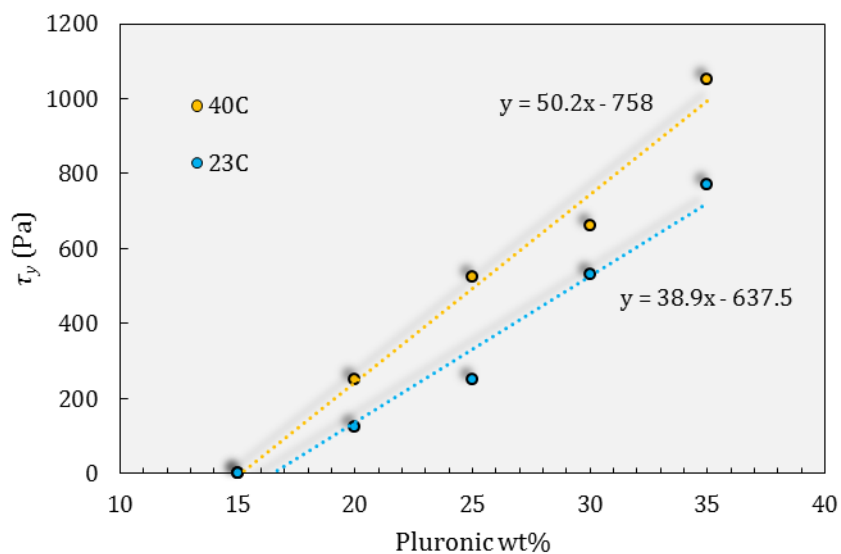


Figure 47. Effect of Pluronic concentration on yield stress. Oscillation tests carried out at 40 °C and 23 °C as specified, and 1 Hz.

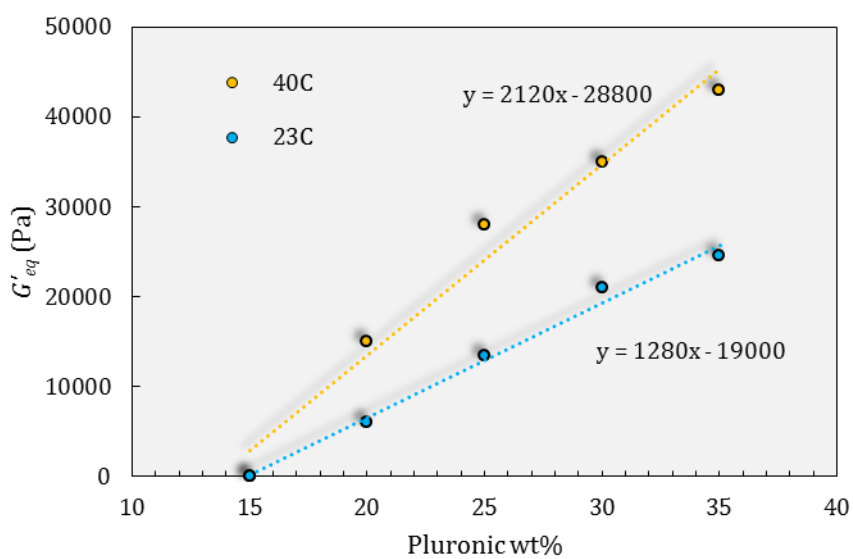


Figure 48. Effect of Pluronic concentration on the equilibrium stiffness. Oscillation tests carried out at 40 °C and 23 °C as specified, and 1 Hz.

Flow

At stresses above the yield stress the gel will begin to flow. Its behaviour in this situation is best studied using flow ramps, such as those depicted in Figure 49. It can be seen that as the shear rate exerted on the gel increases, the flow stress increases modestly. Physically this can be explained by the fact that the gel network is constantly being broken and reformed when sheared. At high shear rate the breakup happens faster than the reformation, so there is less resistance to flow.

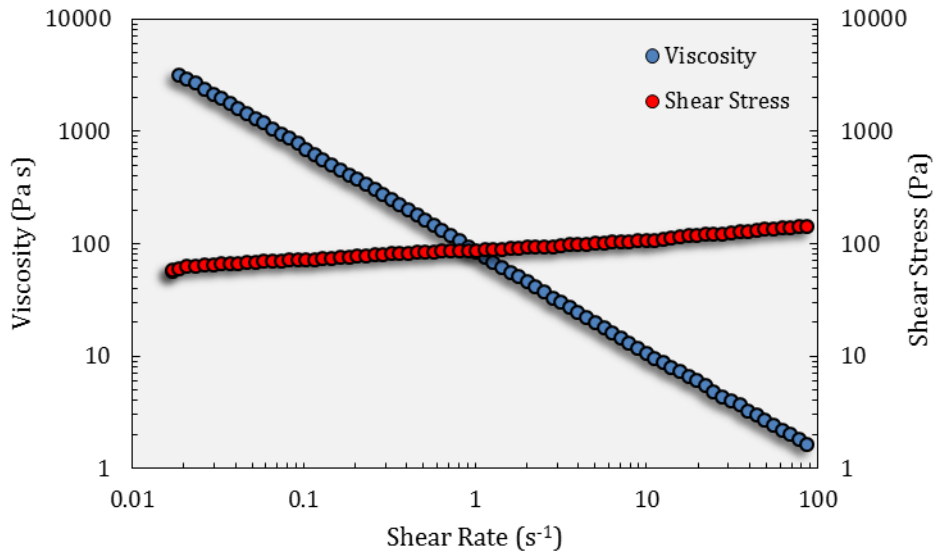


Figure 49. Example flow ramp measurement of a 20wt% Pluronic gel at 23 °C.

Using this data it is possible to calculate two important rheological properties – K and n . This is achieved by using this data alongside a modified Herschel-Bulkley equation;

$$\ln(\tau - \tau_y) = n \ln(\dot{\gamma}) + \ln(K) \quad (3.6)$$

such that n is the gradient of a $\ln(\tau - \tau_y)$ vs. $\ln(\dot{\gamma})$ plot. The τ_y used in these calculations is the τ_y measured from dynamic mechanical analysis, as shown in Figure 45. An example calculation using the data from Figure 49 is presented in Figure 50. This method takes an average value of n over a range of shear rates. Even with very clean data, n will have significant uncertainty due to the instability of differentiation. With this in mind, n was calculated for a range of gel concentrations at shear rates relevant to robocasting (1 - 100 s⁻¹), as seen in Figure 51, which shows that n does not vary significantly with Pluronic concentration, while K increases almost linearly with the Pluronic concentration, Figure 52.

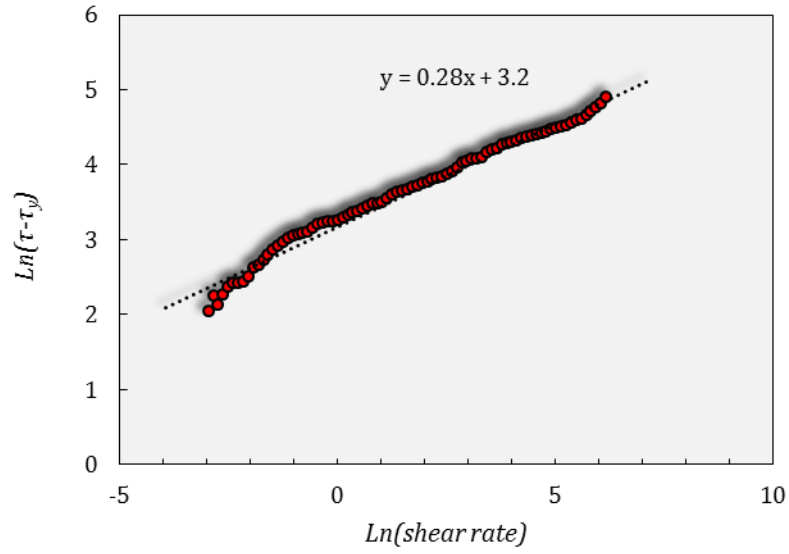


Figure 50. Example calculation of n using the data from Figure 49.

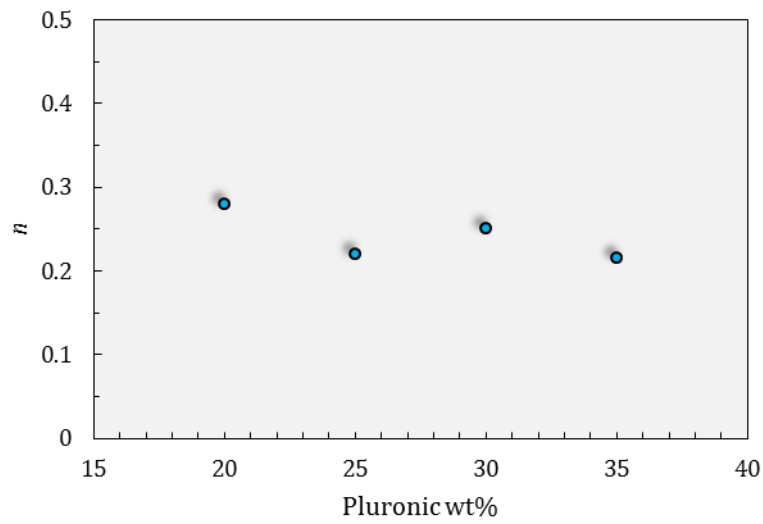


Figure 51. Variation of the shear thinning parameter with Pluronic concentration at 23 °C.

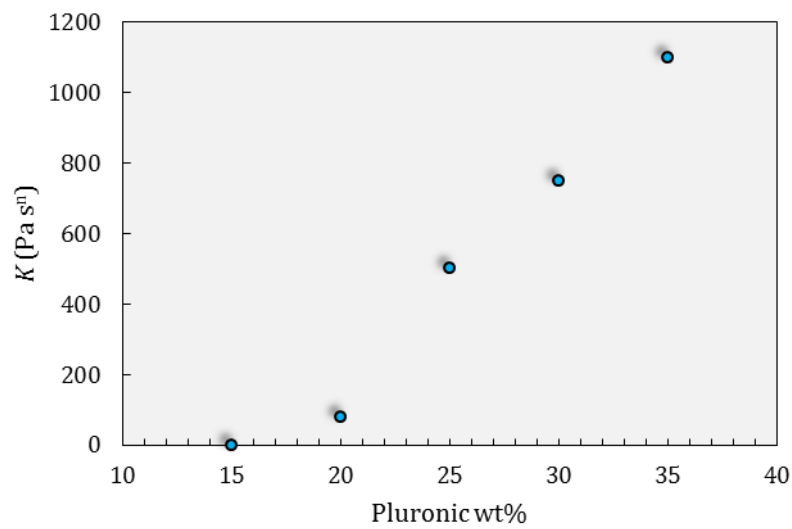


Figure 52. Variation of the reference viscosity with Pluronic concentration at 23 °C.

Powder Pastes

Powder Characterisation

Ceramic pastes were created by adding ceramic powder to the Pluronic hydrogels analysed above. Submicron Al_2O_3 and premixed submicron $\text{SiC}+\text{Al}_2\text{O}_3+\text{Y}_2\text{O}_3$ (at a 90:6:4 mass ratio, referred to as SiC mix herein) were the two powder mixtures used most extensively in this work. The morphologies and size distributions were analysed using SEM and laser scattering, and the results are presented in Figure 53 and 54. The measured $d(0.5)$ of the Al_2O_3 is $0.35\ \mu\text{m}$ and that of the SiC mix is $0.45\ \mu\text{m}$. While the average particle size is similar for the two powders, the size distributions and morphologies are quite different. The Al_2O_3 consists of rounded, uniform particles, while the SiC mix consists of a range of jagged, irregular particles. From SEM images the Al_2O_3 appears to have a tight size distribution, however the distribution obtained from laser scattering indicates a number of particles $5 - 20\ \mu\text{m}$ in size. This is likely due to agglomeration, as sieving was not fine enough to break agglomerates of this size. Laser scattering did not detect any particles below $0.1\ \mu\text{m}$ diameter. Meanwhile the laser scattering and SEM of the SiC mix indicate a significant fraction of very small particles $< 0.1\ \mu\text{m}$ diameter, and no particles $> 3\ \mu\text{m}$ diameter. These differences are likely due to differences in the manufacturing routes of these two materials, and are expected to affect the rheology of the pastes utilising them.

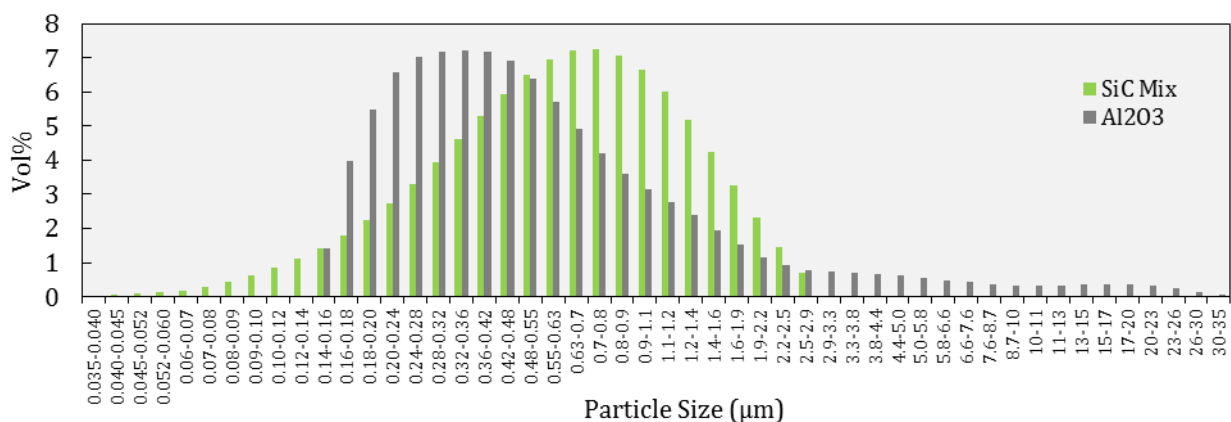


Figure 53. Particle size distributions of the Al_2O_3 (left) and SiC mix (right) powders used in this work, obtained via laser scattering.

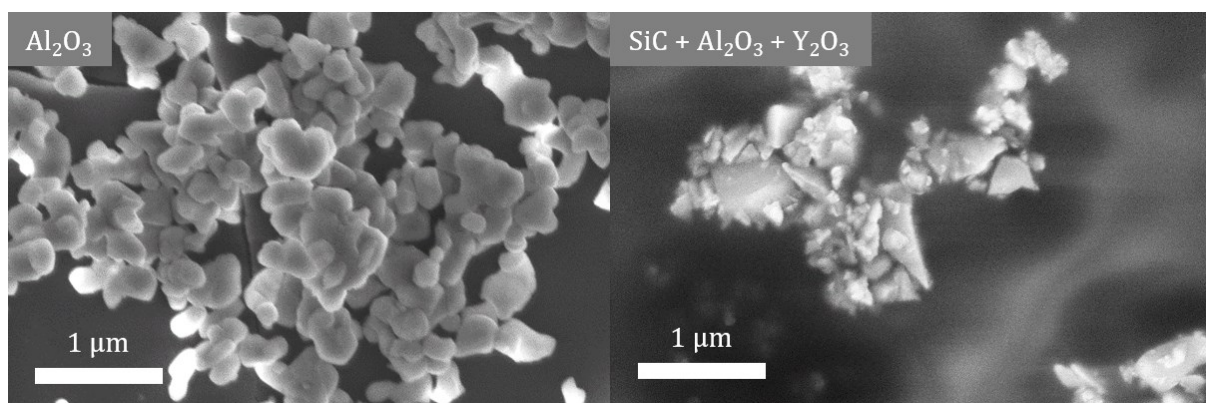


Figure 54. Representative SEM images of the Al_2O_3 and SiC mix powders used in this work.

Effect of Ceramic Powder on Rheology

When mixed with the 25 wt% Pluronic hydrogel analysed above, paste-like materials were formed. The rheological properties of five compositions of SiC mix and Al₂O₃ pastes were tested, with volume fractions ranging from 0 - 48 vol% for SiC and 0 - 39 vol% for Al₂O₃. As is the case with the hydrogels, all of the pastes were shear thinning, with the dominant mechanism coming from the disruption and breakdown of the hydrogel network under shear stress. The volume fraction of ceramics was never high enough to produce dilatant effects from particle network jamming, which would make the pastes difficult to print. When comparing Figures 55 and 56 to Figure 45, it is clear that the viscoelastic properties of the pastes were generally similar to those of the Pluronic hydrogel. The SiC mix and Al₂O₃ pastes both experience a linear viscoelastic region at low stress, maintaining a constant G' (their G'_{eq}). As higher shear stresses are applied, G' falls and G'' rises until they cross at the yield stress. This behaviour mimics that of the hydrogel, however four differences were observed:

- 1- G' is higher at all stresses. This can be explained by considering the particles to be attractively interacting with one another, forming a stiff percolating network. At low strains this network should behave elastically, and thus increases the elastic energy stored when the paste is strained, thereby increasing G' .
- 2- G'' and μ are larger at any stress. This can be attributed to the fact that the flow of the hydrogel is constrained when ceramic particles are present in the paste; when flowing under stress, the hydrogel cannot occupy the same volumes as the ceramic particles, and therefore must flow through smaller cross sectional areas (the spaces between the particles). This leads to increased hindrance of the flow, increasing μ , and more energy lost during flow, increasing G'' .
- 3- τ_y is marginally higher. This can be explained by the same reasoning given above; a larger stress is required to make the hydrogel flow when it is constrained.
- 4- The rise of G'' when τ is near to τ_y is proportionally smaller. This is simply due to the fact that G'' is much larger in the pastes compared to the hydrogel, so the effects causing the rise in G'' are less visible.

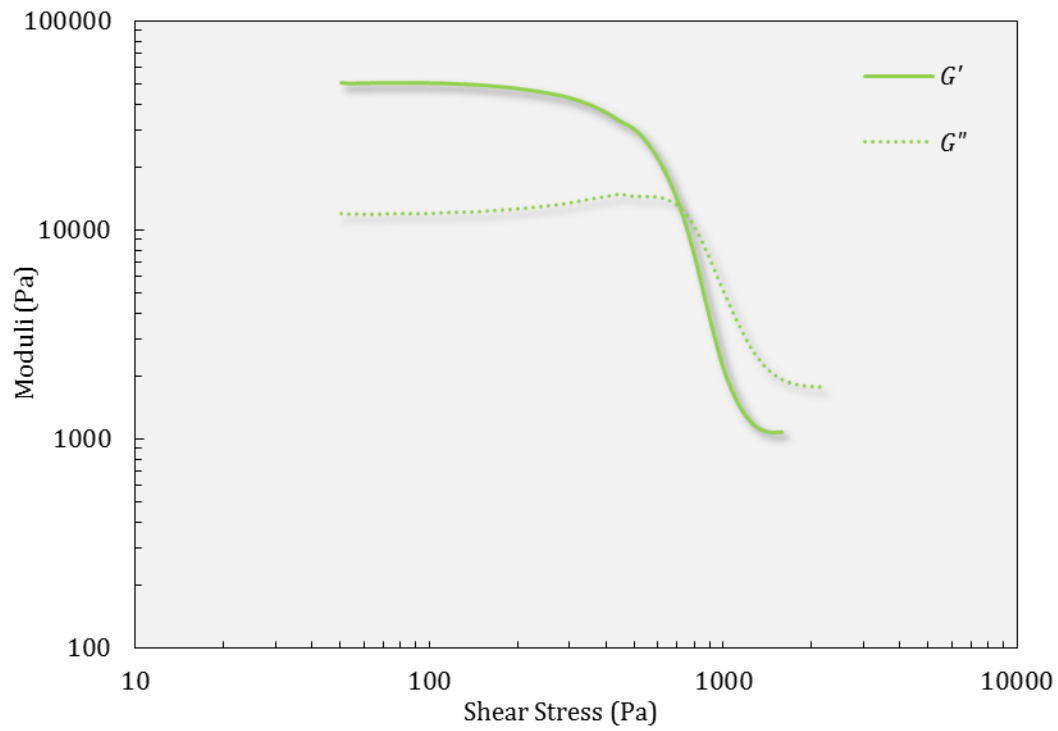


Figure 55. Amplitude sweep of a 33 vol% SiC mix paste at 23 °C. Note the similarity to Figure 45.

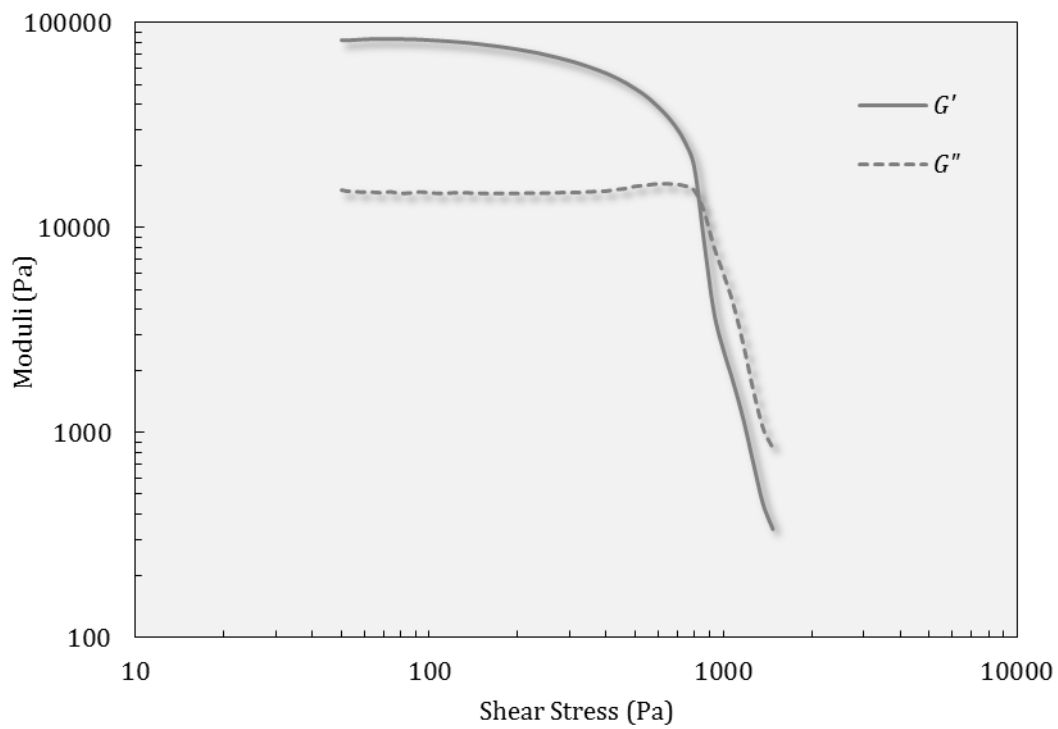


Figure 56. Amplitude sweep of a 33 vol% Al₂O₃ paste at 23 °C. Note the similarity to Figure 45.

Effect of Ceramic Volume Fraction

The four effects described above are pronounced with increased volume fraction of ceramic powder as seen in Figures 57 and 58. As V_f is increased, G'_{eq} increases very rapidly by ~ 3 orders of magnitude, faster than an exponential relationship, while τ_y increases more modestly in a near linear relationship. The increase in G'_{eq} is strongly dependent on the powder used, while the choice of ceramic powder has little effect on the increase in τ_y . The increase in G'_{eq} is due to the particles coming into contact. At low volume fractions (<0.2) these points of contact do not percolate to form a network, therefore G'_{eq} is not strongly affected. However at higher concentrations this network begins to percolate, increasing the G'_{eq} rapidly. This is the same mechanism that gives green bodies (powder compacts) their stiffness, and green bodies of a comparable volume fraction have a similar elastic modulus to our pastes.[117,118] The τ_y of the Pluronic gel is an order of magnitude larger than the τ_y exhibited by inter-particle interactions in colloidal pastes, so the effect of these interactions is insignificant compared to the strength of the Pluronic gel. The increase of τ_y with particle volume fraction can be attributed to the fact that the flow of the hydrogel is more constricted at higher volume fractions of ceramic particles. This effect has been reported for ceramic injection moulding systems[119] and can be fit with a modified Krieger-Dougherty model[120];

$$\frac{\tau_y}{\tau_{y0}} = \left(1 - \frac{V_f}{V_{fm}}\right)^{-2.5V_{fm}} \quad (3.7)$$

where V_f is the volume fraction, τ_{y0} is the yield stress of the hydrogel, V_{fm} is the volume fraction where the yield stress tends towards infinity and indicates the absolute limit for the ceramic loading. From fitting the Krieger-Dougherty model to the data of these hydrogel-based pastes we find $V_{fm} = 0.69$. This value is thought to vary with the particle size distribution, so in principle this should differ between the SiC and Al₂O₃ pastes, however any differences this imparted on the yield strength were too small to measure in our case. It is also notable that the calculated V_{fm} is close to the maximum random packing of uniform spheres (0.633),[121] indicating that this trend simplifies to geometric considerations.

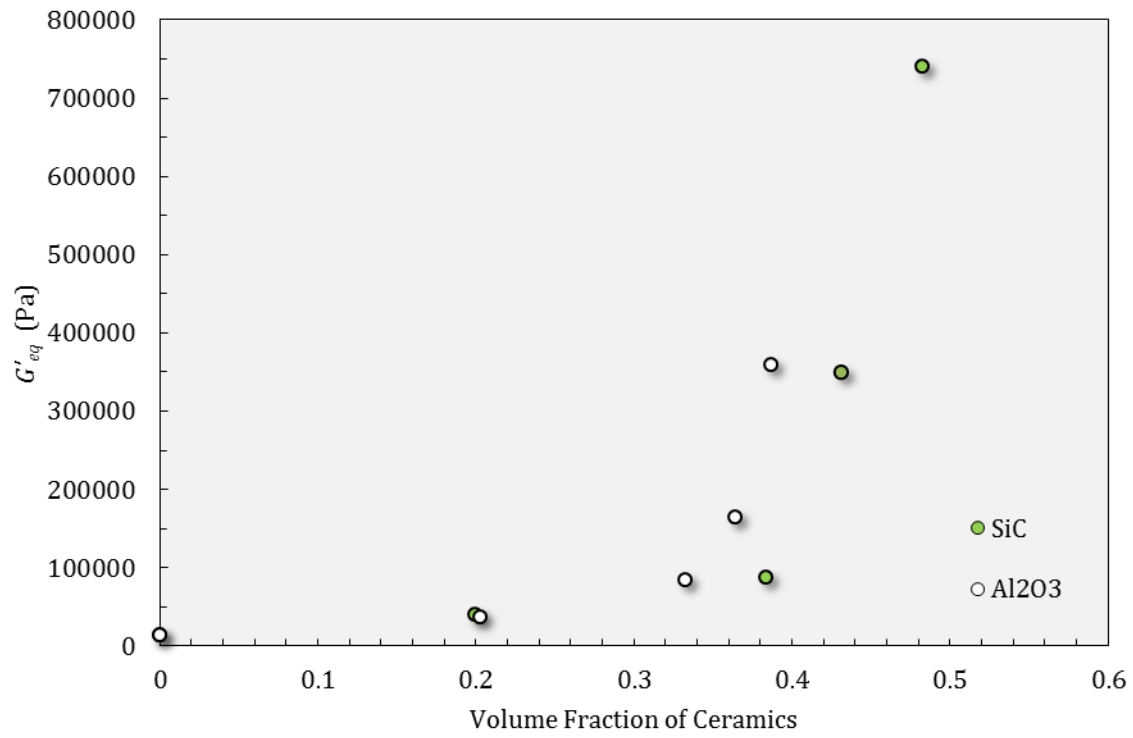


Figure 57. The effect of V_f on the equilibrium storage modulus of SiC mix and Al₂O₃ pastes.

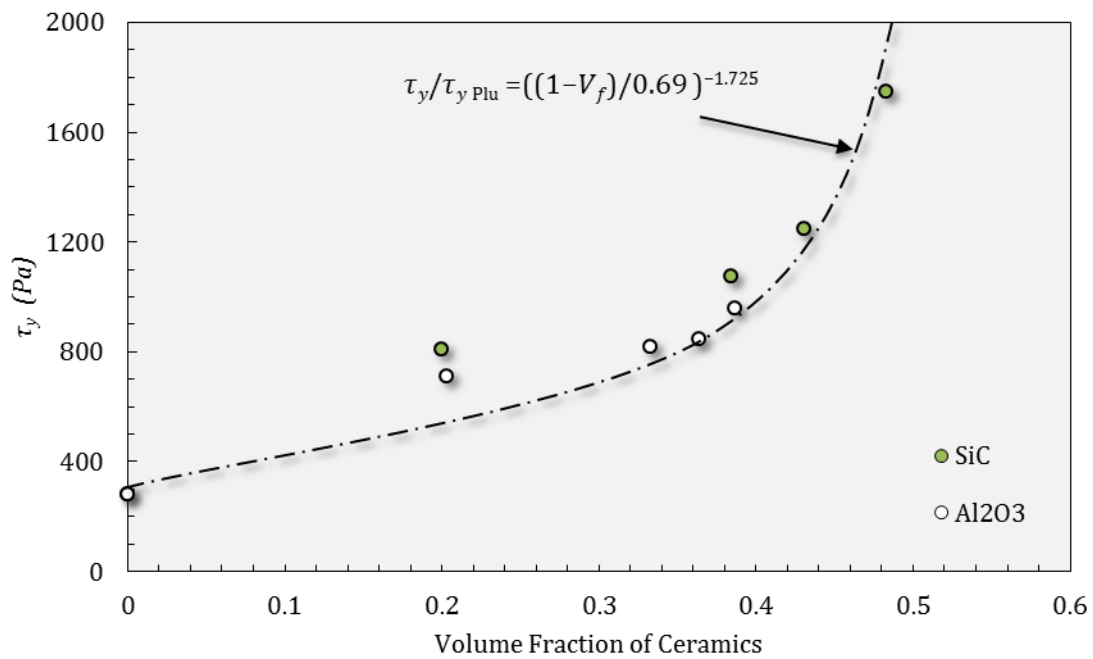


Figure 58. The effect of V_f on the yield stress of SiC mix and Al₂O₃ pastes, with a fit to the Krieger-Dougherty model (dash-dot line).

Effect of Surface Chemistry

In order to study the effect of the surface chemistry of the ceramic powders on rheology the dispersant Dolapix was added to Al_2O_3 pastes during mixing. Dolapix is a common polyelectrolyte dispersant used for processing of a range of oxide ceramics. The addition of 0.5 wt% Dolapix (with respect to the weight of the ceramic powder) caused G'_{eq} and K to fall dramatically, seen in Figures 59-62.*** The Dolapix adsorbs to the Al_2O_3 particles' surfaces, providing electrosteric stabilisation. This prevents attractive interactions between the particles, thereby preventing them from forming a rigid network. Similar effects of the strength of inter-particle interactions on G'_{eq} have also been observed in colloidal pastes, which exhibit G'_{eq} from 30 - 150 kPa.[45] This shows that the inter-particle interactions play a big role in determining the G'_{eq} of the pastes, and can be used to tune this rheological property as required. On the other hand τ_y is not as significantly affected by the dispersion of the ceramic powder, as seen in Figure 59. In hydrogel pastes the majority of the strength comes from the hydrogel itself, not the particle network. This leads to an important finding – the hydrogel is simply acting as a carrier for the ceramic particles, in a similar manner to ceramic-polymer suspensions used in injection moulding.

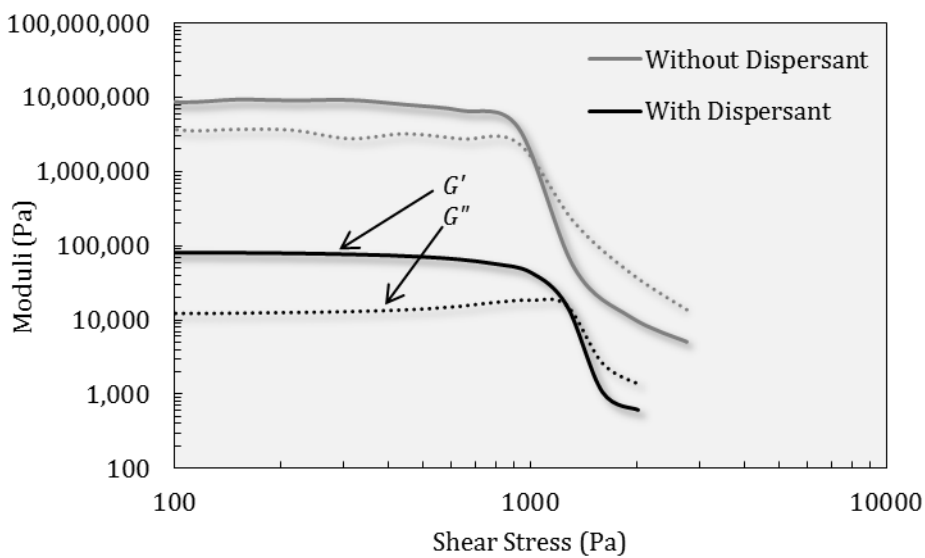


Figure 59. The effect of dispersants on the storage and loss moduli of 39 vol% Al_2O_3 pastes.

*** In terms of flow and elastic properties, no measureable difference was seen between Pluronic hydrogels containing and not containing 0.5 wt% Dolapix. In pastes the overall wt% of Dolapix is lower than this (as they are 0.5 wt% WRT the ceramic mass).

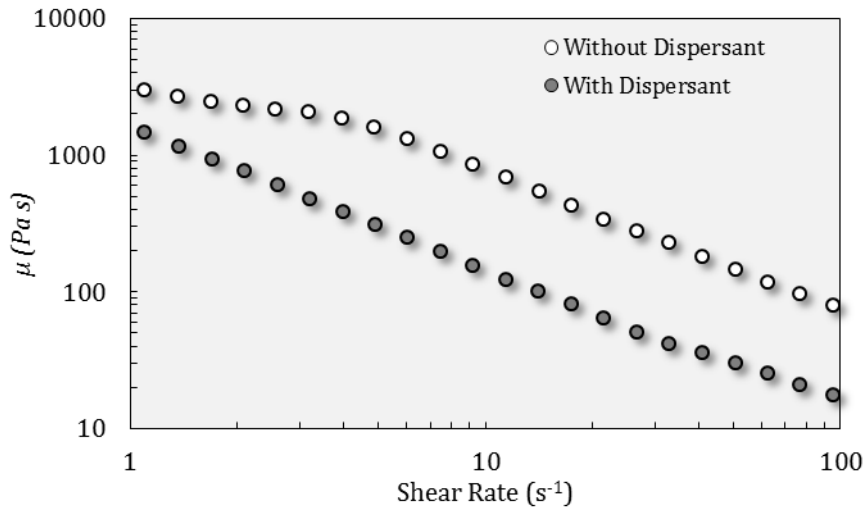


Figure 60. The effect of dispersants on the viscosity of 35 vol% Al₂O₃ pastes.

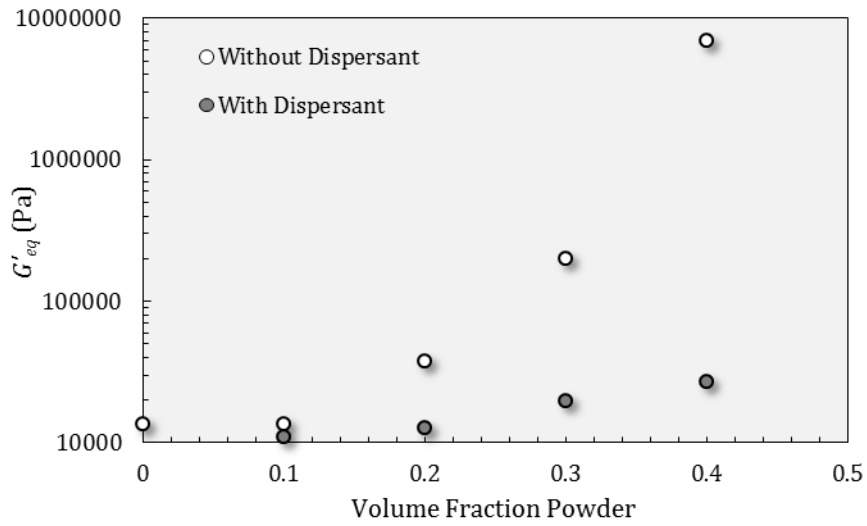


Figure 61. The effect of dispersion on the equilibrium storage modulus of Al₂O₃ pastes.

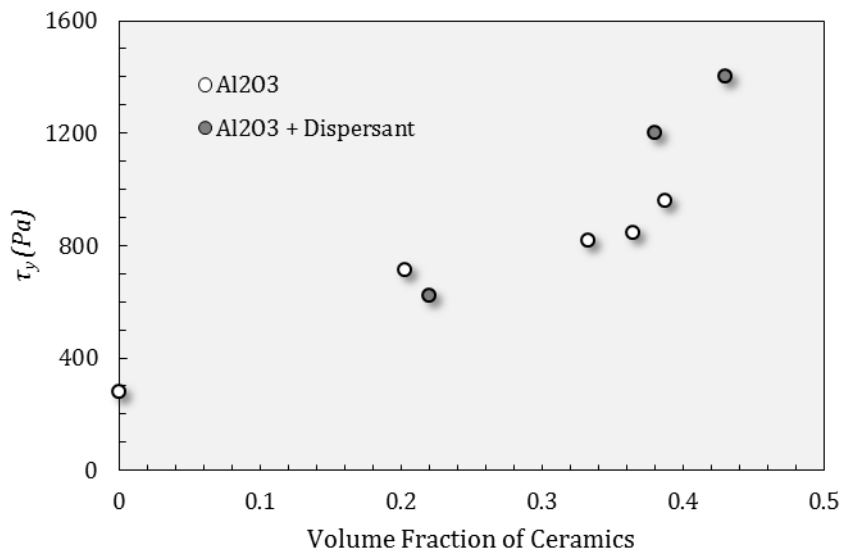


Figure 62. The effect of dispersion on the yield stress of Al₂O₃ pastes.

Platelet Pastes

Pastes can also be produced by mixing ceramic platelets into the hydrogel. For reasons discussed in Chapter V we used a mixture of microscopic alumina platelets and submicron alumina powder at a 7:3 weight ratio (herein referred to as the platelet mix). This was mixed with the 25 wt% Pluronic hydrogel and 0.5 wt% dispersant (with respect to the Al_2O_3) to aid mixing and defoaming. High resolution SEM was used to measure the size and morphology of the platelets which revealed the platelets to be irregular in shape, with an average width of $\sim 5 \mu\text{m}$ and an average thickness of $\sim 0.5 \mu\text{m}$, as seen in Figure 63, giving them an aspect ratio of 10. Although their shape was irregular, it is clear that many surfaces adopt crystallographically favourable orientations; as such there is a tendency for them to be somewhat hexagonal in shape. An in-depth analysis of the structure and properties of this unusual material can be found in Chapter V.

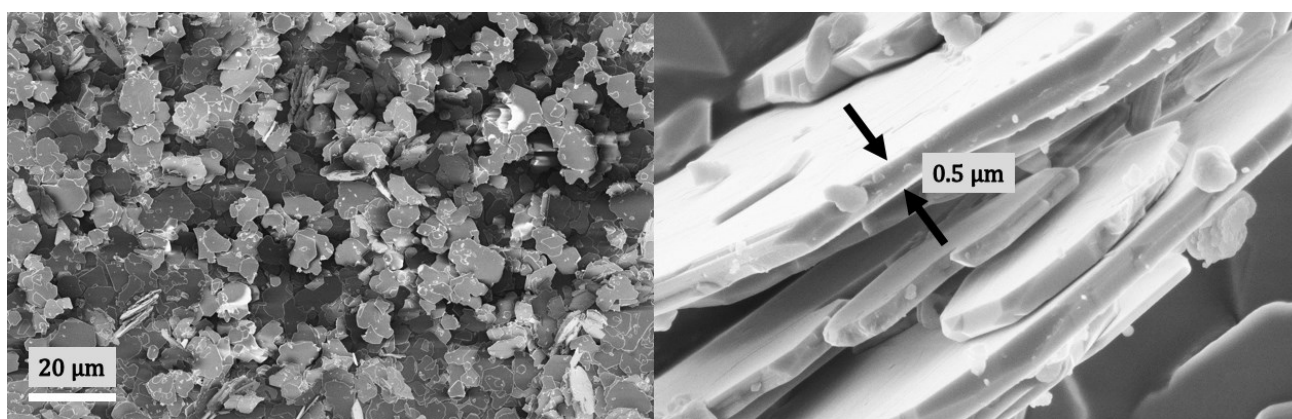


Figure 63. SEM images of the Al_2O_3 platelets.

As with the powder pastes covered above, the platelet pastes take on the viscoelastic characteristics of the base hydrogel, possessing a linear viscoelastic region, a yield stress, and shear thinning behaviour. Also as above, the platelet pastes have higher G' , G'' , τ_y and K than the base hydrogel, for the same reasons attributed to the powder pastes. The effect of the volume fraction of the platelet mix in the paste was studied in detail. As with the dispersed Al_2O_3 powder pastes, the yield stress increases mildly with volume fraction, while G'_{eq} increases more rapidly. The n of the pastes is in the range 0.15 - 0.35 and is not significantly affected by volume fraction, as the base shear thinning mechanism (breakup of the Pluronic network) is unchanged with volume fraction.

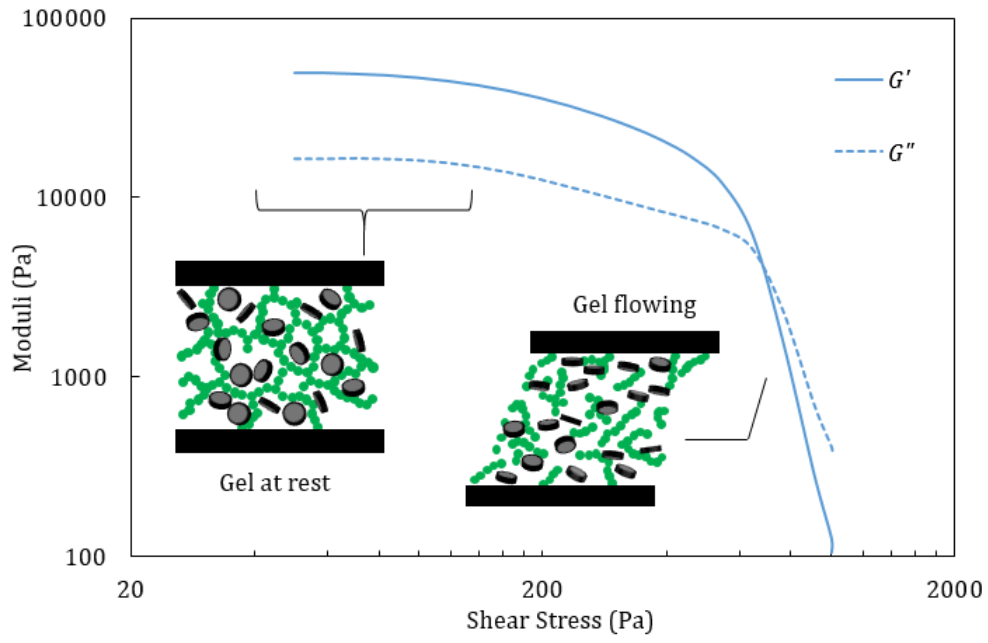


Figure 64. Representative amplitude sweep of an example platelet mix paste.

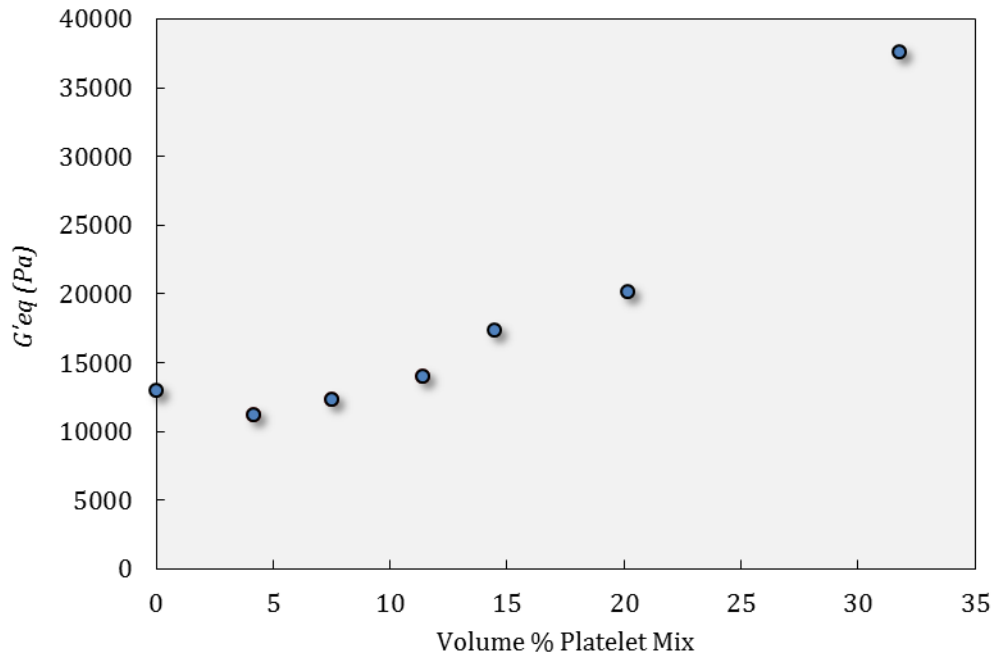


Figure 65. Effect of volume fraction on the equilibrium storage modulus of platelet pastes.

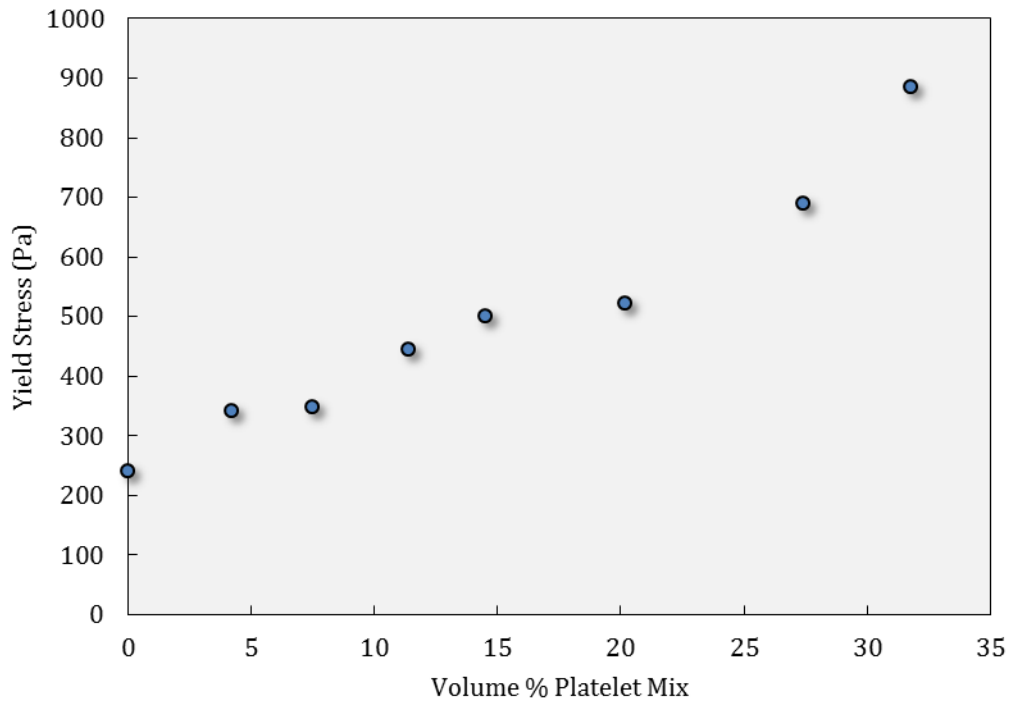


Figure 66. Effect of volume fraction on the yield stress of platelet pastes.

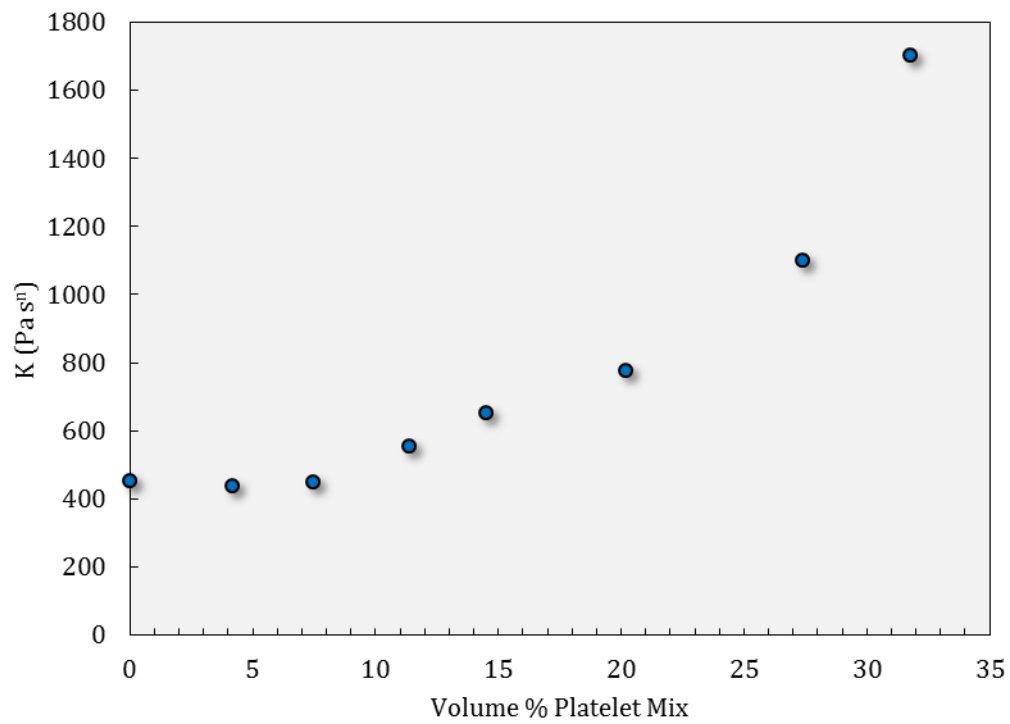


Figure 67. Effect of volume fraction on the reference viscosity of platelet pastes.

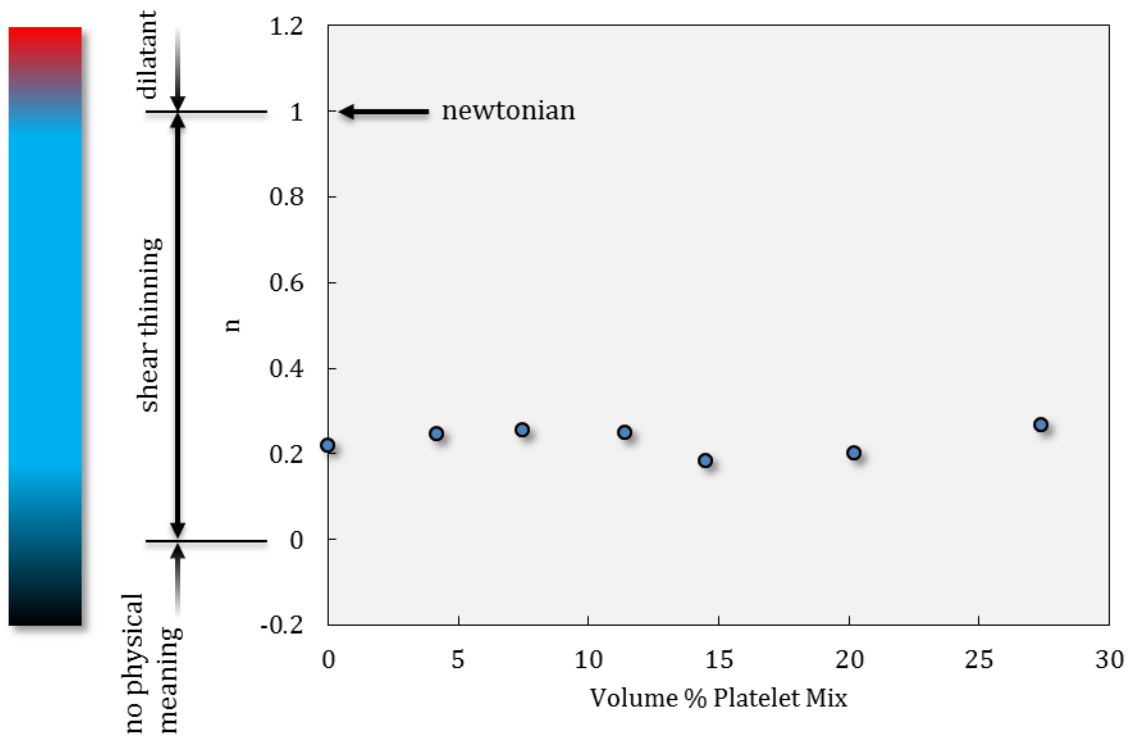


Figure 68. Effect of volume fraction on the shear thinning parameter of platelet pastes.

Rheology of Platelet Pastes verses Powder Pastes

The morphology and size of particles in a fluid can have a substantial effect on the viscoelastic properties of a system. This is because irregular and high aspect ratio particles cannot pack together easily, forming cage-like structures with large unoccupied space. This means that as one increases the volume fraction of these particles, the viscosity of the system can increase more rapidly than would be expected from spherical particles. The difficulty in packing anisotropic particles increases as their aspect ratio increases. Despite this widely accepted finding, the strength, equilibrium storage modulus, and reference viscosity of dispersed platelet pastes were all found to be of the same order of those of the dispersed Al_2O_3 powder pastes of equivalent volume fraction. This is demonstrated when these data sets are combined to give Figures 69 and 70. There are two possible reasons for this:

- 1- The platelets pack in a manner that allows easy flow.
- 2- The Al_2O_3 powder is much smaller than the platelets (nanometer rather than micrometer scale). Such small particles are known to have their own packing difficulties, so this emulates the packing difficulties of the platelets.

That said, one way in which these platelet pastes do significantly differ from their powder counterparts is the stability of air bubbles in the pastes. During planetary mixing air inevitably becomes trapped in the paste, and this necessitates a final defoaming (centrifuging) step prior to printing. In powder-based pastes, 2 - 10 minutes of defoaming at 2200 RPM was found to be sufficient. In the platelet pastes much longer times were required, and even after 50 minutes, the highest volume fraction pastes were still found to contain a very small amount of trapped air. One reason for this behaviour is that the morphology of the platelets allowed them to stabilise air bubbles by pinning the liquid-gas interface. This is most effective for particles with sharp edges or corners, such as the edges and step edges of the platelets, whereas rounded particles, such as the powders, are less effective at pinning the interface. This mechanism has been quantitatively studied in the literature,[122] and is illustrated schematically in Figure 72. From this reasoning, two possible arrangements around the bubbles exist, shown in Figure 73. These appear to be equivalent from a pinning perspective, however the concentric arrangement should be more stable to perturbations (the platelets are more vulnerable to outside forces, such as being knocked by other platelets); therefore the concentric arrangement should be more common. This was found to be the case for all bubbles observed, as seen in Figure 71.

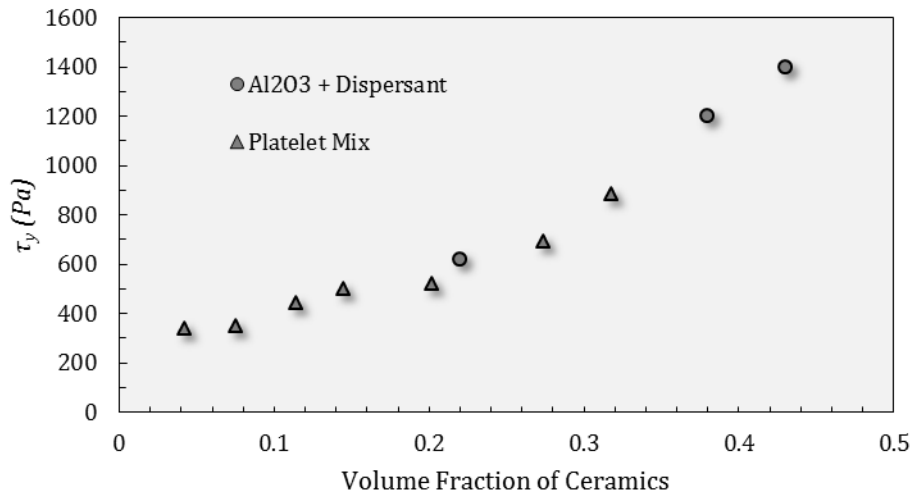


Figure 69. Effect of volume fraction of Al_2O_3 powder compared to Al_2O_3 platelets on the yield strength.

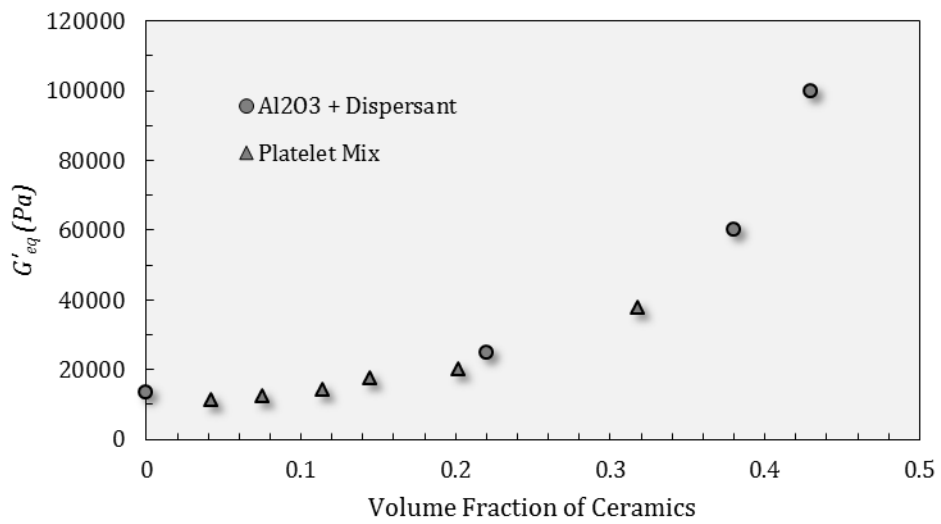


Figure 70. Effect of volume fraction of Al_2O_3 powder compared to Al_2O_3 platelets on the equilibrium storage modulus.

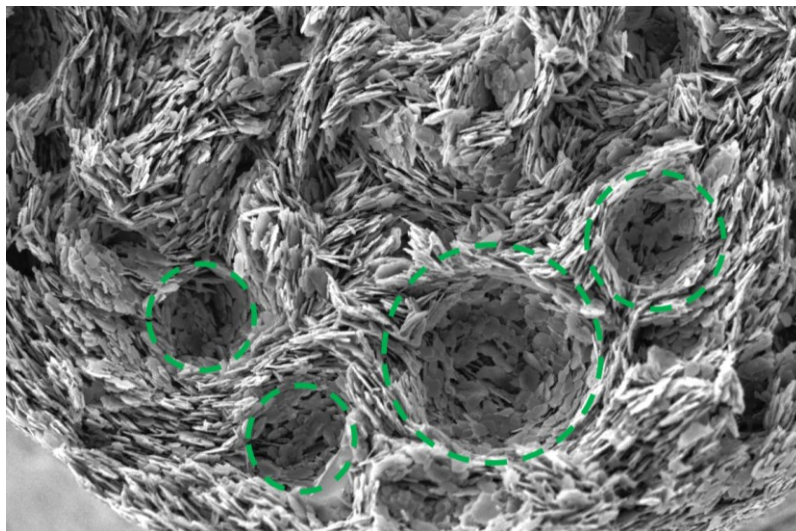


Figure 71. SEM image of the cross section of dried platelet paste, with the location of several bubbles marked. Note the conformity of the platelets to the surface of each bubble.

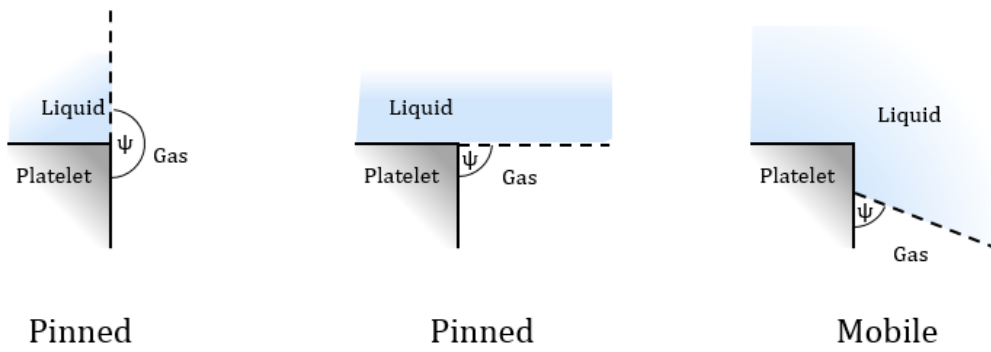
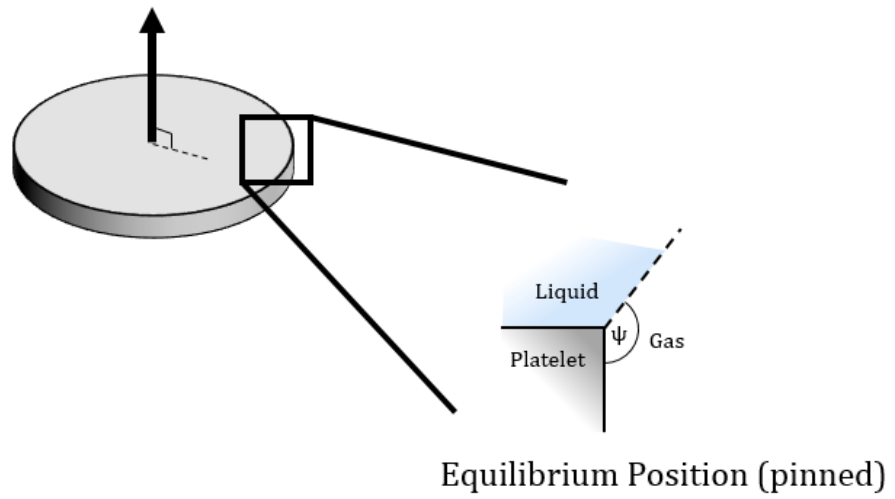


Figure 72. Schematic illustrating the range of angles over which the liquid-gas interface can be pinned by sharp particles such as platelets, stabilising bubbles.

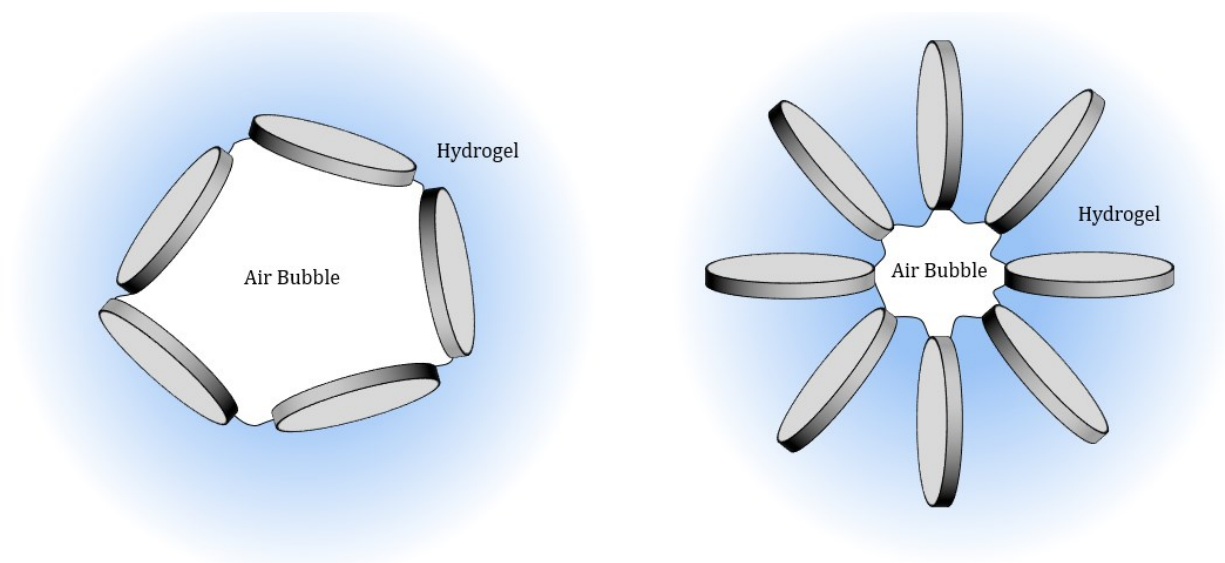


Figure 73. Two possible platelet arrangements stabilising a bubble. Left “concentric”, right “radial”.

Fibre Pastes

The last group of pastes covered in this work is pastes based on short (discontinuous) fibres. Two types of short fibres were available for this work: SiC whiskers and carbon fibres. As with other materials, it was possible to produce pastes by simply mixing ceramic fibres into the aforementioned hydrogel.

SiC Whisker Pastes

Upon examination using SEM, the SiC whiskers were found to have a ridged shape, and an average diameter and length of $\sim 1\ \mu\text{m}$ and $\sim 25\ \mu\text{m}$ respectively, as seen in Figure 74. When mixed with a 25 wt% Pluronic gel, very viscous, stiff pastes were formed, even at volume fractions as low as 0.1. These pastes had desirable elastic properties for robocasting, as demonstrated in Figure 74, however their flow properties were generally poor, exhibiting high K ($820\ \text{Pa}\ \text{s}^n$) and, most importantly, a high n (0.91). This meant that the pastes were almost dilatant, likely due to the fibres continuously locking together. This behaviour makes them difficult for robocasting, and combined with the serious health precautions required when working with this material,[89] this led to the decision to discontinue work with these fibres.

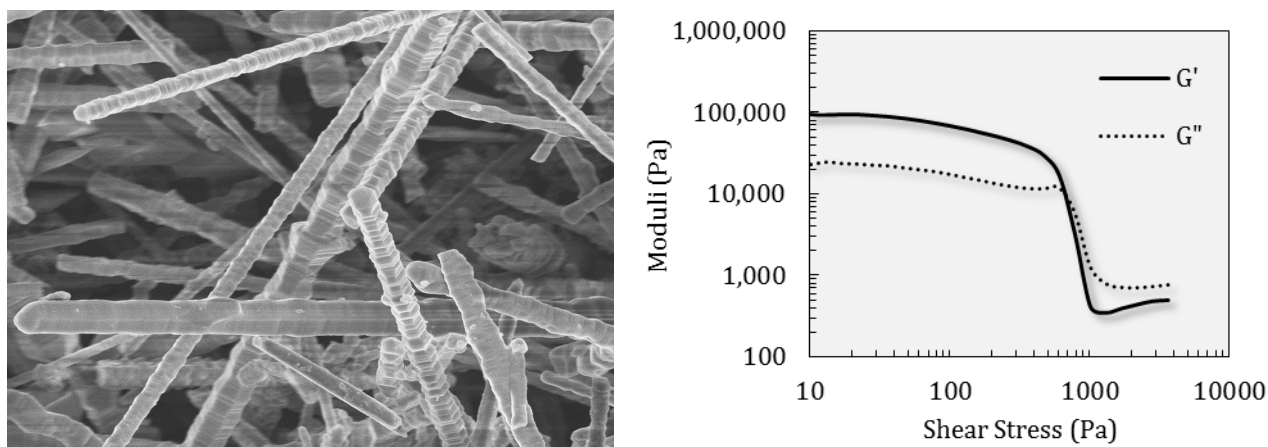


Figure 74. SEM image of SiC whiskers and oscillation amplitude ramp of a 10 vol% SiC whisker paste.

Carbon Fibre Pastes

Polyacrylonitrile (PAN)-derived short carbon fibres were then chosen due to their commercial availability. This manufacturing method gives rise to very uniform fibres with a complex internal structure consisting of crystallites of graphite aligned with the **a** and **b** axis in the direction of the fibre. These crystallites are embedded in amorphous carbon, and the properties of the fibres depend upon the ratio of graphitic to amorphous carbon (with more graphitic fibres being stiffer, but more amorphous fibres being stronger).[88] These fibres represent a new challenge for producing aqueous (hydrogel) pastes as they are intrinsically hydrophobic, whereas all of the other materials used in pastes thus far are hydrophilic to some extent. Additionally the sharp edges at the ends of the fibres may help stabilise bubbles further.

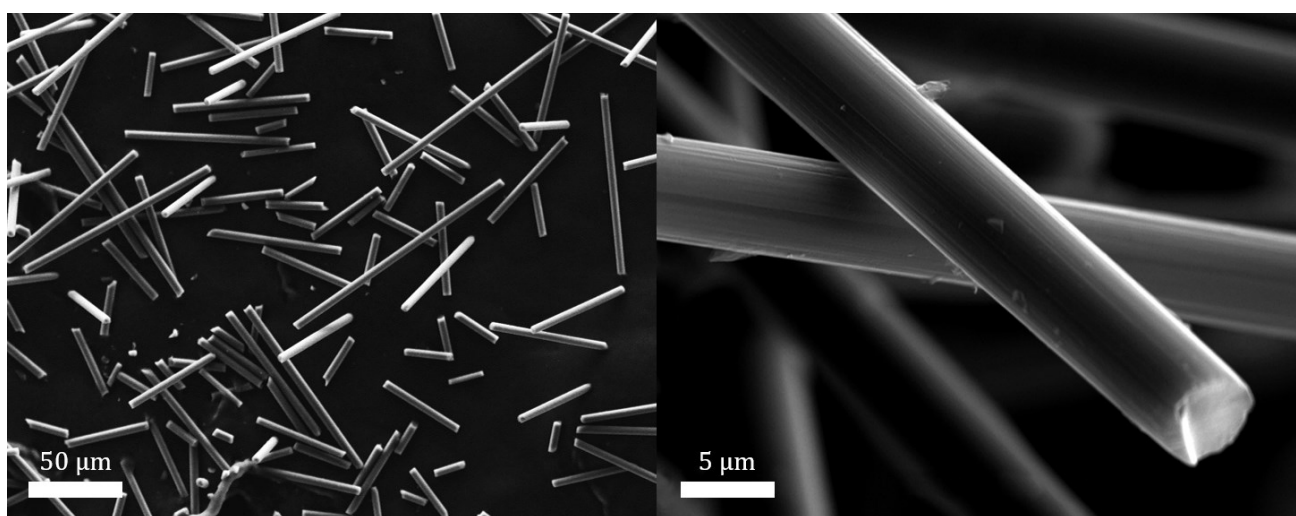


Figure 75. SEM images of chopped/milled carbon fibres.

A familiar viscoelastic response was observed during amplitude sweeps, as seen in Figure 76, however both the G'_{eq} and τ_y were lower than that of the raw hydrogel. As the volume fraction of carbon fibres increases, both of these parameters fall, as seen in Figures 77 and 78. This is the opposite trend to that of the powder and platelet pastes, and can be explained simply by the presence of microscopic air bubbles in the paste. These hydrophobic fibres unsurprisingly stabilise air bubbles in these water based pastes, resulting in more bubbles in the more concentrated pastes which could not be removed by defoaming. This effect was the dominant factor over the rheology of these pastes.

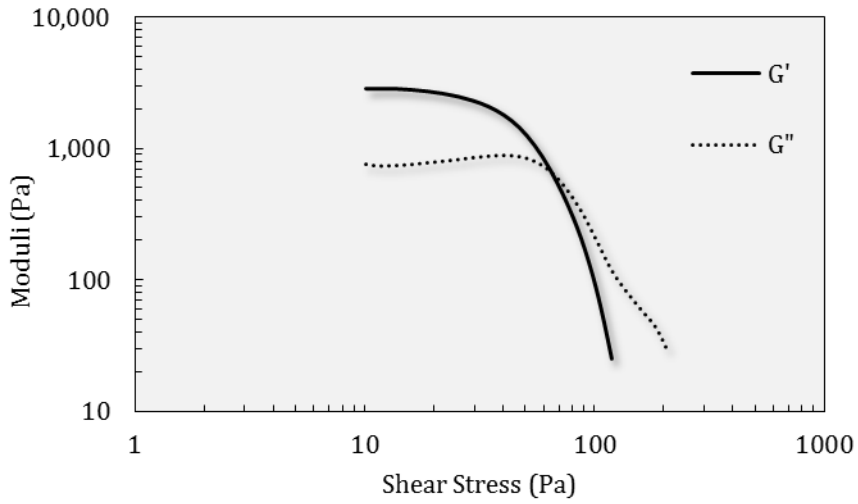


Figure 76. Amplitude sweep of a 10 vol% carbon fibre paste.

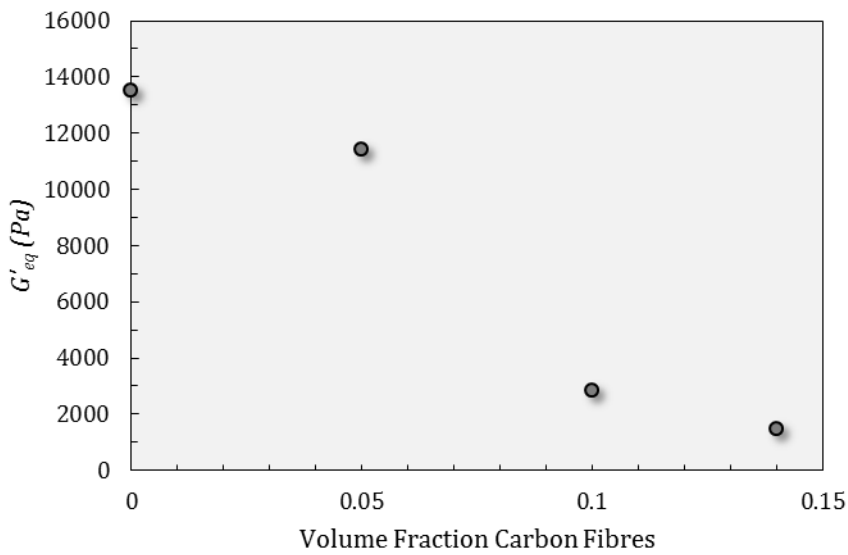


Figure 77. Effect of carbon fibre volume fraction on equilibrium storage modulus.

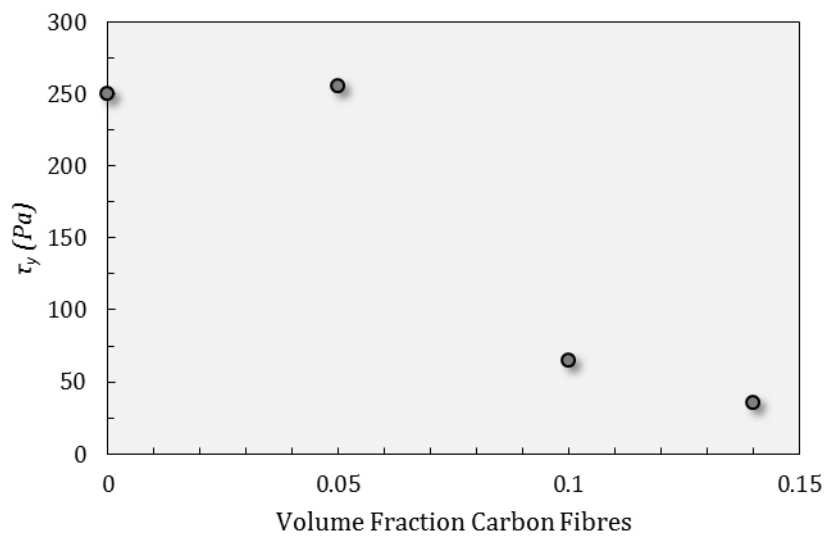


Figure 78. Effect of carbon fibre volume fraction on yield stress.

General Discussion

A New Meaning of 'Printability'

As discussed in Chapter I, there have been two attempts to quantify printability based on the rheology of the paste, however both of these only set out minimum criteria for the yield stress and storage modulus in order to resist the forces of gravity and surface tension.[45,57] However, in this work neither of these forces were ever observed to directly cause printing to fail. Thus we postulate that printability can be defined more deeply than has been attempted in the literature so far.

The reason the term 'printability' has come into use is because it is a very natural concept to researchers working with robocasting; a five minute conversation with one of these individuals will reveal this much. Simply by observing and probing with a spatula, such researchers are able to identify whether various substances are 'printable' with ease, as if it were a firmly defined property; however, this is far from being the case. Printability should encompass each of the rheological properties discussed earlier in the chapter, and thus it should be possible for it to be quantified by a figure of merit. In order to construct this, one must identify which properties result in good prints when maximised, and which improve the print when minimised. This can be answered as follows:

- G'_{eq} should be maximised, as it is responsible for the structural integrity of the part during printing. A high G'_{eq} will mean minimal elastic deformation of the part from the forces acting on it during printing.
- n , K and τ_y should be minimised, as they reduce the force required to bend the filament 90° as it exits the nozzle. This force is applied to the existing printed layers, so reducing it reduces the amount of strain the part experiences during printing. Minimising these parameters has a side benefit of reducing the pressure required for extrusion, and allows adjacent printed filaments to fuse together more easily, allowing printing of dense parts.
- Despite the point above, there exists a minimum τ_y required to resist surface forces and gravity, maintaining shape and stability.
- γ_y should be minimised as it encompasses the amount of elastic energy stored in the paste. A low γ_y means the paste is not compressed much during extrusion, and so when the ram stops moving the paste stops extruding immediately.

Putting these inferences together, the following **paste specific** figure of merit can be constructed:***

*** A more rigorous, mathematical approach to constructing these figures of merit is presented in Appendix I. This gives rise to the same result as the simple reasoning used here.

$$\Phi = \frac{G'_{eq}}{\tau_y} \quad (3.8)$$

This arises from balancing the force that the nozzle imparts on the printed body with the body's resistance to this force. Pastes with larger Φ should excel in printing higher aspect ratio parts, as the part will deform less during printing, and so will result in better packing/stacking of the printed filaments. If the elastic strain is too large then the part is pulled over due to the force illustrated in Figure 79. In high aspect ratio parts, this force results in a large deformations (the top of the part being dragged through the air), which cause collapse of the top of the part as it is no longer supported by the underlying layers. This was the only intrinsic cause of failure encountered during printing throughout this thesis. γ_y is encompassed in Φ , which can be rewritten using Equation 3.4 to give Equation 3.9 (assuming G' is invariant with stress). One might postulate that K and n should also play a role in defining the force F exerted on the printed part. This is true, although this is a time (flow rate) dependent consideration. At the limit where flow rate tends to zero, F tends towards proportionality with τ_y , thus for sufficiently slow printing speeds Φ should be an appropriate yardstick for comparing pastes (while keeping printing parameters and nozzle sizes constant).

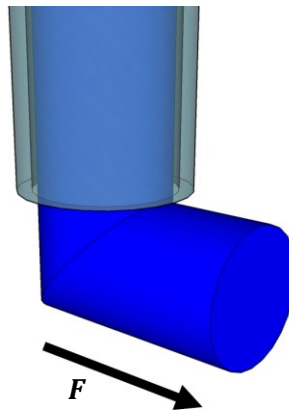


Figure 79. Schematic demonstrating the deformation of the paste filament during printing. As it exits the nozzle, it is bent by 90°, imparting a lateral force on the substrate/existing printed part.

$$\Phi = \frac{1}{\gamma_y} \quad (3.9)$$

Another way of bringing many of the above concepts together is to plot the G'_{eq} against the τ_y of each paste. This is presented in Figure 80, where points closer to the top left of the plot possess higher Φ .

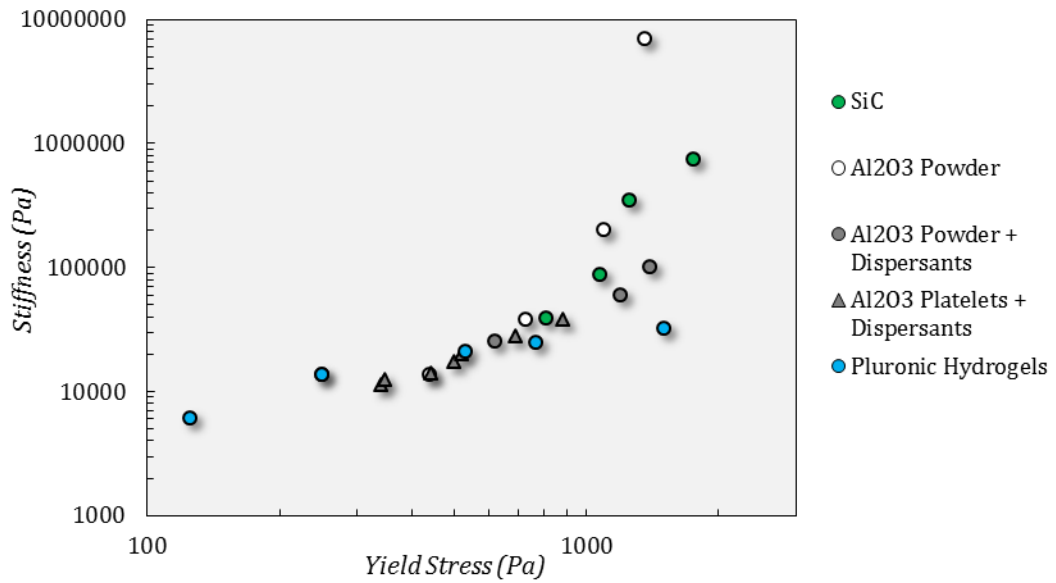


Figure 80. Plot of stiffness against yield stress of a range of pastes from this work.

Using the same approach a range of pastes from the literature were plotted in Figure 81. Pastes which were considered successful by the authors are denoted in Figure 82, allowing a map of printability to emerge. This can be further aided by considering some fundamental requirements for yield stress, such as a minimum yield stress to allow the part of a set height to be self-supporting, and the maximum force the printer can apply, both of which have been marked to create an envelope of printability.

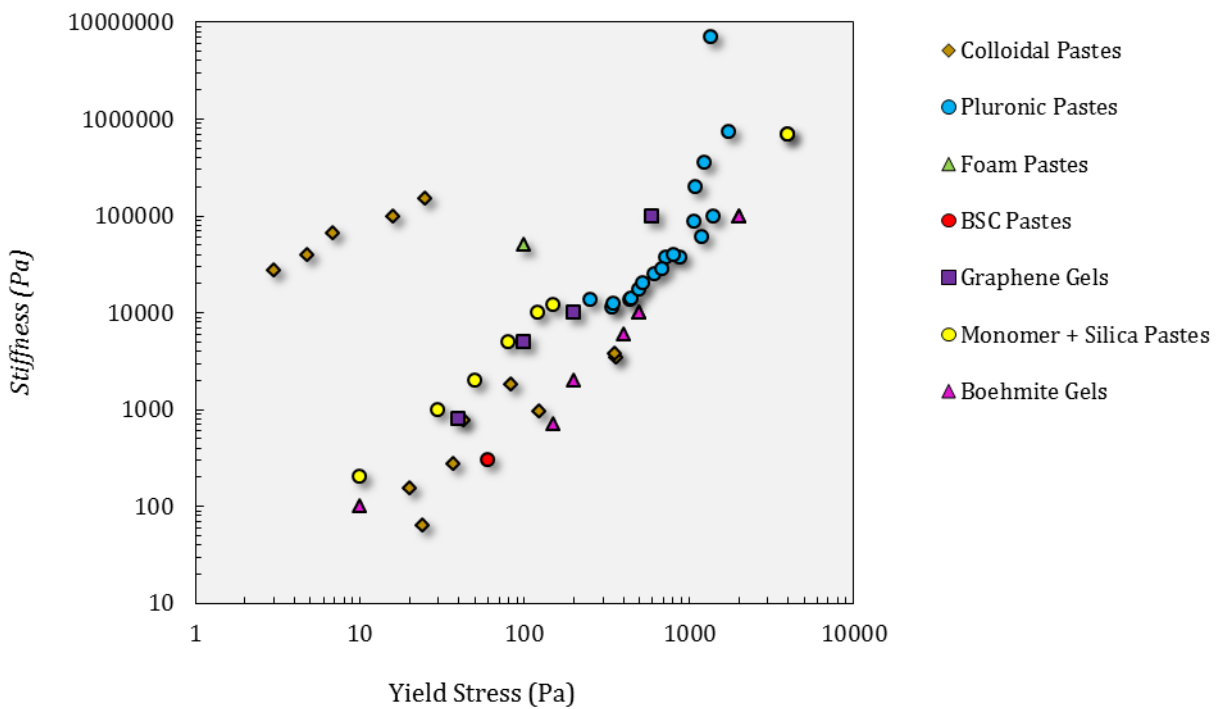


Figure 81. The plot from Figure 80, including pastes from the literature.

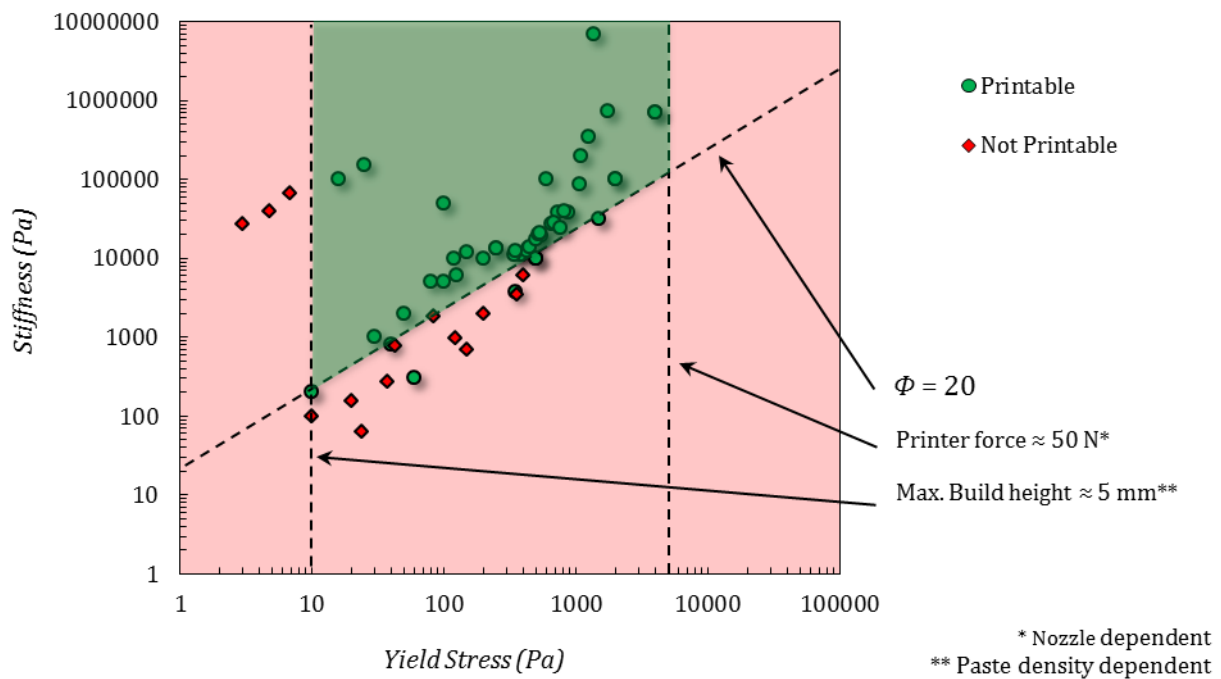


Figure 82. The plot from Figure 81, denoting which pastes were declared printable or not by the respective authors. A minimum figure of merit, and limitations on the yield stress are included to create a map.

From Figure 82 it is clear that the figure of merit holds some merit. Pastes with an insufficient yield stress to build macroscopic objects, or with a Φ below 20 tend to have been subjectively declared unprintable by the respective authors. The upper limit on yield stress (where the maximum force that the printer can apply becomes the limiting factor) has not been probed here or in the literature, as these pastes rarely ever make it to the printer due to difficulties when mixing and transferring these extremely dry, viscous materials between syringes.

Optimising Pluronic Hydrogels and Pastes using Φ

Pluronic hydrogels are very complex materials. In the concentration and temperature range tested we have measured the viscoelastic properties of three different phases (liquid, hard gel, soft gel), and there exist more that cannot be detected by rheological measurements (liquid pre- and post- micelle formation). Not only can Pluronic micelles form different shapes (such as spheres and rods),[123] but these micelles pack together in a wide variety of crystal structures (such as lamella, FCC, BCC) upon gelation.[116] This gives rise to a large number of possible structures. For this work it is important to use knowledge of the rheological behaviour of basic Pluronic gels to help us to select appropriate mixing conditions, printing conditions and paste compositions. This is complicated by the fact that these considerations are interdependent; certain printing conditions may be ideal for one paste, but inappropriate for another.

One of the key findings in this chapter is that Pluronic pastes adopt the viscoelastic behaviour of the hydrogel, with G'_{eq} , K , and τ_y simply increasing, in most cases linearly, with Pluronic concentration and volume fraction of ceramic material. n was not found to significantly change with volume fraction.

For Pluronic gels, the maximum Φ was found at 25 wt% Pluronic. Below 20 wt% no gel was formed, so Φ is undefined. Above 25wt% both parameters fall steadily. Based on this metric, 25 wt% is the best choice for the gel used in each paste. Not only did this offer the best printing performance, but it also minimised the volume fraction of organics in the paste (good for burn-out) and possessed an appropriate T_{gel} to allow printing at room temperature.

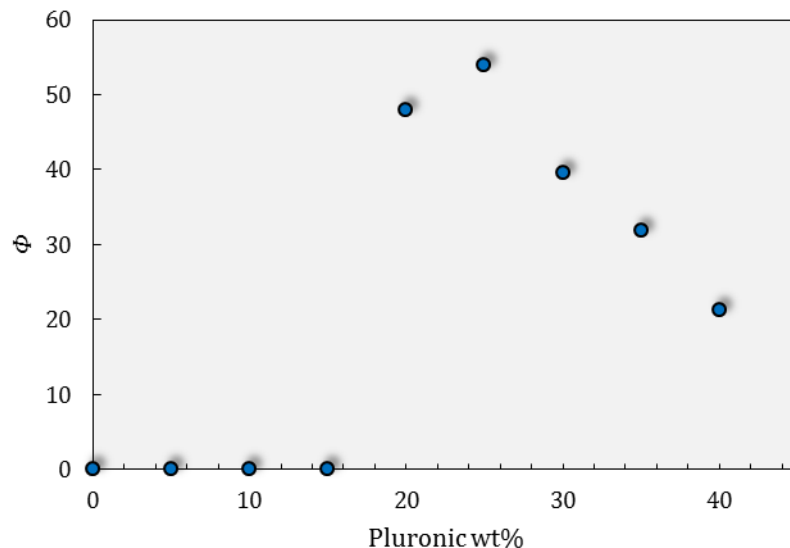


Figure 83. Variation of elastic figure of merit with concentration of raw Pluronic gels at 23 °C.

For pastes the main variables under the control of the user are volume fraction and dispersion, the effects of which are presented in Figure 84. Increasing volume fraction initially causes Φ to decrease

slightly, until the volume fraction is high enough to start to form a stiff network. This network does not exist for dispersed pastes, thus Φ does not substantially increase at high volume fractions when a dispersant is used. All pastes are less printable than the 25 wt% Pluronic gel, with the exception of the highly loaded undispersed pastes. That said, all of these systems were printable to some degree, so the minimum Φ required for printing could not be ascertained.

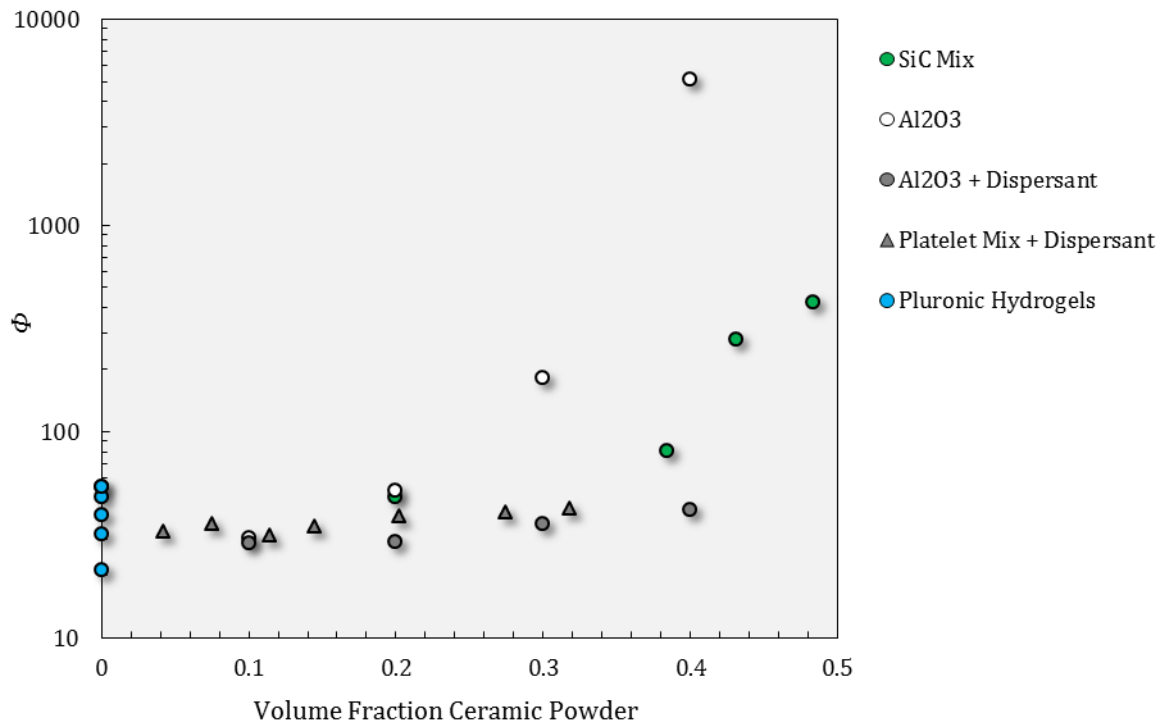


Figure 84. Elastic figure of merit for a range of pastes.

A Brief Comparison to Other Paste Systems for Robocasting

Hydrogel pastes differ fundamentally from colloidal pastes (the most common paste systems currently used in robocasting). In colloidal pastes τ_y can vary by an order of magnitude by subtly controlling the interactions between the ceramic particle surfaces (the basis for the gel structure).[45] Conversely, in hydrogel pastes τ_y is not strongly affected by surface interactions, as τ_y is orders of magnitude higher and is dominated by the strength of the hydrogel network, not the particle network. Other rheological properties of the hydrogel pastes are comparable to reported colloidal paste systems. The hydrogel pastes have a similar range of G'_{eq} (10 - 1000 kPa), somewhat lower useful ceramic volume fractions (0.3 - 0.45) and somewhat larger viscosity parameters ($K = 2 - 6 \text{ kPas}^n$). Overall, the Pluronic pastes tend to exhibit moderately high Φ , depending on the powder and dispersion, and importantly unlike other systems their Φ never drops below 20.

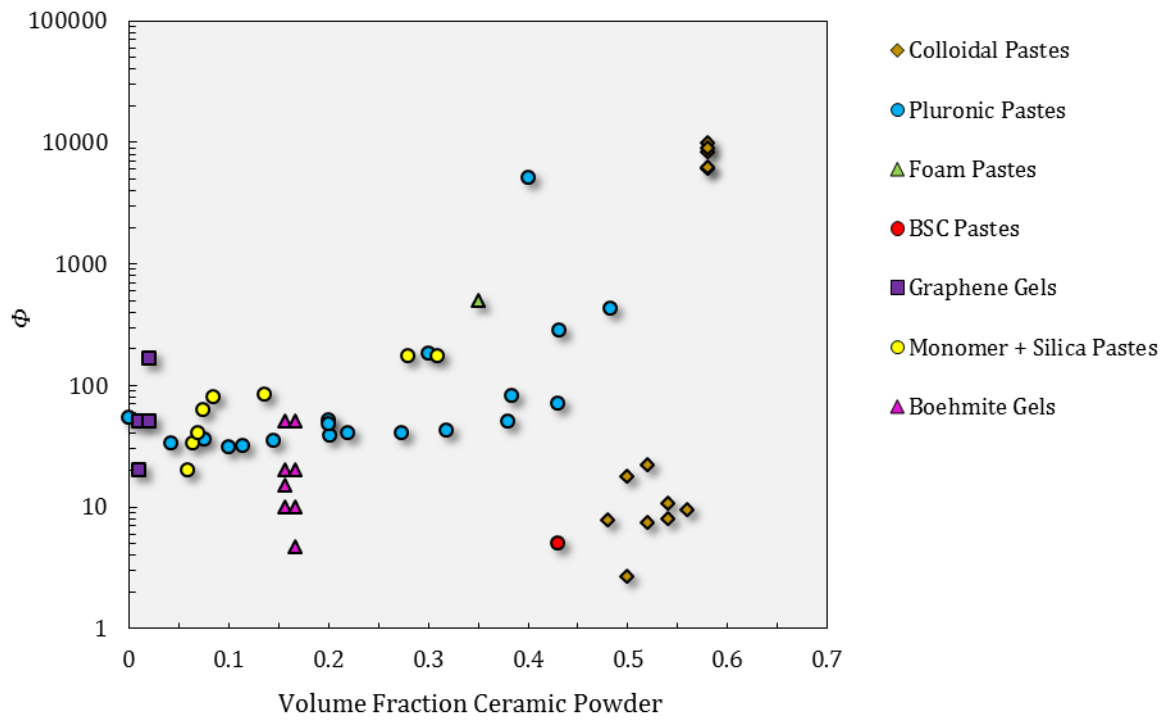


Figure 85. Comparison of paste systems from the literature using the figure of merit. Colloidal pastes,[45,85] BSC (block co-polymer surfactant) pastes,[124] foam pastes,[59] graphene gels,[125] monomer pastes.[100,126]

Conclusions

A detailed rheological study was conducted on the gelation, yielding, and flow behaviour of Pluronic hydrogels in the 15 - 45 wt% concentration range, using oscillatory and flow based measurements. This study was used to select the most appropriate concentration gel for robocasting: 25 wt%.

Pastes were then formulated consisting of this 25 wt% gel mixed with SiC and Al₂O₃ based ceramic powders. The rheological properties of these pastes were then studied, and it was found that the surface chemistry has a strong effect on G'_{eq} , but little effect on τ_y . Both of these properties also increase dramatically with increasing volume fraction of ceramic powder. In a similar manner, pastes were then formulated consisting of the same hydrogel mixed with either Al₂O₃ platelets, or short carbon fibres. Overall these were found to possess reasonably similar rheological properties to equivalent powder pastes. This illustrates the flexibility of the Pluronic hydrogel in allowing very different materials to be made into pastes for robocasting, allowing a wide variety of materials to be printed.

Lastly, a model was proposed to allow comparison of the suitability of different pastes for robocasting based on their measured rheological properties – in other words a parameter that determines 'printability' was constructed. This parameter was calculated for each of the pastes studied above, as well as a range of pastes presented in the literature, in order to assess its usefulness in evaluating printability of a diverse range of pastes.

Chapter IV – Monolithic Ceramic Parts

Introduction

Reports of the mechanical properties of monolithic parts produced by robocasting are relatively scarce in the literature. This is in part due to the fact that most work using robocasting has produced scaffolds rather than dense monolithic parts. Additionally there are no published reliability studies for ceramic parts produced by robocasting. The following chapter aims to fill this gap by demonstrating the printing, post-processing and mechanical properties of oxide and non-oxide ceramic materials produced by robocasting, and to explore the limitations of the robocasting technique for simple shapes. Al_2O_3 was selected as the model oxide ceramic since this is one of the most commonly used structural ceramics worldwide. Liquid phase sintered SiC was taken as the model non-oxide ceramic, in part to illustrate the power of the hydrogel when fabricating pastes of mixtures of powders with differing surface chemistry and surface charge in water. Moreover, these materials are representative of two large families of structural ceramics in terms of processing, properties and applications and, when considered together, can inform on robocasting of most structural ceramic materials.

Printing Parameters

Paste Selection

When formulating and selecting the paste to print dense, monolithic parts, there are a number of conflicting factors. As mentioned in Chapter II, the paste must be homogenous, reasonably low viscosity, have an adequate storage modulus and yield strength, and a high volume fraction of ceramic powder. This was expanded upon in Chapter III with the introduction of the figure of merit. With this in mind, the highest feasible volume fraction pastes were selected as this maximises the figure of merit, reduces drying shrinkage, and increases green density. Thus, SiC pastes of 39.4 vol% and Al₂O₃ pastes of 35.3 vol% were used to print the proceeding parts, as these were the maximum attainable volume fractions of these materials before the printer approached maximum extrusion force and handling became difficult.

Print Speed

In general faster print speeds are preferable as the total build time is roughly proportional to print speed, and faster extrusion speeds were found to result in more stable flow. Capillary rheometry of pastes found stable flow in the range from 2.5 to 30 mm/s, as seen in Figure 87. All extrusion tests were carried out via displacement control, as this should be more accurate and uniform than pressure control, and a larger maximum pressure can be applied. These tests also confirmed that the extrudate does not experience any 'die-swell' (where the filament expands as it exits the nozzle); conversely, the filaments appeared unaffected in videos taken at different extrusion speeds, seen in Figure 88. This may be due to the vector nature of the shear thinning of the paste – its viscosity is high in the horizontal direction, which may resist die-swell. On the other hand, high printing speeds require larger extrusion force and reduce the accuracy of the tool path when changing direction, causing sharp corners to become rounded. This is because any machine will have a fixed acceleration limit (due to the inertia of the print head), and when the direction is changed the head decelerates to zero in one direction and then accelerates up to the print speed in the new direction. While this is occurring the nozzle is still extruding material, and so excess material is deposited at points where velocity changes. This is shown in Figure 86. The issue is exacerbated by faster print speeds because the acceleration and deceleration takes longer, and because the nozzle is extruding at a faster rate while this occurs. With each of these factors taken into consideration, 10 mm s⁻¹ was found to be an appropriate choice.

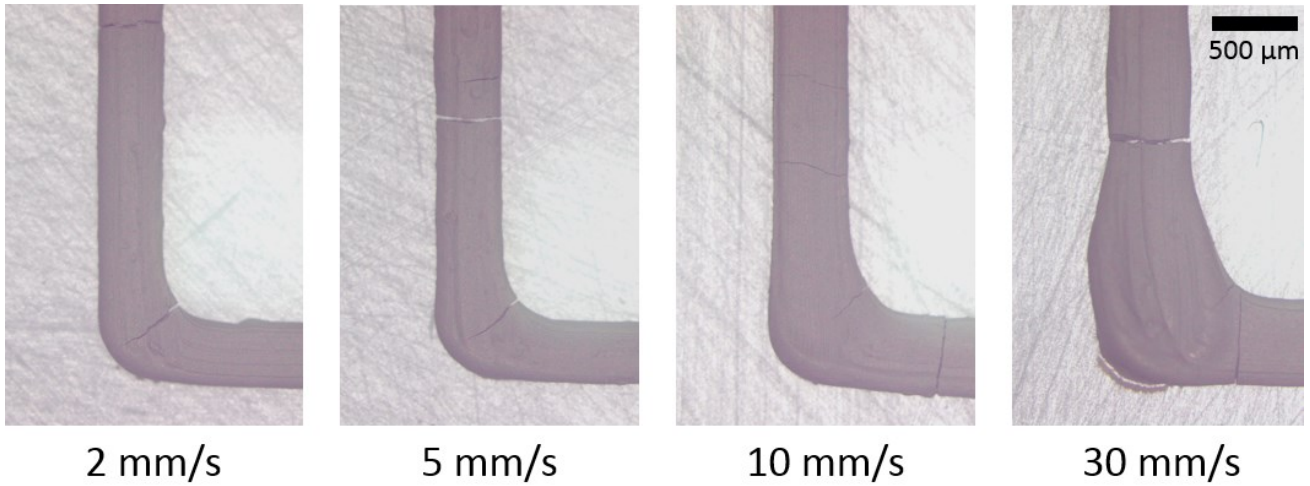


Figure 86. Printing a single line turning 90° at three different speeds. The paste in this case is 36 vol% SiC, however this effect is not strongly dependent on the paste. Cracks are due to rapid drying.

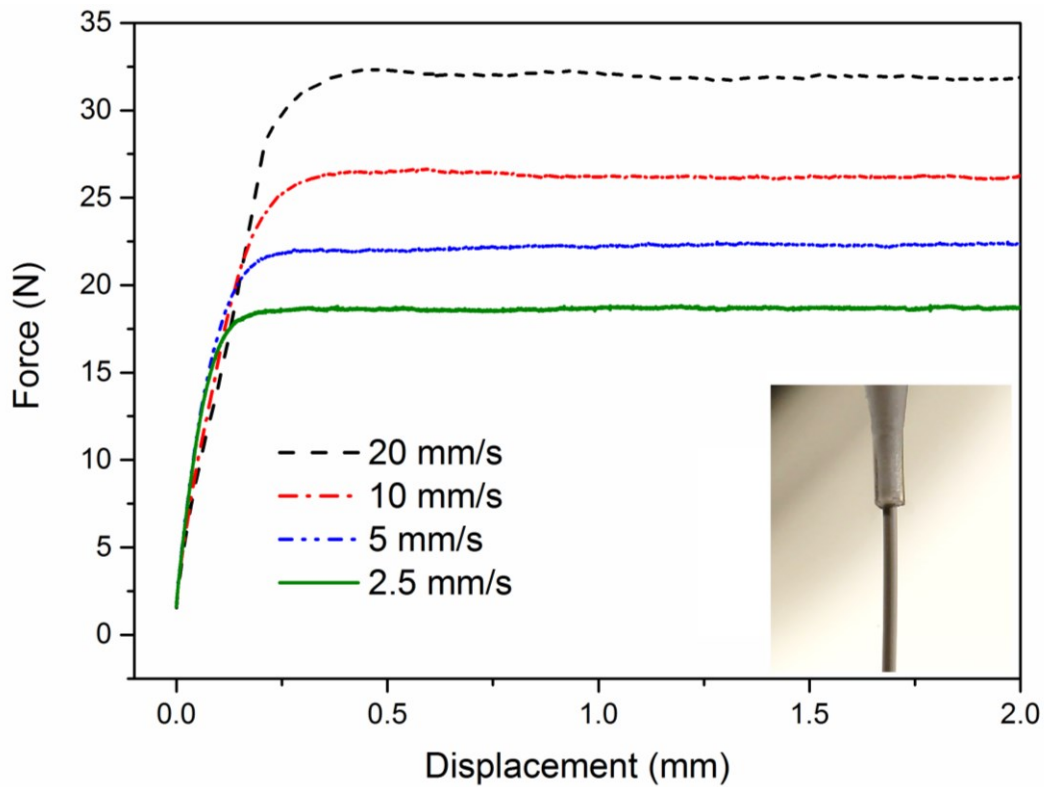


Figure 87. Flow curves from capillary rheometry of a 35 vol% alumina paste through a 0.2 mm conical nozzle at various extrusion speeds. This indicates that larger lead-ins are required for faster printing speeds.

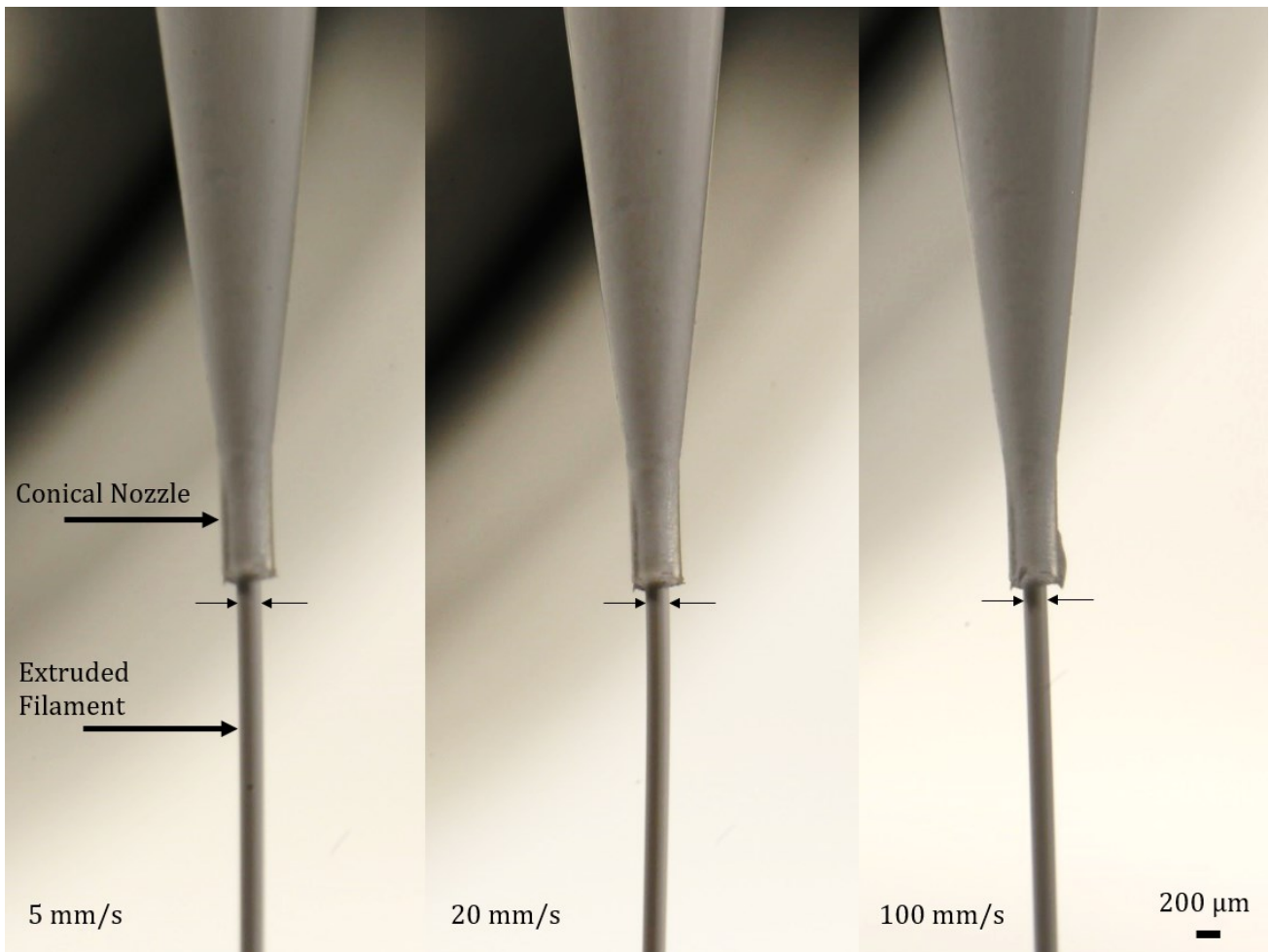


Figure 88. Video stills of extrusion at different rates through a 0.2 mm nozzle showing the lack of die-swell, even at very high extrusion speeds.

Raster Pattern

When choosing the pattern that the nozzle moves to fill in the part (known as the raster pattern), the main objective is to minimise the amount of space between the filaments (in order to squeeze paste into the space between filaments) without overfilling. While a range of infill patterns are used in extrusion-based AM (such as honeycomb, concentric etc.), theoretically the closest packed structure possible here is a hexagonal layout of filaments. This pattern was chosen as the aim is to produce solid, monolithic parts. Next, the spacing between the filaments must be decided. If the printed filaments do not overlap enough, defects are left at the triple points between filaments; however, if the overlap is too great then excess paste will build up around the nozzle and the part will bulge outwards, resulting in poor resolution. Both of these effects are shown in Figure 90 for the Pluronic gel (which is transparent, and so allows defect to be visible immediately). For all parts the optimal filament spacing was empirically found to be $d/1.2$, where d is the diameter of the nozzle (corresponding to a 17% overlap). This spacing was also used for the layer height.

Furthermore, for the squeezing process to produce a good interface between adjacent filaments the extruded filaments have to be reasonably smooth when exiting the nozzle. If the filament's surface is macroscopically rough, as shown in Figure 92, then small pockets of air become trapped between filaments, leaving defects after sintering, as seen in Figure 93.

A convenient piece of G-code was written to facilitate quick printing of large numbers of simple parts using different parameters. This code utilised nested repeat functions to drastically reduce the size of the file, which would otherwise become prohibitively large/long – printing 20 test bars through a 200 μm nozzle using RoboCAD results in a G-code file 40,000 lines long, which can take minutes to compile, whereas using nested repeats the same part can be printed using a file 45 lines long. This is presented in Appendix III.

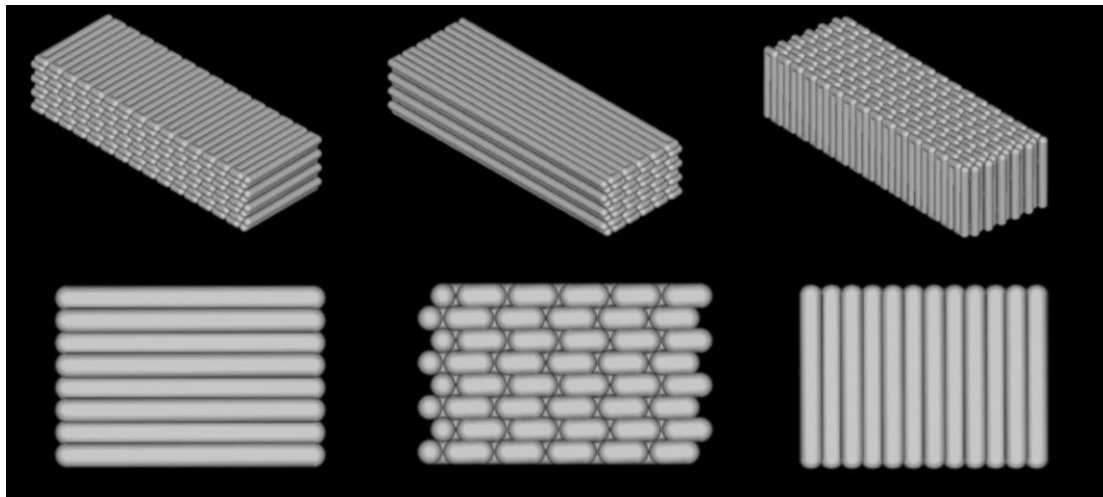
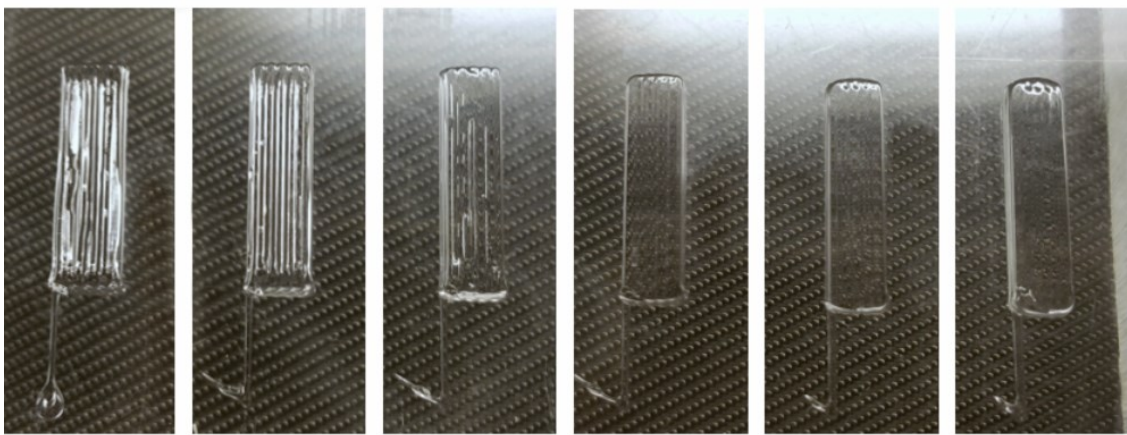
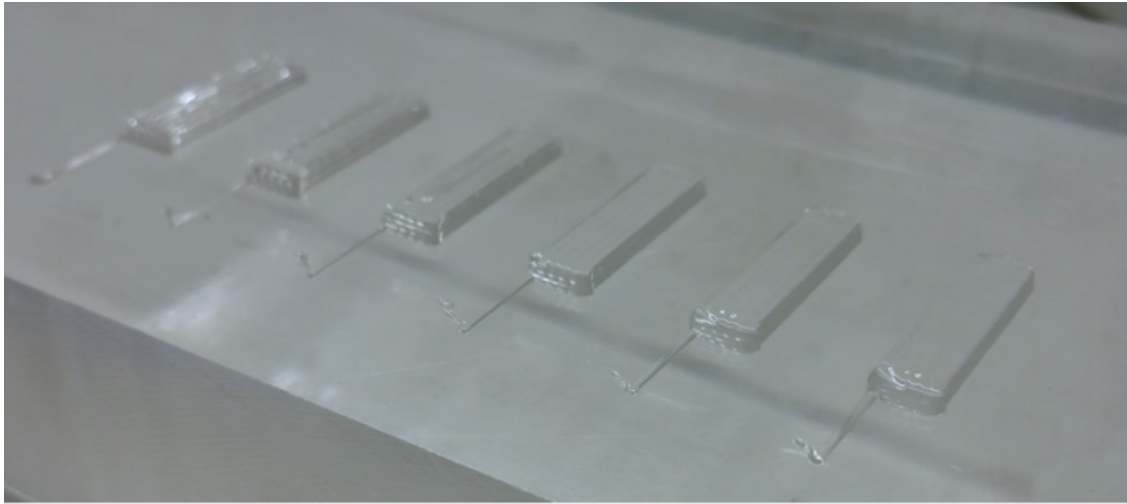


Figure 89. Schematic showing the three testing orientations of test bars: widthwise, lengthwise and heightwise.



0% 5% 10% 15% 20% 25%

% Filament Overlap

Figure 90. Pluronic bars printed with different filament spacing, showing the presence of inter-filament defects when the spacing is larger than 85% of the nozzle diameter. Note the decrease in the part definition at larger overlaps.

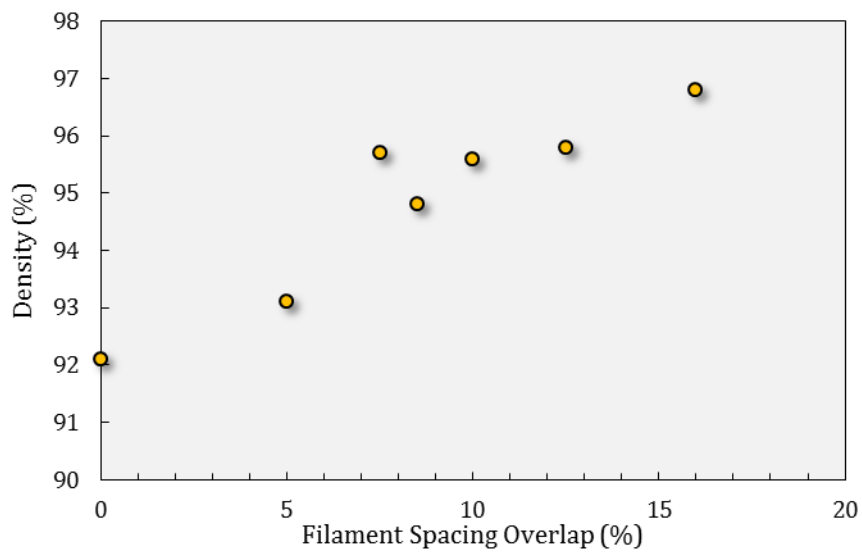


Figure 91. Densities of Al_2O_3 bars printed with different filament overlap spacing. Overlaps above 16% were not attempted as they were found to cause the part to distort and material to build up around the nozzle.

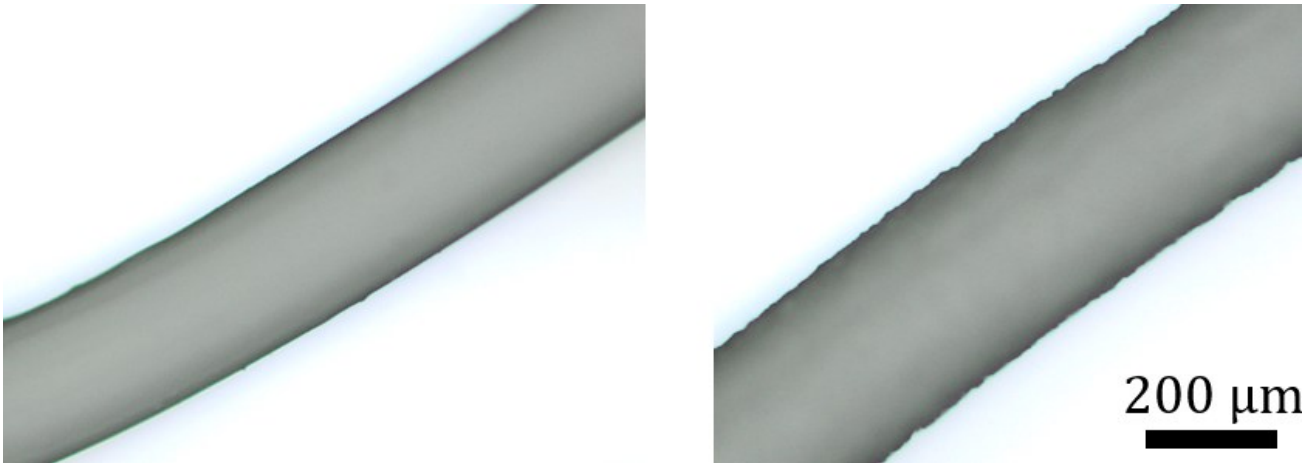


Figure 92. Optical microscopy of a single printed filament of an optically smooth paste compared to a visually rough one. The latter was less well mixed, and resulted in inter-filament defects.

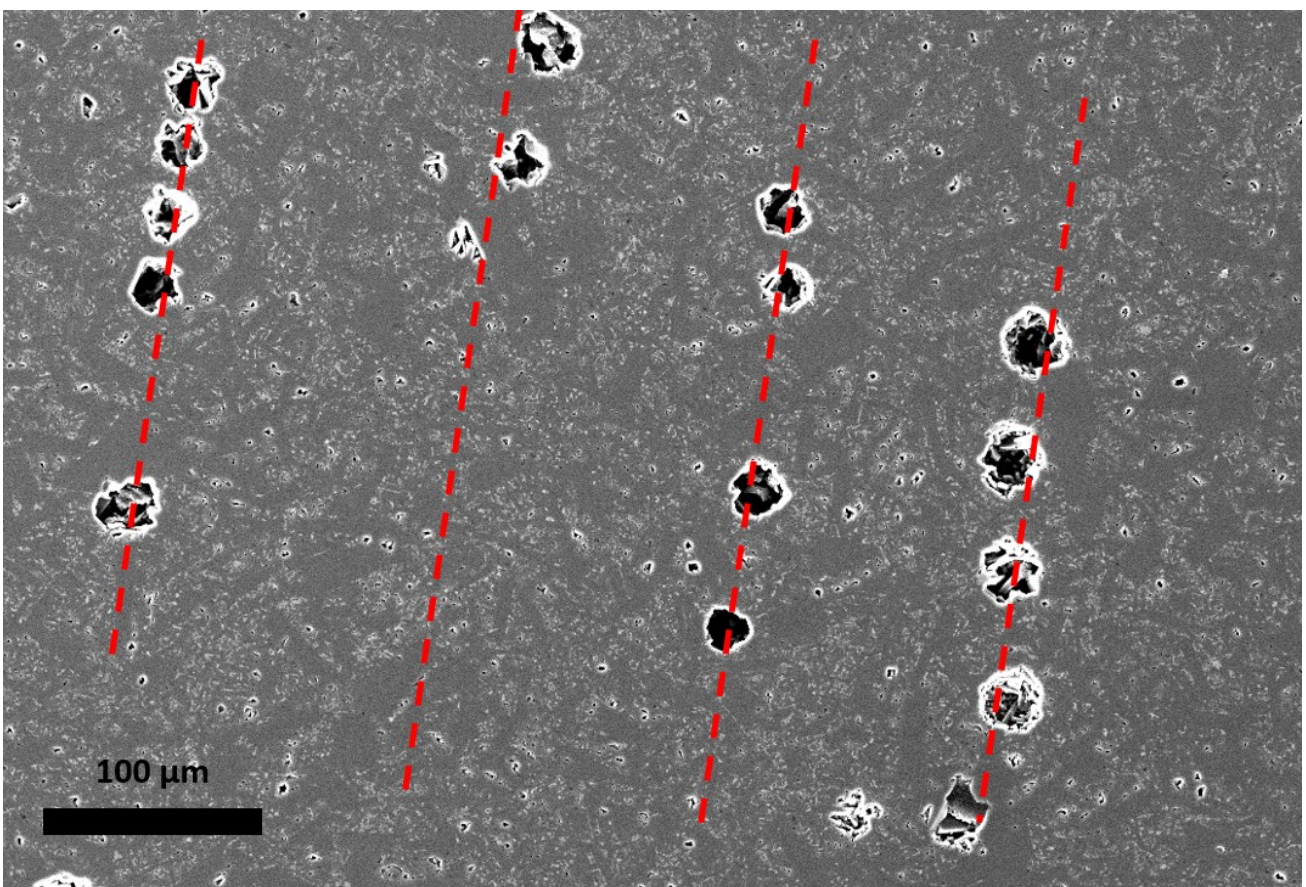


Figure 93. SEM image of a polished section of a printed SiC bar, with the boundaries between filaments indicated. This paste was poorly mixed, resulting in rough filaments, which catch air between them when squeezed together, resulting in periodic defects.

Substrate Material

The substrate was found to play an important role in the quality of the printed part. As discussed later in this chapter, the roughness of the substrate imprints onto the bottom of the part which can result in defects if the substrate is not smooth. Most significantly, the part must detach from the substrate as it shrinks during drying, otherwise the part will not dry uniformly, warp and often crack. In order to prevent this PTFE was chosen for its hydrophobic properties. These substrates were polished to 3 μm , however despite this larger parts were still found to stick to some degree. In these cases a thin layer of oleic acid was spread onto the substrate in order to prevent the parts from sticking to the substrate.

Nozzle Selection

The 0.2 mm conical nozzle was chosen as it allowed better than 100 μm resolution and printing times of 5 - 10 minutes per bar. The volumetric flow rate of paste is proportional to the square of the nozzle diameter, thus the printing time increases by a factor of four if we were to switch to a 0.1 mm nozzle. Conical nozzles extrude at lower pressures (typically around half that of a straight nozzle, see Figure 94) due to the absence of a dead zone and the overall lower shear rate that the geometry imposes on the paste as it's extruded. Nozzles up to 1.54 mm and down to 0.1 mm have been successfully used to print monolithic parts, however the dimensional accuracy of the larger nozzles is poor and the large pressure and long printing times required for the smaller nozzles were unacceptable.

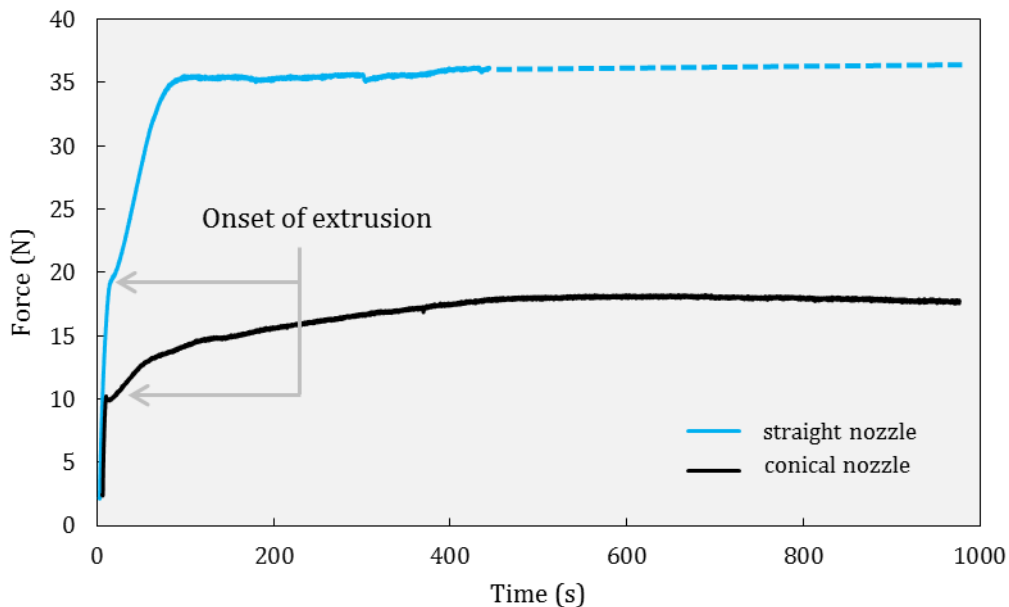


Figure 94. Constant displacement rate extrusion tests for an Al_2O_3 paste using a conical or straight nozzle, showing the lower equilibrium pressure when using conical nozzles. Also note the longer equilibration time.

Drying

Oil Bath

Other work in the literature reports scaffolds being printed in an oil bath to allow better control over drying and temperature,[1,61,77,80,127] however when printing monolithic parts the oil environment was found to leave periodic, inter-filament defects, see Figure 95. This is likely due to the oil being trapped between adjacent filaments as they are squeezed together, possibly due to the high viscosity of the oil. This results in large voids after burn-out. The mechanical properties of these parts were not tested in detail as their density was found to be low, and preliminary inspection of the fracture surfaces revealed defects >1mm in size which would result in very poor mechanical performance.

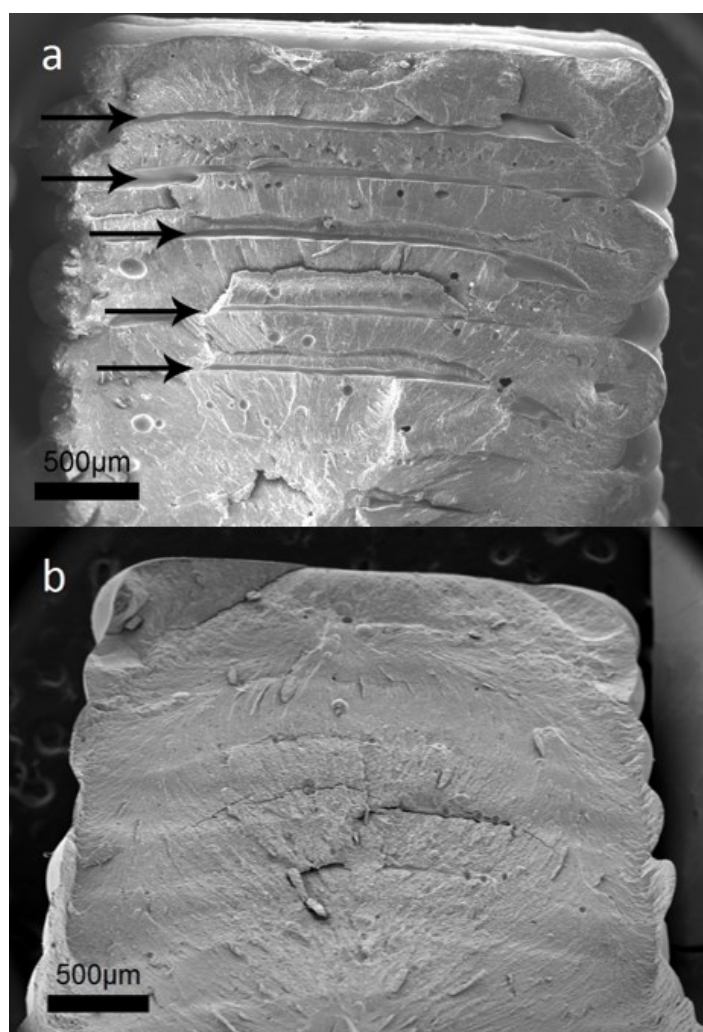


Figure 95. Fracture surface of a green body test bar printed in the widthwise orientation, in oil (a) and air (b). Long inter-filament printing defects are indicated in the part printed in oil. Some drying cracks and sagging are present in b due to excessively fast drying.

Air Drying

Successful samples were printed in air at >65% humidity, which allowed drying to take place independently after printing had finished. This is necessary for two reasons. Firstly, at atmospheric humidity the rate of drying is not well controlled during printing, so the part can dry excessively quickly; cracks were common in green bodies if the drying rate was too fast or the part did not detach from the substrate adequately. This problem was most pronounced when using smaller nozzles, due to the higher surface area to volume ratio of the partially printed parts. Secondly, the part shrinks as it dries. This means that if drying is occurring during printing, then freshly printed layers will be misaligned with respect to the drier layers below. Cracks typically formed during the separate drying step and not during printing. Two commonly seen problems when printing test bars were their centre warping upwards, resembling an archway, as seen in Figure 96, or a void appearing in the middle of the bottom of the bar, as seen in Figure 97. One explanation for both of these effects is that drying occurs at the outer surfaces first. Once the extremities have dried the inner sections of the bars then dry, however they cannot shrink freely as the extremities cannot shrink further. This leads to the bars bending instead, or in extreme cases voids opening up on the bottom of the bar to facilitate shrinkage. This can be overcome by slowing the drying rate, and by applying a further non-stick layer such as oleic acid (margarine) to the substrate, which allows the part to slide over the substrate during drying and shrink in an isotropic manner.



Figure 96. A SiC test bar showing the arching effect, likely due to drying too fast.

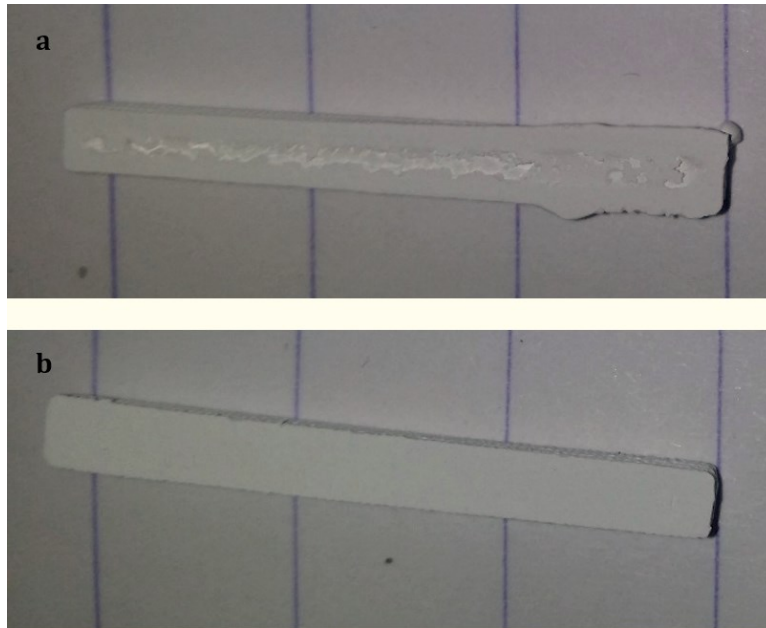


Figure 97. Void formed on the bottom of a green test bar where the bar did not fully detach from the substrate (a), compared to green test bar where the bar did fully detach (b). In this case, the nozzle was too close to the substrate in (a), causing the paste to be forced against the substrate when printing the first layer, forming a strong bond.

The other factor strongly affecting the drying process is the amount of liquid in the paste in the first place. The hydrogel used is 75 vol%/wt% water, and most pastes were 50 - 70 vol% hydrogel, so these pastes are ~35 - 50 vol% water. Generally speaking, larger volume fractions of water in the printed part should result in greater drying shrinkage.** Given that drying cracks were such a prevalent problem throughout this work, there is clearly a large drive to decrease the volume fraction of water in the paste. However, as outlined in Chapter III, this decreases the printability of the paste in many cases and makes handling the paste more difficult in all cases. It also increases the pressure required for extrusion. Clearly there is a balance to be struck, and the pastes chosen to produce the parts in this chapter represent this compromise. Using the above parameters it was possible to print a range of geometries including arbitrary CAD files and scaffolds. A selection of these are shown in Figure 98.

**Although the relationship between volume fraction of water and drying shrinkage was not necessarily 1:1, and depends strongly on the packing of the particles in the paste.

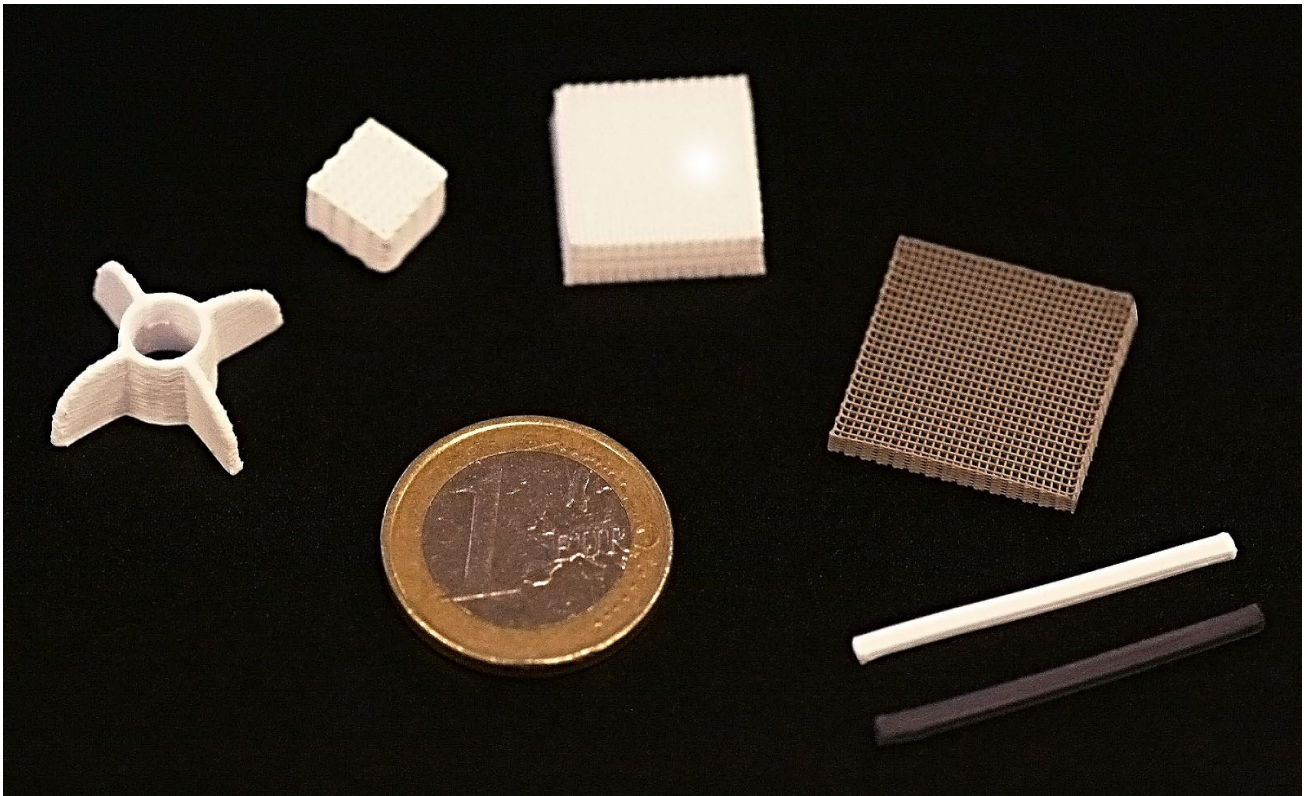


Figure 98. A selection of Al_2O_3 and SiC parts.

Characterisation and Mechanical Properties

Interestingly, the burn-out step was never problematic for any parts made in this work, despite the fact that the parts contained a reasonably high volume fraction of organics from the Pluronic (~15 vol%). This may be due to the fact that the parts are reasonably small (cm scale), and that heating rates were not particularly high. Nonetheless, this was not investigated further.

Following burn-out, green alumina parts were found to sinter to $97\pm 1\%$ density with an average grain size of $1.40\ \mu\text{m}$. The sintering conditions used are very typical for this material; abnormally high temperatures and long hold times were not required for good densification (as is the case for AM methods such as binder jetting). Figure 100 shows residual porosity at triple points and inside grains. These pores were $<2\ \mu\text{m}$ in diameter. Silicon carbide parts reached $95\pm 1.5\%$ density during sintering, which is comparable to silicon carbide produced by robocasting in other work.[77] The average grain size was $4.38\ \mu\text{m}$, however the microstructure is littered with irregular, elongated grains over $20\ \mu\text{m}$ in length. Porosity tended to be localised to silicon carbide grain boundaries isolated from the yttria-alumina rich phase, and was typically $\sim 15\ \mu\text{m}$ in diameter. This second phase was identified as yttrium aluminate monoclinic using XRD, see Figure 99. This is in close agreement with other spectra reported in the literature of liquid phase sintered SiC processed at similar temperatures.[128]

The only parts made by robocasting for which the literature reports Weibull moduli are lattices.[129,130] Weibull analysis requires large numbers of uniform test samples, and as such it is usually long and tedious to perform manually; however, AM is well suited to produce 10s of samples without user intervention. The mean strengths and Weibull moduli of our monolithic samples of each material printed in three different orientations are summarised in Table 5. The strength data, also shown in Table 5, are comparable to the strength of some commercially available SiC and Al_2O_3 . [131,132] Fractography revealed that the SiC samples exhibit a mix of intergranular and transgranular fracture, while it is clear that the Al_2O_3 samples predominantly failed inter-granularly, as is typical of these materials. Hardness (at 5 kg load) was found to be $18.6\pm 0.8\ \text{GPa}$ for Al_2O_3 and $23.4\pm 2\ \text{GPa}$ for SiC. The toughness was estimated from measuring the radial crack lengths from these indents,[133] and gave a value of $3.31\pm 0.23\ \text{MPa}\sqrt{\text{m}}$ for Al_2O_3 and $3.11\pm 0.17\ \text{MPa}\sqrt{\text{m}}$ for SiC. Again, these properties are roughly comparable to those of commercially available material. A more rigorous method to measure toughness would be via single edge notched beam bending; however, for dense, non-transforming materials, the indentation method gives a reasonable estimate and demonstrates that this property is in the expected range. The Weibull moduli are similar to moduli reported for scaffolds produced by robocasting which range from 3 - 9.[129] This result suggests that critical defects may originate in the individual filaments, as both scaffolds and monolithic parts are built up of individual

extruded filaments. Therefore, if these two different structures possess similar reliability, then it is likely that the defect distribution is within the common building blocks (the filaments). On the other hand, we have shown that strength and Weibull moduli were somewhat lower for the samples printed in the widthwise and heightwise directions. This suggests that, at least in these two orientations, the defect distribution is related to the orientation of the filaments. This leads to an important design consideration; our data show that greater strength and reliability can be achieved when critical areas are rastered in the direction parallel to the expected force vectors for the part in its final application.

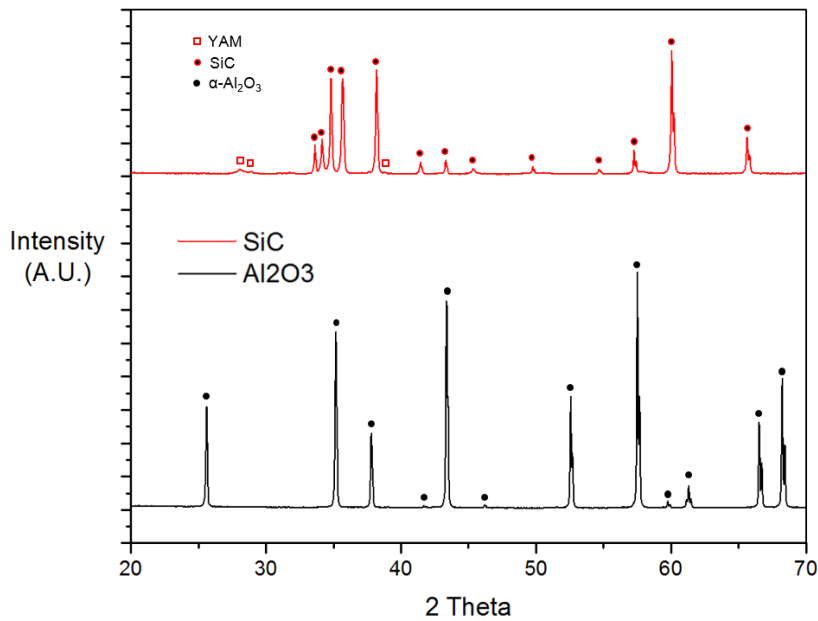


Figure 99. XRD spectra of the sintered SiC and Al₂O₃ parts showing peaks associated with the SiC, α -Al₂O₃ and peaks identified as yttrium aluminate monoclinic (YAM).

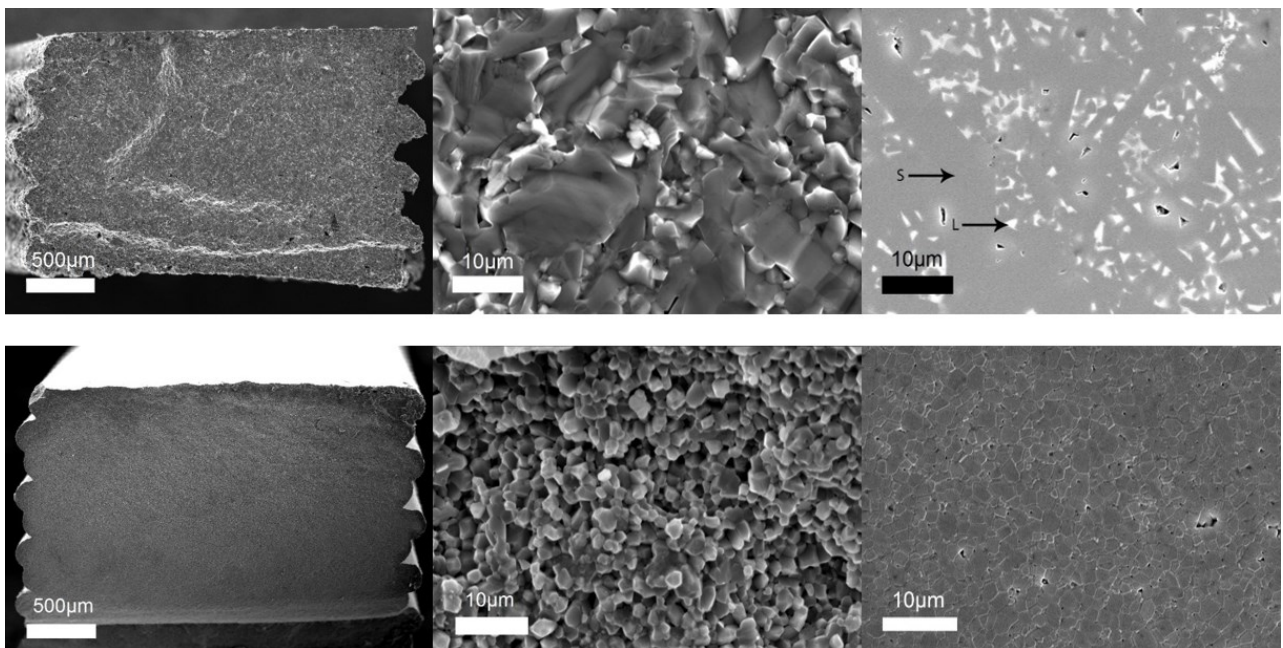


Figure 100. Fracture surfaces and polished sections of a SiC part (top) and an Al₂O₃ part (bottom). Both parts show characteristic step edges on the sides of the part, however they are quite flat besides this, indicating good bonding between filaments. The SiC

shows mixed inter- and trans-granular fracture, whereas the Al₂O₃ shows inter-granular fracture. The two phases are visible in the polished SiC, and the grain structure is visible in the Al₂O₃.

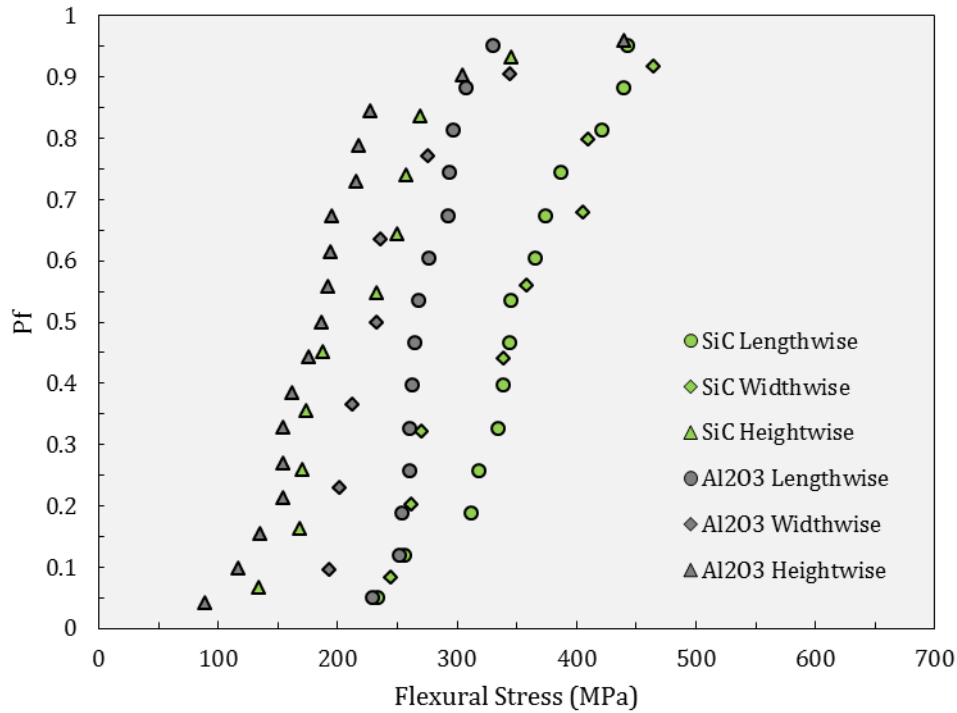


Figure 101. Probability of failure of Al₂O₃ and SiC parts printed in the lengthwise, widthwise and heightwise orientations, tested in 4-point bending.

Table 5. Strengths and Weibull moduli of each material printed in each orientation.

		m	Avr. Strength (MPa)	σ₀ (MPa)	Defect size (μm)	Overall Avr. Strength (MPa)
SiC	Lengthwise	6.1	351	377	25.1	305±60
	Widthwise	4.4	344	378	26.1	
	Heightwise	3.8	219	242	64.4	
Al₂O₃	Lengthwise	8.9	275	297	46.2	232±27
	Widthwise	4.8	243	265	59.2	
	Heightwise	3.0	195	220	92.0	

The following equation can be used to calculate the defect size from these data;[134]

$$a = \left(\frac{K}{Y \sigma} \right)^2 \quad (4.1)$$

where a is the defect size, K is the fracture toughness, σ is the strength and Y is the shape factor (1.77 for high aspect ratio defects).[135] The average critical defect size was calculated as $\sim 50 \mu\text{m}$ in Al₂O₃

parts and $\sim 65 \mu\text{m}$ in SiC parts; however, there was significant anisotropy, so the direction-specific defect sizes are listed in Table 5. From smallest to largest, four possible defects were identified:

- 1- **Residual pores after sintering.** The distribution of these defects should not depend on printing orientation. It is likely that these are the critical defects in the lengthwise and widthwise SiC samples as pores of this size were common throughout the microstructure. These pores are due to the inherent difficulties densifying this material without applied pressure, and may also be exacerbated by inhomogeneous mixing of the paste.
- 2- **Inhomogeneities in the paste.** This includes small bubbles and agglomerates. It is unknown whether the distribution of these defects depend on printing orientation, as long inhomogeneities may or may not orient in the paste during printing. The defect seen in Figures 103 and 104 is thought to be an example of one of these defects post-sintering. Effective defoaming and mixing may reduce these defects greatly, however they cannot be completely ruled out. They are the most likely strength-limiting defect in the lengthwise and widthwise Al_2O_3 samples as the others are either not applicable or are too small.
- 3- **Air trapped between filaments during printing.** The filaments of paste were found to bond together very well during printing; the interface was not visible after sintering and grains were found to readily grow across where the interface would have been, as seen in Figure 102. However, this is the only defect which unambiguously depends on the printing direction, and thus they must be present in both materials to account for the anisotropy of the Weibull modulus observed. This is hypothesised as the critical defect in all heightwise parts due to the lower strength in this orientation compared to the lengthwise samples.
- 4- **Surface defects.** As with all ceramic parts produced via AM, there are step edges which arise from the layer-by-layer nature of the printing process, seen on the sides of the bars in Figure 102. Decreasing the nozzle size reduces the size of the step edges (they are roughly as large as the nozzle radius); however, this greatly increases build time and increases the pressure required to extrude. This is particularly problematic for high volume fraction pastes. The substrate that the part is printed onto may also play a role, as the roughness of the substrate is imprinted onto the bottom of the part. If the roughness is larger than the critical defect size then this too will limit strength. These issues were overcome by the polishing prescribed by ASTM C1161–13. The strength of unpolished lengthwise Al_2O_3 parts was found to be $\sim 170 \text{ MPa}$ with a Weibull modulus of 1.7. These values are much lower than the equivalent polished parts, thus we deem that some form of surface finishing is necessary (such as polishing, sand blasting etc.).

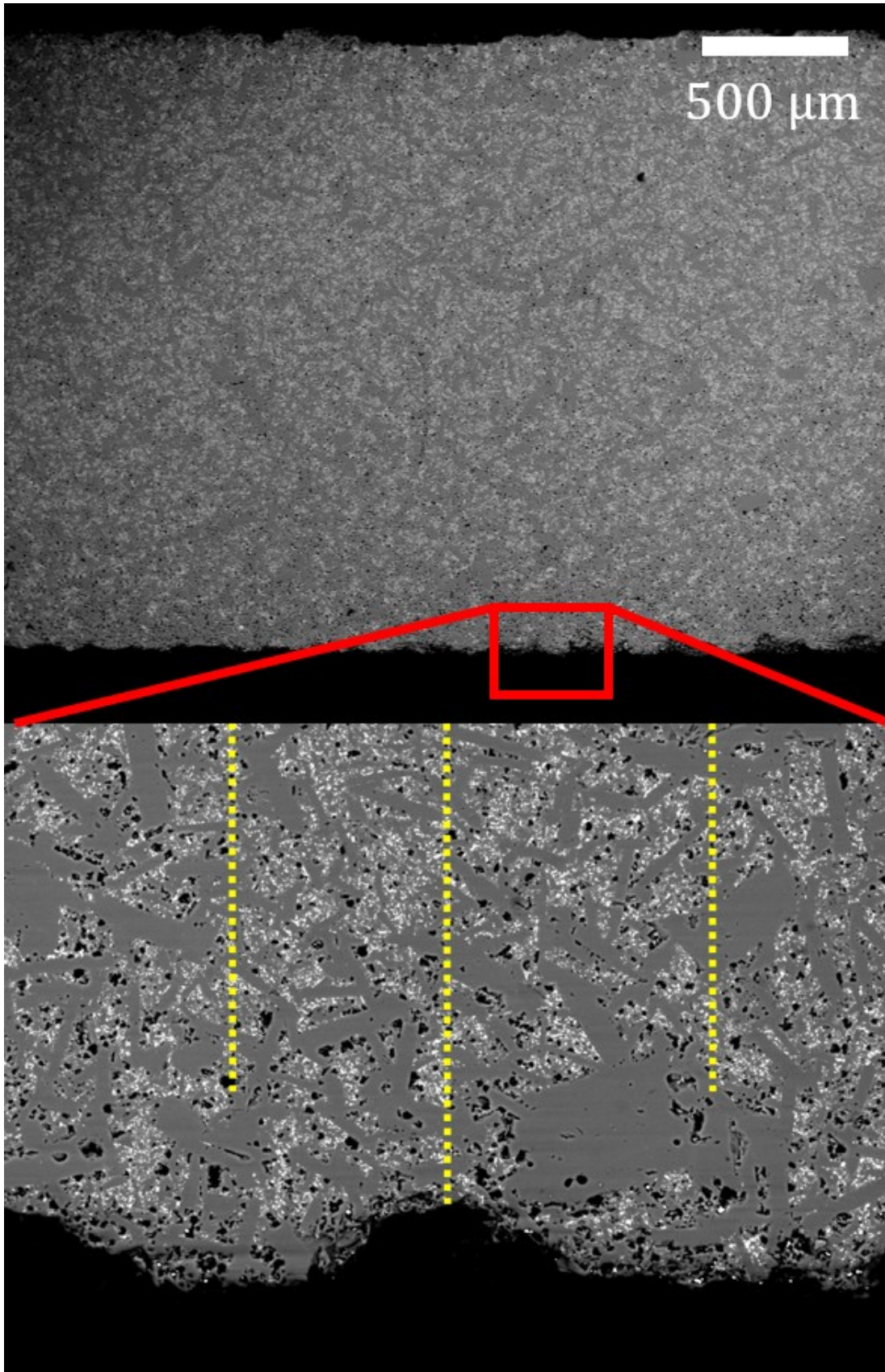


Figure 102. SEM image of a polished cross section of a SiC part, showing the boundary between two printed filaments. No inter-filament defects are visible, and grains are seen to readily grow across this boundary.

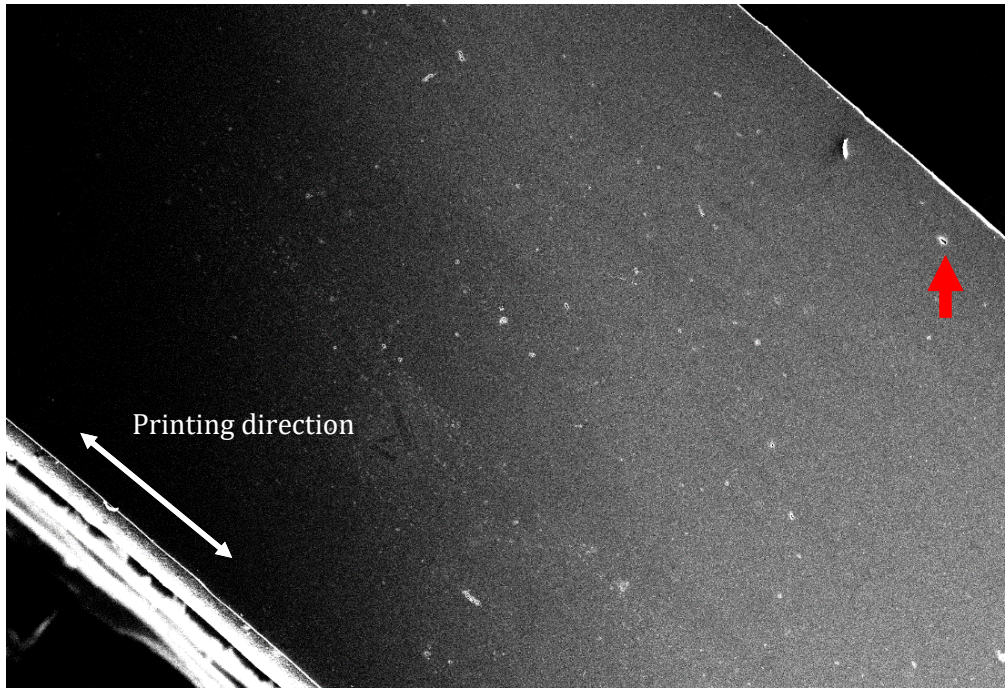


Figure 103. Polished surface of a lengthwise Al₂O₃ bar, with the defect from Figure 104 indicated. Note the general tendency for defects to be elongated in the printing direction.

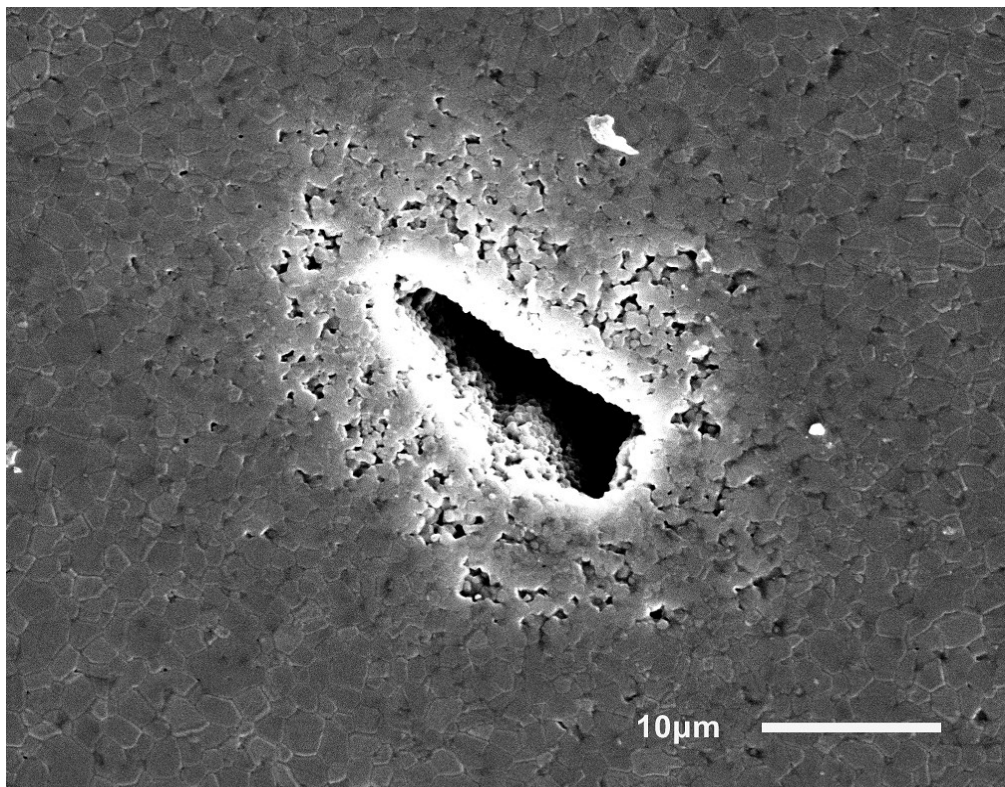


Figure 104. A defect found in the polished Al₂O₃. Although the defect appears to be ~20 µm in size, it could be considered to be 40 µm due to the surrounding area of poor densification.

Some Example Parts

Various test parts were printed throughout this work in order to demonstrate some of robocasting's capabilities. A number of these are presented below.

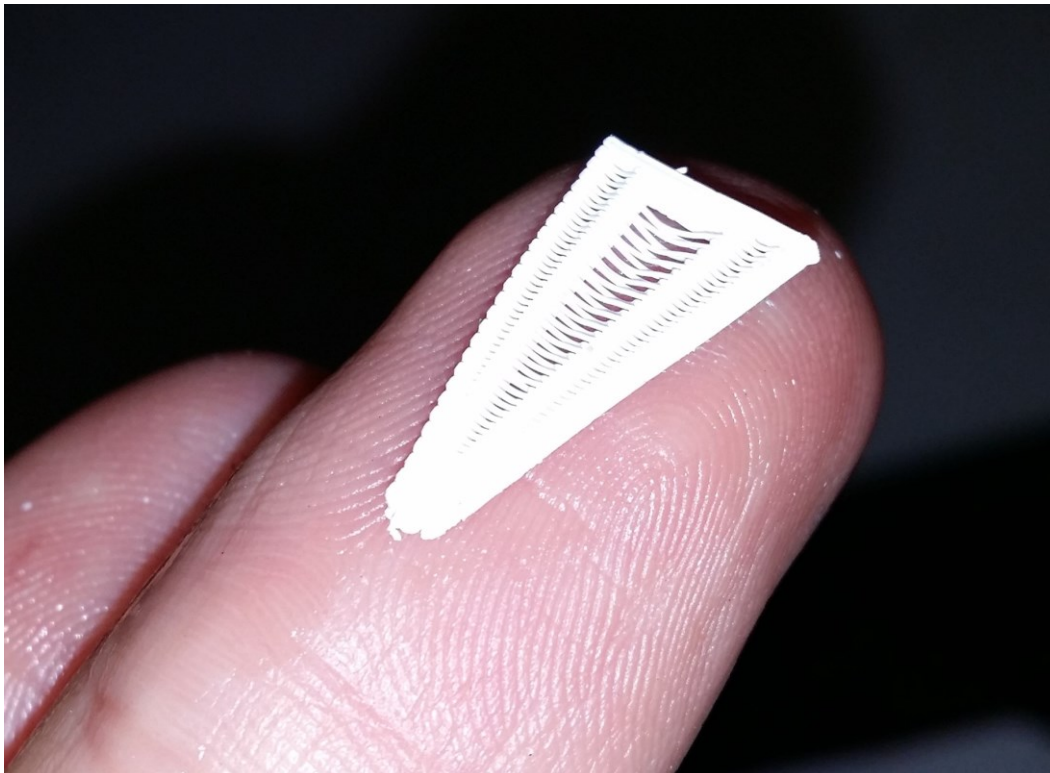


Figure 105. An Al_2O_3 truss structure (used for testing the maximum spanning ability of the paste).

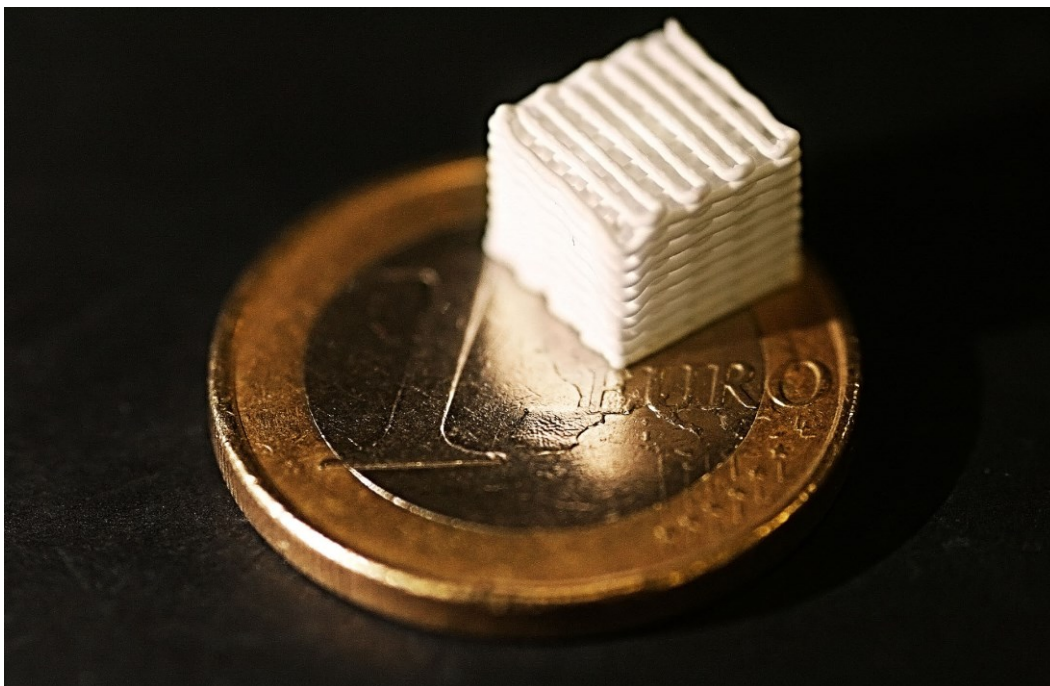


Figure 106. A printed Al_2O_3 scaffold.

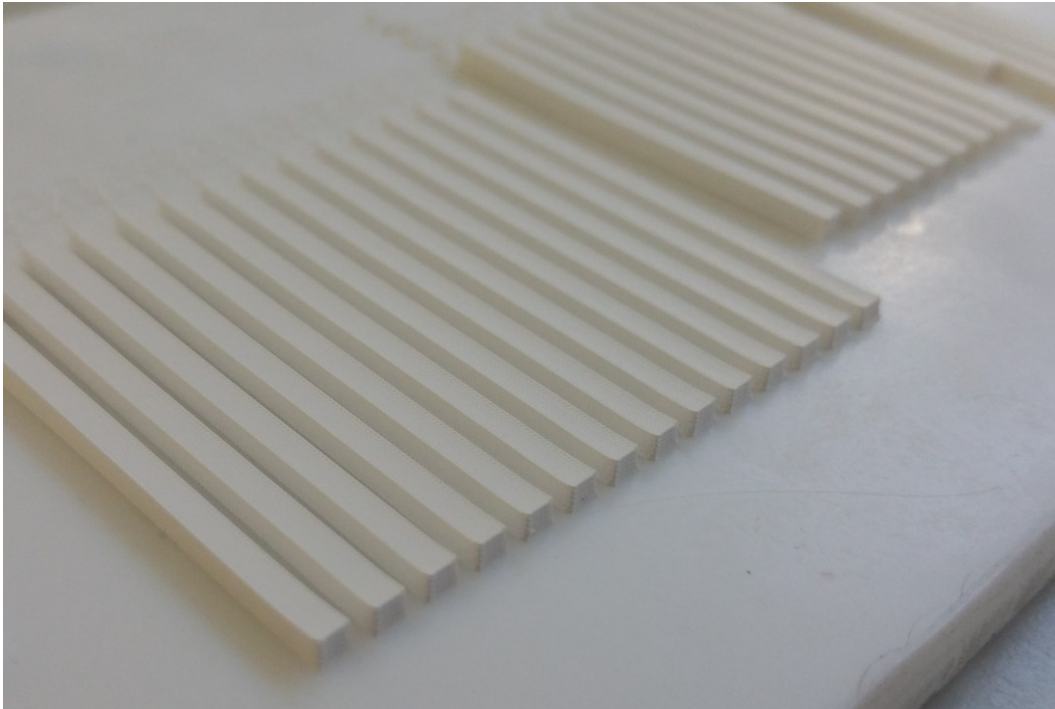


Figure 107. An array of test bars after printing. AM is particularly well suited to making a large number of the same part, making Weibull analysis much more user friendly.

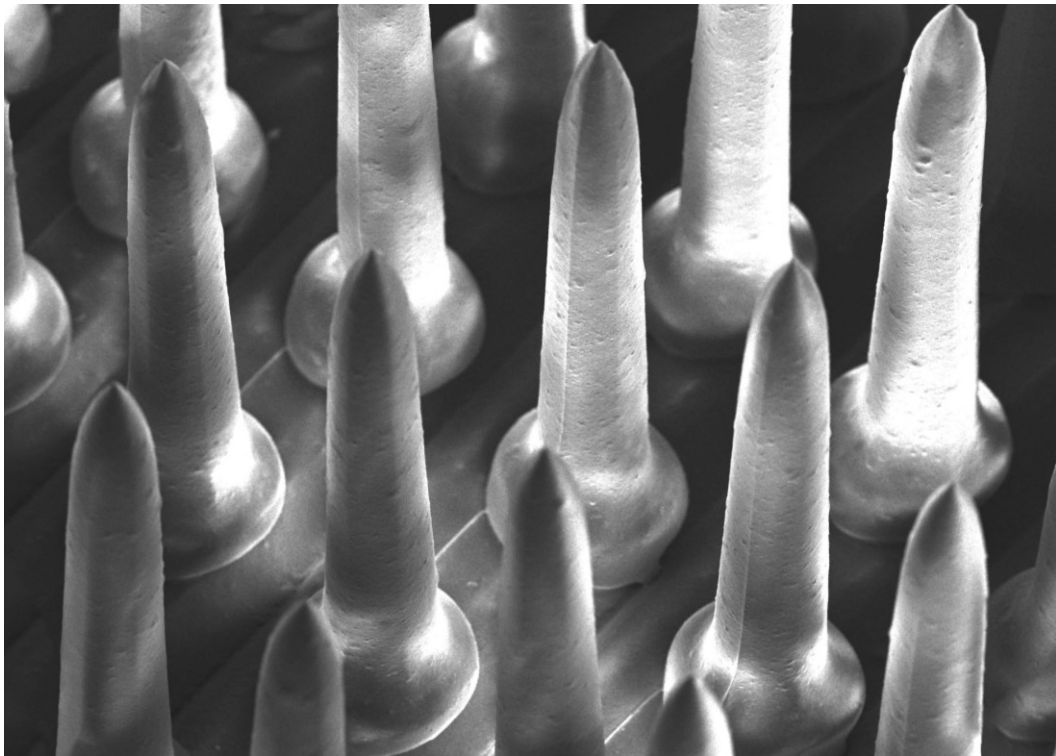
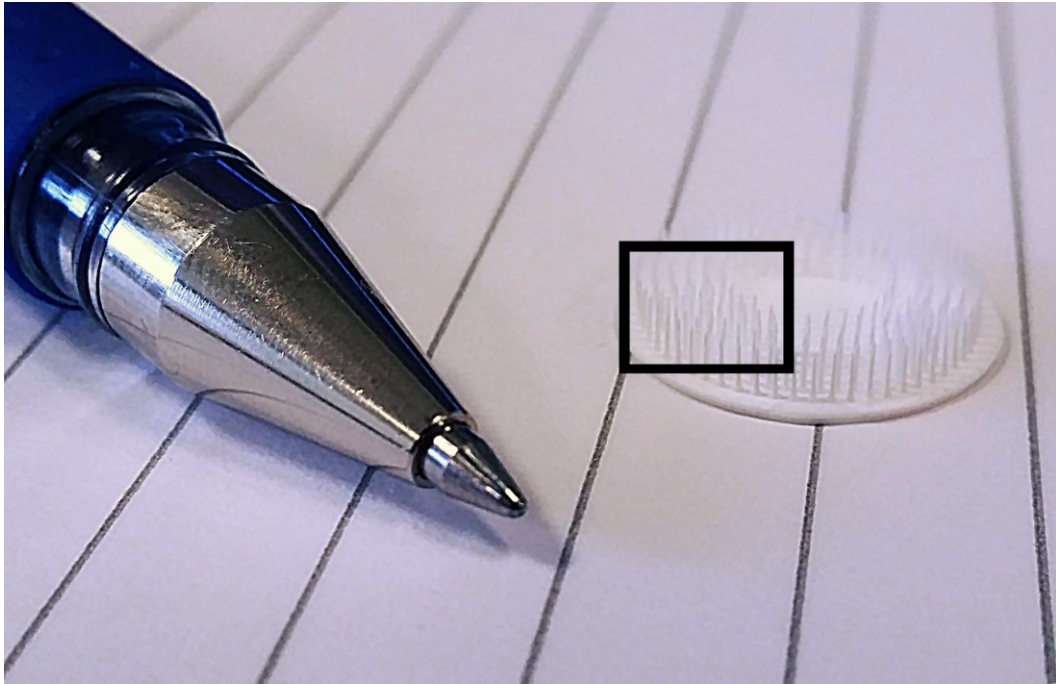


Figure 108. Al_2O_3 micropillars of diameter $\sim 250 \mu m$ and height 2.2 mm. These structures require extremely homogenous pastes and a lot of care with respect to the G-code which can be found in Appendix II.

General Discussion

Strong evidence is presented that suggests that printing in an oil bath is not compatible with dense, monolithic parts using the printing parameters and pastes optimised for this purpose. This is due to the oil being trapped between printed filaments, resulting in large gaps between the filaments after sintering. This is unfortunate, as printing in oil presents a number of advantages. However, it still may be possible using different paste formulations, oils with lower viscosities, or oils with other wetting characteristics.

The sintering parameters used were deliberately chosen to be similar to conventional parameters, as if robocasting is to be considered a feasible technique then it must be able to fit into present production lines. In other words, the green body that it produces must be similar to a green body produced via conventional methods to allow it to be post-processed in a conventional manner. Principally this means that a green body with a small fraction of organics and an acceptable green density is required. The best evidence that this goal was achieved is the fact that parts experienced no issues during burn-out using moderate heating rates, and sintered to high density using reasonable temperatures and hold times. It is thus postulated that robocasting should be compatible with existing production lines for small ceramic parts.

The question now is whether parts produced via robocasting are suitable for existing applications. The two main considerations are whether robocasting can be used to print parts to a high degree of accuracy, and whether appropriate materials properties can be achieved in this material, the latter of which is the main focus of this research. In this respect, there is much promise – the mechanical strengths of both classes of ceramics reported in this preliminary study are sufficient for some low-end structural applications. However, reliability (encompassed in the Weibull moduli) is somewhat below expectations for high-performance applications, such as Weibull moduli in the 100s, as is the case for some load-bearing implants. One can speculate that this is in part due to the fact that the samples are made in a research laboratory, using processes with frequent user interventions. The mixing of the pastes requires frequent ‘judgement calls’, and so is certainly not standardized. The polishing of the test bars introduces variability into the quality of the material due to the manual nature of this task, and the drying step is not fully controlled. It is undoubtable that automating these processes further would increase the Weibull moduli. However, the anisotropy of the Weibull moduli (lower for the widthwise and heightwise parts) hints at a worrying fact – that the printing process inherently produces defects in the final parts, either through oriented inhomogeneities or pores between filaments. Also, all of the above properties have only been demonstrated for mm and cm scale parts. Larger parts are likely to encounter difficulties with sagging, poor dimensional control during printing, and problems with

drying. Nonetheless this may not be a significant barrier, as many of the target applications for printed parts are small, high value components.

Now we have begun to address the question of whether it is feasible to fit robocasting into existing production runs, and that it is possible to achieve acceptable mechanical properties for some applications, we can begin to answer the question of whether it *should* be used for these applications. In short, what value can robocasting add over existing technologies? This question has two main answers:

- 1- Can robocasting produce parts that are not presently possible using other methods?
- 2- Can robocasting more economically produce parts that are currently being produced via other methods?

At the time of writing, robocasting has been used to produce complex scaffolds for two decades. These structures are quite unique; other methods cannot produce macroscopic scaffolds with such smooth filaments. This work focusses more on the second question, and begins to qualify an affirmative answer. Now that the mechanical performance of material produced via robocasting has been examined in detail, the foundations have been laid to allow robocasting to be used in short production runs of small structural ceramic parts. Due to the general benefits of AM over traditional manufacturing methods, this may result in quicker lead times and cost savings. However it still remains to be seen whether the geometries of real parts can be reproduced via robocasting with a high enough degree of accuracy and reproducibility for real world applications.

Comparison to Other AM Techniques

Making a direct comparison with mechanical properties reported for other AM techniques is not straightforward. This is because mechanical properties are scarcely reported for AM of ceramics, and when they are they may not be representative of the technique as a whole. With this in mind, the most common ceramic produced by AM (alumina) and the most common strength test (bending) were selected and the highest reported values for strength and density are reviewed for each available technique. This is presented in Figure 109. Clearly (and unsurprisingly) there is a strong relationship between density and strength. As such, bending strengths are not reported for some techniques that have poor densification, such as regular BJ. Our data compare favourably to that reported for other techniques, with moderate strength and amongst the lowest porosity. Furthermore, much of the literature only reports the strongest direction (e.g. lengthwise), whereas our reported values in Figure 109 demonstrate the three orthogonal directions. It is notable that our reported strength appears to break with the strength-porosity trend somewhat, as the average strength is lower than would be expected for such a low porosity. If the critical defects are pores, then this indicates that our pores are

higher aspect ratio and worse oriented to cause failure than those found in parts produced by the other reported techniques.

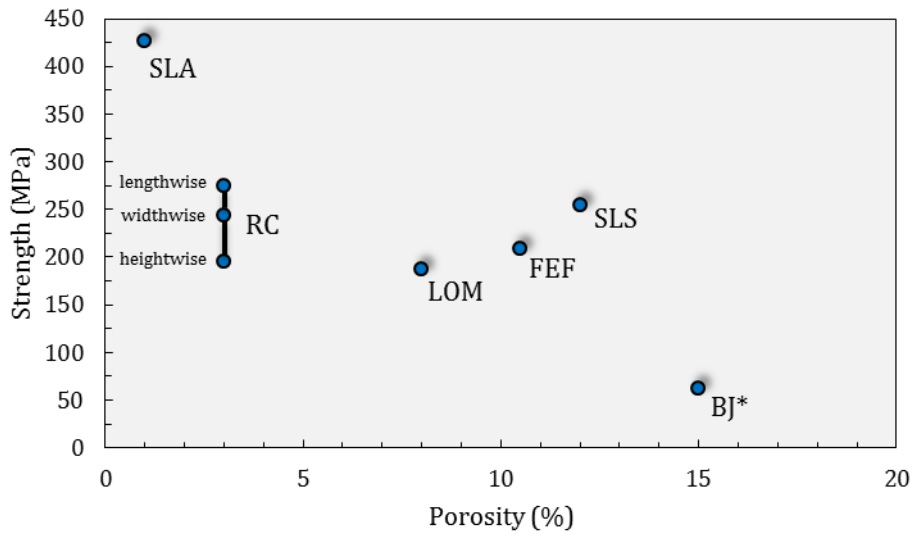


Figure 109. Comparison of the highest reported bending strength of alumina parts produced by various AM techniques. The strengths of the SLA,[18] FEF,[136] BJ,[137] and RC (this work) were all measured using 4 point bending, while the LOM[138] and SLS[139] was either not stated or 3 point bending. The BJ material was infiltrated with a slurry prior to sintering to aid densification.

Conclusions

Simple pastes based on a hydrogel Pluronic F-127 were found to be suitable for robocasting of reasonably high volume fraction SiC and Al₂O₃ pastes through small nozzles. This approach has been used to print test bars which achieved near full density and average strengths of 300 MPa for SiC and 230 MPa for Al₂O₃ after sintering. In order to examine the effect of printing orientation, and the printing process more generally on the properties of the material, test bars were printed in three different orientations and their mechanical properties compared. Weibull analysis was performed on these data sets. The parts printed in the lengthwise orientation were found to possess the highest strengths and Weibull moduli, while parts printed in the heightwise possessed the lowest. An exhaustive study of potential sources of defects allowed identification of three types of defects that are believed to limit strength: residual porosity, inter-filament defects, and agglomerates in the paste. The second two are postulated to be responsible for anisotropic Weibull moduli and strength in each material. Using these data, we have begun to answer the question of whether robocasting can, and should, be considered to industrially produce structural ceramic parts.

Chapter V – Ceramic Platelet Composites

Introduction

One way to improve the mechanical properties of materials is to control their structure and internal architecture. Blueprints for the design of composites to achieve this are abundant in natural biomaterials. These materials offer hints about how to combine strength and toughness, a goal that has been difficult to reach in modern materials science.[140] Many natural materials exhibit a remarkable level of complexity, with intricate structures at a range of length scales. Some well-studied examples include mammalian cortical bone,[141] nacre[142] and certain areas of crustacean exoskeletons,[143] each of which demonstrate a variety of microstructural designs able to direct crack propagation in three dimensions and to control fracture, generating strengths and toughness that are well beyond that of their constituent materials.

While the complexity of these structures has been known for some time, the advent of AM offers the level of microstructural control needed to produce artificial analogues of these materials. In order to produce macroscopic parts with this level of detail, a technique is needed which combines μm -scale structural control with practical printing speeds. Robocasting is a strong candidate to achieve this goal. The shear forces arising from extrusion have been shown to align short carbon fibres during printing, giving close control over fibre orientation.[100] Magnetic fields have also been used to precisely align platelets during robocasting.[126] When combined with other processes robocasting can produce a range of composite systems with controlled architecture. For example, printed ceramic scaffolds have been infiltrated with liquid metals[97] and liquid polymers[71] to create a novel class of interpenetrating phase composites.

In this Chapter alumina platelets are analysed in detail, and used to produce a range of complex ceramic/polymer composite systems using robocasting. We use the rheology of the platelet paste and the shear forces during printing to build macroscopic composites with highly textured microstructures on multiple length scales, inspired by a number of natural materials such as bone and nacre. Toughening mechanisms in these unusual materials are studied in detail using an *in-situ* double cantilever beam (DCB) test which was developed specifically for this work. It is shown that the microstructures can be used to control crack propagation via twist and tilt. In this way it is possible to replicate natural toughening strategies and build highly mineralized materials that retain strength while enhancing toughness.

Platelet Characterisation

Recently there has been a surge of interest in platelet-like reinforcements in composites, specifically micron-scale Al_2O_3 platelets which have been used extensively in a number of composite studies.[142,144–148] These platelets are favoured as they are oxidation resistant, stable, crystalline, and can be mass produced with a consistent morphology. Despite the interest they have received, the mechanical properties of individual platelets are still unknown. These properties are needed when designing composites as they allow for the interfacial strength to be tailored to maximise the reinforcing and toughening effect of the platelets, and thus optimise the mechanical properties of the material.

In order to measure the strength of individual platelets micro- 3 point bending was performed. The procedure and the results are presented in Figure 112 and Table 6. Ten samples were successfully tested, and while this number is low for a full analysis, it was the largest practical number given the excessively large time taken to prepare each specimen.

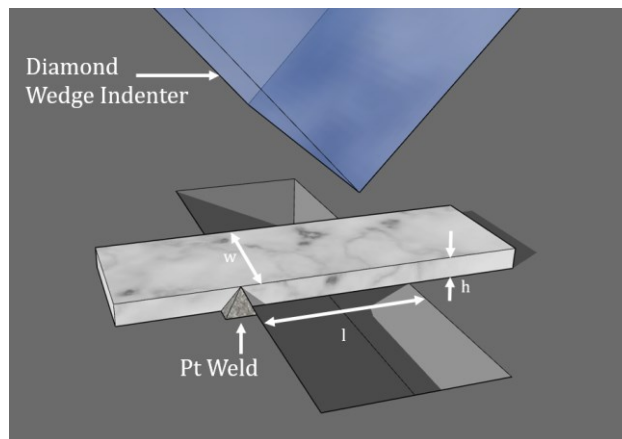


Figure 110. Schematic showing the setup and dimensions of the micro- 3 point bending.



Figure 111. An array of trenches milled into a silicon substrate.

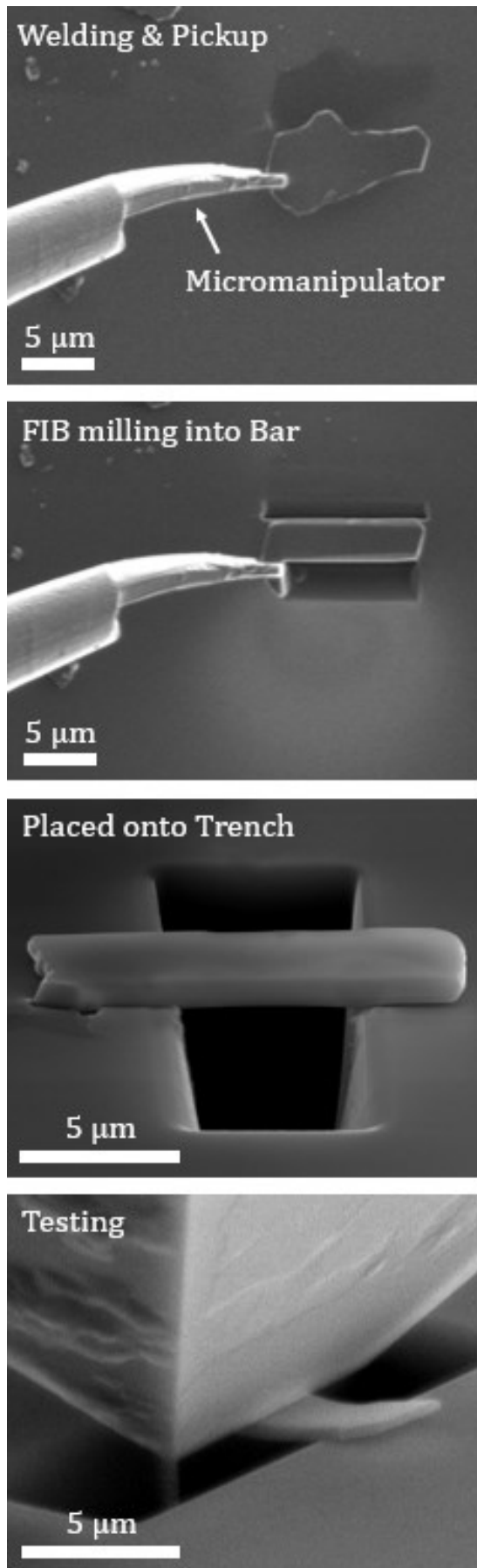


Figure 112. SEM images showing the pickup, milling, placement, and testing of a platelet.

Table 6. Results from the 10 successful micro-3 point bend tests of platelets.

ID	l (μm)	h (μm)	w (μm)	f _{max} (mN)	Strength (GPa)
1	5.30	0.41	2.58	0.34	6.1
2	5.65	0.60	2.12	0.65	7.2
3	5.65	0.87	2.76	1.14	4.7
4	5.57	0.94	3.18	1.07	3.2
5	5.57	0.43	2.78	0.39	6.4
6	5.57	0.51	2.15	0.24	3.6
7	5.57	0.44	5.02	0.67	5.8
8	5.57	0.51	3.82	0.63	5.3
9	5.57	0.50	3.30	0.38	3.9
10	5.57	0.79	3.35	1.61	6.5
				Average	5.3
				Std. Dev.	1.3

The force-displacement curves resulting from these tests show a linear trend for all the samples, however a small drop was often observed at low loads, as shown in Figure 113. This drop corresponds to the platelet detaching from the substrate where it is being held either by the small Pt weld or by surface forces. By the time of failure all platelets had detached from the substrate and were bending freely, so this constraint was not considered to be affecting the measured strengths. At these scales plastic deformation is a possibility, but despite the high stresses it is unlikely that these platelets are experiencing a high enough shear stress (4.3 - 10.7 GPa [149]) to allow slip to occur. Any deviation from linearity in the force-displacement curves would be evidence for plastic deformation occurring, but this was not observed.

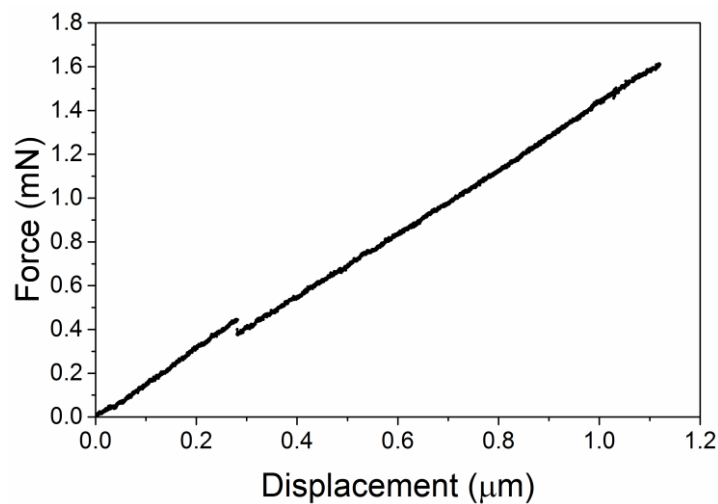


Figure 113. An example force-displacement plot for specimen ID 10.

Due to the small data set size, the Weibull modulus, m , of the platelets was calculated using the probability estimator $P_f = \frac{i-0.3}{N+0.4}$ [150] where i is the rank of the platelet strength and N is the set size (10 samples). This was then used to construct a Weibull plot, as seen in Figure 114. From this plot the characteristic stress, σ_0 , was found to be 5.82 GPa. Typical Weibull analysis assumes all of the tested samples to be of identical dimensions, however this is not practical in this test due to variation in the thickness and morphology of the platelets. Therefore a more complete analysis was developed to offset the effect of variation in sample area and volume on m . This is given in Appendix IV. The procedure consists of correcting the effective failure strength for sample area or volume using Equations 5.1 or 5.2:

$$\sigma_{i \text{ area corrected}} = \left(\frac{l_i w_i}{A_{ref}(m+1)} \right)^{1/m} \cdot \sigma_i \quad (5.1)$$

$$\sigma_{i \text{ volume corrected}} = \left(\frac{l_i w_i t_i}{2V_{ref}(m+1)^2} \right)^{1/m} \cdot \sigma_i \quad (5.2)$$

(where l is the bar length, w is the bar width, t is the bar thickness, m is the Weibull modulus, A_{ref} is the reference area, V_{ref} is the reference volume), and calculating the Weibull modulus using the corrected stress values. For simplicity, A_{ref} and V_{ref} were set to $1 \mu\text{m}^2$ and $1 \mu\text{m}^3$ respectively. As the expression for the corrected stress involves m , it can only be solved iteratively by first assuming m from the uncorrected data then cyclically calculating the new m until its value converges. Convergence typically occurs to two decimal places after 3 - 4 iterations. This adjustment accounts for the differences in volume or area between the samples in the 3 point bending configuration, allowing for the strength of a reference size to be estimated for each sample. This method may prove to be a useful general tool in other applications requiring Weibull analysis of non-uniform samples in 3 point bending.

Defect Analysis

If the critical defects are believed to be on the surface of the samples then the area correction should be used, while if they are believed to exist within the volume of the samples then the volume correction should be used. When corrected for the reference area, the Weibull modulus decreases from 3.9 to 3.7, and the average strength is 8.42 GPa. When corrected for the reference volume m increases from 3.9 to 4.0 and the average strength is 2.93 GPa. These moduli are similar in magnitude to other brittle materials tested in this configuration.[151,152] The different crystallographic orientations of the platelets may contribute to the scatter in measured strengths, as the fracture energy of alumina can vary by a factor of 2.3 between different fracture planes.[153] The distribution of defects in the platelets, and measurement uncertainties in the procedure may also contribute to the data scatter, and

therefore lower the Weibull modulus. These effects are thought to be minimal for macroscopic tests,[154] however we have found that measurement uncertainties can give rise to >10% variation in measured strength, therefore this might significantly lower the apparent Weibull modulus.

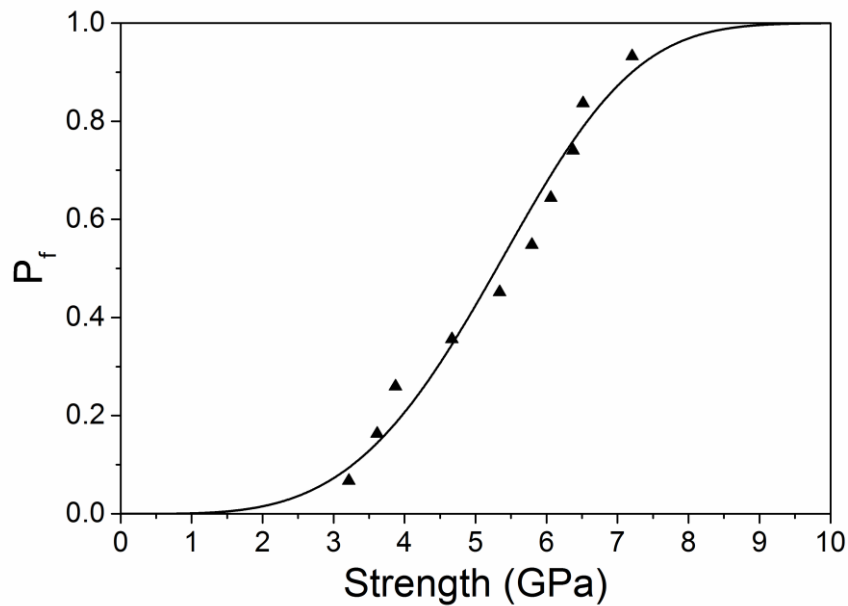


Figure 114. Weibull plot of the data, including the fitted Weibull distribution.

While we have not measured the toughness, K_{IC} , of the platelets, it is most likely within the range between the value calculated from the surface energy (2.12 MPa \sqrt{m})[155] to the value measured from macroscopic tests of sapphire (2.35 MPa \sqrt{m}).[156] Assuming a shape factor of 1.36,[157] the average defect size was calculated to be 28 - 34 nm. Two possible candidates for the critical defects have been identified: surface defects such as step edges, and growth defects inside the sample. Step edges have been observed on platelet surfaces, as shown in Figure 115, which could act as stress concentrators when oriented correctly.

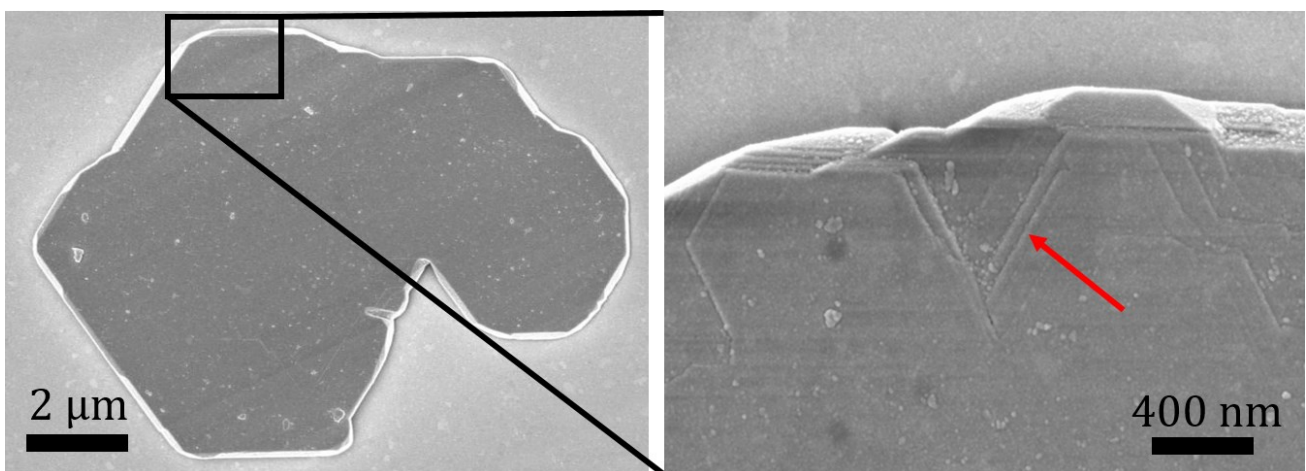


Figure 115. SEM images showing step edges on the face of a platelet.

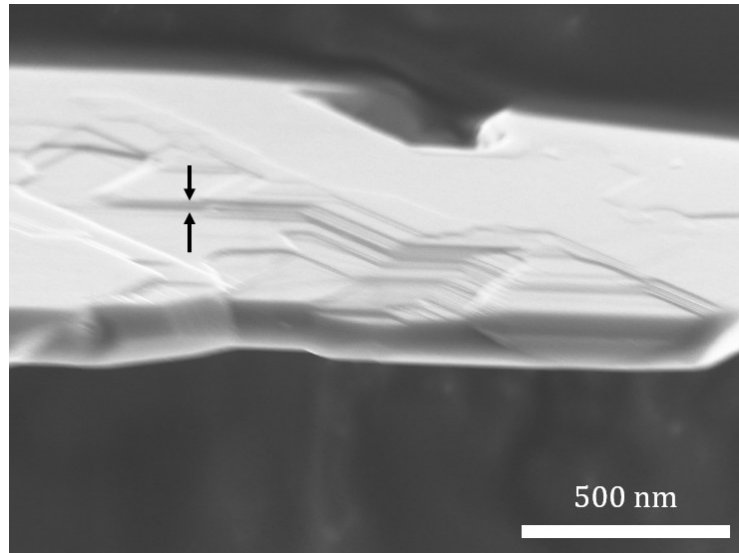


Figure 116. An attempted measurement of the size of the step edges on a platelet.

Preliminary SEM measurements of side-on platelets, as shown in Figure 116, revealed these steps to be ~10 - 30 nm in height, so they are in the correct size range to be responsible for failure. TEM analysis of one platelet also revealed a complex defective region in the centre of the platelets. This defective region was ~50nm thick, flanked by perfect crystalline α -Al₂O₃ on either side, oriented with the [0001] direction perpendicular to the platelet surface. High-resolution TEM and electron diffraction of this central region, shown in Figure 117, suggests the presence of stacking faults and impurities in this region. EDS was performed on this area, which revealed these impurities to be sodium and fluorine rich, as shown in Figure 118. Furthermore, it was noticed that voids were present inside the platelets from the fracture surfaces of platelets, but only platelets that had been heat treated at 1550 °C, as shown in Figure 119. This is strong evidence that the internal defects are NaF, as this material would evaporate at these temperatures, leaving behind voids. Further TEM analysis also identified dislocations and nano-twinning throughout the platelets, as shown in Figure 120.

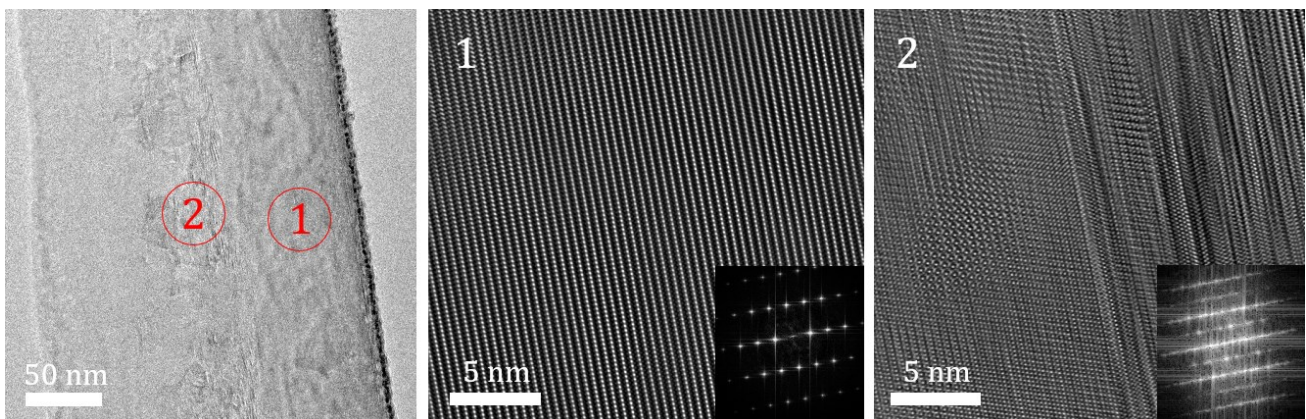


Figure 117. TEM image of the cross-section of a platelet with two areas of interest analysed in higher resolution, with their diffraction patterns inset. Obtained by Dr. Na Ni.

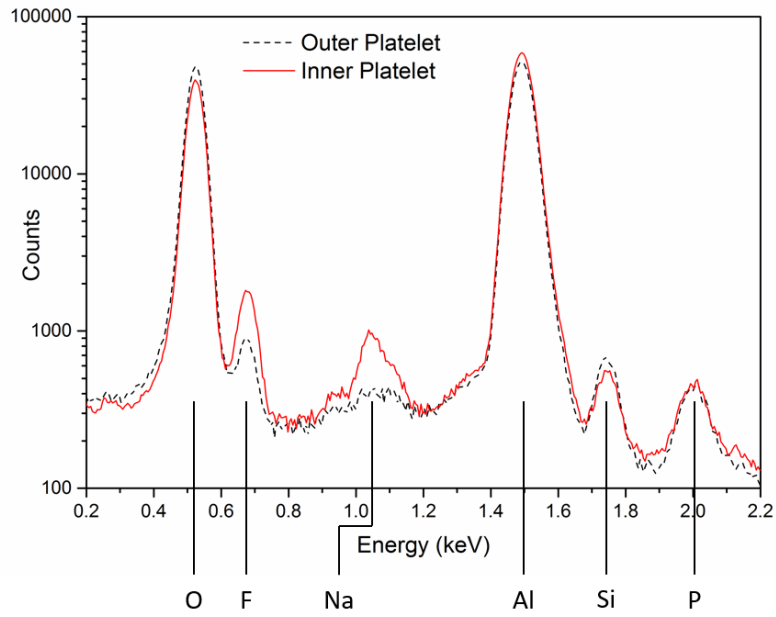


Figure 118. EDS Spectra gathered from the central defective region of a platelet and from a defect-free region of a platelet. F and Na were detected in much greater concentration in the central region, indicating the presence of impurities. Obtained by Dr. Na Ni.

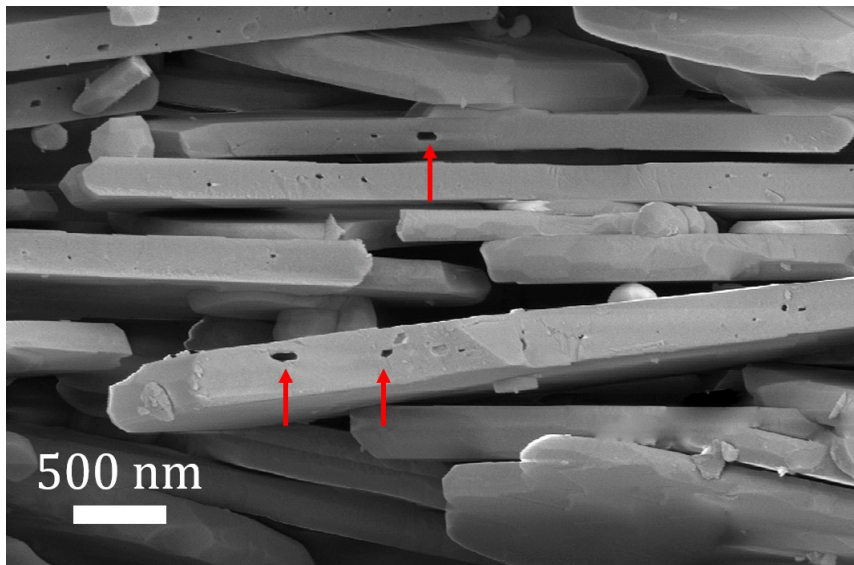


Figure 119. Cross section of a scaffold of platelets following heat treatment at 1550 °C, with some voids inside the platelets indicated.

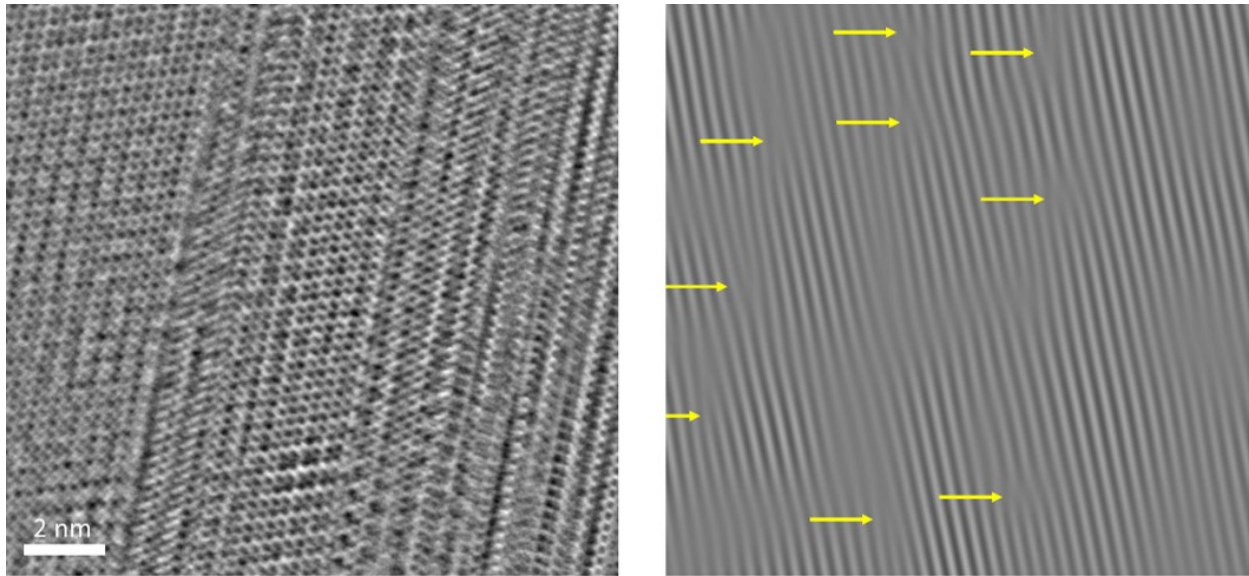


Figure 120. High resolution TEM showing nano-twinning. Inverse fast Fourier transform processed TEM image showing the presence of edge dislocations. Obtained by Dr. Na Ni.

Impurities remaining from the growth process have been observed at the central twin plane of topotaxially grown alumina platelets in other work.[158] It is therefore possible that these platelets also possess this feature in the form of Na and F. Upon bending, the region of the specimen which experiences the highest tensile stress is the bottom face of the bar. Considering that these defects lie close to the neutral axis of the bar, where tensile stress is at a minimum, they cannot be responsible for the mode-I failure of the samples. Most platelets were ejected from the test area and lost when they failed, however some remained on the trench allowing for analysis of the fracture surface. In some cases, the crack was observed to propagate in mode-I to the middle of the platelet, then deflect into mode-II parallel to the surface, thus we propose that these platelets typically fail by mode-I fracture starting at step edges and other surface defects, and the crack is then occasionally deflected by the defective central region and turns into mode-II, as seen in Figure 121. As we expect the surface defects to be responsible for failure, then we should use the area-adjusted Weibull modulus, 3.7, as the true Weibull modulus. Previous work has suggested that, for a simplified system, the minimum criteria for a crack to deflect at an interface is that the fracture energy of the interfacial material is less than a quarter of the bulk fracture energy.[159] This criteria was determined by considering a crack growing in a laminated material, however the same principles should be applicable here. Accordingly, from this we can state that the middle defective region must possess a less than a quarter of the fracture energy than that of the rest of the platelet.

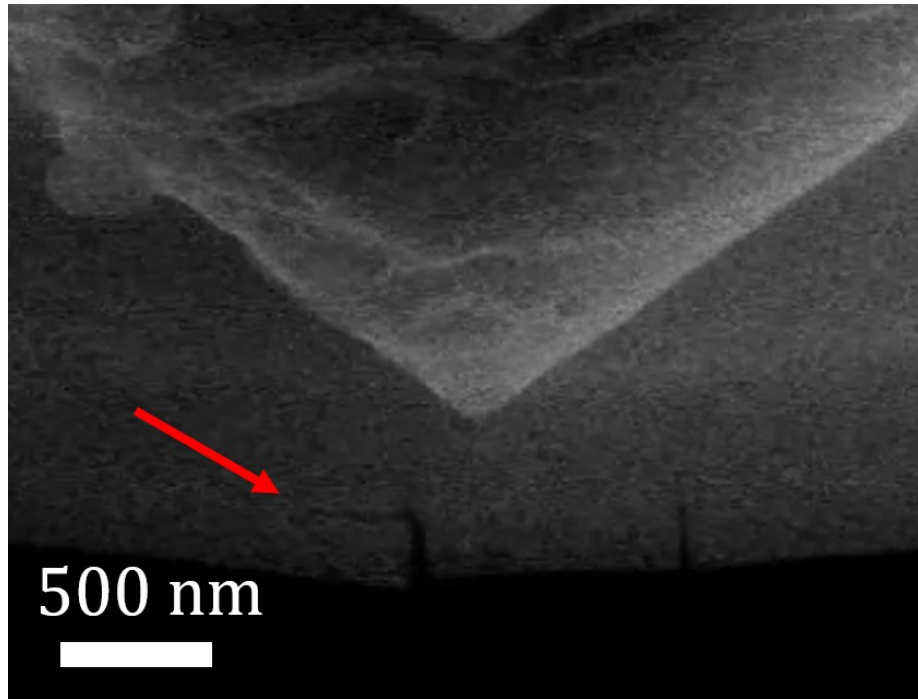


Figure 121. Example of a crack turning to mode-II during bend testing of a platelet.

Comparison to other alumina particles

The macroscopic bending strength of single crystal alumina typically ranges from 0.5 - 1.0 GPa,[160,161] which is substantially lower than the average bending strength of 5.3 GPa measured in these tests. Meanwhile microscopic sapphire fibres have been shown to possess strength of 2.9 GPa.[152] This is in accordance with previous studies where large increases in strength at small scales have been extensively reported for a range of materials.[162–164] This result can be correlated with the lower probability of finding defects within smaller sized samples, and with the smaller size of these critical defects. In our case a spherical defect cannot be larger than 0.9 - 0.4 μm (the range of platelet thicknesses tested). However if we scale the characteristic strength of the platelets to typical macroscopic dimensions (2.5x2.5x25mm)[160] then the expected strength would be just 0.01-0.1 GPa, therefore in proportion to macroscopic sapphire the platelets are significantly more defective.

The elastic modulus was calculated from the collected data, and was in the range of 30 - 50 GPa. This is substantially lower than the expected value for macroscopic alumina. This was attributed to compliance of the frame. Future efforts could attempt to measure the strain from image analysis of the videos which may yield more accurate results.

These basic data gathered on the platelets can help us design composites which use these platelets, allowing their mechanical properties to be fully optimised in the following sections of this chapter.

Platelet Alignment during Extrusion

As one might expect, the platelets in the pastes analysed in Chapter III align in various ways when the paste is sheared/flows. A range of printing nozzles were used to extrude these pastes, ranging in diameter from 0.15 - 1.54 mm, all of which resulted in some level of alignment. The alignment results in a distinct structure in the printed material, shown in Figure 122. This can be described by dividing each filament into two regions:

- The outer 'shell' of the extruded filament, where the platelets align with the normal of the platelet face perpendicular to the direction of flow as well as perpendicular to the nozzle wall, giving concentric circles of platelets.
- The central 'core' of the extruded filament, where the alignment is more random, thus no concentric rings are observed. However the normal may still align perpendicular to the flow direction.

A study was conducted to assess how the diameter of the nozzle affects the relative size of these two regions. In order to study this, filaments of 31 vol% platelet mix paste were extruded through a range of nozzles and collected on a non-stick surface and allowed to dry. They were then fractured carefully with tweezers, imaged with SEM, and the size of the two regions was measured by eye in ImageJ. A number of these fracture surfaces are presented in Figures 123 and 124. The alignment of the platelets parallel to the flow direction happens easily, as it was observed in all conditions. Within the range studied, the nozzle radius does not significantly affect the size of the core relative to the radius of the filament. One exception to this is the smallest nozzle tested.*** This is due to the fact that the radius of this nozzle is of the same order of magnitude as the diameter of the platelets, so boundary/surface effects are likely to become significant.

This same procedure from above was repeated while varying the length of the nozzle. In contrast, this variable was found to have a significant effect on the relative radius of the core. The core shrinks significantly as the length of the nozzle is increased, as illustrated in Figure 124. Thus one can stipulate that the concentric alignment of the platelets occurs as the paste is travelling down the length of the nozzle. This is logical, as it is the place where the paste experiences the greatest shear forces. This is strong evidence that the concentric alignment is due to the variable shear forces experienced during flow, and not generally due to boundary/edge effects. These data were used to select appropriate nozzles for printing highly aligned preforms.

*** The 0.15 mm diameter nozzle was the smallest nozzle attempted, which clogged frequently, and smaller nozzles clogged almost instantly.

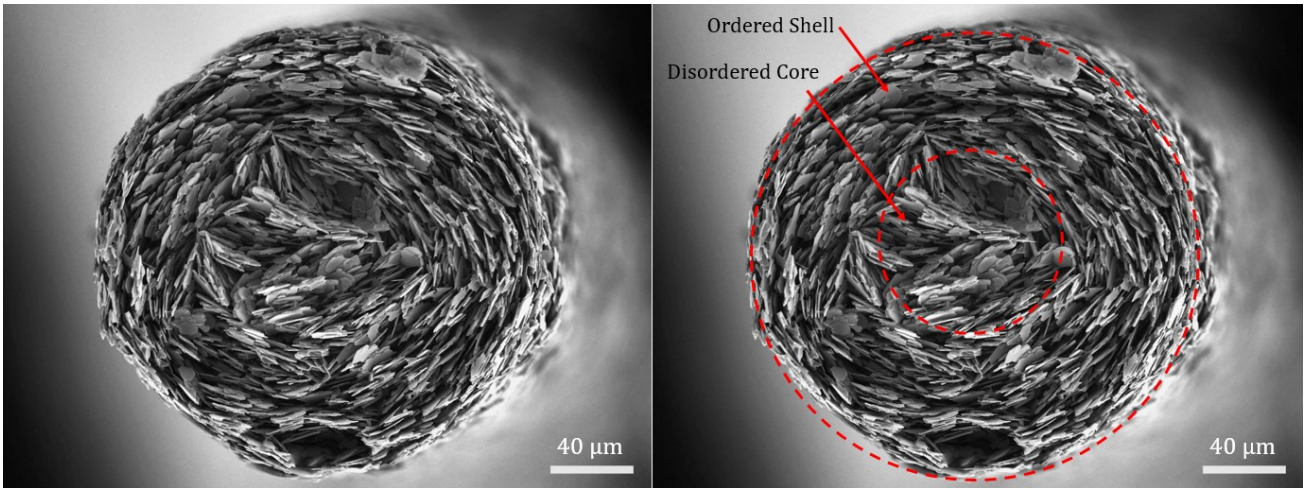
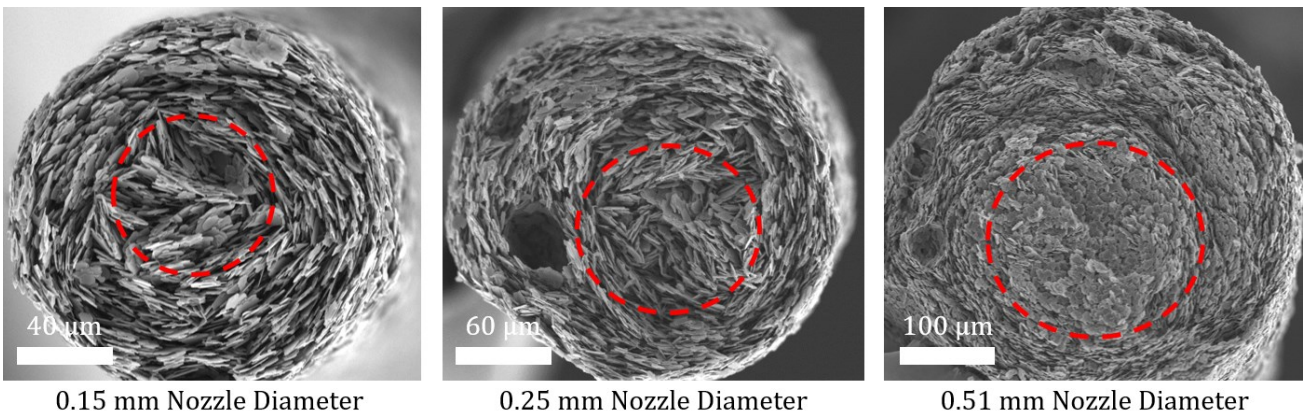


Figure 122. SEM image of a cross section of a single printed filament, with the disordered core marked, surrounded by the ordered shell.

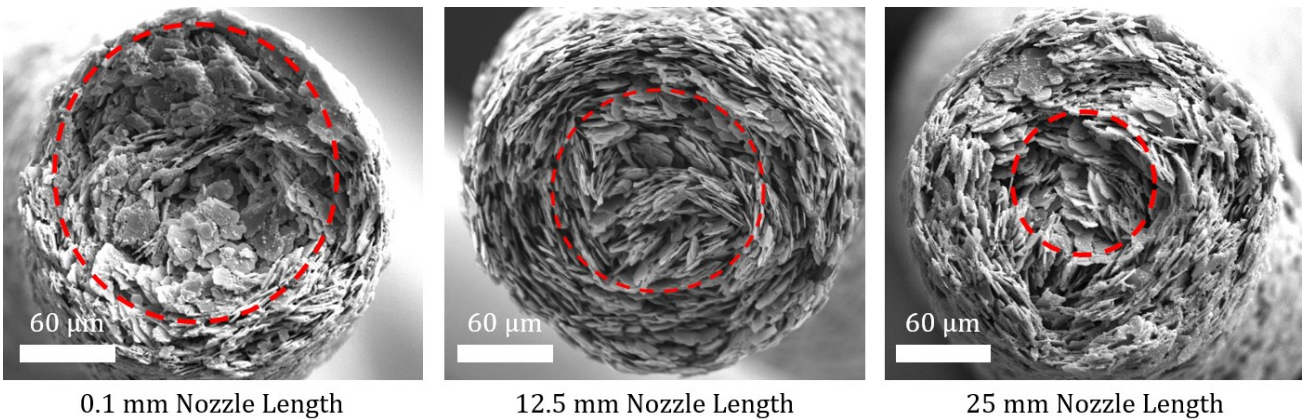


0.15 mm Nozzle Diameter

0.25 mm Nozzle Diameter

0.51 mm Nozzle Diameter

Figure 123. Cross sections of filaments extruded through 0.15, 0.25 and 0.51 mm diameter nozzles, all 12.5 mm length.



0.1 mm Nozzle Length

12.5 mm Nozzle Length

25 mm Nozzle Length

Figure 124. Cross sections of filaments extruded through 0.1, 12.5 and 25 mm length nozzles, all 0.25 mm diameter.

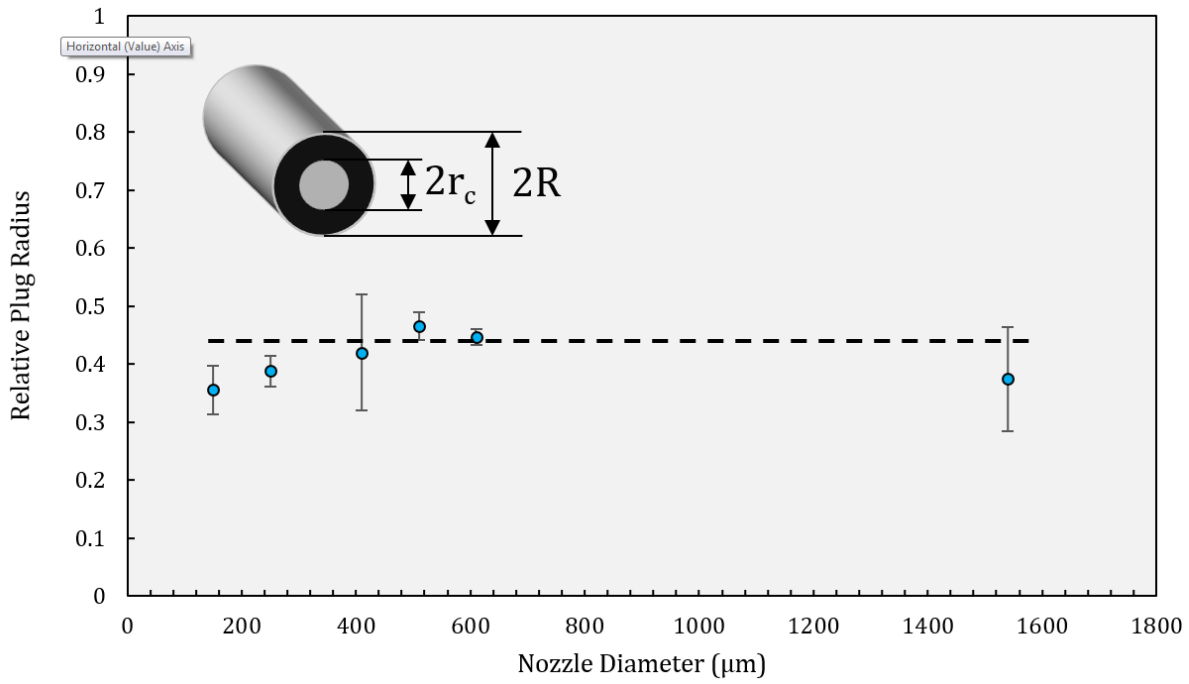


Figure 125. Variation of the relative radius of the un-aligned core with nozzle diameter.

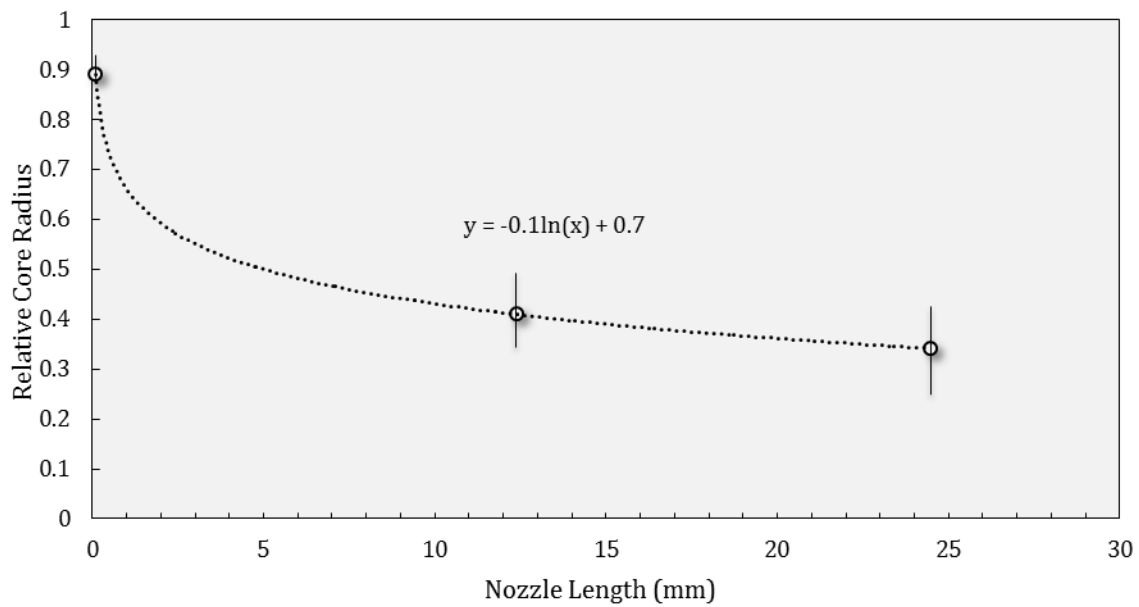


Figure 126. A number of measurements such as in Figure 124 of the average relative core radius, plotted against nozzle length for 0.41 mm diameter nozzles.

A Mechanistic Look at the Processes behind Platelet Alignment

Approximating the printing nozzle as a uniform channel with a circular cross-section, the velocity, V , at any point, r , across the radius of the nozzle can be calculated by applying the constitutive equation for Herschel-Bulkley fluids to the Navier-Stokes equations[54];

$$V(r) = \frac{n R}{\tau_w(n+1)} \left(\frac{1}{K}\right)^{\frac{1}{n}} \left[(\tau_w - \tau_y)^{\frac{n+1}{n}} - \left(\frac{\tau_w r}{R} - \tau_y\right)^{\frac{n+1}{n}} \right] \quad (5.3)$$

where R is the total radius of the nozzle and τ_w is the drag stress of the channel wall. τ_w can be calculated by a simple balance of forces from the overall pressure drop across the length of the nozzle; $\Delta P = \frac{2\tau_w L}{R}$ where L is the length of the nozzle. When plotted using the rheological parameters measured in Chapter III, Equation 5.3 gives a parabolic velocity profile such that the velocity is at a minimum closest to the nozzle wall, and maximum across a core region where the shear stress is lower than the paste's yield stress. This is shown in Figure 127. When differentiated with respect to radial position, Equation 5.3 gives the radial velocity gradient;

$$\frac{dV(r)}{dr} = \left(\frac{1}{K}\right)^{\frac{1}{n}} \left[\left(\frac{\tau_w r}{R} - \tau_y\right)^{\frac{1}{n}} \right] \quad (5.4)$$

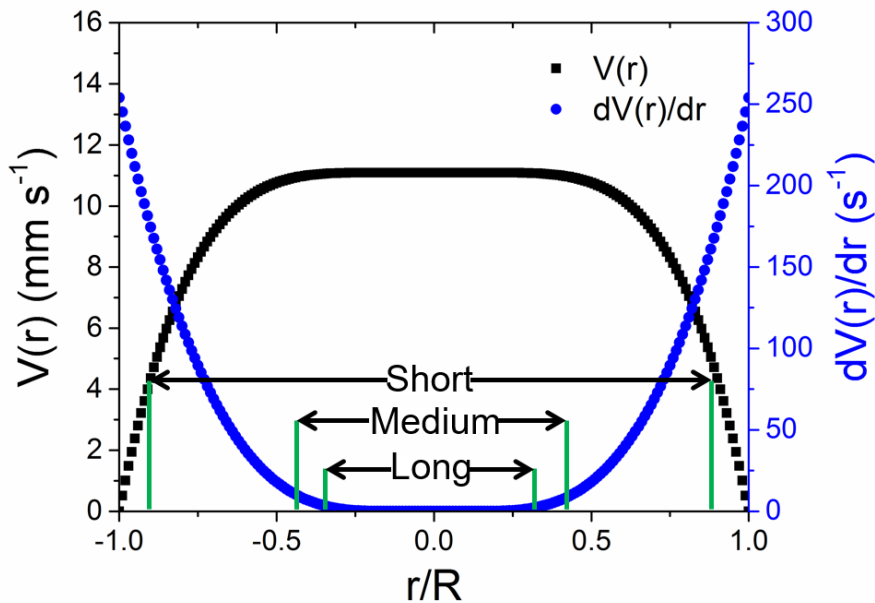


Figure 127. Velocity profile and velocity gradient across the diameter of the nozzle during printing of a 31 vol% platelet mix paste, calculated by plugging the rheological parameters measured in Chapter III into Equations 5.3 and 5.4. The relative plug radii for the short (0.1mm), medium (12.4mm) and long (24.5mm) nozzles are marked.

This velocity gradient is responsible for the tangential alignment of the platelets, giving the concentric ring structure in the ordered shell. Mechanistically this can be explained as follows – any platelets aligned radially (the face normal parallel to the nozzle wall, as in Figure 128) will experience a torque and rotate in the velocity gradient. Meanwhile platelets oriented with their face normal perpendicular to the nozzle wall do not straddle the velocity gradient, and therefore will not be affected by it, maintaining their orientation. This results in tangentially oriented platelets increasing in number extrusion. A core of material at the centre of the nozzle should show no alignment because the shear stress is low here. Equation 5.4 correctly predicts that the radius of the nozzle should not affect the relative radius of the core region. Furthermore, the overall model correctly predicts the effect of the nozzle length on the level of alignment – all pastes experience the same velocity gradient whether in a long nozzle or a short one, however longer nozzles increase the amount of time that the paste is subject to the aligning velocity gradient, thus increase the level of alignment.

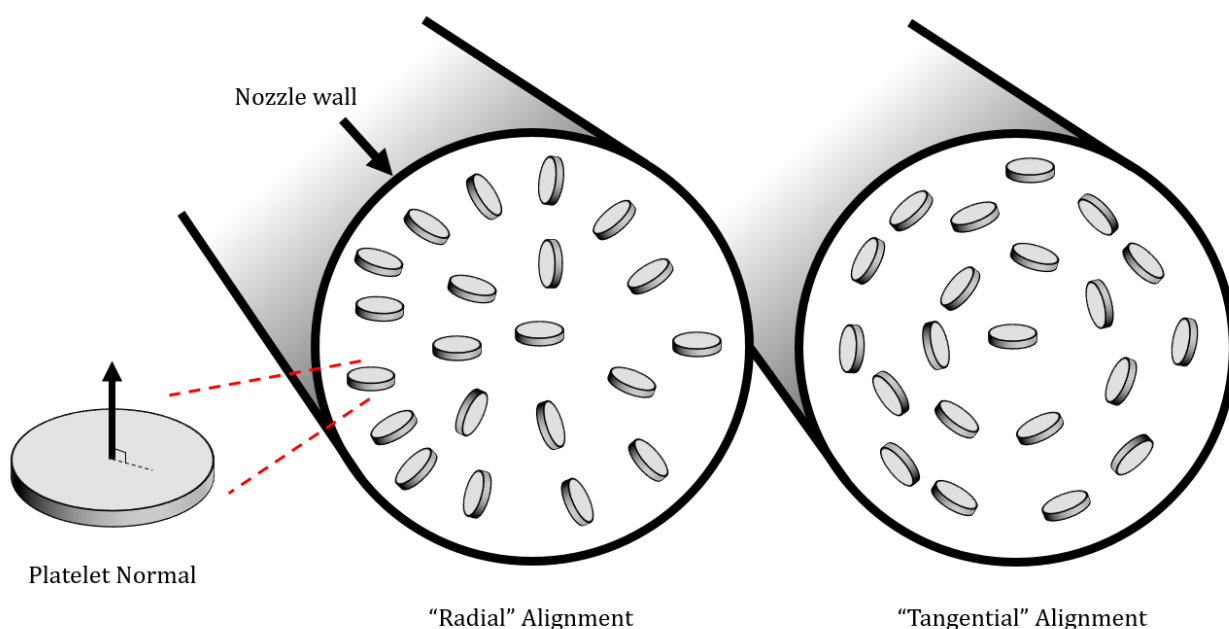


Figure 128. Schematics showing two possible aligned platelet structures in the printing nozzle.

One thing that is less clear is the effect of rheological parameters such as n and K on the size of the core. Broadly speaking, larger n should result in larger cores (as the velocity profile becomes less flattened and more parabolic for less shear thinning flows), however this is more difficult to measure. It was found that pastes with higher volume fractions of platelets give improved levels of alignment compared to low volume fraction pastes. This may be due to the role of platelet-platelet interactions in instigating alignment, and illustrates the benefits of using pastes systems (such as the Pluronic hydrogel system) which facilitate high volume fractions of ceramic materials.

Microstructural Design

Post Processing

Following printing and drying a porous green part of ~50 vol% ceramic material is obtained. Isostatic pressing can be used to increase the volume fraction of ceramics in this green part to ~64 vol%. During sintering the platelets were found to sinter very poorly. This is due to the platelet faces being very stable, and so sintering is hindered by the lack of driving force. This can be overcome by adding alumina powder to the printing paste, as the powder is of much higher surface energy, so sinters everything together in its effort to reduce surface energy. After sintering the preforms are strong (~50 MPa in 3 point bending) and therefore easy to handle. This robustness simplifies subsequent processing steps greatly. The remaining ~36 vol% of porosity can be infiltrated with a second phase to produce a composite material. The preforms were filled with a mixture of epoxy resin and hardener via vacuum infiltration. Once infiltration was complete, the part was removed from the beaker of epoxy-hardener mixture and cured, leading to composite parts with a final porosity below 0.5% as estimated from the Archimedes density. The whole process is compatible for a range of geometries, so it is possible to produce composite objects from CAD files, as demonstrated in Figure 129.

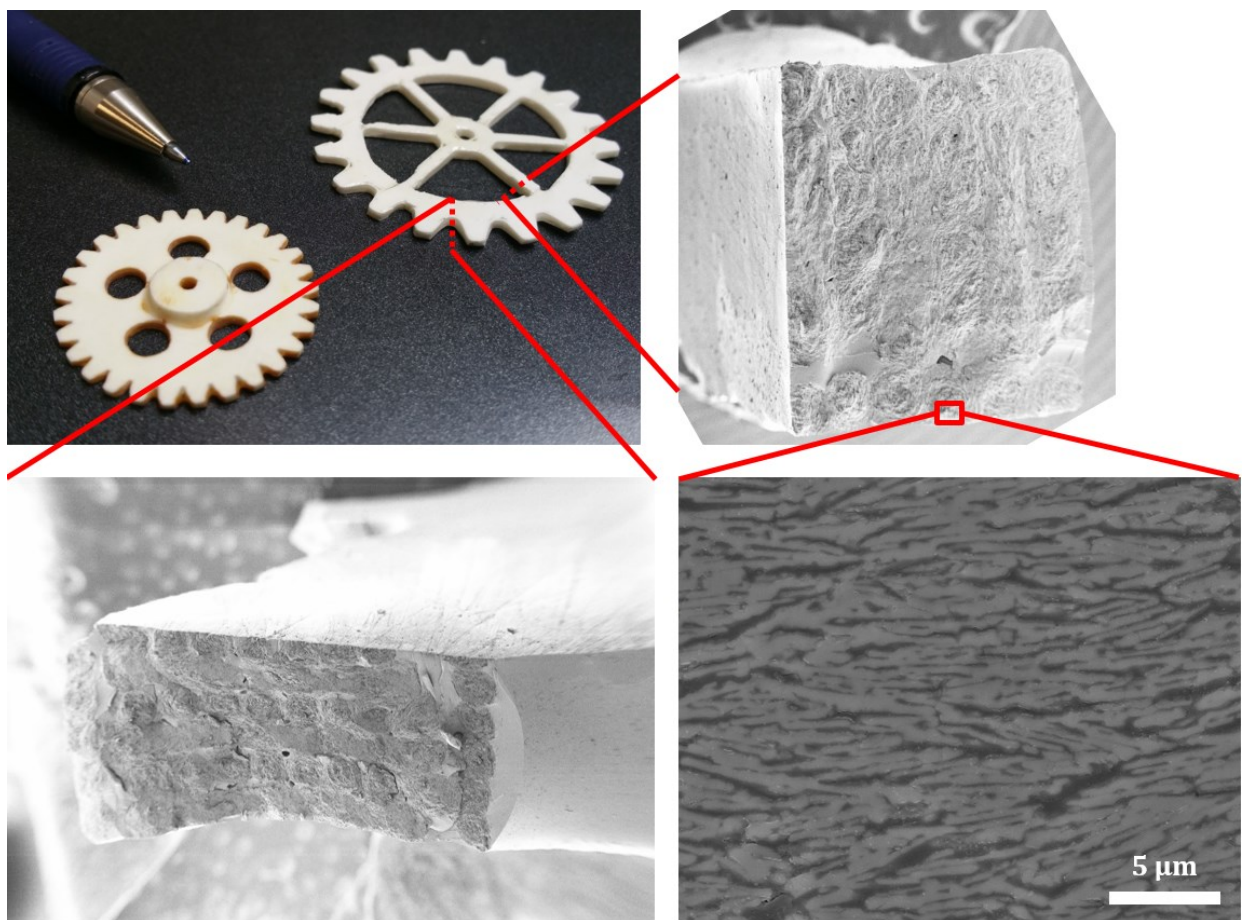


Figure 129. Two composite cog wheels printed from CAD files. SEM images of fracture surfaces of these parts reveals the hierarchical structures of the aligned platelets.

Characterisation and Mechanical Properties

The orientation of the alignment of the platelets has a large effect on the mechanical properties of the composites. As seen in Table 7, bending strength was found to increase by ~60% when the platelets were oriented parallel to the direction of tension (trans-filament) compared to them being oriented perpendicular to the direction of tension (inter-filament). Single edge notched beam (SENB) fracture toughness also increased by ~25% in the trans-filament direction. These two effects are likely to be related, with the increase in toughness giving rise to an increase in strength.

Other properties such as elastic modulus and compressive strength were not found to vary significantly with platelet orientation. The composites consist of a strong network of alumina platelets sintered together at their points of contact by the alumina powder. This network imparts a high Young's modulus, in the same range as many engineering alloys. Hardness varied with loading direction with respect to the platelet orientation; samples exhibited lower hardness when indented parallel to the filament direction. This can be explained by considering that there are many weak interfaces in this direction that can be split open by the indenter. This fracture results in larger indents, thus a lower hardness.

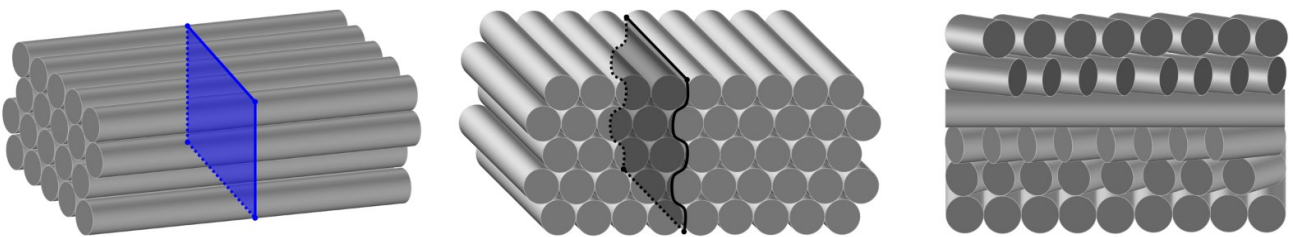


Figure 130. Schematic diagrams showing the orientation of the printed filaments in the lengthwise (trans-filament), widthwise (inter-filament) and Bouligand composites. Possible fracture planes are indicated where possible.

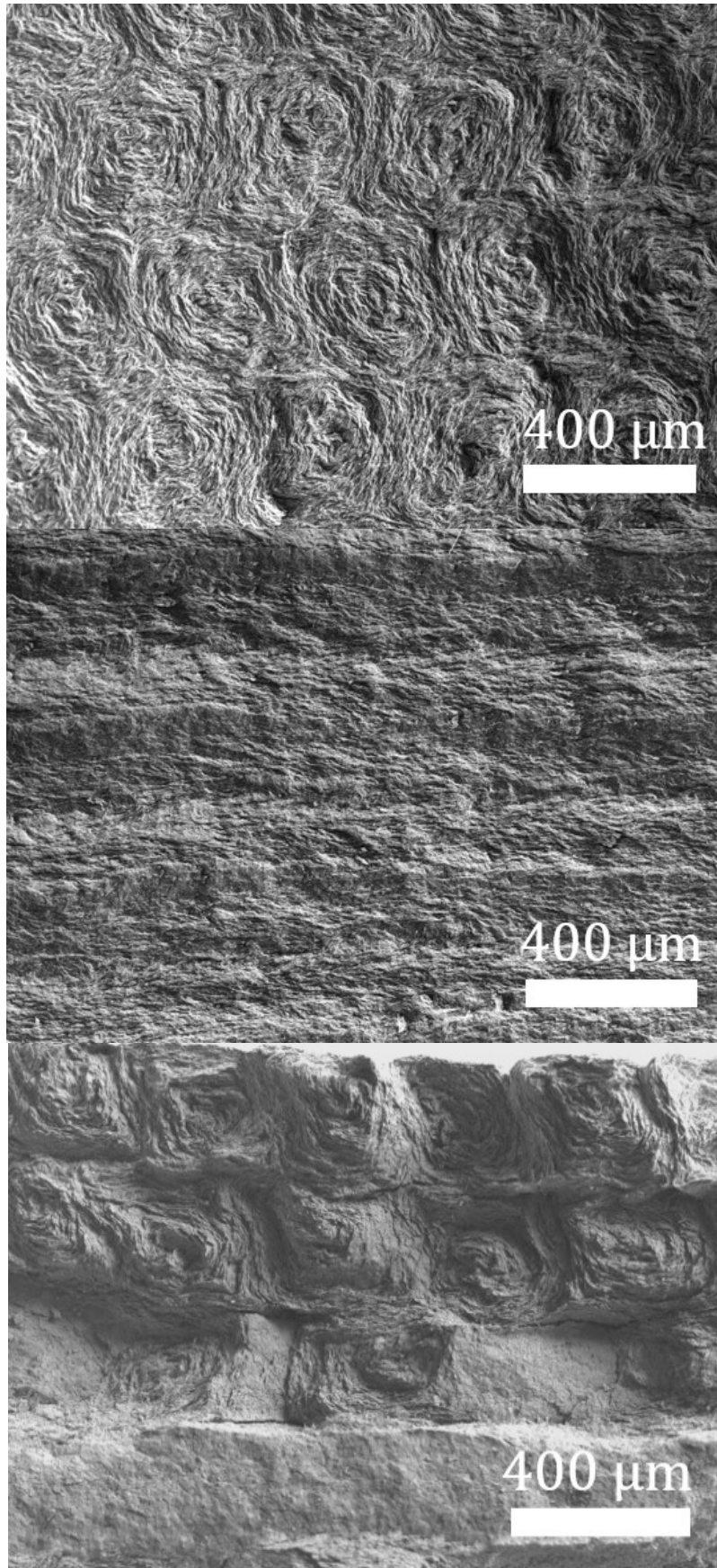


Figure 131. Representative SEM images of fracture surfaces of the three composites from Figure 130 following three point bend testing. Clear similarities exist between these materials and natural analogues such as bone.

Table 7. Mechanical properties for the three composite materials.

Orientation	Flexural Strength (MPa)	K_{Ic} (MPa \sqrt{m})	Young's Modulus (GPa)	Hardness (GPa) (perpendicular /parallel to filaments)	Compressive Strength (MPa)	Density (gcm ⁻³)
Trans-filament	202±10	3.0±0.3	99.1±0.6	3.04±0.70/	452	2.86
Inter-filament	125±12	2.4±0.6		2.52±0.12		
Bouligand	159±42	3.1±0.6		-	435	

Details of the toughening mechanisms acting in the composites were revealed by *in-situ* double cantilever beam testing inside an SEM. This test allows long (>1 mm) crack paths to be closely monitored in high resolution and correlated to the stress intensity, K_I , to obtain crack resistance curves (R-curves) for each printing direction. In this way it is possible to evaluate the effect of large mesostructural features on crack propagation, compared to traditional bending tests with relatively thin beams which have limited applicability in accurately measuring K_I in such long cracks.

The 'Novel' *in-situ* DCB Setup

The development of the novel *in-situ* DCB technique in this work was driven by three motivations:

1. It was found to be very difficult to fracture materials in a stable manner in four or three point bending. This is due to the fact that in this configuration the stress intensity increases with crack length, namely $K \propto \sqrt{c}$ where c is the crack length. Thus in a material with a flat R-curve cracks will accelerate until they are a significant fraction of the speed of sound in the material. Making meaningful measurements in such short times is virtually impossible. Having a material with a rising R-curve helps the situation by slowing the crack, and will bring the crack to a standstill if the increase crack resistance with respect to crack length exceeds the increase in K with respect to crack length. This criteria is not always met however, even for some high performance composite materials, so we have sought a testing configuration where K decreases with c , in order to promote stable fracture such that it is possible to study our unusual set of toughening mechanisms in detail.
2. Although traditional three point bending SENB tests allow for several mm of crack propagation before reaching the bottom of the sample, the validity of measurements made decreases with crack length. This is because the shape factor drifts from its initial value as the process zone ahead of the crack tip starts to impinge upon the bottom of the sample, inflating the measured crack resistance of the material. For this reason, standards generally limit the maximum crack length over which meaningful measurements can be taken.[135] This issue is much less significant in the DCB set-up, as the sample can be several cm tall, allowing many mm of crack propagation before this effect becomes prevalent. This is important when studying materials

with meso-scale features, which require significant crack lengths to probe the full scale of their structures and repeat units.

3. Lastly, it is highly desirable to be able to track the crack in real time, so that K can be correlated to events occurring at the crack tip. In most materials these events will be the crack travelling through various microstructural features, so high resolution microscopy is required to observe them. SEM is the obvious choice for the *in-situ* imaging technique due to its availability, resolution and flexibility.

In this setup the stress intensity at the crack tip can be calculated using;[165]

$$K_I = \sqrt{\frac{3E^2 h^2 d^3}{4c^4}} \quad (5.5)$$

where E is the young's modulus, h is the horizontal displacement of each arm, d is the half width of the sample and c is the length of the crack and arms. As K_I is inversely proportional to c^4 , the crack exhibits a high degree of stability, and can be grown over a long distance (>5 mm) in a very controlled manner.

Application of DCB to the Platelet Composites

Using the *in-situ* DCB setup the R-curves for the three printed composites were measured and are presented in Figure 133. Clearly the curves vary significantly between the different printed structures. For the trans- and inter-filament directions, K_I rises very steeply before levelling off after ~ 50 and ~ 200 μm respectively. In the trans-filament material the rise is primarily due to bridging. As the crack grows, platelet bridges behind the crack tip are pulled out and so the K_I saturates; 50 μm is roughly the length over which pull out is observed. Meanwhile crack deflection is likely to be the main contributor to toughness in the inter-filament sample, see Figure 136. The crack should reach maximum deflection after deflecting around one filament. This is consistent with the fact that the R-curve for this material saturates after ~ 200 μm and the diameter of each filament is ~ 300 μm .

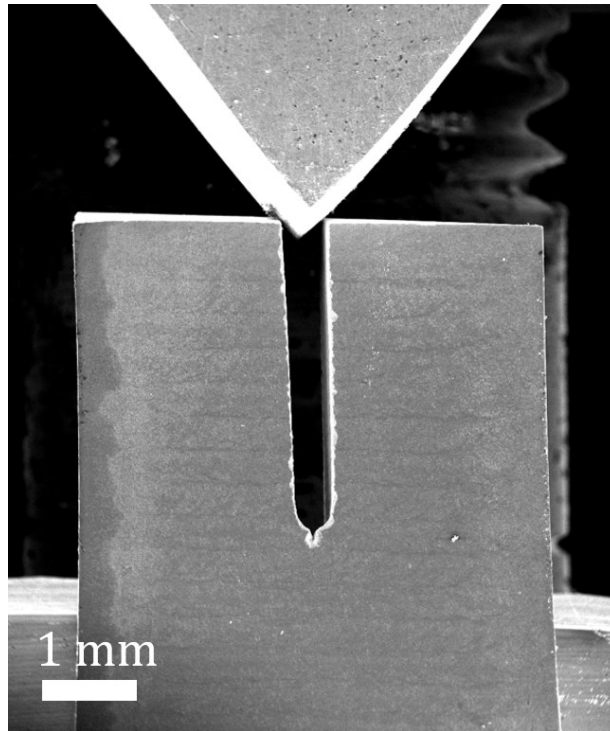


Figure 132. SEM image showing a lengthwise sample ready to be tested via DCB. The steel wedge can be seen at the top of the image.

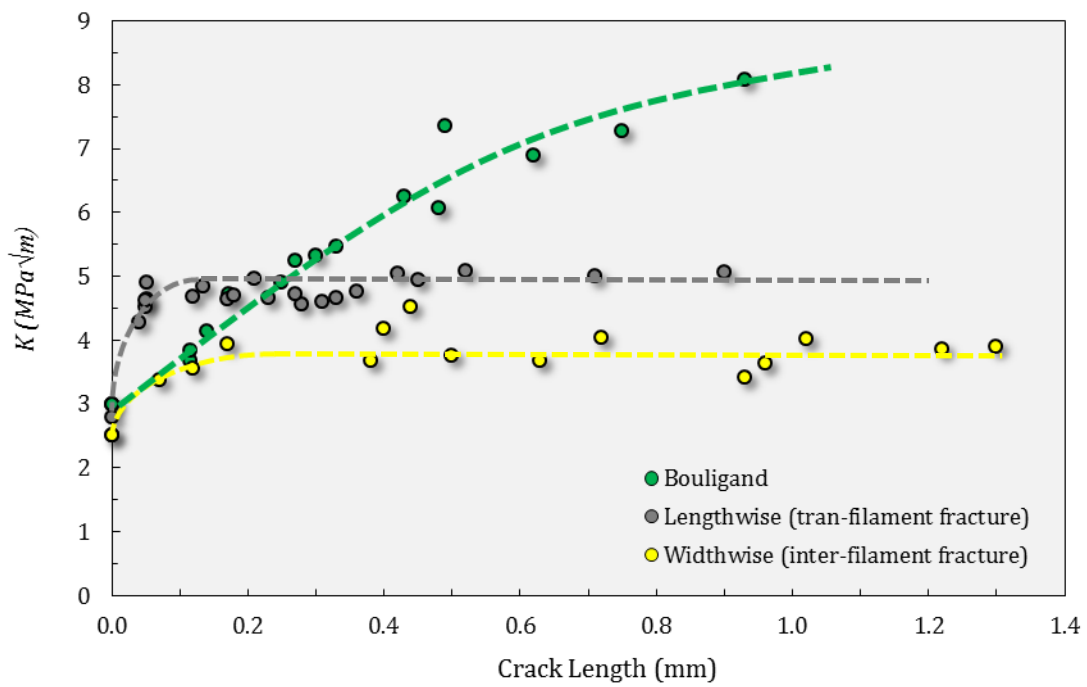


Figure 133. R-curves from in-situ DCB testing of multiple samples of the three composite materials, using the K_{Ic} as the K_I at zero crack length. The overlaid curves are to aid the eye.

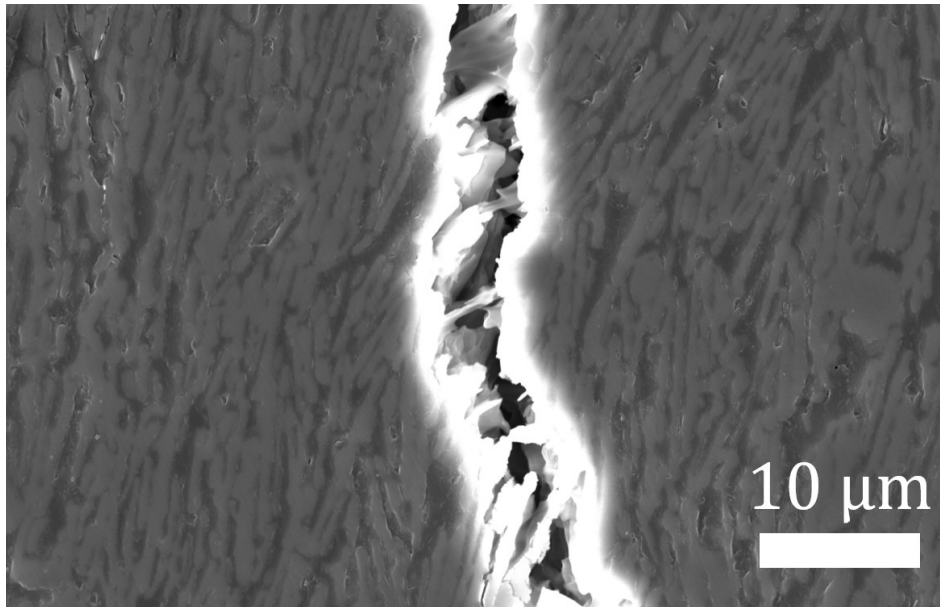


Figure 134. SEM image of a crack during DCB testing of an inter-filament sample, showing individual platelets bridging. The composite microstructure is also visible on the polished areas – the darker phase is the epoxy, while the lighter phase is the platelets in cross section.

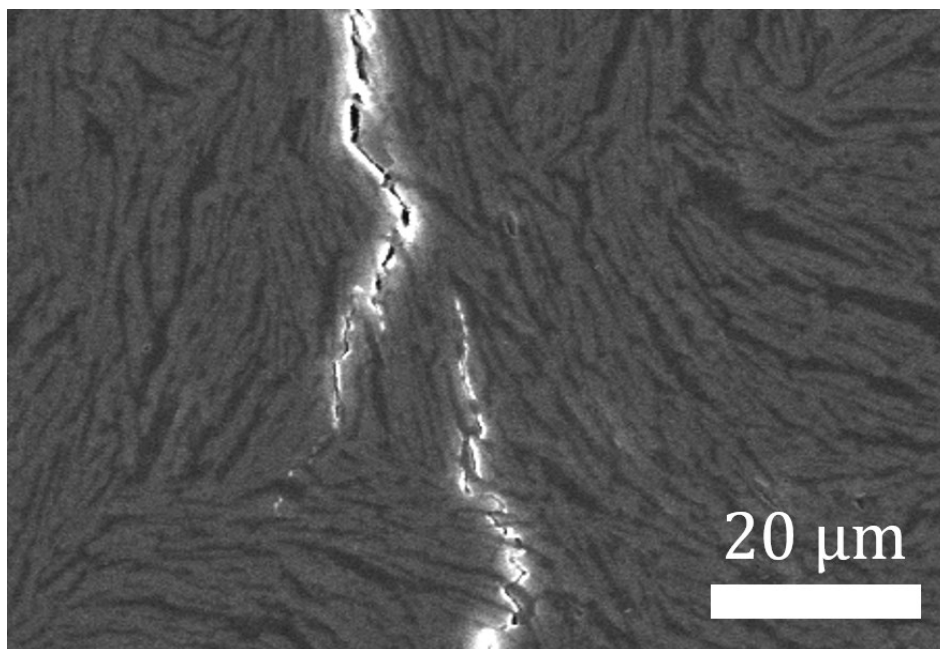


Figure 135. SEM image of a crack during DCB exhibiting crack deflection resulting in larger scale bridging.

Bouligand composite structures were produced by rotating the raster direction during printing by 30° with respect to the previous layer. These type of structures are often found in natural materials, such as the dactyl club of the mantis shrimp, due to their ability to enhance impact resistance and toughness.[144,166] The primary mechanisms responsible for these improvements are thought to be the smooth transition of elastic modulus between rotated layers as well as cracks propagating helically. This greatly increases the surface area of cracked material and changes to a less favourable mode of crack propagation, increasing the energy absorbed during fracture.[166] In the literature crack bending has been effectively used to control fracture in two dimensions for man-made materials.[167] In

ceramic composites weak interfaces are often used to deflect cracks, but these are usually randomly distributed in the microstructure, with the exception of laminates which can only provide deflection in one particular direction (where the weak path is placed 90° with respect to the crack propagation).[168–170] Printing allows greater control over this microstructural feature. As previously demonstrated, the inter-filament direction is less strong and less tough than the trans-filament direction, so cracks should preferentially grow on this plane. This has been shown to result in delamination of the printed layers, as well as the crack following the contours of the printed filaments, both shown in Figure 136.

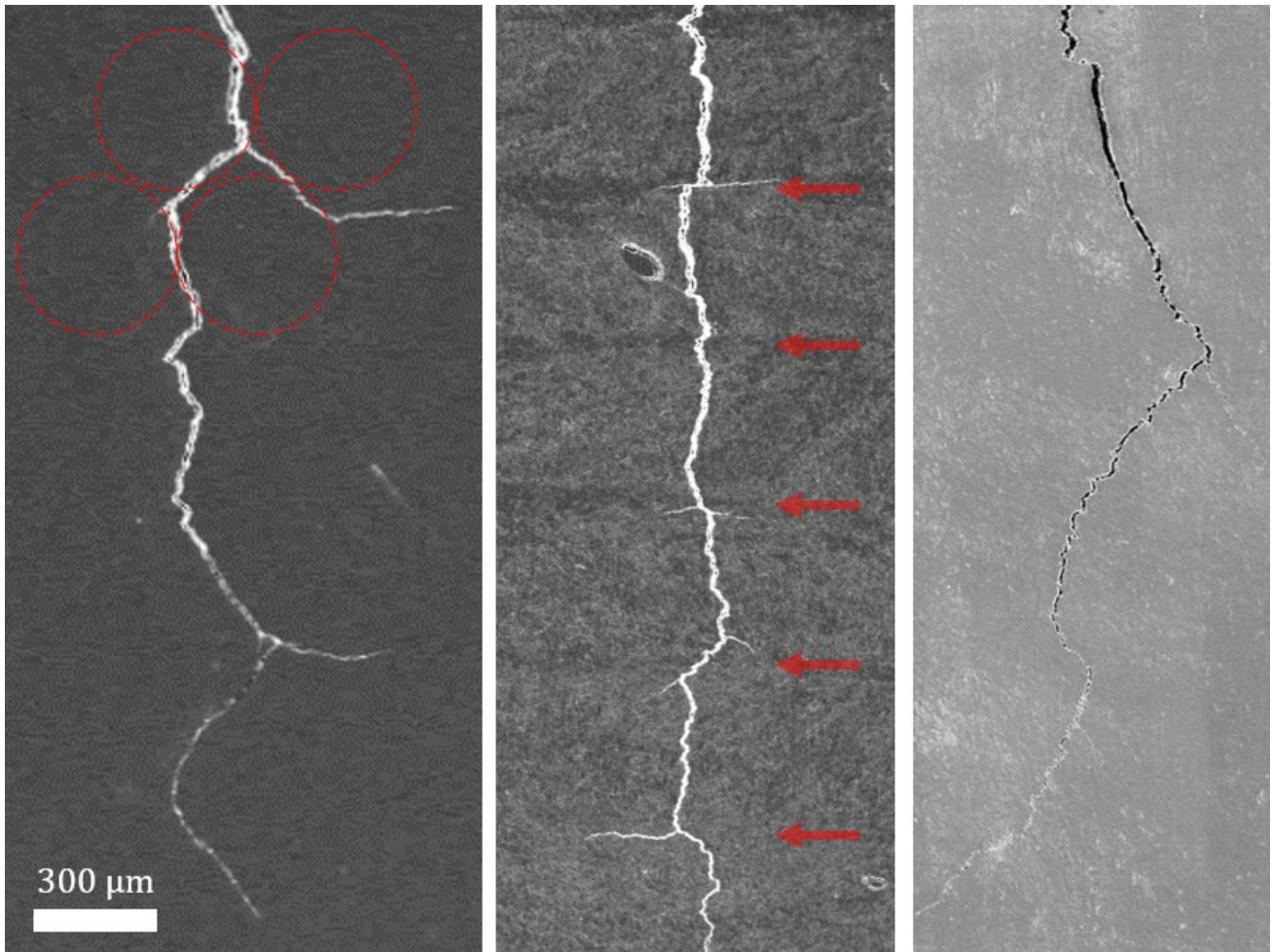


Figure 136. Stills from videos of in-situ DCB testing of a inter-filament (left) a trans-filament (middle) and a Bouligand composite (right). The boundaries between printed layers is indicated for the trans-filament samples, and the contours of the printed filaments is indicated for the inter-filament sample.

The fact that the crack preferentially propagates on some planes and not others means that we can control the propagation if we can control the location and orientation of these planes with the printing process. This can result in materials with a higher toughness if we use this control to direct cracks onto planes which are more difficult to grow on, such as twisted and tilted planes. The twisting and tilting manoeuvres are illustrated in Figure 137.

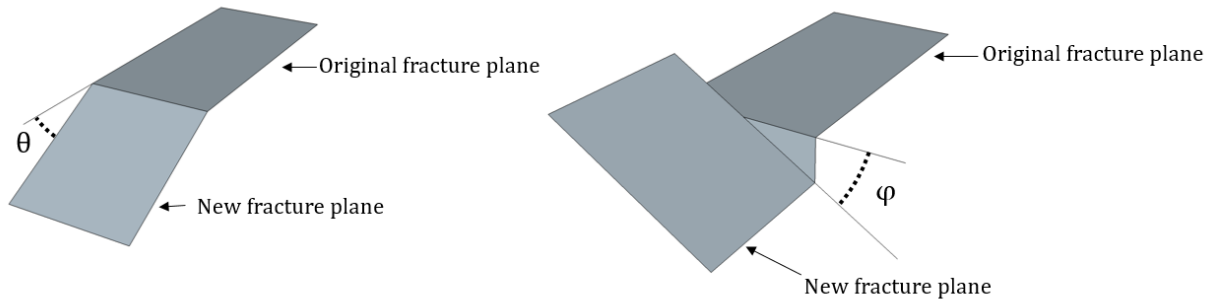


Figure 137. Schematic illustrations of a crack moving off its original plane of propagation via tilting (left) and twisting (right). The angle of tilt/twist is indicated.

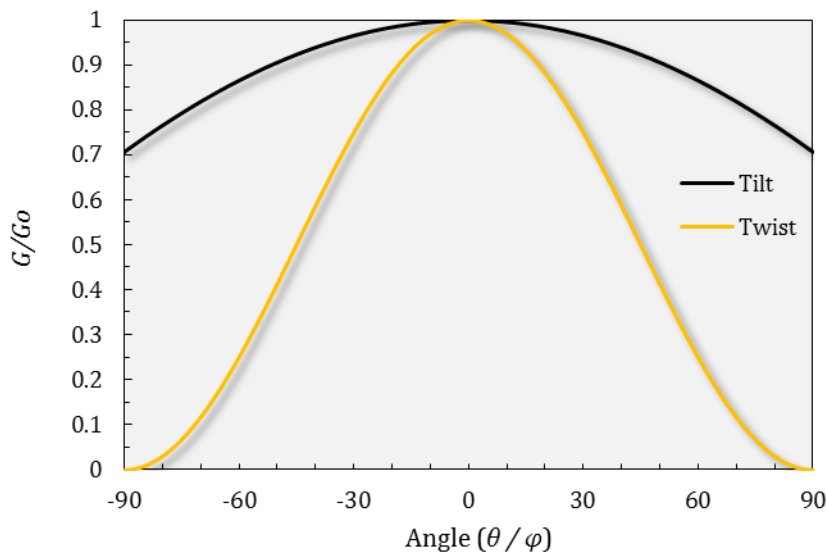


Figure 138. The effect of tilt and twist on reducing the strain energy release rate of a crack.

In an isotropic material each of these manoeuvres are energetically unfavourable for crack propagation – the crack prefers to propagate on its original plane, in purely mode-I fracture. The relationship between the strain energy release rate that the crack tip experiences (G_I) and the angle of this twist (φ) or tilt (θ) is given by:[155]

$$G(\varphi) = G_{1c} \cos^2(\varphi) \quad (5.6)$$

$$G(\theta) = G_{1c} \cos^2\left(\frac{\theta}{2}\right) \quad (5.7)$$

Thus twisting results in a faster decrease in G_I (less favourable propagation) than tilting. G_I even falls to zero (meaning the crack cannot propagate at all) at a twist of 90° . In the Bouligand material, as the crack grows it encounters the boundaries between printed layers rotated 30° with respect to one another. Whether the crack either twists, or continues on its current plane is determined by the relative magnitude of the strain energy release rate and the fracture resistance along the different paths. The G_{1c}

of the material (calculated from the K_{1c}) is fairly anisotropic, with the inter-filament critical strain energy release rate, G_{1c}^{inter} , only 64% of the trans-filament critical strain energy release rate, G_{1c}^{trans} ;

$$G_{1c}^{inter} / G_{1c}^{trans} \approx 0.64 \quad (5.8)$$

A crack propagating in the trans-filament direction will deflect onto a path of inter-filament propagation if the decrease in crack resistance given by Equation 5.8 is larger than decrease in crack driving force from Equation 5.6. In other words, there are two competing effects during crack propagation which try to maximise G – the microstructure is trying to twist the crack, but twisted cracks have lower G , so twisting will only occur when the microstructural effect is greater than the twisting effect. We can calculate the maximum twist angle simply by applying this principle to Equations 5.8 and 5.6. This leads to the finding that in theory it is possible to guide the crack to a twist angle of $\cos^{-1}\sqrt{0.64} = 36.9^\circ$. When this occurs over consecutive layers this has the effect of raising the R-curve by a factor of 3 with respect to the other inter- and trans-filament materials, as seen in Figure 133. However SEM fractography, shown in Figure 139, revealed that the crack to only twists up to an angle of $\varphi \approx 18^\circ$. This mechanism alone does not explain all of the increase in K_I for the Bouligand material presented in Figure 3c compared to the other two structures, as a twist of $\varphi = 18^\circ$ accounts for only a 10% decrease in crack driving force. However, twisting will also generate friction between the crack surfaces as they open. As the crack grows, the area generating this friction should increase linearly, thus crack resistance should also increase linearly. It can be observed that, in opposition to the inter- or trans-filament fractures, the R-curve does not reach a plateau but rather rises steadily for distances up to 1 mm, which points to the triggering of a different toughening mechanism.

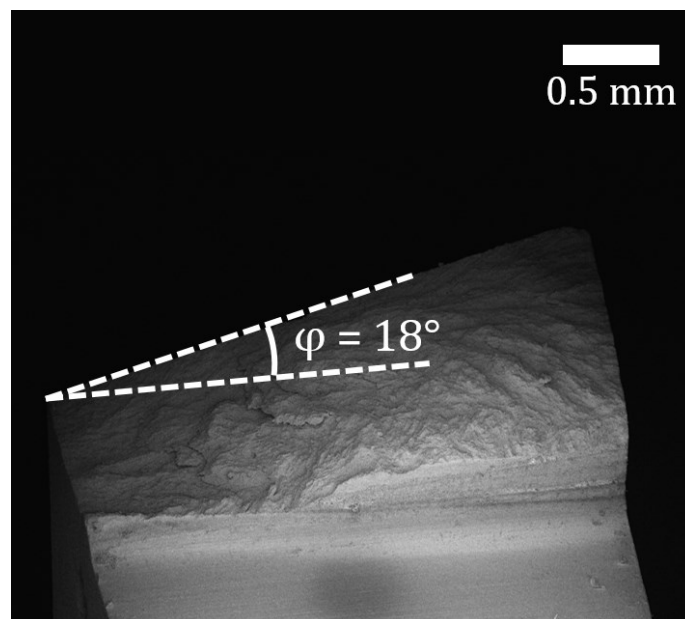


Figure 139. SEM image of the fracture surface of a Bouligand composite, showing a twist of $\sim 18^\circ$.

Using the same principles as above, the maximum crack tilt can be calculated using Equations 5.8 and 5.7, giving $2 * \cos^{-1}\sqrt{0.64} = 73.7^\circ$. This explains the behaviour illustrated in Figure 136, where the crack follows the perimeter of the printed filaments via tilting. This also goes towards explaining the delamination behaviour in Figure 136, where the crack temporarily deflects up to $\theta = 90^\circ$, changing to entirely mode II fracture until the crack re-nucleates and returns to mode I in the next printed layer, however other mechanisms must also be present to allow the full tilt to 90° . While some possibilities have been suggested above, in the context of this work it was not possible to fully nail down this mechanism acting in this unusually complex new material.

Conclusions

In summary, we have used robocasting to build ceramic scaffolds based on Al_2O_3 platelets with complex shapes and unique hierarchical structures. This was done by manipulating the velocity gradients during extrusion and the rheology. Composites with high ceramic content were fabricated by infiltrating these preforms with epoxy. The architecture of the printed filaments can be used to direct crack propagation (twisting and tilting) at the microscopic level in three dimensions. As an example we have shown how toughness increases significantly by altering the fracture behaviour on a mechanistic level in microscopic ceramic Bouligand structures, and we have developed a mathematical model to predict the extent of the twisting/tilting. In this way it is possible to tailor and improve the anisotropic properties and fracture resistance and reach mechanical properties which compare favourably with many engineering materials. These results show how the combination of AM with microstructural control opens new possibilities in the control of fracture, enhancing toughness and defect tolerance while maintaining a high specific strength.

Chapter VI – Ceramic Fibre Composites

Introduction

Monolithic ceramic materials show great promise for a diverse range of applications due to their mechanical properties, low density, and corrosion resistance. However, the principle reason many of these uses have not come to fruition is their low toughness, typically below $10 \text{ MPa}\sqrt{\text{m}}$, resulting in reliability issues and catastrophic rather than graceful failure behaviour. Composites are a promising solution – combining a ceramic's properties with another material's. This can greatly enhance toughness and result in improved failure behaviour. Composites with carbon, SiC or glass fibres have received the most attention and development to date, but there has only been a limited number of attempts to produce these composites via AM, as outlined in Chapter I. This is particularly attractive, as a number of applications of these materials are high value, low volume components and hence particularly suited for AM. This chapter will build on that work, attempting to produce short carbon fibre reinforced composites using robocasting, exploiting various aspects of the printing process to control and enhance the composite's microstructure. Both polymer matrix (PMC) and ceramic matrix composites (CMC) are attempted in this chapter, via two different approaches, both of which use robocasting to align and deposit the short carbon fibres. The PMCs will be produced by printing a paste of carbon fibres which will then be infiltrated with polymer matrix following drying and burn-out, while the CMCs will be produced by printing a paste consisting of the fibres and the matrix powder together.

Fibre Reinforced Polymer Matrix Composites

Paste Selection

As outlined in Chapter III, pastes containing short carbon fibres suffer from serious issues with bubbles. This was found to be the limiting factor on the maximum volume fraction of fibres that can be mixed into the paste; since as the volume fraction of fibres is increased, bubbles become increasingly difficult to remove. Higher volume fractions of fibres are desirable as this should result in an increase in their reinforcing effect in the final material. A good compromise between these two factors was found to be 20 vol% fibres. This paste was found to contain minimal bubbles following appropriate defoaming, and was easily printable.

Printing and Fibre Alignment

Printing was carried out using the same parameters used for monolithic parts. No issues with nozzle blocking occurred, despite the fact that some of the carbon fibres were longer than the diameter of the nozzle. This is evidence that the fibres are aligning in the printing direction, parallel to the flow; if any fibre was oriented perpendicular to the flow direction at the time that it reached the exit of the nozzle, then it would cause blocking.

There is a very strong tendency for the fibres to align in the printing direction, as is the case with the platelet pastes from Chapter V. However, unlike the platelet pastes, the fibre pastes show superior alignment when using the short conical nozzle compared to the long channel nozzle. This observation contradicts the model presented in Chapter V, as the paste should experience high shear forces for more time in the long nozzle, and the shear forces have been identified as the cause of the alignment. One explanation for this discrepancy is the length of the fibres. If a fibre is straddling the centreline of the nozzle channel, then it experiences opposing moments, as shown in Figure 142. This may result in fibres which straddle the centreline, maintaining their misaligned orientation. Meanwhile, with the conical nozzles a much lower fraction of the fibres initially straddle the centreline (due to the large width of the nozzle higher up), and so virtually all the fibres will have a chance to become aligned before they enter the narrow section of the nozzle. Furthermore the conical nozzles afford the fibres more freedom of motion due to their size, and do not have a 'dead zone' such as the region where the diameter rapidly changes in the long nozzles, which may cause additional misalignment.

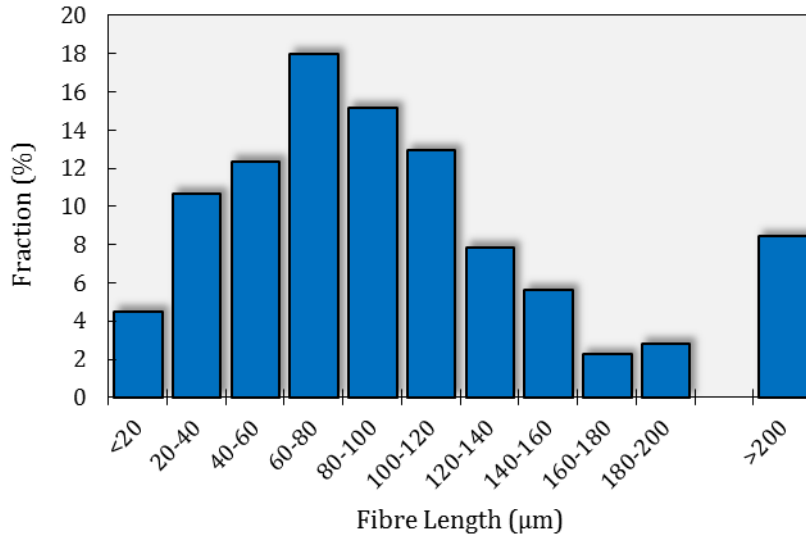


Figure 140- Distribution of fibre lengths of 180 fibres, measured using optical microscopy.

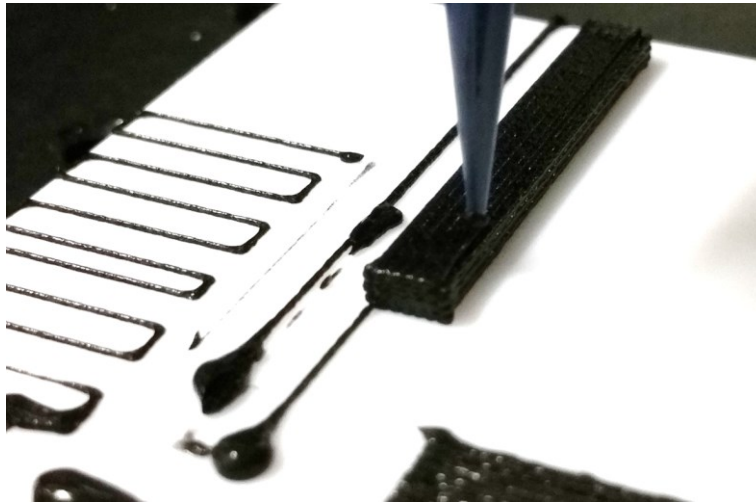


Figure 141. Printing a test bar using the carbon fibre paste.

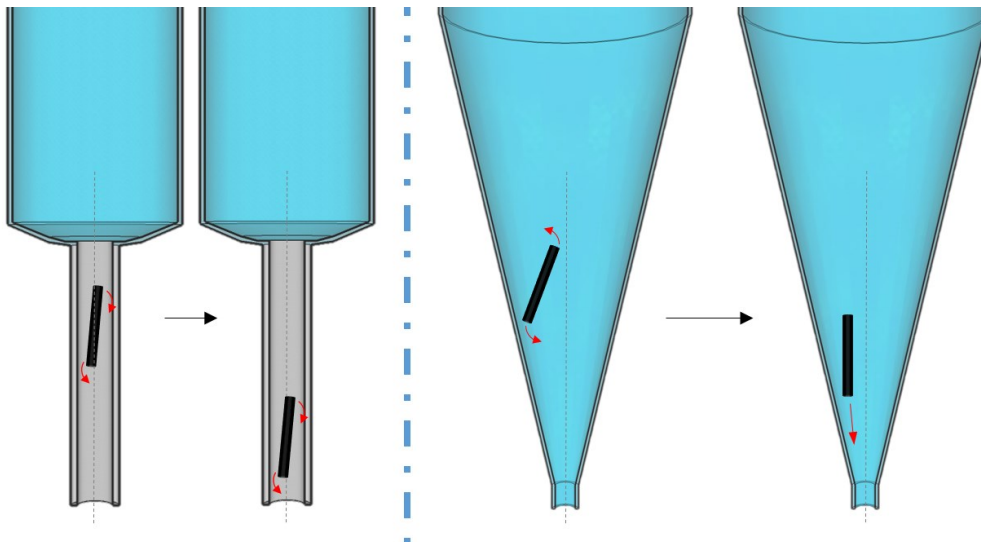


Figure 142. Schematics showing a single fibre travelling down the long straight nozzle (left) and the conical nozzle (right). The moments acting on the fibre due to the velocity gradient across the nozzles are marked by red arrows.

Post Processing

Following printing the parts are dried in the same manner described for the parts in Chapter IV. They are then isostatically pressed to remove any remaining bubbles, and the Pluronic is burnt out under argon at 600 °C. This is to protect the carbon fibres from oxidation since initial attempts to burn-out in air resulted in the fibre damage presented in Figure 143.

At this stage the samples consist of the carbon fibres and a small amount of residual carbon from the Pluronic burn-out, so they are very fragile and must be handled with great care. They are then infiltrated with the liquid epoxy resin and hardener in the same manner used to produce the platelet composites in Chapter V, and cured to give an aligned short carbon fibre polymer matrix composite (PMC).

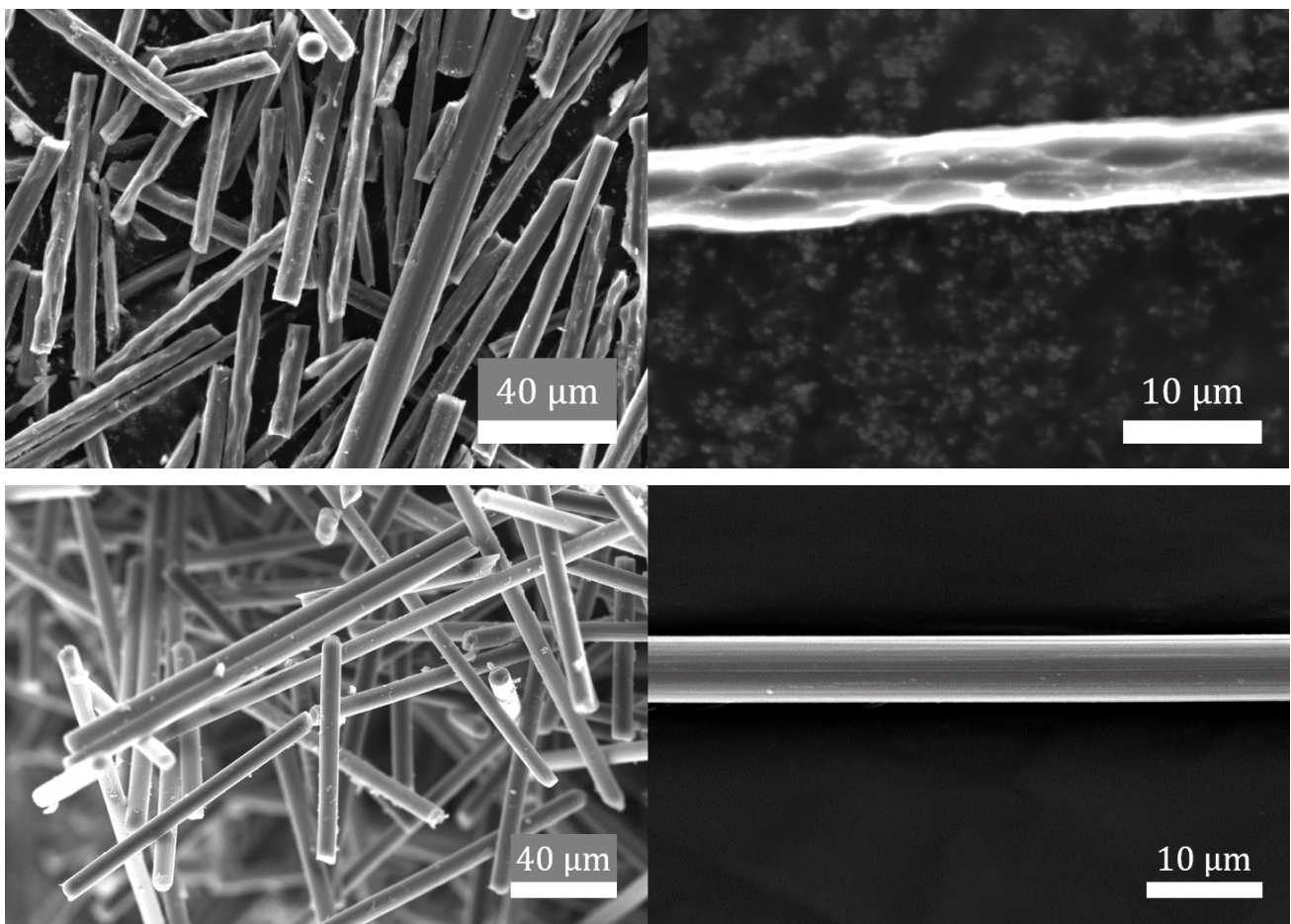


Figure 143. Carbon fibres after burn-out for 1 hour at 600 °C in air (top) and in argon (bottom), showing oxidation damage in the top images.

Microstructure

From the microstructure, Figure 144, it can be seen that infiltration is complete; there are no visible voids or bubbles and no unfilled gaps between fibre bundles.

The printing process results in a very high degree of alignment of the carbon fibres in the printing direction, which is maintained during the burn-out and infiltration processes. Nonetheless, the alignment is not perfect; a small fraction of fibres appear to be misaligned by several degrees. This is evidenced by the appearance of elliptical-shaped fibres in the cross section, Figure 144, and also more directly by pulled-out fibres in Figure 145. Due to the difficulties in handling these delicate parts, it was not possible to determine whether this slight misalignment was present before drying or occurred later on; however, compared to similar composites in the literature it was deemed acceptable.[104,171,172]

Another prominent feature of the microstructure is the non-uniform distribution of the fibres. The microstructure consists of clusters of fibres punctuated with large voids 100s of microns in size, which contain little or no fibres, as seen in Figure 145. Using ImageJ, the final volume fraction of fibres was measured to be 23 vol%.

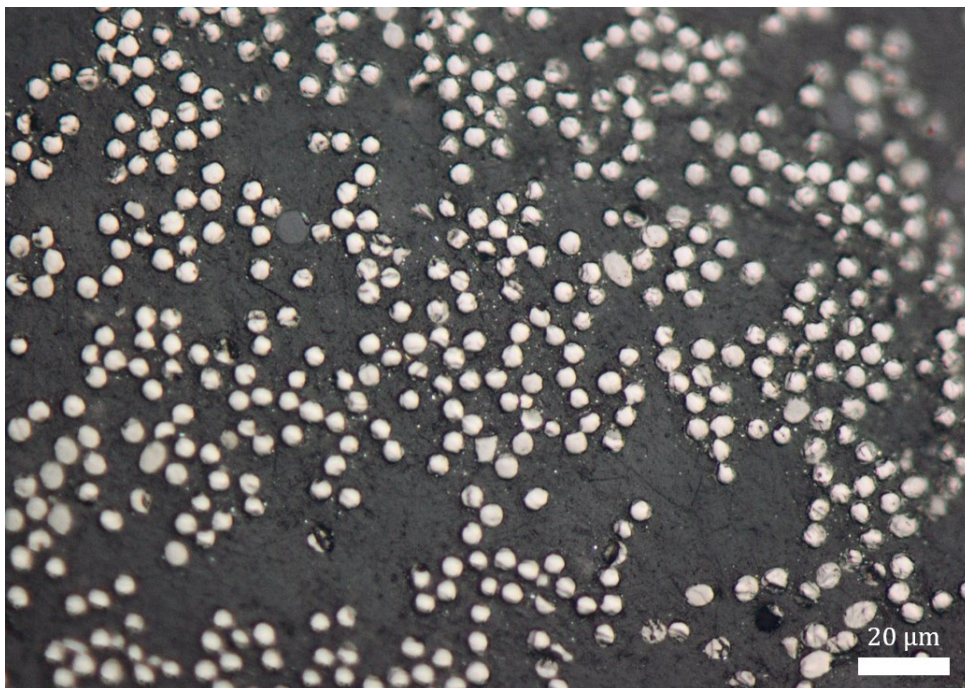


Figure 144. Optical micrograph of a polished section of the resulting PMC, showing very strong fibre alignment perpendicular to the sectioned surface.

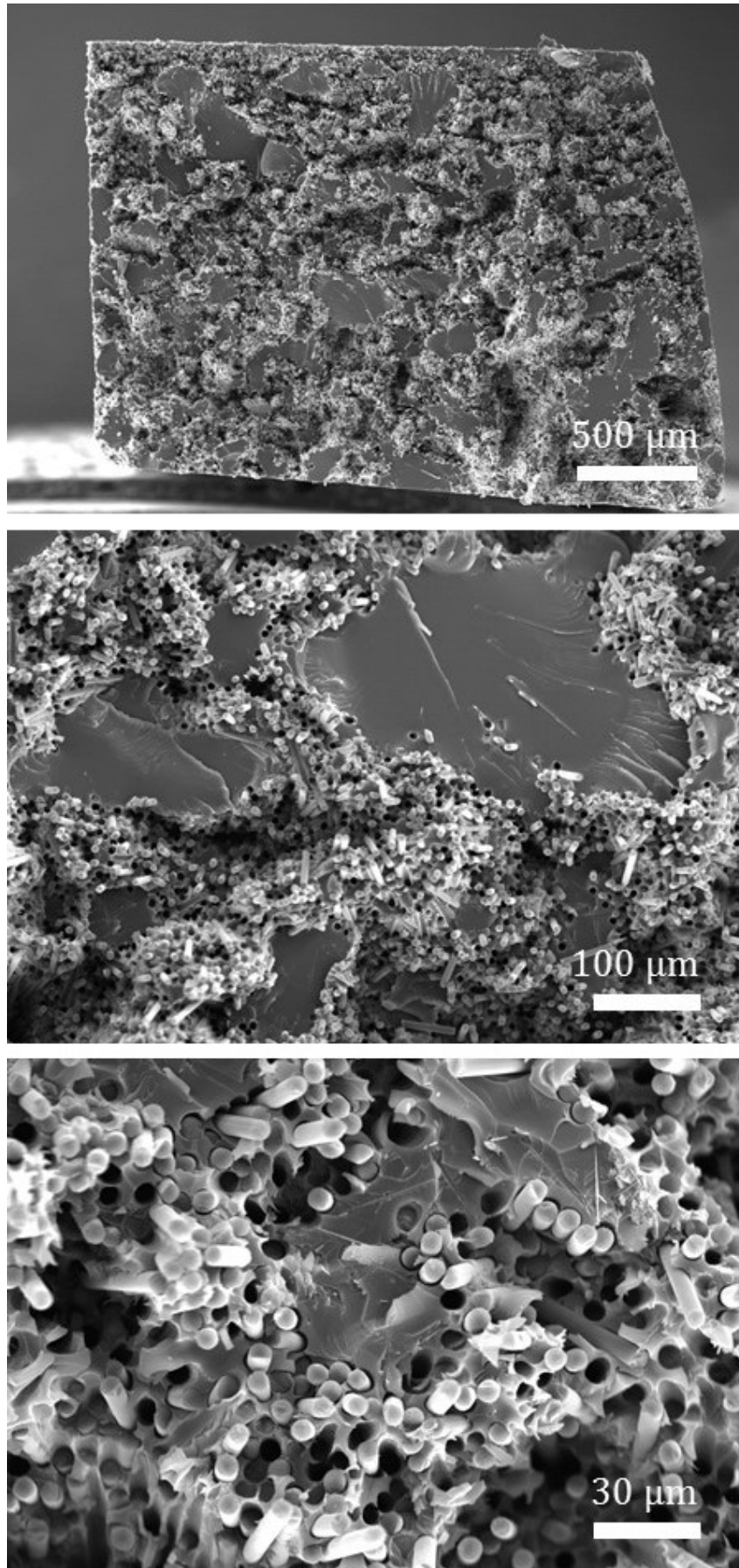


Figure 145. SEM images of a fracture surface of the PMC, showing the fibre rich and fibre poor regions.

Mechanical Properties

The strength of this composite was measured using 3 point bending, following the standards laid out in Chapter II. As can be seen in Figure 149, they fail abruptly, but not in an entirely brittle manner – the bar did not snap into two pieces upon failure. This behaviour has been shown for similar carbon fibre reinforced polymers (CFRP) in 3 point bending.[173] It can be attributed to the fibre pull-out mechanism – the matrix breaks at the point of failure but the fibres do not, so additional work and extension are required to separate the two halves. Strength values are presented in Table 8.

Toughness was measured by 3 point bending of single edge notched beams. As can be seen in Figure 150, force-displacement curves revealed stable crack initiation and steady growth across the full thickness of the sample. The K_{IC} was calculated using the Griffith equation, and the load at which crack initiation occurs was determined by observing the point of substantial delineation of the force-displacement curve. The work of fracture was calculated by fitting a high order polynomial to the force-displacement curves, and integrating this polynomial. These data are presented in Table 8.

Table 8. Mechanical properties of the PMC compared to the matrix (properties given by manufacturer).

Material	Strength (MPa)	K_{IC} (MPa√m)	Work of Fracture (kJ/m ²)	Failure Strain (%)	Density (g/cm ³)
PMC (this work)	211 ± 34.6	3.52 ± 0.25	1.93 ± 0.08	1.01 ± 0.15	1.29
Epoxy	115 ± 5.00	0.78 ± 0.07	0.21 ± 0.02	6.00 ± 1.00	1.14

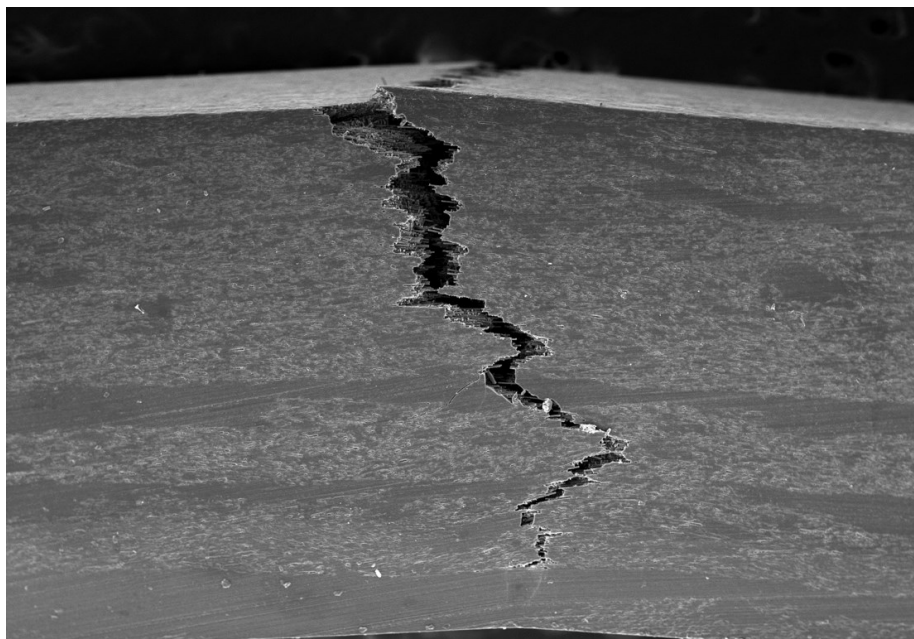


Figure 146. Fracture of the composite in 3 point bending, showing extensive crack deflection and fibre pull-out.

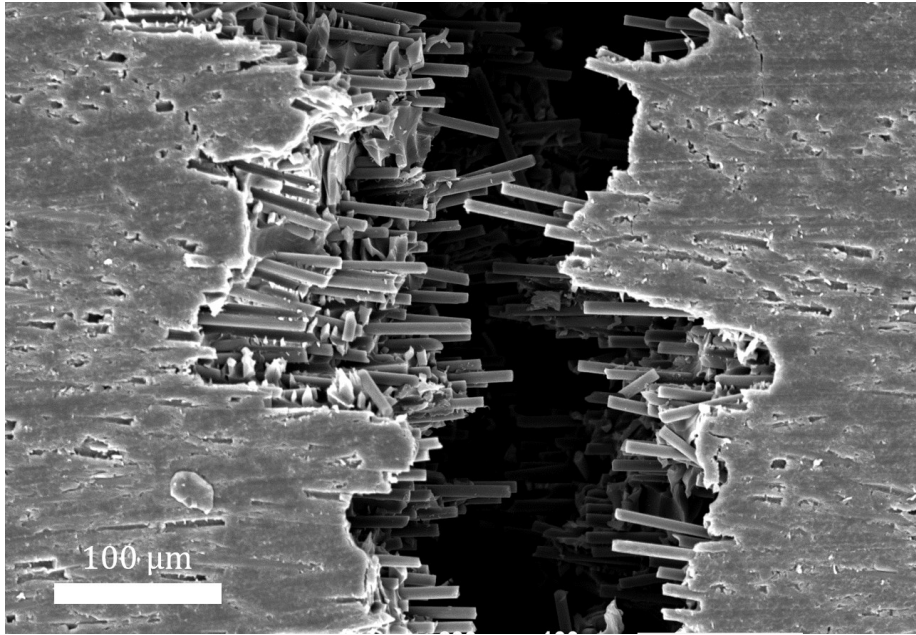


Figure 147. Close up of Figure 146.

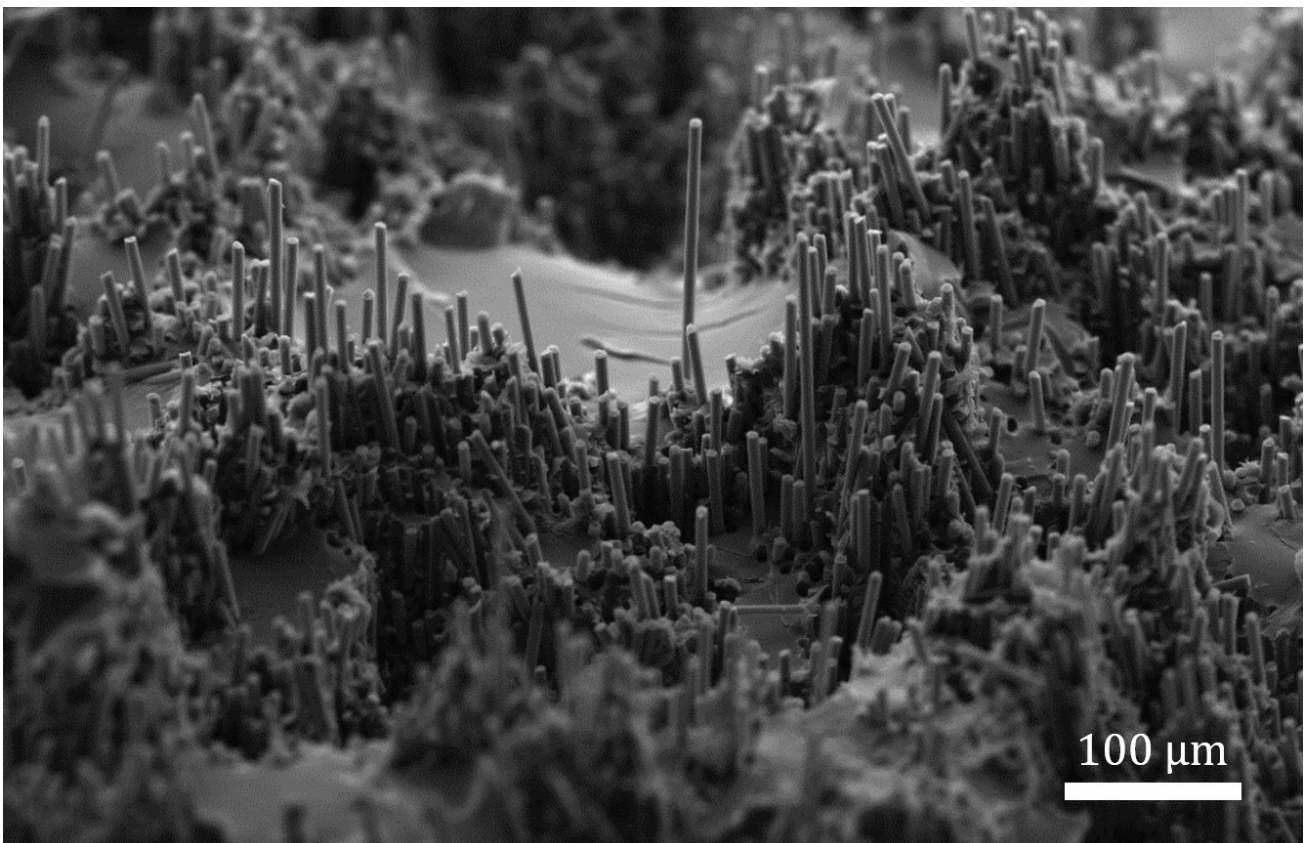


Figure 148. Fracture surface of the composite showing up to 300 μm of fibre pull-out.

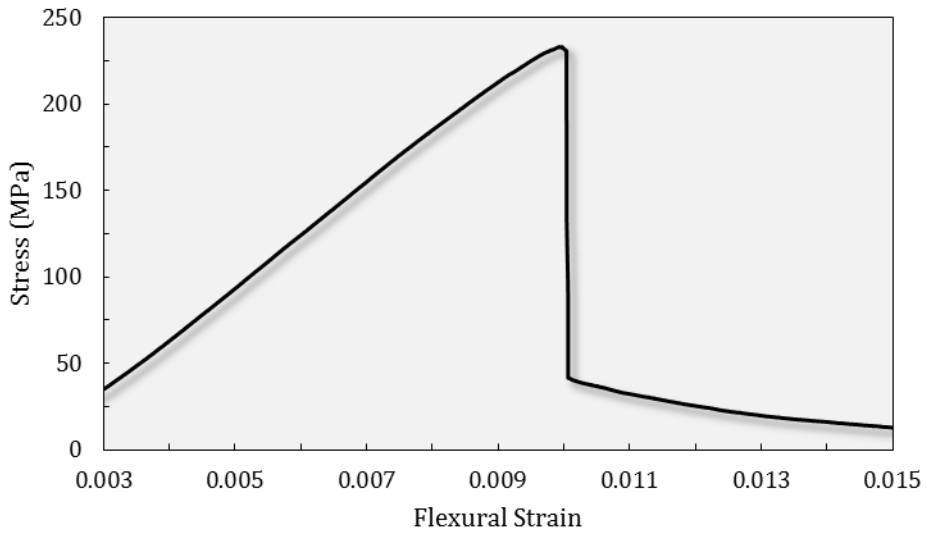


Figure 149. Stress strain curve of a polished PMC part tested in 3 point bending.

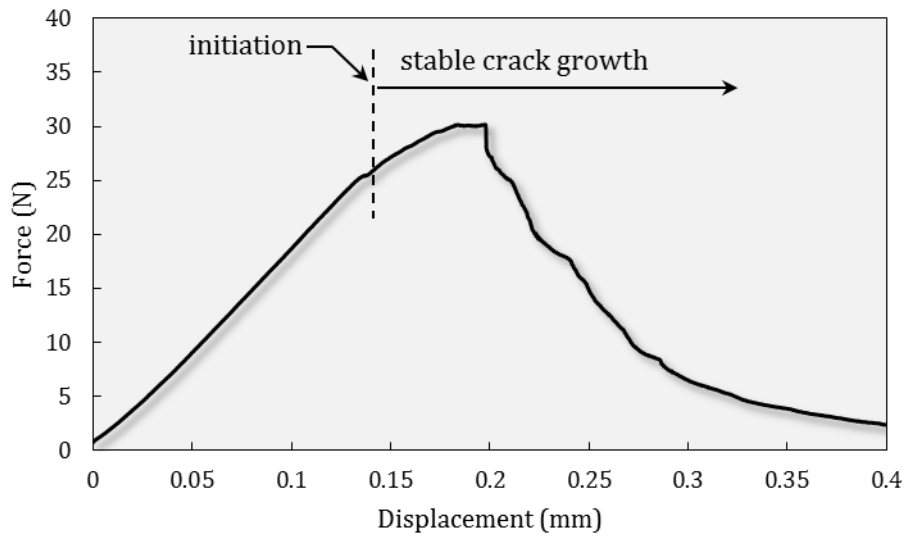


Figure 150. Stress strain curves of a notched PMC part.

Fibre Reinforced Ceramic Matrix Composites (CMC)

Paste Selection and Printing

Contrary to the PMCs produced above where the matrix was infiltrated into a printed fibre pre-form, the CMCs were produced by printing a paste with the carbon fibres mixed in with the matrix material. This was due to the fact that it is more difficult to infiltrate a ceramic matrix into a fibre preform (as was the case with the fibre-epoxy system above). In order to minimise the number of variables, when formulating the pastes the volume fraction of short carbon fibres with respect to the matrix material was maintained at 10 vol% for the SiC based pastes and 20 vol% for the Al₂O₃ based pastes. The overall volume fraction of solids in all the pastes was kept constant at 40 vol% with respect to the hydrogel. A number of different matrices were attempted: Al₂O₃, liquid phase sintered SiC and solid state sintered SiC. Due to the large number of variables in paste formulation, a full rheological analysis of these pastes was not carried out, however from initial inspections all pastes were printable, exhibiting sufficient stiffness and strength without exhibiting excessively high viscosity.

These pastes experienced issues with bubbles, similar to the pastes containing only carbon fibres examined in Chapter III, although not to such a large extent. The same mixing procedure used for the pastes for monolithic ceramics (Chapter IV) was used for these composite pastes, although a longer defoaming time of 30 minutes was required to combat the issue of bubbles. As seen in Figure 151 the paste retained a rough, grainy appearance, even after excessive mixing. This is due to the dimensions of the carbon fibres.

Printing proceeded using the same conditions as those presented in Chapter IV, although the 0.2 mm nozzle was exchanged for a 0.41 mm nozzle in order to produce preliminary parts faster. As with the above pure fibre pastes, no issues with blocking of this nozzle were observed, and strong alignment in the printing direction is apparent, see Figures 152 and 153.

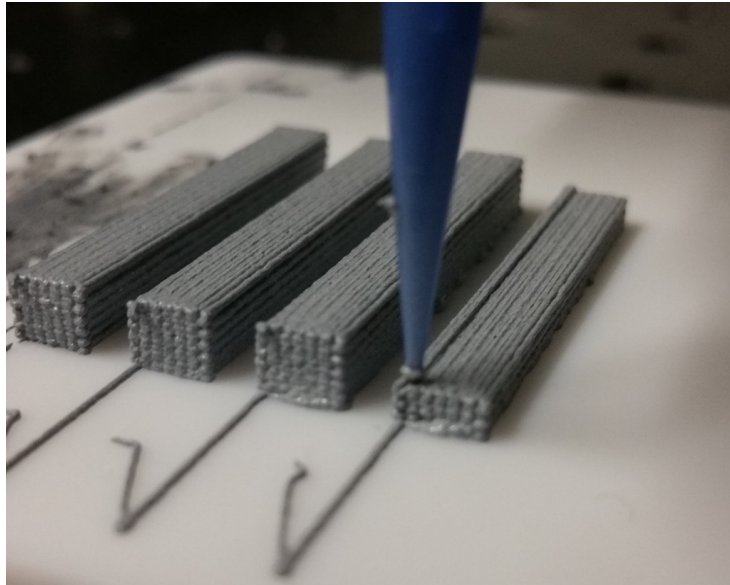


Figure 151. Printing test bars using the $Al_2O_3 - C_f$ paste with a 0.41 mm diameter conical nozzle.

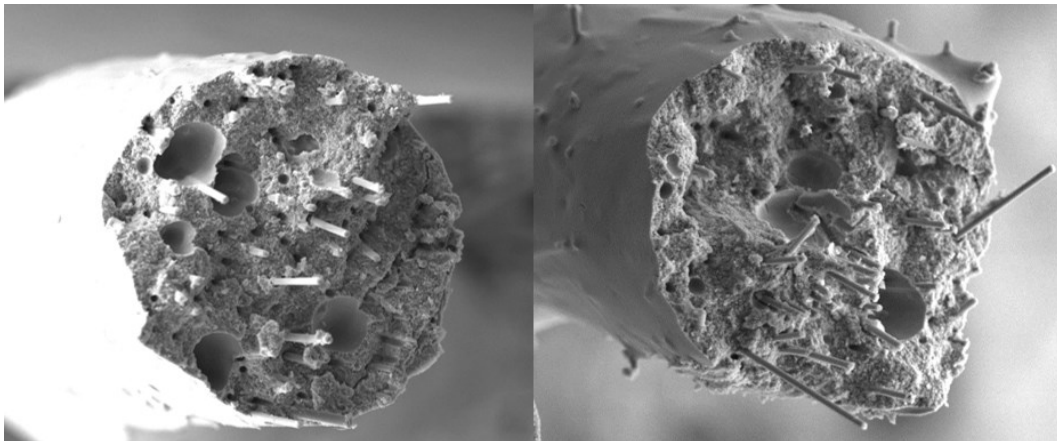


Figure 152. Fracture surface of a single green filament of $Al_2O_3 - C_f$ paste, extruded through conical (left) and 25 mm (right) 0.41mm diameter nozzles, demonstrating superior fibre alignment using the conical nozzle.

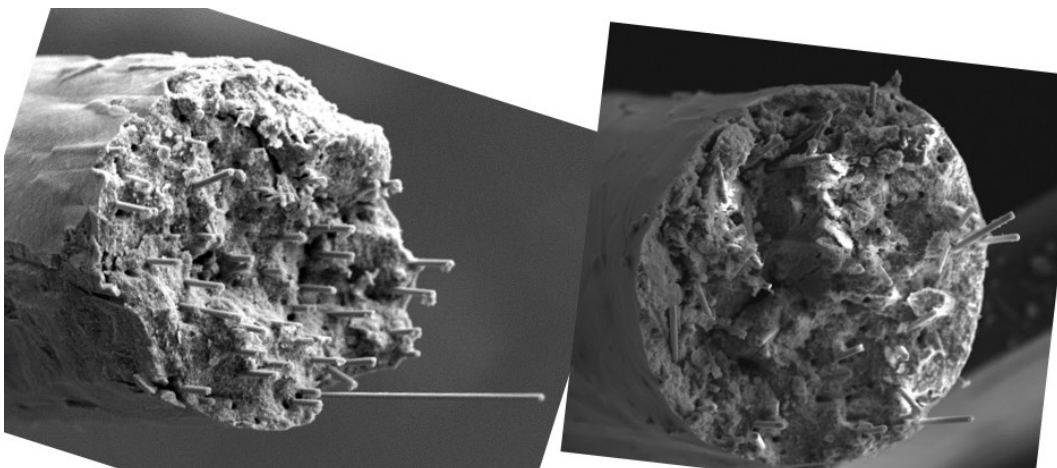


Figure 153. Fracture surface of a single green filament of $SiC - C_f$ paste, extruded through conical (left) and 25 mm (right) 0.41mm diameter nozzles.

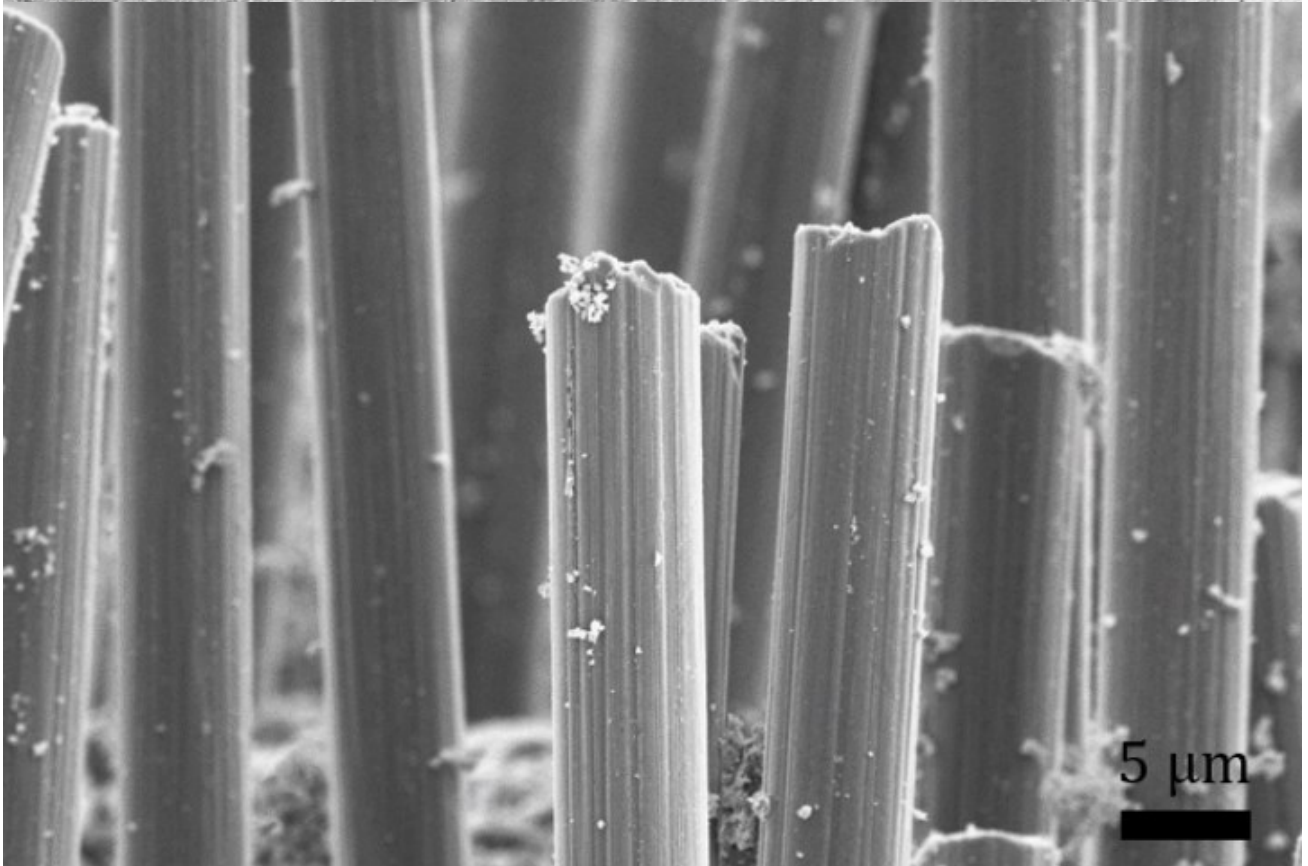
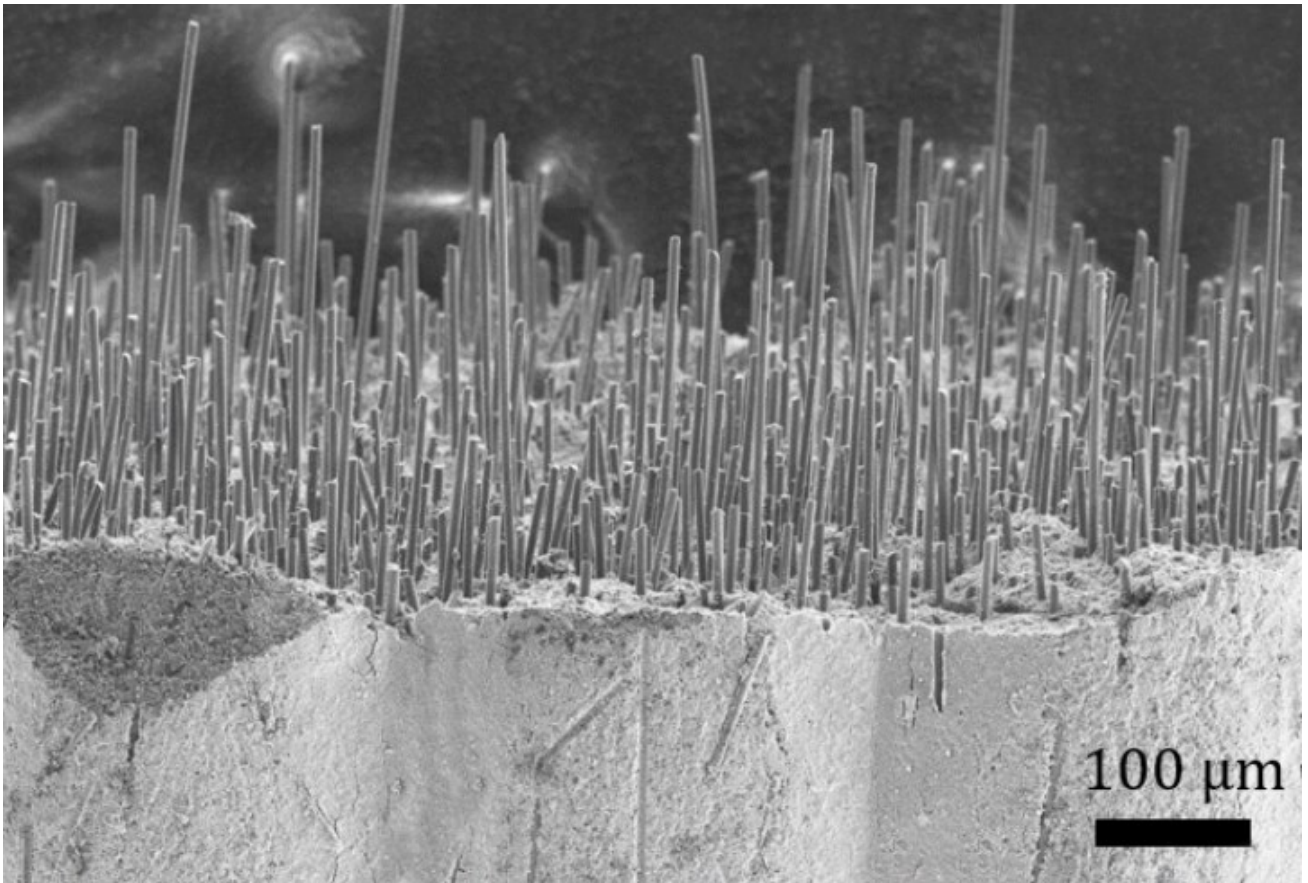


Figure 154. Fracture surface of a green SiC - C_f part.

Post Processing

As with the platelet composites in Chapter V, printed parts were isostatically pressed in order to increase the green density and aid sintering. Burn-out was carried out at 600 °C in an argon atmosphere, in the same manner as the monolithic SiC parts. Sintering was carried out at temperatures dictated by the matrix, see Table 9.

Table 9. Sintering conditions for the different matrices.

Matrix	Temperature (°C)	Time (hr)
Al ₂ O ₃	1550	1
SiC + Al ₂ O ₃ (6 wt%) + Y ₂ O ₃ (4 wt%)	2000	1
SiC + B ₄ C (0.1 - 60 wt%)	2150-2100	0.5-1

Sintering was found to be the crucial step in fabricating these CMCs. The Al₂O₃ - C_f samples were sintered at 1550 °C in Ar. This resulted in parts with a density of 2.99 gcm⁻³, which is 85% of theoretical density determined from the rule of mixtures (3.52 gcm⁻³). This is in the range of values that are obtained for CMCs produced by CVI,[174] which is generally accepted for certain applications. However, when examining the microstructure of this CMC, extensive cracking is revealed, as shown in Figure 157. This is most likely due to the thermal expansion mismatch between the fibres and the matrix. Polycrystalline Al₂O₃ has a thermal expansion coefficient of $\sim 8 \times 10^{-6} \text{ K}^{-1}$,[132] whereas carbon fibres typically have a thermal expansion coefficient of $-0.5 \times 10^{-6} \text{ K}^{-1}$ parallel to the fibre axis.[175] Thus, following sintering the part cools by $\sim 1500 \text{ K}$, and the matrix attempts to shrink considerably while the fibres attempt to expand. The interaction between the two puts the fibres under compressive stress, and the matrix under tensile stress. It is this tensile stress that may cause the cracking. This form of cracking has been seen with other material combinations in the literature.[176] Additionally, the formation of Al₃C₄ is likely at temperatures $>1400 \text{ °C}$,[177] which is an undesirable compound due to its reactivity and poor mechanical properties. These issues, combined with the fact that this material combination is not widely used for applications to the author's knowledge, led to the decision to abandon the Al₂O₃ - C_f system.

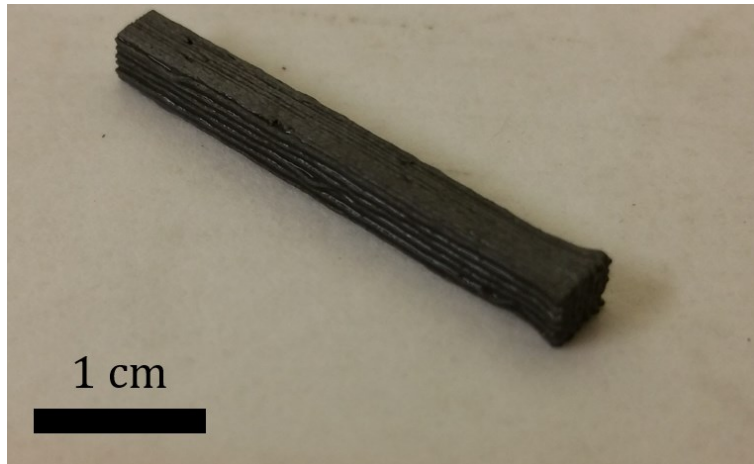


Figure 155. An $Al_2O_3 - C_f$ test bar after burn-out and sintering. The black colour is from residual carbon from the Pluronic.

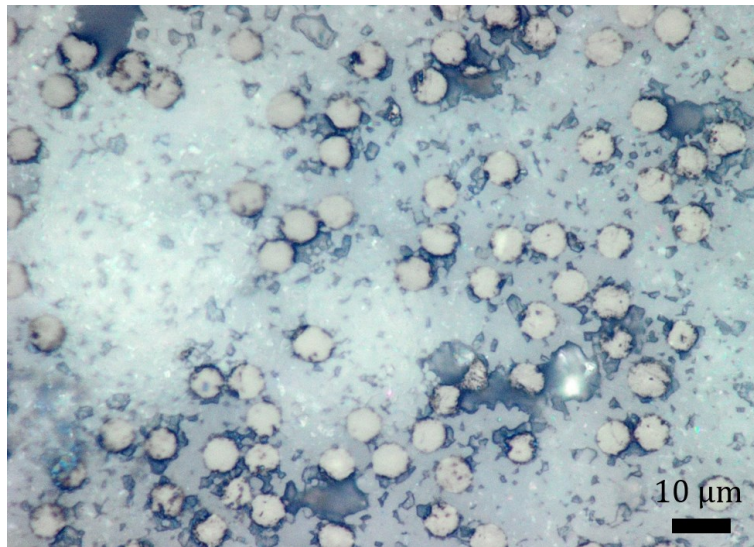


Figure 156. Optical micrograph of a polished cross section of the $Al_2O_3 - C_f$ CMC, showing reasonable densification of the matrix.

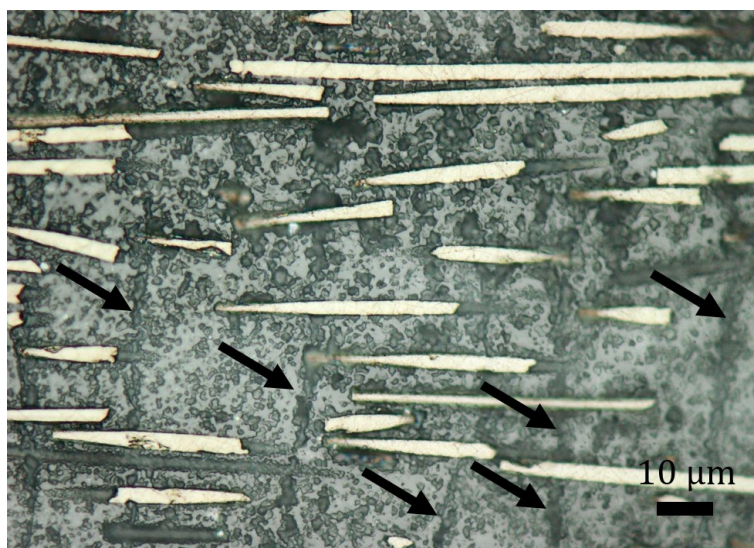


Figure 157. Optical micrograph of a polished section perpendicular to the fibres of the $Al_2O_3 - C_f$ CMC, showing cracking perpendicular to the fibres.

Unlike the $\text{Al}_2\text{O}_3 - \text{C}_f$ CMCs, $\text{SiC} - \text{C}_f$ is a widely studied CMC.[178–180] One reason for this is that the thermal expansion mismatch between SiC and C_f is lower, as SiC has a thermal expansion coefficient of $\sim 4 \times 10^{-6} \text{ K}^{-1}$, [176] roughly half that of Al_2O_3 .

Initially, the same liquid phase sintered SiC as seen in Chapter IV was formulated to include the carbon fibres. Following burn-out at 600°C under argon and sintering, a composite of 94% theoretical density was obtained, which appeared to be free of any large cracks. However, upon closer inspection via SEM, the process had resulted in the consumption of the fibres, as seen in Figure 158. One possible explanation is that the fibres react with the $\text{Al}_2\text{O}_3\text{-Y}_2\text{O}_3$ liquid, forming $\text{Al}_3\text{C}_4 + \text{CO}_2$, both of which are gaseous at the sintering temperature. The fact that the fibres appear pristine in the $\text{Al}_2\text{O}_3 - \text{C}_f$ samples suggests that this reaction would only be occurring at temperatures above 1550°C .

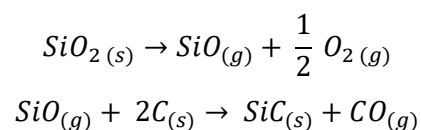
Next, the matrix was switched for a solid state sintering system, $\text{SiC-B}_4\text{C}$, and the sintering conditions were adjusted such that they were appropriate for this material.[181] The resulting CMCs again showed good densification, and the fibres appeared more intact than previous attempts. However closer inspection revealed matrix grains growing into the fibre and an unusual internal structure of the fibre, resembling a layered material. For comparison, a pristine fibre is presented in Figure 160. Thus, the sintering temperature and time was lowered to 2100°C and 0.5 hours. This appeared to reduce the issue of grain growth into the fibres while maintaining acceptable densification of the matrix, but the unusual internal structure of the fibre was still present, and no substantial pull-out of the fibres was observed. It was postulated that the SiO_2 and B_2O_3 layers present on the surface of the powders were melting and reacting with the fibres at the sintering temperature, therefore the parts were held at 1600°C for 3 hours in order to evaporate these oxides before proceeding to higher temperatures. Parts which were only held at 1600°C and not sintered showed good fibre integrity, however parts that were sintered following this hold did not differ from previous parts – the fibres still showed the unusual internal structure.

Following these data it was apparent that the damage was coming from contact with the matrix at elevated temperatures. One explanation for the unusual internal structure forming in the fibres is that the sintering process is causing them to convert from amorphous carbon into graphite. In order to test this hypothesis Raman spectroscopy was performed on fracture surfaces of green bodies and sintered bodies, and spectra were obtained from the fibres in the microstructure. The resulting spectra are plotted in Figure 161, and show a clear increase in the G peak with respect to the D peak. This indicates an increase in the graphitic nature of the fibres.[88] Amorphous carbon fibres can typically withstand very high temperatures without graphitisation due to their strong covalent bonding. We therefore propose that their conversion to graphite is catalysed by the matrix, specifically the B_4C . This effect has

been reported in the literature, and is attributed to the carbon dissolving in the B_4C (which can take on a wide range of carbon compositions), and isothermally re-precipitating as graphite via a complex mechanism.[182] In order to prevent this, we have attempted to coat the fibres in SiC to provide a diffusion barrier. To achieve this, a procedure developed for converting C foams into SiC[183] was repurposed in order to coat the fibres with a layer of SiC. This resulted in a thin, rough coating of SiC on the fibre surface, approximately 150 nm thick, as shown in Figure 162. However when these coated fibres were used to produce CMCs, not only was the graphitisation issue still present, but the fibres appeared even more integrated into the matrix, possibly because the SiC coating allowed for a more commensurate interface with the matrix (Figure 159). The fact that graphitisation proceeded nonetheless indicates that either the coating is not uniform and complete, or that the boron carbide was able to penetrate the coating, potentially via the grain boundaries, and catalyse the graphitisation of the fibres.

As the coating method failed, attempts were made to slow down the catalytic graphitisation by reducing the fraction of boron carbide in the matrix down to as low as 0.1 wt%. Even at these very low concentrations, the fibres were still observed to graphitise following sintering.

In order to verify that the boron carbide was responsible for this issue, a CMC was produced with a matrix consisting entirely of SiC. In this case fracture surfaces indicate that fibres retain their amorphous character, however, the matrix material predictably did not sinter. This confirms that the boron carbide is responsible for the graphitisation. Another notable observation from these samples is the presence of a coating on the surface of the fibres, see Figure 159. It is possible that this is a SiC coating, formed from reacting with oxides that have evaporated from the surface of the SiC powder, according to the reaction below:



Lastly, it is also clear for this sample that the fibres also have a shrinkage mismatch with the matrix in their radial direction, evidenced by a gap opening up between the fibre's circumference and the matrix. This may be due to either the thermal expansion mismatch, or the fact that the matrix shrinks during sintering while the fibres do not.

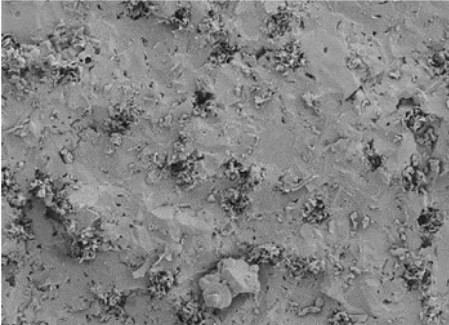
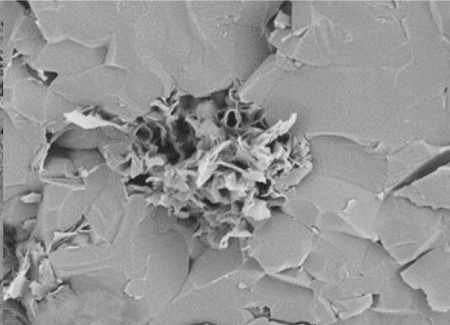
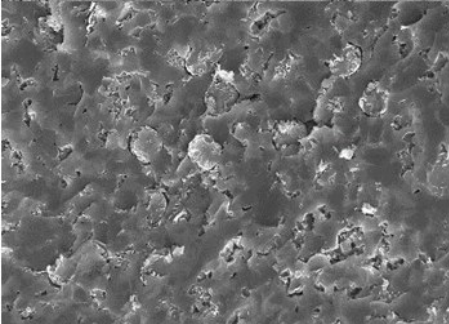
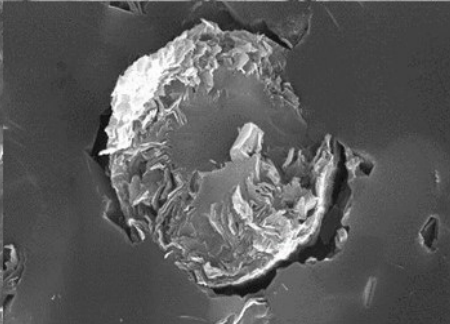
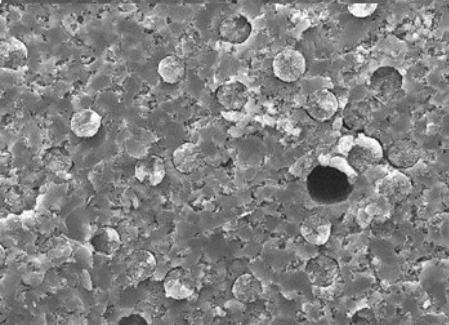
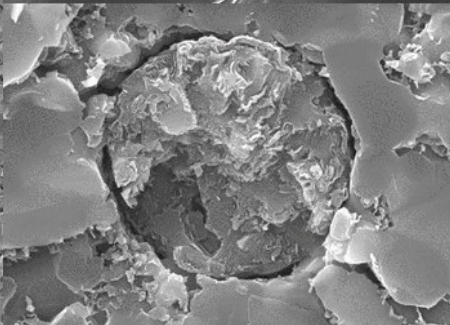
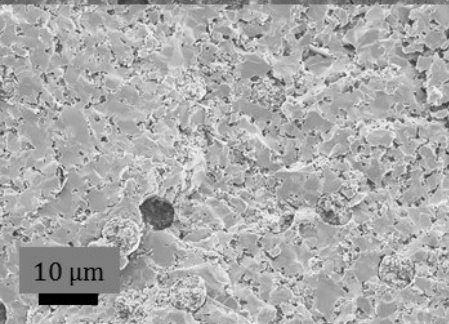
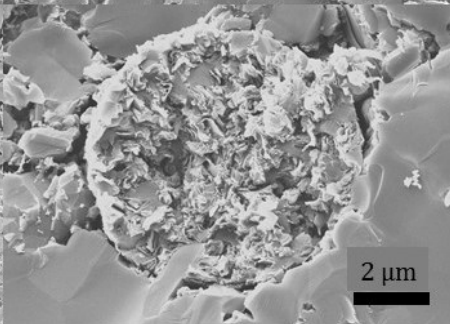
		Matrix Composition	Sintering Conditions
		90w% SiC 6wt% Al ₂ O ₃ 4 wt% Y ₂ O ₃	2000°C 1 hr
		40 wt% SiC 60 wt% B ₄ C	2150°C 1 hr
		40 wt% SiC 60 wt% B ₄ C	2100°C 0.5 hr
		40 wt% SiC 60 wt% B ₄ C	1600°C 3 hr 2100°C 0.5 hr

Figure 158. Fracture surfaces of various matrix compositions and sintering conditions attempted with the aim of preventing fibre degradation.

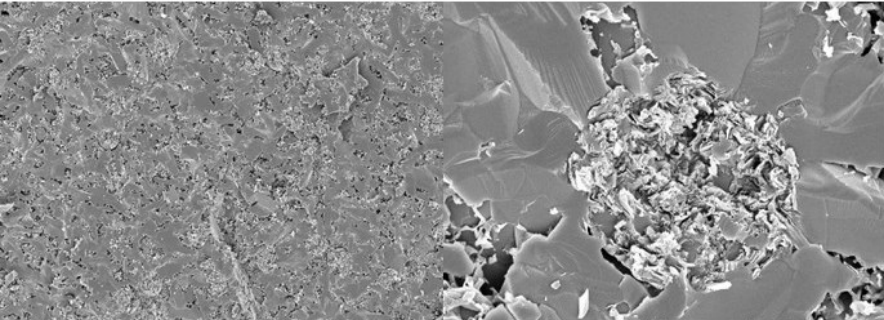
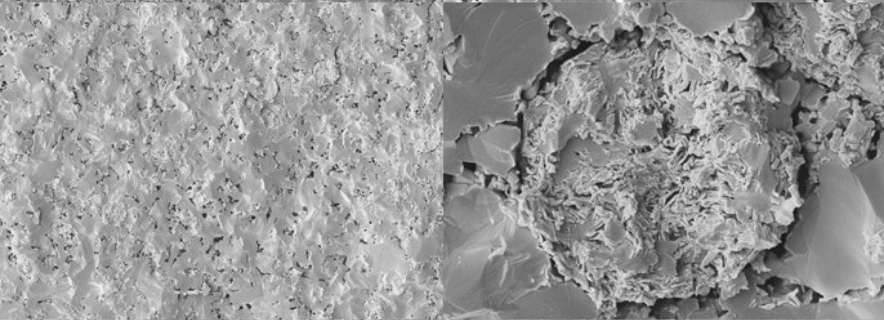
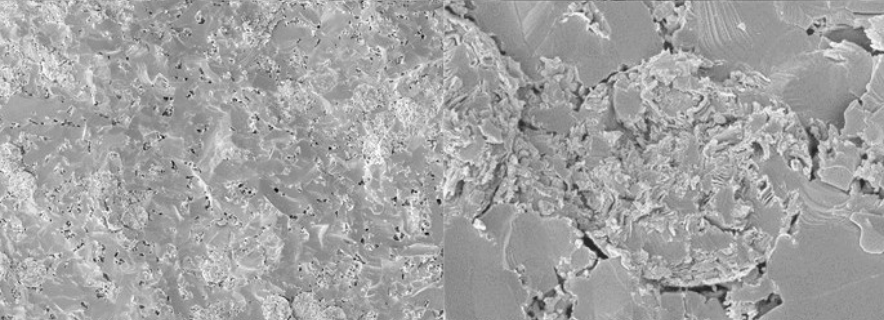
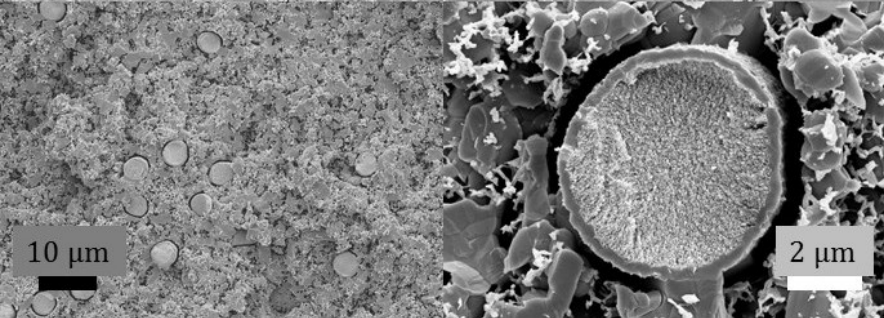
	Matrix Composition	Sintering Conditions
	95 wt% SiC 5 wt% B ₄ C Coated Fibres	2100°C 0.5 hr
	98 wt% SiC 2 wt% B ₄ C	2100°C 0.5 hr
	99.9 wt% SiC 0.1 wt% B ₄ C	2100°C 0.5 hr
	100 wt% SiC	2100°C 0.5 hr

Figure 159. Fracture surfaces of various matrix compositions and sintering conditions attempted with the aim of preventing fibre degradation.

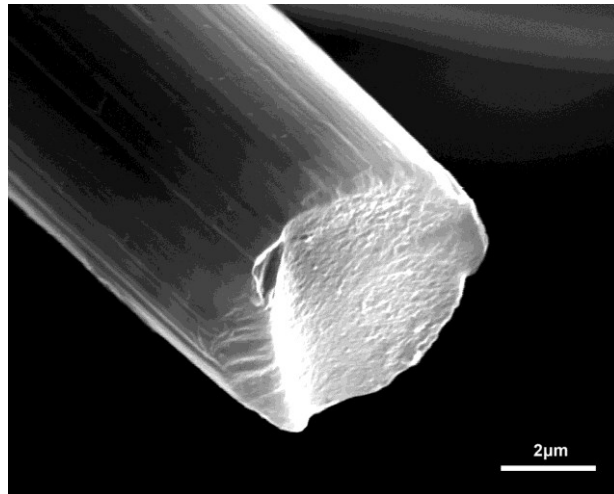


Figure 160. SEM image of a fracture surface of a pristine fibre.

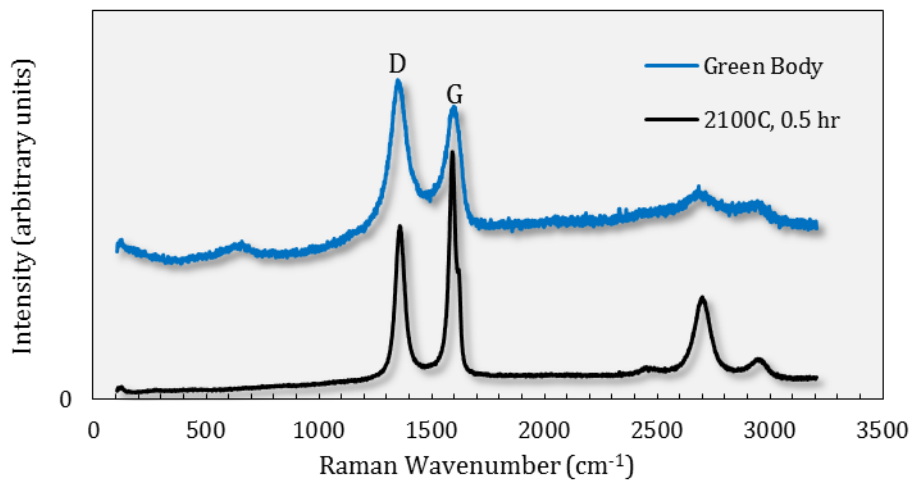


Figure 161. Raman spectroscopy of a fibre from the green body (pristine) and a fibre following sintering at 2100 C in a 2 wt% B₄C matrix, demonstrating graphitisation, manifested in a relative increase in the G peak with respect to the D peak.

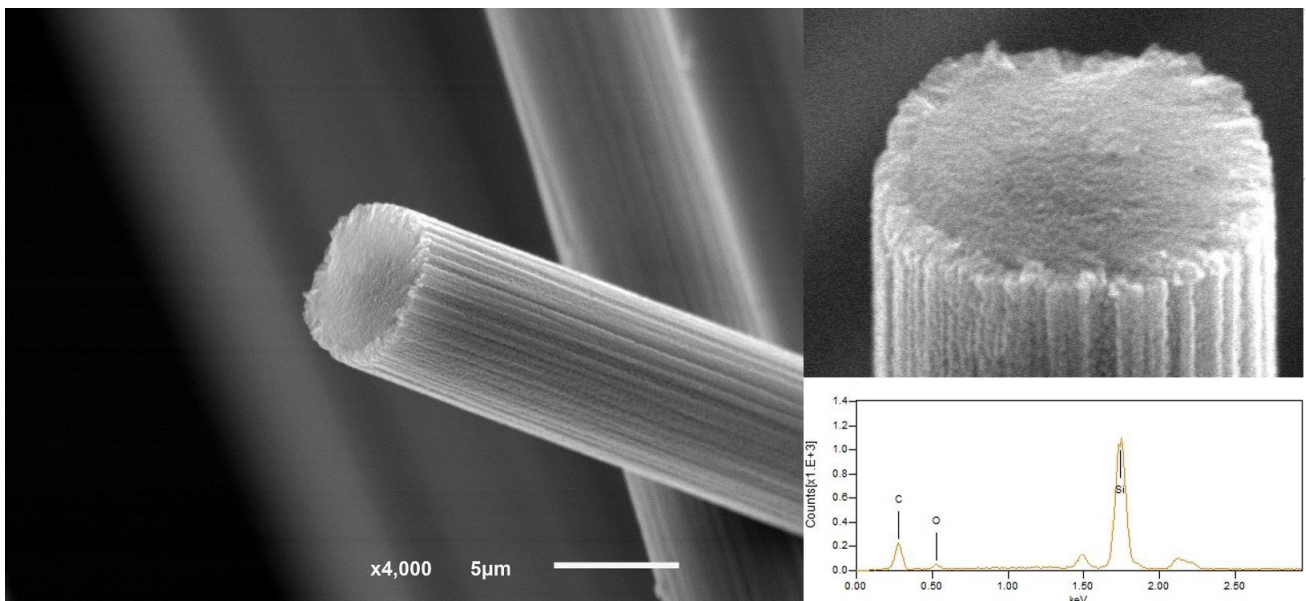


Figure 162. SEM of the fracture surface of a fibre following coating with a layer of SiC. EDS of the fibre confirmed the presence of Si (evidence for the presence of SiC) and O (evidence for the presence of SiO₂). The small peaks to the left and right of the Si peak are from the Au coating used to increase the sample's conductivity during SEM.

General Discussion & Future Work

Fibre Reinforced Polymer Matrix Composites

We have shown in this work that it is possible to use robocasting to produce highly aligned short carbon fibre PMCs with attractive mechanical properties. However, this process presented some issues with fibre distribution throughout the matrix – samples exhibited many fibre free regions. It is not clear at what stage in the process the fibre free regions appear in the PMC's microstructure, although two explanations are possible: either they form in the paste, clustering together leaving fibre poor areas, or they form during infiltration due to trapped gas expanding during evacuation, leaving a gap which is filled with epoxy. Whatever the cause, removing them would clearly improve the mechanical performance of this material as it would result in the material possessing a higher volume fraction of the reinforcing phase.

Figure 163 shows a basic schematic of a fibre in a matrix experiencing stress parallel to the fibre orientation. The critical fibre length, L_c , is where the fibre is long enough to allow the fibre-matrix interface sufficient area to transfer just enough load to the fibre to cause failure of the fibre. Thus a simple balance of forces can be constructed;

$$\frac{2\pi r L \tau}{2} = \sigma \pi r^2 \quad (6.1)$$

where r is the fibre radius, τ is the shear strength of the fibre-matrix interface, and σ is the tensile strength of the fibre. Rearranging, this becomes:

$$L_c = \frac{\sigma r}{\tau} \quad (6.2)$$

σ is given as 3150 MPa from the manufacturer of the fibres,[184] and τ has been measured by fibre push-out to be 44 MPa for the carbon-epoxy system,[185] thus L_c for this system is 251 μm . The average length of the fibres is reported as 100 μm by the manufacturer,[184] thus most fibres will experience pull-out, rather than fracture, which is in line with the observations presented in this chapter.

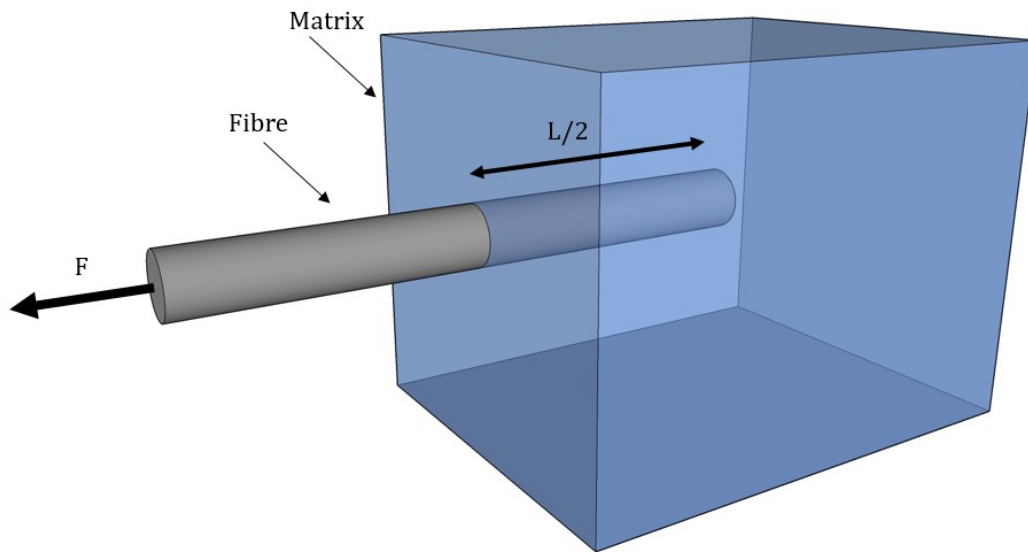


Figure 163. Schematic showing fibre pull-out from the matrix.

It is clear that extensive pull-out and crack deflection occur during fracture of these composites, whether they are notched or not. These are the two most prominent toughening mechanisms known to occur in this class of composites. The fact that the crack in the notched samples can grow with such stability implies that this material possesses R-curve behaviour (given the inherent instability of 3 point bending), as is expected from such fibre reinforced materials. The measured strength and K_{IC} of this composite are reasonably low when compared to the highly optimised, autoclave cured, continuous fibre reinforced epoxy composites produced by industry (which can reach strengths of 1 - 2 GPa and $K_{IC} \gg 10 \text{ MPa}\sqrt{\text{m}}$).[88] This was anticipated, as short fibre composites rarely come close to competing with the properties of equivalent continuous fibre composites. Despite this, our PMC still possesses higher strength than continuous carbon fibre reinforced epoxy produced by additive manufacturing.[102] The printed PMC compares very favourably to other short fibre reinforced epoxy composites, as outlined in Table 10, and is among the strongest short fibre reinforced epoxy reported in the literature. Additionally, the procedure allows for a high degree of control over the orientation of the fibres. All of the parts for this chapter were printed with the fibres oriented in one direction, however it is possible for the raster pattern to be edited by the user, allowing the fibre orientation to be changed from layer to layer, or even within a single layer.

Table 10. Comparison of short carbon fibre-epoxy composites from the literature. * Indicates that these are the highest reported values in the corresponding work. ** Indicates significantly longer fibres were used.

Material	Strength (MPa)	K_{1c} (MPa \sqrt{m})	Fibre Content (vol%)
This work	211	3.5	20
Compton 2014 [100]	75	-	17.4
Zhang 2004* [171]	112	-	15
Zhang 2007* [186]	108	-	15
Dong 2014* [187]	130	0.9	3
Tekinalp 2014* [104]	70	-	40
Hitchen 1994** [188]	127	5.2	14.4

The promising properties of this PMC can be attributed to the high degree of fibre alignment (imparted upon the fibres by the printing process), the high volume fraction of reinforcing fibres (facilitated by the versatile Pluronic paste), and the fact that the fibre length is reasonably close to the optimal (critical) length, L_c . It is highly likely that the properties of these composites can be greatly improved by eliminating the fibre-free voids in the microstructure (hence raising the volume fraction of fibres in the part), and by further tuning the interfacial strength and fibre length such that $L = L_c$. From a practical standpoint, the strength of the brown bodies (the fibre preform following burn-out) needs to be improved. This would allow larger, more complex parts to be infiltrated without causing part damage or misalignment of the fibres.

Fibre Reinforced Ceramic Matrix Composites

Overall, the delicacy of the carbon fibres themselves caused the failure of the attempts to produce a CMC via robocasting, despite multiple approaches and strategies to protect them. This issue is inherent to the very high temperatures required to densify the matrix, where unexpected chemical reactions and physical changes are difficult to avoid, and thermal expansion mismatches give rise to very large stresses upon cooling. This is in line with the literature, where few attempts at producing CMCs using sintering have been reported, and even fewer have succeeded.

That aside, there are a number of potential paths forward. If the high temperatures are avoided, then the unexpected reactions and thermal expansion mismatches can be mitigated significantly. Two approaches which involve lower temperature processing are chemical vapour infiltration and reaction bonded SiC. The former has been successful at creating C-SiC composites, but requires specialised equipment, very long processing times and results in moderately high residual porosity. This process would be applicable to the aligned carbon fibre preforms used to produce PMCs earlier in this chapter. Reaction bonded SiC is processed at lower temperatures (around the melting point of Si), and could be

a promising alternative approach, although this process often inflicts damage to the fibres, and leaves a large volume fraction of residual silicon in the microstructure.[174]

Alternatively, a more advanced fibre coating could be used to mitigate the fibre damage issues, with a focus on providing barriers to diffusion. Furthermore, in order to produce an effective CMC, the fibre-matrix bond would need to be tailored to the length and strength of the fibres, so an effective coating would find utility regardless. This is starkly shown for the CMC consisting of a SiC matrix, which still doesn't show any significant fibre pull-out, despite the lack of densification of the matrix. Lastly, novel sintering techniques such as spark plasma sintering may help to reduce fibre damage, as they greatly reduce the time spent at high temperatures.

Conclusions

Robocasting has been used to produce aligned short carbon fibre preforms which can be infiltrated with an epoxy matrix to give PMCs. The mechanical properties of these composites compare very favourably to analogues produced using other techniques, either by AM or by traditional methods. The printing process results in good fibre alignment in the printing direction, but the fibre distribution is non-uniform, which has yet to be explained. Overall this new procedure appears to offer encouraging progress in the production of CFRP via AM, a material with industrial significance.

On the other hand, such progress was not attained for the CMC materials which have been attempted. While there were some promising results that hint at a route forwards, in reality it is not possible to claim any real success in robocasting of CMCs. We have successfully produced a range of green bodies comprising of highly aligned carbon fibres in ceramic powder matrices, but these never came to fruition. This was principally due to post-processing causing damage to the fibres, and thermal expansion mismatch between the fibres and the chosen matrices.

References

- [1] J.A. Lewis, J.E. Smay, J.N. Stuecker, J. Cesarano, Direct Ink Writing of Three-Dimensional Ceramic Structures, *J. Am. Ceram. Soc.* 89 (2006) 3599–3609. doi:10.1111/j.1551-2916.2006.01382.x.
- [2] D.M. Keicher, J.L. Jelliosn, L.P. Schanwald, J.A. Romero, Towards a Reliable Laser Spray Powder Deposition System Through Process Characterization, *Int. Tech. Conf. Soc. Adv. Mater. Process Eng. Proc.* (1995).
- [3] V.K. Balla, S. Bose, A. Bandyopadhyay, Processing of bulk alumina ceramics using laser engineered net shaping, *Int. J. Appl. Ceram. Technol.* 5 (2008) 234–242.
- [4] K.R. Trubey, S. Culpepper, Y. Maruyama, S.C. Kinnamon, N. Program, F. Collins, Effect of Second Phase Doping on Laser Deposited Al₂O₃ Ceramics, *Am. J. Physiol.* (2006) 568–577.
- [5] F. Niu, D. Wu, G. Ma, J. Wang, M. Guo, B. Zhang, Nanosized microstructure of Al₂O₃-ZrO₂ (Y₂O₃) eutectics fabricated by laser engineered net shaping, *Scr. Mater.* 95 (2015) 39–41.
- [6] S.A. Bernard, V.K. Balla, S. Bose, A. Bandyopadhyay, Direct laser processing of bulk lead zirconate titanate ceramics, *Mater. Sci. Eng. B Solid-State Mater. Adv. Technol.* 172 (2010) 85–88.
- [7] F.Y. Niu, D.J. Wu, S. Yan, G.Y. Ma, B. Zhang, Process Optimization for Suppressing Cracks in Laser Engineered Net Shaping of Al₂O₃ Ceramics, *J. Mater.* (2016) 2–7. doi:10.1007/s11837-016-2191-8.
- [8] C. Deckard, Method and apparatus for producing parts by selective sintering, US4863538 A, 1986.
- [9] T. Childs, M. Berzins, Selective laser sintering of an amorphous polymer—simulations and experiments, *Proc. Inst. Mech. Eng.* 213 (1999) 333–349. doi:10.1243/0954405991516822.
- [10] Y.-A. Song, W. Koenig, Experimental Study of the Basic Process Mechanism for Direct Selective Laser Sintering of Low-Melting Metallic Powder, *CIRP Ann. - Manuf. Technol.* 46 (1997) 127–130. doi:10.1016/S0007-8506(07)60790-2.
- [11] J. Wilkes, Y.-C. Hagedorn, W. Meiners, W. Konrad, Additive manufacturing of ZrO₂ Al₂O₃ ceramic components by selective laser melting, *Rapid Prototyp. J.* 19 (2013) 51–57. doi:10.1108/13552541311292736.
- [12] P. Bertrand, F. Bayle, C. Combe, P. Goeuriot, I. Smurov, Ceramic components manufacturing by selective laser sintering, *Appl. Surf. Sci.* 254 (2007) 989–992. doi:10.1016/j.apsusc.2007.08.085.
- [13] M.C. Leu, E.B. Adamek, T. Huang, G.E. Hilmas, F. Dogan, Freeform Fabrication of Zirconium Diboride Parts using Selective Laser Sintering, in: *Proc. Solid Free. Fabr.*, 2008; pp. 194–205.
- [14] M. Huang, D.Q. Zhang, Z.H. Liu, J. Yang, F. Duan, C.K. Chua, S.C. Lim, M.S. Yip, Comparison study of fabrication of ceramic rotor using various manufacturing methods, *Ceram. Int.* 40 (2014) 12493–12502. doi:10.1016/j.ceramint.2014.04.104.
- [15] J.C. Nelson, N.K. Vail, J.W. Barlow, J.J. Beaman, D.L. Bourell, H.L. Marcuss, Selective Laser Sintering of Polymer-Coated Silicon Carbide Powders, *Ind. Eng. Chem. Res.* 34 (1995) 1641–1651.
- [16] E. Juste, F. Petit, V. Lardot, F. Cambier, Shaping of ceramic parts by selective laser melting of powder bed, *J. Mater. Res.* (2014) 1–9. doi:10.1557/jmr.2014.127.

- [17] M. Griffith, J.W. Halloran, Freeform Fabrication of Ceramics via Stereolithography, *J. Am. Ceram. Soc.* 79 (1996).
- [18] M. Schwentenwein, J. Homa, Additive Manufacturing of Dense Alumina Ceramics, *Int. J. Appl. Ceram. Technol.* 12 (2015) 1–7. doi:10.1111/ijac.12319.
- [19] G. Mitteramskogler, R. Gmeiner, R. Felzmann, S. Gruber, C. Hofstetter, J. Stampfl, J. Ebert, W. Wachter, J. Laubersheimer, Light curing strategies for lithography-based additive manufacturing of customized ceramics, *Addit. Manuf.* 1 (2014) 110–118. doi:10.1016/j.addma.2014.08.003.
- [20] E. Johansson, O. Lidström, J. Johansson, O. Lyckfeldt, E. Adolfsson, Influence of Resin Composition on the Defect Formation in Alumina Manufactured by Stereolithography, *Materials (Basel)*. 10 (2017) 138. doi:10.3390/ma10020138.
- [21] J.R. Tumbleston, D. Shirvanyants, N. Ermoshkin, R. Januszewicz, A.R. Johnson, D. Kelly, K. Chen, R. Pinschmidt, J.P. Rolland, A. Ermoshkin, E.T. Samulski, J.M. Desimone, Continuous liquid interface production of 3d objects, *Science (80-.)*. 347 (2015) 1343–1352.
- [22] M. Feygin, S.S. Pak, Laminated object manufacturing apparatus and method, US5876550 A, 1995.
- [23] Y. Zhang, X. He, J. Han, S. Du, Ceramic green tape extrusion for laminated object manufacturing, *Mater. Lett.* 40 (1999) 275–279. doi:10.1016/S0167-577X(99)00089-0.
- [24] D.A. Klosterman, R.P. Chartoff, N.R. Osborne, G.A. Graves, A. Lightman, G. Han, A. Bezeredi, S. Rodrigues, Development of a curved layer LOM process for monolithic ceramics and ceramic matrix composites, *Rapid Prototyp. J.* 5 (1999) 61–71. doi:10.1108/13552549910267362.
- [25] M.C. Halbig, M. Singh, Additive Manufacturing of SiC Based Ceramics and Ceramic Matrix Composites, (2015).
- [26] S. Liu, F. Ye, L. Liu, Q. Liu, Feasibility of preparing of silicon nitride ceramics components by aqueous tape casting in combination with laminated object manufacturing, *Mater. Des.* 66 (2015) 331–335. doi:10.1016/j.matdes.2014.10.079.
- [27] E.M. Sachs, M. Cima, J. Cornie, Three-Dimensional Printing: Rapid Tooling and Prototypes Directly from a CAD Model, *CIRP Ann. - Manuf. Technol.* 39 (1990) 201–204. doi:10.1016/S0007-8506(07)61035-X.
- [28] E.M. Sachs, M.J. Cima, J. Cornie, Dimensional Printing: Rapid Tooling and Prototypes Directly from CAD Representation, *Solid Free. Fabr. Symp.* (1990) 27–47.
- [29] K. Lu, W.T. Reynolds, 3DP process for fine mesh structure printing, *Powder Technol.* 187 (2008) 11–18. doi:10.1016/j.powtec.2007.12.017.
- [30] H. Seitz, W. Rieder, S. Irsen, B. Leukers, C. Tille, Three-dimensional printing of porous ceramic scaffolds for bone tissue engineering, *J. Biomed. Mater. Res. - Part B Appl. Biomater.* 74 (2005) 782–788. doi:10.1002/jbm.b.30291.
- [31] E. Vorndran, C. Moseke, U. Gbureck, 3D printing of ceramic implants, *MRS Bull.* 40 (2015) 127–136. doi:10.1557/mrs.2015.326.
- [32] C. Sun, X. Tian, L. Wang, Y. Liu, C.M. Wirth, J. Günster, D. Li, Z. Jin, Effect of particle size gradation on the performance of glass-ceramic 3D printing process, *Ceram. Int.* 43 (2017) 578–584.

doi:10.1016/j.ceramint.2016.09.197.

- [33] B. Cappi, E. Özkol, J. Ebert, R. Telle, Direct inkjet printing of Si₃N₄: Characterization of ink, green bodies and microstructure, *J. Eur. Ceram. Soc.* 28 (2008) 2625–2628. doi:10.1016/j.jeurceramsoc.2008.03.004.
- [34] S. Onagoruwa, S. Bose, A. Bandyopadhyay, Fused deposition of ceramics (FDC) and composites, in: *Solid Free. Fabr. Symp.*, 2001: pp. 224–231.
- [35] M.K. Agarwala, V.R. Jamalabad, N.A. Langrana, A. Safari, P.J. Whalen, S.C. Danforth, Structural quality of parts processed by fused deposition, *Rapid Prototyp. J.* 2 (1996) 4–19. doi:10.1108/13552549610732034.
- [36] R. Atisivan, S. Bose, A. Bandyopadhyay, Porous Mullite Preforms via Fused Deposition, *J. Am. Ceram. Soc.* 84 (2001) 221–223. doi:10.1111/j.1151-2916.2001.tb00635.x.
- [37] J. Cesarano, Robocasting: Direct fabrication of ceramics from colloidal suspensions, in: *Proc. Solid Free. Fabr. Symp.*, 1997: pp. 25–36.
- [38] J. Cesarano, B.H. King, H.B. Denham, Recent Developments in Robocasting of Ceramics and Multimaterial Deposition, in: *Proc. Solid Free. Fabr. Symp.*, 1998.
- [39] Q. Li, J.A. Lewis, Nanoparticle Inks for Directed Assembly of Three-Dimensional Periodic Structures, *Adv. Mater.* 15 (2003) 1639–1643. doi:10.1002/adma.200305413.
- [40] M. Xu, J.A. Lewis, Phase Behavior and Rheological Properties of Polyamine-Rich Complexes for Direct-Write Assembly, *Langmuir.* 23 (2007) 12752–12759.
- [41] T. Huang, M.S. Mason, G.E. Hilmas, M.C. Leu, Freeze-form extrusion fabrication of ceramic parts, *Virtual Phys. Prototyp.* 1 (2006) 93–100. doi:10.1080/17452750600649609.
- [42] R. Vaidyanathan, J. Walish, J.L. Lombardi, S. Kasichainula, P. Calvert, K.C. Cooper, The extrusion freeforming of functional ceramic prototypes, *J. Mater.* 52 (2000) 34–37. doi:10.1007/s11837-000-0066-4.
- [43] A. Ghazanfari, W. Li, M.C. Leu, G.E. Hilmas, A novel extrusion-based additive manufacturing process for ceramic parts, *Solid Free. Fabr. Symp.* (2016) 1509–1529.
- [44] C.M. Larson, J.J. Choi, P. a. Gallardo, S.W. Henderson, M.D. Niemack, G. Rajagopalan, R.F. Shepherd, Direct Ink Writing of Silicon Carbide for Microwave Optics, *Adv. Eng. Mater.* (2015) n/a-n/a. doi:10.1002/adem.201500298.
- [45] J.E. Smay, C. Joseph, J.A. Lewis, Colloidal Inks for Directed Assembly of 3-D Periodic Structures, *Langmuir.* 84 (2002) 5429–5437. doi:10.1021/la0257135.
- [46] B.A. Tuttle, J.E. Smay, J. Cesarano, J.A. Voigt, T.W. Scofield, W.R. Olson, J.A. Lewis, Robocast Pb(Zr_{0.95}Ti_{0.05})O₃ Ceramic Monoliths and Composites, *J. Am. Ceram. Soc.* 74 (2001) 872–874.
- [47] J.E. Smay, G.M. Gratson, R.F. Shepherd, J. Cesarano, J.A. Lewis, Directed Colloidal Assembly of 3D Periodic Structures, *Adv. Mater.* 14 (2002) 1279–1283.
- [48] E. Munch, J. Franco, S. Deville, P. Hunger, E. Saiz, A.P. Tomsia, Porous ceramic scaffolds with complex architectures, *JOM.* (2008).
- [49] M. Vadnere, G. Amidon, S. Lindenbaum, J. Haslam, Thermodynamic studies on the gel-sol transition of

some pluronic polyols, *Int. J. Pharm.* 22 (1984) 207–218. doi:10.1016/0378-5173(84)90022-X.

- [50] Q. Fu, E. Saiz, A.P. Tomsia, Direct ink writing of highly porous and strong glass scaffolds for load-bearing bone defects repair and regeneration., *Acta Biomater.* 7 (2011) 3547–54. doi:10.1016/j.actbio.2011.06.030.
- [51] W.H. Herschel, R. Bulkley, Konsistenzmessungen von Gummi-Benzollosungen, *Kolloid-Zeitschrift.* 39 (1926) 291–300. doi:10.1007/BF01432034.
- [52] D. Therriault, S.R. White, J.A. Lewis, Rheological behavior of fugitive organic inks for direct-write assembly, *Appl. Rheol.* 17 (2007) 1–8.
- [53] L. Bergström, Shear thinning and shear thickening of concentrated ceramic suspensions, *Colloids Surfaces A Physicochem. Eng. Asp.* 133 (1998) 151–155. doi:10.1016/S0927-7757(97)00133-7.
- [54] S.M. Peker, S.S. Helvacı, *Solid-Liquid Two Phase Flow*, Elsevier, 2008.
- [55] J. Cesarano III, A review of robocasting technology, *Solid Free. Addit. Fabr. a Mater.* 542 (1999) 133–139. doi:10.1557/PROC-542-133.
- [56] E.B. Duoss, M. Twardowski, J.A. Lewis, Sol-Gel Inks for Direct-Write Assembly of Functional Oxides, *Adv. Mater.* 19 (2007) 3485–3489. doi:10.1002/adma.200701372.
- [57] A.M. Barki, L. Bocquet, A.J. Stevenson, Linking rheology and printability for dense and strong ceramics by Direct Ink Writing, *Sci. Rep.* 7 (2017). doi:10.1038/s41598-017-06115-0.
- [58] C. Minas, D. Carnelli, E. Tervoort, A. Studart, 3D Printing of Emulsions and Foams into Hierarchical Porous Ceramics, *Adv. Mater.* (2016). doi:10.1002/adma.201603390.
- [59] J.T. Muth, P.G. Dixon, L. Woish, L.J. Gibson, J.A. Lewis, Architected cellular ceramics with tailored stiffness via direct foam writing, *Proc. Natl. Acad. Sci.* (2017) 201616769. doi:10.1073/pnas.1616769114.
- [60] Y.-W. Moon, I.-J. Choi, Y.-H. Koh, H.-E. Kim, Macroporous alumina scaffolds consisting of highly microporous hollow filaments using three-dimensional ceramic/camphene-based co-extrusion, *J. Eur. Ceram. Soc.* (2015). doi:10.1016/j.jeurceramsoc.2015.08.017.
- [61] T. Schlordt, S. Schwanke, F. Keppner, T. Fey, N. Travitzky, P. Greil, Robocasting of alumina hollow filament lattice structures, *J. Eur. Ceram. Soc.* 33 (2013) 3243–3248. doi:10.1016/j.jeurceramsoc.2013.06.001.
- [62] Y. Luo, D. Zhai, Z. Huan, H. Zhu, L. Xia, J. Chang, C. Wu, Three-Dimensional Printing of Hollow-Struts-Packed Bioceramic Scaffolds for Bone Regeneration, *ACS Appl. Mater. Interfaces.* 7 (2015) 24377–24383. doi:10.1021/acsami.5b08911.
- [63] R.B. Rao, K.L. Krafcik, A.M. Morales, J.A. Lewis, Microfabricated Deposition Nozzles for Direct-Write Assembly of Three-Dimensional Periodic Structures, *Adv. Mater.* 17 (2005) 289–293. doi:10.1002/adma.200400514.
- [64] A. Zocca, P. Colombo, C.M. Gomes, J. Günster, Additive Manufacturing of Ceramics: Issues, Potentialities, and Opportunities, *J. Am. Ceram. Soc.* 98 (2015) 1983–2001. doi:10.1111/jace.13700.
- [65] S. Zhao, J. Zhang, M. Zhu, Y. Zhang, Z. Liu, C. Tao, Y. Zhu, C. Zhang, Three-dimensional printed strontium-containing mesoporous bioactive glass scaffolds for repairing rat critical-sized calvarial

defects, *Acta Biomater.* 12 (2015) 270–280. doi:10.1016/j.actbio.2014.10.015.

- [66] M.M. Farag, H. Yun, Effect of gelatin addition on fabrication of magnesium phosphate-based scaffolds prepared by additive manufacturing system, *Mater. Lett.* 132 (2014) 111–115. doi:10.1016/j.matlet.2014.06.055.
- [67] J. Franco, P. Hunger, M.E. Launey, A.P. Tomsia, E. Saiz, Direct write assembly of calcium phosphate scaffolds using a water-based hydrogel, *Acta Biomater.* 6 (2010) 218–28. doi:10.1016/j.actbio.2009.06.031.
- [68] S. Eqtesadi, A. Motealleh, A. Pajares, P. Miranda, Effect of milling media on processing and performance of 13-93 bioactive glass scaffolds fabricated by robocasting, *Ceram. Int.* 41 (2015) 1379–1389. doi:10.1016/j.ceramint.2014.09.071.
- [69] B. Román-Manso, A. De Pablos, M. Belmonte, M.I. Osendi, P. Miranzo, Microstructural designs of spark-plasma sintered silicon carbide ceramic scaffolds, *Boletín La Soc. Española Cerámica Y Vidr.* 53 (2014) 93–100. doi:10.3989/cyv.132014.
- [70] S. Eqtesadi, A. Motealleh, A. Pajares, F. Guiberteau, P. Miranda, Improving mechanical properties of 13 – 93 bioactive glass robocast scaffold by poly (lactic acid) and poly (ϵ -caprolactone) melt infiltration, *J. Non. Cryst. Solids.* (2015). doi:10.1016/j.jnoncrysol.2015.02.025.
- [71] F. Martínez-Vázquez, A. Pajares, F. Guiberteau, P. Miranda, Effect of Polymer Infiltration on the Flexural Behavior of β -Tricalcium Phosphate Robocast Scaffolds, *Materials (Basel).* 7 (2014) 4001–4018. doi:10.3390/ma7054001.
- [72] M. Maas, U. Hess, K. Rezwan, The contribution of rheology for designing hydroxyapatite biomaterials, *Curr. Opin. Colloid Interface Sci.* 19 (2014) 585–593. doi:10.1016/j.cocis.2014.09.002.
- [73] Robocasting Enterprises, www.robocasting.net, (n.d.).
- [74] B. Román-Manso, S.M. Vega-Díaz, A. Morelos-Gómez, M. Terrones, P. Miranzo, M. Belmonte, Aligned carbon nanotube/silicon carbide hybrid materials with high electrical conductivity, superhydrophobicity and superoleophilicity, *Carbon N. Y.* 80 (2014) 120–126. doi:10.1016/j.carbon.2014.08.046.
- [75] C. San Marchi, M. Kouzeli, R.B. Rao, J.A. Lewis, D.C. Dunand, Alumina–aluminum interpenetrating-phase composites with three-dimensional periodic architecture, *Scr. Mater.* 49 (2003) 861–866. doi:10.1016/S1359-6462(03)00441-X.
- [76] H.B. Denham, J. Cesarano, B.H. King, P. Calvert, Mechanical behavior of robocast alumina, in: *Proc. Solid Free. Fabr. Symp., Albuquerque, NM, and Livermore, CA (United States)*, 1998: pp. 589–596. doi:10.2172/291158.
- [77] K.-P. Cai, B. Román-Manso, J.E. Smay, J. Zhou, M.I. Osendi, M. Belmonte, P. Miranzo, Geometrically Complex Silicon Carbide Structures Fabricated by Robocasting, *J. Am. Ceram. Soc.* 95 (2012) 2660–2666. doi:10.1111/j.1551-2916.2012.05276.x.
- [78] M.L. Fisher, M. Colic, M.P. Rao, F.F. Lange, Effect of silica nanoparticle size on the stability of alumina/silica suspensions, *J. Am. Ceram. Soc.* 84 (2001) 713–718. doi:10.1111/j.1151-2916.2001.tb00731.x.

- [79] A. Ghazanfari, W. Li, M.C. Leu, J. Watts, G. Hilmas, Mechanical characterization of parts produced by ceramic on-demand extrusion process, *Int. J. Appl. Ceram. Technol.* (2017) 1–9. doi:10.1111/ijac.12665.
- [80] X. Liu, M.N. Rahaman, G.E. Hilmas, B.S. Bal, Mechanical properties of bioactive glass (13-93) scaffolds fabricated by robotic deposition for structural bone repair, *Acta Biomater.* 9 (2013) 7025–7034. doi:10.1016/j.actbio.2013.02.026.
- [81] J.N. Stuecker, J. Cesarano, D.A. Hirschfeld, Control of the viscous behavior of highly concentrated mullite suspensions for robocasting, *J. Mater. Process. Technol.* 142 (2003) 318–325. doi:10.1016/S0924-0136(03)00586-7.
- [82] A. Li, A.S. Thornton, B. Deuser, J.L. Watts, M.C. Leu, G.E. Hilmas, R.G. Landers, Freeze-form Extrusion Fabrication of Functionally Graded Material Composites Using Zirconium Carbide and Tungsten, *Solid Free. Fabr. Symp.* (2012) 467–479.
- [83] D.A. Hirschfeld, J.N. Stuecker, J. Cesarano, G.P. He, Robocasting and Mechanical Testing of Aqueous Silicon Nitride Slurries, (2000) 1–8.
- [84] T. Huang, G.E. Hilmas, W.G. Fahrenholtz, M.C. Leu, Dispersion of zirconium diboride in an aqueous, high-solids paste, *Int. J. Appl. Ceram. Technol.* 4 (2007) 470–479. doi:10.1111/j.1744-7402.2007.02157.x.
- [85] W.J. Costakis, L.M. Rueschhoff, A.I. Diaz-Cano, J.P. Youngblood, R.W. Trice, Additive manufacturing of boron carbide via continuous filament direct ink writing of aqueous ceramic suspensions, *J. Eur. Ceram. Soc.* (2016). doi:10.1016/j.jeurceramsoc.2016.06.002.
- [86] W.E. Frazier, Metal additive manufacturing: A review, *J. Mater. Eng. Perform.* 23 (2014) 1917–1928. doi:10.1007/s11665-014-0958-z.
- [87] R.O. Ritchie, The conflicts between strength and toughness, *Nat. Mater.* 10 (2011) 817–822. doi:10.1038/nmat3115.
- [88] S.J. Park, B.J. Kim, *Carbon fibers and their composites*, CRC Press, 2005. doi:10.1007/978-94-017-9478-7_8.
- [89] J.D. Birchall, D.R. Stanley, M.J. Mockford, G.H. Pigott, P.J. Pinto, Toxicity of silicon carbide whiskers, *J. Mater. Sci. Lett.* 7 (1988) 350–352. doi:10.1007/BF01730738.
- [90] I. Tsao, S.C. Danforth, A.B. Metzner, Rheological Behavior of Injection-Moldable Silicon Powder-Silicon Carbide Whisker Formulations, *J. Am. Ceram. Soc.* 76 (1993) 2977–2984. doi:10.1111/j.1151-2916.1993.tb06598.x.
- [91] M. Belmonte, J.S. Moya, P. Miranzo, Obtention of highly dispersed platelet-reinforced Al203 composites, *J. Mater. Sci.* 29 (1994) 179–183.
- [92] T. Ozben, E. Kilickap, O. Çakir, Investigation of mechanical and machinability properties of SiC particle reinforced Al-MMC, *J. Mater. Process. Technol.* 198 (2008) 220–225. doi:10.1016/j.jmatprotec.2007.06.082.
- [93] C. Kjelgaard, Challenges in composites, *Aircr. Technol.* 1 (2012) 52–57. http://www.gkn.com/aerospace/media/GKN_Aerospace_in_the_media/Challenges-in-composites.pdf.

- [94] N.P. Padture, Advanced structural ceramics in aerospace propulsion, *Nat. Mater.* 15 (2016) 804–809. doi:10.1038/nmat4687.
- [95] G. Marsh, Composites flying high, *Reinf. Plast.* 58 (2014) 14–18. doi:10.1016/S0034-3617(14)70133-X.
- [96] P.D. Mangalgi, Composite materials for aerospace applications, *Bull. Mater. Sci.* 22 (1999) 657–664. doi:10.1007/BF02749982.
- [97] M.L. Young, R.B. Rao, J.D. Almer, D.R. Haeffner, J.A. Lewis, D.C. Dunand, Load partitioning in Al₂O₃–Al composites with three-dimensional periodic architecture, *Acta Mater.* 57 (2009) 2362–2375. doi:10.1016/j.actamat.2009.01.019.
- [98] R. Soundararajan, G. Kuhn, R. Atisivan, S. Bose, A. Bandyopadhyay, Processing of Mullite – Aluminum Composites, *J. Am. Ceram. Soc.* 84 (2001) 509–513.
- [99] K. Subramanian, N.K. Vail, J.W. Barlow, H. Marcus, Selective laser sintering of alumina with polymer binders, *Rapid Prototyp. J.* 1 (1995) 24–35. doi:10.1108/13552549510086844.
- [100] B.G. Compton, J.A. Lewis, 3D-Printing of Lightweight Cellular Composites., *Adv. Mater.* 26 (2014) 5930–5935. doi:10.1002/adma.201401804.
- [101] G. Gozdz, Three dimensional printer with composite filament fabrication, US20150108677 A1, 2014.
- [102] R. Matsuzaki, M. Ueda, M. Namiki, T.-K. Jeong, H. Asahara, K. Horiguchi, T. Nakamura, A. Todoroki, Y. Hirano, Three-dimensional printing of continuous-fiber composites by in-nozzle impregnation., *Sci. Rep.* 6 (2016) 23058. doi:10.1038/srep23058.
- [103] T.M. Llewellyn-Jones, B.W. Drinkwater, R.S. Trask, 3D printed components with ultrasonically arranged microscale structure, *Smart Mater. Struct.* 25 (2016) 02LT01. doi:10.1088/0964-1726/25/2/02LT01.
- [104] H.L. Tekinalp, V. Kunc, G.M. Velez-garcia, C.E. Duty, L.J. Love, A.K. Naskar, C. a Blue, S. Ozcan, Highly oriented carbon fiber–polymer composites via additive manufacturing, *Compos. Sci. Technol.* 105 (2014) 144–150. doi:10.1016/j.compscitech.2014.10.009.
- [105] W.Y. Li, O.T. Sørensen, Texture Formed by Platelet Alignment in Ceramic Platelet Ceramic Matrix Composites, *Textures Microstruct.* 24 (1995) 53–65. doi:10.1155/TSM.24.53.
- [106] T. George, V. Deshpande, H.N.G. Wadley, Hybrid carbon fiber composite lattice truss structures, *Compos. Part A Appl. Sci. Manuf.* 65 (2014) 135–147. doi:10.1016/j.compositesa.2014.06.011.
- [107] L. Bergström, Rheological properties of Al₂O₃–SiC whisker composite suspensions, *J. Mater. Sci.* 31 (1996) 5257–5270. doi:10.1007/BF00355933.
- [108] R. Gadow, Current Status and Future Prospects of CMC Brake Components and Their Manufacturing Technologies, *Ceram. Eng. Sci. Proc.* (2000) 15–30.
- [109] C. Ferraro, E. García-Tuñón, V. G. Rocha, S. Barg, M.D. Fariñas, T.E.G. Álvarez-Arenas, G. Sernicola, F. Giuliani, E. Sáiz, Light and Strong SiC Networks, *Adv. Mater.* (2016) 12. doi:10.1002/adfm.201504051.
- [110] P.C. Giorgia Franchin, Larissa Wah, Direct Ink Writing of Ceramic Matrix Composite structures, *J. Am. Ceram. Soc.* (2017) 1–5. doi:10.1111/ijlh.12426.

- [111] J.H. She, K. Ueno, Densification behavior and mechanical properties of pressureless-sintered silicon carbide ceramics with alumina and yttria additions, *Mater. Chem. Phys.* 59 (1999) 139–142.
- [112] M.C. Leu, L. Tang, B. Deuser, R.G. Landers, G.E. Hilmas, S. Zhang, J. Watts, Freeze-Form Extrusion Fabrication of Composite Structures, *Solid Free. Fabr. Symp.* (2011) 111–124.
- [113] S. Baud, F. Thevenot, A. Pisch, C. Chatillon, High temperature sintering of SiC with oxide additives: I. Analysis in the SiC-Al₂O₃ and SiC-Al₂O₃-Y₂O₃ systems, *J. Eur. Ceram. Soc.* 23 (2003) 1–8. doi:10.1016/S0955-2219(02)00067-5.
- [114] ASTM C1161-13, Standard Test Method for Flexural Strength of Advanced Ceramics at Ambient Temperature, ASTM International, West Conshohocken, PA, 2013, www.astm.org, (n.d.).
- [115] International Association for the Properties of Water and Steam, <http://www.iapws.org/relguide/viscosity.html>, Date Accessed- 25/05/2017. (2008).
- [116] S. Liu, L. Li, Multiple phase transition and scaling law for poly(ethylene oxide)-poly(propylene oxide)-poly(ethylene oxide) triblock copolymer in aqueous solution, *ACS Appl. Mater. Interfaces.* 7 (2015) 2688–2697. doi:10.1021/am507749w.
- [117] D. Korachkin, D.T. Gethin, R.W. Lewis, J.H. Tweed, D.M.M. Guyoncourt, D.T. Gethin, R.W. Lewis, J.H. Tweed, D.M.M. Guyoncourt, D. Korachkin, D.T. Gethin, R.W. Lewis, J.H. Tweed, Measurement of Young's modulus and tensile failure properties of green powder compacts Measurement of Young's modulus and tensile failure properties of green powder compacts, *Powder Metall.* 51 (2008) 150–159. doi:10.1179/174329008X284994.
- [118] T.J. Carneim, D.J. Green, Mechanical Properties of Dry-Pressed Alumina Green Bodies, *J. Am. Ceram. Soc.* 84 (2001) 1405–1410.
- [119] M.J. Edirisinghe, H.M. Shaw, K.L. Tomkins, Flow behaviour of ceramic injection moulding suspensions, *Ceram. Int.* 18 (1992) 193–200. doi:10.1016/0272-8842(92)90095-U.
- [120] I.M. Krieger, T.J. Dougherty, A Mechanism for Non-Newtonian Flow in Suspensions of Rigid Spheres, *J. Rheol. (N. Y. N. Y.)* 3 (1959) 137. doi:10.1122/1.548848.
- [121] F.A.L. Dullien, *Porous media: fluid transport and pore structure*, Academic press, 2012.
- [122] E. Saiz, a. P. Tomsia, R.M. Cannon, Ridging effects on wetting and spreading of liquids on solids, *Acta Mater.* 46 (1998) 2349–2361. doi:10.1016/S1359-6454(98)80016-5.
- [123] J.K. Armstrong, B.Z. Chowdhry, M.J. Snowden, S.A. Leharne, Effect of Sodium Chloride Upon Micellization and Phase Separation Transitions in Aqueous Solutions of Triblock Copolymers: a High-Sensitivity Differential Scanning Calorimetry, *Langmuir.* 14 (1998) 2004–2010. doi:10.1021/la9710839.
- [124] E. García-Tuñón, S. Barg, R. Bell, J.V.M. Weaver, C. Walter, L. Goyos, E. Saiz, Designing smart particles for the assembly of complex macroscopic structures, *Angew. Chem. Int. Ed. Engl.* 52 (2013) 7805–8. doi:10.1002/anie.201301636.
- [125] C. Zhu, T.Y. Han, E.B. Duoss, A.M. Golobic, J.D. Kuntz, C.M. Spadaccini, M.A. Worsley, Highly compressible 3D periodic graphene aerogel microlattices, *Nat. Commun.* 6 (2015) 1–8. doi:10.1038/ncomms7962.

- [126] D. Kokkinis, M. Schaffner, A. Studart, Multimaterial magnetically assisted 3D printing of composite materials, *Nat. Commun.* 6 (2015) 8643. doi:10.1038/ncomms9643.
- [127] Z. Fu, M. Freihart, L. Wahl, T. Fey, P. Greil, N. Travitzky, Micro- and macroscopic design of alumina ceramics by robocasting, *J. Eur. Ceram. Soc.* 37 (2017) 3115–3124. doi:10.1016/j.jeurceramsoc.2017.03.052.
- [128] G. Magnani, L. Beaulardi, L. Pilotti, Properties of liquid phase pressureless sintered silicon carbide obtained without sintering bed, *J. Eur. Ceram. Soc.* 25 (2005) 1619–1627. doi:10.1016/j.jeurceramsoc.2004.05.014.
- [129] P. Miranda, A. Pajares, E. Saiz, A.P. Tomsia, F. Guiberteau, Mechanical properties of calcium phosphate scaffolds fabricated by robocasting, *J. Biomed. Mater. Res. - Part A.* 85 (2008) 218–227. doi:10.1002/jbm.a.31587.
- [130] M. Genet, M. Houmard, S. Eslava, E. Saiz, A.P. Tomsia, A two-scale Weibull approach to the failure of porous ceramic structures made by robocasting: possibilities and limits., *J. Eur. Ceram. Soc.* 33 (2013) 679–688. doi:10.1016/j.jeurceramsoc.2012.11.001.
- [131] R.G. Munro, Material Properties of a Sintered α -SiC, *J. Phys. Chem. Ref. Data.* 26 (1997) 1195–1201. doi:10.1063/1.556000.
- [132] R.G. Munro, Evaluated Material Properties for a Sintered Alpha -Alumina, *J. Am. Ceram. Soc.* 80 (1997) 1919–1928. doi:10.1111/j.1151-2916.1997.tb03074.x.
- [133] B.R. Lawn, A.G. Evans, D.B. Marshall, Elastic/Plastic Indentation Damage in Ceramics: The Median/Radial Crack System, *J. Am. Ceram. Soc.* 63 (1980).
- [134] ASTM, ASTM C1322 – 15- Standard Practice for Fractography and Characterization of Fracture Origins in Advanced Ceramics, (n.d.). doi:10.1520/C1322-15.2.
- [135] ASTM, C1322 – 15- Standard Practice for Fractography and Characterization of Fracture Origins in Advanced Ceramics, (n.d.). doi:10.1520/C1322-15.2.
- [136] T. Huang, M.S. Mason, X. Zhao, G.E. Hilmas, M.C. Leu, Aqueous-based freeze-form extrusion fabrication of alumina components, *Rapid Prototyp. J.* 15 (2009) 88–95. doi:10.1108/13552540910943388.
- [137] S. Maleksaeedi, H. Eng, F.E. Wiria, T.M.H. Ha, Z. He, Property enhancement of 3D-printed alumina ceramics using vacuum infiltration, *J. Mater. Process. Technol.* 214 (2014) 1301–1306. doi:10.1016/j.jmatprotec.2014.01.019.
- [138] Y. Zhang, X. He, S. Du, J. Zhang, Al₂O₃ ceramics preparation by LOM (laminated object manufacturing), *Int. J. Adv. Manuf. Technol.* 17 (2001) 531–534. doi:10.1007/s001700170154.
- [139] Z.H. Liu, J.J. Nolte, J.I. Packard, G.E. Hilmas, F. Dogan, M.C. Leu, Selective Laser Sintering of High-density Alumina Ceramic Parts, *Proc. 35th Int. Matador Conf.* (2007).
- [140] F. Libonati, M.J. Buehler, *Advanced Structural Materials by Bioinspiration*, (2017) 1–19.
- [141] R.O. Ritchie, M.J. Buehler, P. Hansma, Plasticity and toughness in bone, *Phys. Today.* 62 (2009) 41–47. doi:10.1063/1.3156332.
- [142] F. Bouville, E. Maire, S. Meille, B. Van de Moortèle, A.J. Stevenson, S. Deville, Strong, tough and stiff bioinspired ceramics from brittle constituents, *Nat. Mater.* 13 (2014) 508–514.

doi:10.1038/nmat3915.

- [143] J.C. Weaver, G.W. Milliron, A. Miserez, K. Evans-Lutterodt, S. Herrera, I. Gallana, W.J. Mershon, B. Swanson, P. Zavattieri, E. DiMasi, D. Kisailus, The Stomatopod Dactyl Club: A Formidable Damage-Tolerant Biological Hammer, *Science* (80-.). 336 (2012) 1275–1280. doi:10.1126/science.1218764.
- [144] H. Le Ferrand, F. Bouville, T.P. Niebel, A. Studart, Magnetically assisted slip casting of bioinspired heterogeneous composites, *Nat. Mater.* 14 (2015). doi:10.1038/nmat4419.
- [145] D.K. Shukla, S. V. Kasisomayajula, V. Parameswaran, Epoxy composites using functionalized alumina platelets as reinforcements, *Compos. Sci. Technol.* 68 (2008) 3055–3063. doi:10.1016/j.compscitech.2008.06.025.
- [146] L.J. Bonderer, A. Studart, L.J. Gauckler, Bioinspired Design and Assembly of Platelet Reinforced Polymer Films, *Science* (80-.). 319 (2008) 1069–1073.
- [147] R.M. Erb, R. Libanori, N. Rothfuchs, A. Studart, Composites Reinforced in Three Dimensions by Using Low Magnetic Fields, *Science* (80-.). 335 (2012) 199–204.
- [148] M. Kotoul, J. Pokluda, P. Šandera, I. Dlouhý, Z. Chlup, A.R. Boccaccini, Toughening effects quantification in glass matrix composite reinforced by alumina platelets, *Acta Mater.* 56 (2008) 2908–2918. doi:10.1016/j.actamat.2008.02.024.
- [149] A. Montagne, S. Pathak, X. Maeder, J. Michler, Plasticity and fracture of sapphire at room temperature: Load-controlled microcompression of four different orientations, *Ceram. Int.* 40 (2014) 2083–2090. doi:10.1016/j.ceramint.2013.07.121.
- [150] B. Bergman, On the Estimation of the Weibull Modulus, *J. Mater. Sci. Lett.* 3 (1984) 689–692. <https://drive.google.com/open?id=0BwDenrliobpFR1pOV2YyS1d1WW8>.
- [151] M.G. Mueller, M. Fornabai, G. Žagar, A. Mortensen, Microscopic strength of silicon particles in an aluminium-silicon alloy, *Acta Mater.* 105 (2016) 165–175. doi:10.1016/j.actamat.2015.12.006.
- [152] J.B. Davis, J. Yang, A.G. Evans, Effects of composite processing on the strength of sapphire fiber-reinforced composites, *Acta Metall. Mater.* 43 (1995) 259–268. doi:10.1016/0956-7151(95)90281-3.
- [153] P. Becher, Fracture-Strength Anisotropy of Sapphire, *J. Am. Ceram. Soc.* 59 (1976) 59–61. doi:10.1111/j.1151-2916.1976.tb09390.x.
- [154] R. Bermejo, P. Supancic, R. Danzer, Influence of measurement uncertainties on the determination of the Weibull distribution, *J. Eur. Ceram. Soc.* 32 (2012) 251–255. doi:10.1016/j.jeurceramsoc.2011.09.008.
- [155] S.M. Wiederhorn, Brittle Fracture and Toughening Mechanisms in Ceramics, *Annu. Rev. Mater. Sci.* 14 (1984) 373–403. doi:10.1146/annurev.ms.14.080184.002105.
- [156] M. Yoshinori, Y. Wang, Fracture toughness of single crystal alumina in air and a simulated body environment, *J. Biomed. Mater. Res. - Part A.* 28 (1994) 813–817. <http://onlinelibrary.wiley.com/doi/10.1002/jbm.820280708/abstract>.
- [157] N. Alford, J. Birchall, K. Kendall, High Strength Ceramics through Colloidal Control to Remove Defects, *Nature.* 330 (1987) 51–53.
- [158] E.A.D. White, J.D.C. Wood, The growth of highly perfect alumina platelets and other oxides by solvent

vapour transport, *J. Mater. Sci.* 9 (1974) 1999–2006. doi:10.1007/BF00540549.

- [159] M.Y. He, A.G. Evans, Crack Deflection at an Interface between Dissimilar Elastic Materials: Role of Residual Stresses, *Int. J. Solids Struct.* 31 (1994) 3443–3455. doi:10.1016/0020-7683(94)90025-6.
- [160] P. Gurjyants, M. Starostin, V.N. Kurlov, F. Théodore, J. Delepine, Effect of growth conditions on the strength of shaped sapphire, *J. Cryst. Growth.* 198–199 (1999) 227–231. doi:10.1016/S0022-0248(98)01131-2.
- [161] C.A. Klein, Flexural strength of sapphire: Weibull statistical analysis of stressed area, surface coating, and polishing procedure effects, *J. Appl. Phys.* 96 (2004) 3172–3179. doi:10.1063/1.1782272.
- [162] N. Jaya, M. Alam, Small-scale mechanical testing of materials, *Curr. Sci.* 105 (2013) 1073–1099. <http://eprints.iisc.ernet.in/47969/>.
- [163] G. Žagar, V. Pejchal, M.G. Mueller, A. Rossoll, M. Cantoni, A. Mortensen, The local strength of microscopic alumina reinforcements, *Acta Mater.* 100 (2015) 215–223. doi:10.1016/j.actamat.2015.08.026.
- [164] D. Jang, L.R. Meza, F. Greer, J.R. Greer, Fabrication and deformation of three-dimensional hollow ceramic nanostructures, *Nat. Mater. Lett.* 12 (2013) 893–8. doi:10.1038/nmat3738.
- [165] B. Lawn, *Fracture of Brittle Solids- Second Edition*, Cambridge University Press, 1993.
- [166] J.C. Weaver, G.W. Milliron, a. Miserez, K. Evans-Lutterodt, S. Herrera, I. Gallana, W.J. Mershon, B. Swanson, P. Zavattieri, E. DiMasi, D. Kisailus, The Stomatopod Dactyl Club: A Formidable Damage-Tolerant Biological Hammer, *Science* (80-.). 336 (2012) 1275–1280. doi:10.1126/science.1218764.
- [167] N.P. Mitchell, V. Koning, V. Vitelli, W.T.M. Irvine, Fracture in sheets draped on curved surfaces, *Nat. Mater.* 16 (2017) 89–93. <http://arxiv.org/abs/1512.04061v5><http://www.nature.com/doi/10.1038/nmat4733>.
- [168] W.J. Clegg, K. Kendall, N. Alford, T.W. Button, J.D. Birchall, A simple way to make tough ceramics, *Nature.* 347 (1990) 455–457. doi:10.1038/347455a0.
- [169] E. Munch, M. Launey, D. Alsem, E. Saiz, A. Tomsia, R. Ritchie, Tough, Bio-Inspired Hybrid Materials, *Science* (80-.). 322 (2008) 1516–1520. doi:10.1126/science.1164865.
- [170] O.T. Picot, V.G. Rocha, C. Ferraro, N. Ni, E. D’Elia, S. Meille, J. Chevalier, T. Saunders, T. Peijs, M.J. Reece, E. Saiz, Using graphene networks to build bioinspired self-monitoring ceramics, *Nat. Commun.* 8 (2017) 14425. doi:10.1038/ncomms14425.
- [171] H. Zhang, Z. Zhang, C. Breidt, Comparison of short carbon fibre surface treatments on epoxy composites I. Enhancement of the mechanical properties, *Compos. Sci. Technol.* 64 (2004) 2021–2029. doi:10.1016/j.compscitech.2004.02.009.
- [172] S. Li, Y. Zhang, J. Han, Y. Zhou, Effect of carbon particle and carbon fiber on the microstructure and mechanical properties of short fiber reinforced reaction bonded silicon carbide composite, *J. Eur. Ceram. Soc.* 33 (2013) 887–896. doi:10.1016/j.jeurceramsoc.2012.10.026.
- [173] A. Godara, L. Mezzo, F. Luizi, A. Warrier, S.V. Lomov, A.W. van Vuure, L. Gorbatikh, P. Moldenaers, I. Verpoest, Influence of carbon nanotube reinforcement on the processing and the mechanical

- behaviour of carbon fiber/epoxy composites, *Carbon* N. Y. 47 (2009) 2914–2923. doi:10.1016/j.carbon.2009.06.039.
- [174] Y. Xu, L. Cheng, L. Zhang, Carbon / silicon carbide composites prepared by chemical vapor infiltration combined with silicon melt infiltration, *Carbon* N. Y. 37 (1999) 1179–1187.
- [175] Y. Kimura, Compatibility between carbon fibre and binary aluminium alloys, *J. Mater. Sci.* 19 (1984) 3107–3114.
- [176] Y. Ding, S. Dong, Q. Zhou, Z. Huang, D. Jiang, Preparation of C/SiC composites by hot pressing, using different C fiber content as reinforcement, *J. Am. Ceram. Soc.* 89 (2006) 1447–1449. doi:10.1111/j.1551-2916.2005.00872.x.
- [177] P. Lefort, D. Tetard, P. Tristant, Formation of aluminium carbide by carbothermal reduction of alumina: Role of the gaseous aluminium phase, *J. Eur. Ceram. Soc.* 12 (1993) 123–129. doi:10.1016/0955-2219(93)90132-B.
- [178] R.R. Naslain, SiC-matrix composites: Nonbrittle ceramics for thermo-structural application, *Int. J. Appl. Ceram. Technol.* 2 (2005) 75–84. doi:10.1111/j.1744-7402.2005.02009.x.
- [179] D. Jaglin, J. Binner, B. Vaidhyanathan, C. Prentice, B. Shatwell, D. Grant, Microwave heated chemical vapor infiltration: Densification mechanism of SiCf/SiC composites, *J. Am. Ceram. Soc.* 89 (2006) 2710–2717. doi:10.1111/j.1551-2916.2006.01127.x.
- [180] R. Naslain, F. Christin, SiC-Matrix Composite Materials for Advanced Jet Engines, *MRS Bull.* (2003) 654–658. doi:10.1557/mrs2003.193.
- [181] L.J. Vandeperre, J. Teo, Pressureless Sintering of SiC-B4C Composites, *Adv. Ceram. Armor IX Ceram. Eng. Sci. Proc.* 34 (2014) 101–108. doi:10.1002/9781118807576.ch10.
- [182] A. Oya, H. Marsh, Phenomena of catalytic graphitization, *J. Mater. Sci.* 17 (1982) 309–322. doi:10.1007/BF00591464.
- [183] S. Chabi, V.G. Rocha, E. Garc, C. Ferraro, E. Saiz, Ultralight, Strong, Three-Dimensional SiC Structures, *ACS Nano.* (2016) 2–7. doi:10.1021/acsnano.5b05533.
- [184] Easy Composites Ltd., (2017).
- [185] D. Grande, J. Mandell, K. Hong, Fibre-matrix bond strength studies of glass, ceramic, and metal matrix composites, *J. Mater. Sci.* 23 (1988) 311–328.
- [186] H. Zhang, Z. Zhang, K. Friedrich, Effect of fiber length on the wear resistance of short carbon fiber reinforced epoxy composites, *Compos. Sci. Technol.* 67 (2007) 222–230. doi:10.1016/j.compscitech.2006.08.001.
- [187] W. Dong, H.C. Liu, S.J. Park, F.L. Jin, Fracture toughness improvement of epoxy resins with short carbon fibers, *J. Ind. Eng. Chem.* 20 (2014) 1220–1222. doi:10.1016/J.Jiec.2013.06.053.
- [188] S.A. Hitchen, S.L. Ogin, P.A. Smith, C. Soutis, The effect of fibre length on fracture toughness and notched strength of short carbon fibre/epoxy composites, *Composites.* 25 (1994) 407–413. doi:10.1016/0010-4361(94)90096-5.
- [189] H.J. Walls, S.B. Caines, A.M. Sanchez, S.A. Khan, Yield stress and wall slip phenomena in colloidal silica gels, *J. Rheol. (N. Y. N. Y.)* 47 (2003) 847–868. doi:10.1122/1.1574023.

- [190] E. Feilden, T. Giovannini, N. Ni, C. Ferraro, E. Saiz, L. Vandeperre, F. Giuliani, Micromechanical strength of individual Al₂O₃ platelets, *Scr. Mater.* 131 (2017) 55–58. doi:10.1016/j.scriptamat.2017.01.008.
- [191] E. Feilden, E.G.-T. Blanca, F. Giuliani, E. Saiz, L.J. Vandeperre, Robocasting of structural ceramic parts with hydrogel inks, *J. Eur. Ceram. Soc.* 36 (2016) 2525–2533. doi:10.1016/j.jeurceramsoc.2016.03.001.
- [192] E. Feilden, C. Ferraro, F. Giuliani, L. Vandeperre, E. Saiz, Progress in novel and unexpected areas, *Mater. Today*. 19 (2016) 544–545. doi:10.1016/j.mattod.2016.11.001.
- [193] E. Feilden, C. Ferraro, Q. Zhang, E.G. Tunon, E. D'Elia, F. Giuliani, L. Vandeperre, E. Saiz, 3D Printing Bioinspired Ceramic Composites, *Sci. Rep.* 7 (2017) 13759. doi:10.1038/s41598-017-14236-9.
- [194] Victoria García Rocha, Esther Garcia-Tunon, Cristina Botas, Foivos Markoulidis, Ezra Feilden, Eleonora D'Elia, Na Ni, Milo Sebastian Peter Shaffer, Eduardo Saiz, Multi-material 3D printing of Graphene-based electrodes for Electrochemical Energy Storage using Thermo-Responsive Inks, *ACS Applied Materials & Interfaces*, doi:10.1021/acsami.7b10285
- [195] Esther García-Tuñón, Ezra Feilden, Han Zheng, Eleonora D'Elia, Alan Leong, Eduardo Saiz, Graphene Oxide: An All-in-One Processing Additive for 3D Printing, *ACS Applied Materials & Interfaces*, doi:10.1021/acsami.7b07717

Appendices

Appendix I – Another Approach to Define Φ

Given;

$$\gamma = d/h$$

and;

$$\tau = F a^2$$

The lateral deflection, d , is the key performance indicator for printing here. This is illustrated in Figure 164 below.

Substituting the above into $G = \tau/\gamma$ and rearranging gives:

$$d = \frac{a^2 h F}{G}$$

a and h can be removed as they are part parameters, not rheological parameters, and for a good paste d should be minimised, therefore the figure of merit should be the reciprocal of d , giving:

$$\Phi \propto \frac{G'_{eq}}{F}$$

(For pastes the shear modulus, G , is generally not measured directly. G'_{eq} is a sensible measure of G , so has been substituted). F can then be approximated as being proportional to the yield stress of the paste, as this is roughly the force required to continuously shear the paste, excluding time dependent factors such as printing speed.

Therefore the **time independent** paste specific figure of merit simply becomes:

$$\Phi = \frac{G'_{eq}}{\tau_y}$$

This simple result does not encompass time dependent effects such as printing speed, but these are printing parameters, not paste properties, therefore they should not be considered in the paste specific figure of merit.

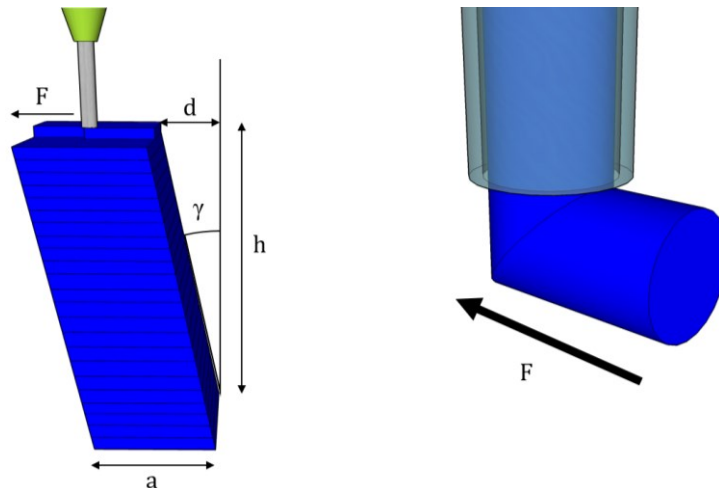


Figure 164. Schematic showing the leaning of a high aspect ratio part due to the force enacted on it to lay down the filament.

Appendix II – A Case Study

During this work an unaffiliated company tentatively asked for a very distinct geometry, a micropillar array, to be produced using robocasting. Each part consisted of roughly 300 micropillars in a specific arrangement on a thin alumina disk.

Given the size of each pillar, it was not possible to print individual pillars using a raster pattern (as most parts are printed) as they were too small to be sliced into an integer number of filaments, and due to their aspect ratio they would require a paste with a very large figure of merit in order to overcome the tilting effects described in Chapter III.

The solution was to print each pillar in one motion, with the nozzle extruding as it travelled up. When the height of the pillar was reached, the plunger was sharply pulled back to cut off flow. This action was packaged in a subroutine with variables available to tweak each aspect of the procedure, allowing for pillars of different geometries etc. The motion of the nozzle between each pillar was then defined using more subroutines to give the array layout required by the company.

This approach was sufficient until the company requested the pillar spacing to be reduced, such that they were <1 pillar diameter apart. The equipment could handle the accuracy of the placement without issue, however the nozzle was found to knock down freshly printed pillars when printing the next pillar. The reason for this is that the pillars were not static; they could be observed to lean away from each other seconds after printing. A litany of effects were ruled out including: charging of the pillars from the nozzle, irregular nozzle shape, upstream flow causing residual stress in the printed material and electrostatic effects from the substrate material. Finally it was discovered that the cause for this behaviour was drying. When two pillars are placed next to each other they dry slower in the region between them, as both pillars are rejecting water vapour into that region, leading to a spot of higher humidity. If they dry faster on the edges facing away from the other, then that side will shrink faster, causing them to lean away from each other. This effect is only temporary; once the middle dried, the pillar returned to an upright position.

The solution to this enigma was very simple – to increase the humidity to $>95\%$ in the enclosure during printing. Once the part is printed it can be allowed to dry, and the pillars do warp, but they never touch, and return to an upright position shortly after.

Again, this worked well until the company requested an even smaller spacing between the pillars, causing the nozzle to hit printed pillars as the leaning problem returned. Humidity could not be increased further without causing possible damage to the printer electronics, therefore another

solution had to be found. This time the problem was solved by changing the order that the pillars were printed, such that adjacent pillars were never printed consecutively. This meant that after printing one pillar, the nozzle went off to print the next one in another area of the part, allowing time before returning to the first area. This time allowed the pillar to complete its leaning cycle and return to upright while the nozzle was elsewhere, and thus wasn't at risk of knocking it over when trying to print adjacent pillars.

All in all, once this unexpected and interesting problem was solved, several batches of parts were produced in an on-demand manner. Despite some unanticipated issues, this case study shows where robocasting, and AM more generally, is able to shine. The agile nature of the process meant that new designs could be made very quickly and inexpensively, and could produce parts which would be very difficult with traditional techniques due to their complexity and fragility.

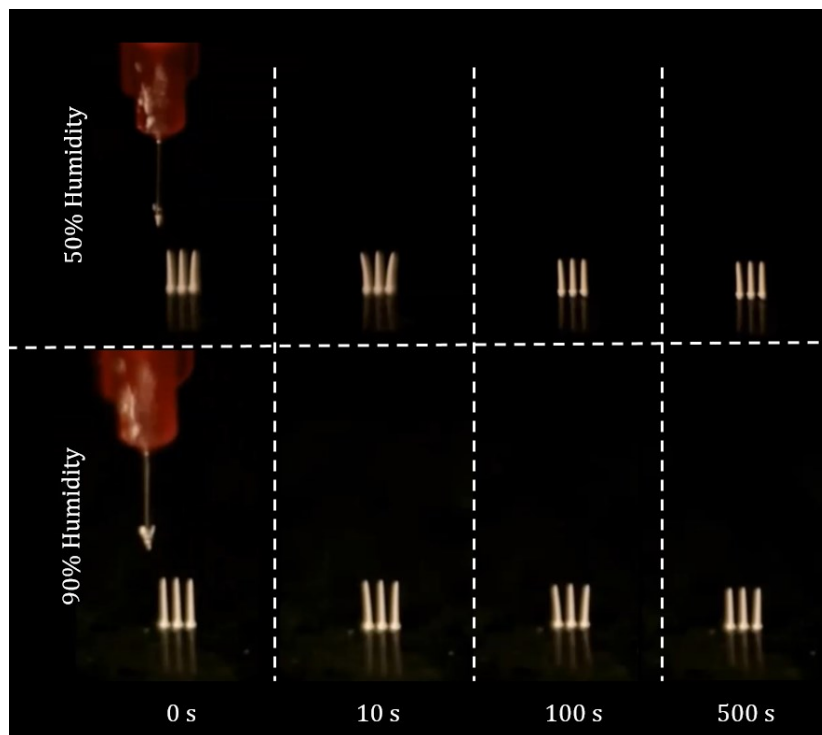


Figure 165. Video stills showing the leaning of three micropillars over time. Higher humidity reduces the speed of leaning, and increases the time required to return to the upright position.

```

$pullup = 5 - $height ;Defines the distance to retract after the pillar is printed
($pullup). The total distance (the retraction plus the height of the pillar ($height) is
set to 5mm.
G1 Z-5 F20 ;Moves the nozzle down 5mm, such that it is ~0.3 mm from the substrate. F20
refers to the speed of the move in mm/s.
G1 A$mag F10 ;Forces the plunger down by a distance of $mag. This begins the extrusion.
G1 Z$height F$speed ;Moves the nozzle up at a predefined speed ($speed) to the height of
the pillar.
G1 A-$mag F10 ;Pulls the plunger back to stop the flow. As material has been extruded,
this results in negative pressure in the syringe. This is recovered in the following
step by moving the plunger down again, enough to account for the material that has left
the syringe, such that the net pressure is zero by the end of the move.
G1 A$recoverplunger
G1 Z$pullup F20 ;Move back to ~5 mm from the substrate.
      DWELL $dwell ;Wait at this position for a defined time ($dwell) to allow for pillar leaning.

```

Figure 166. Commented G-code to print a single micropillar.

Appendix III – A Simple Bit of G-code to Print Large Numbers of Test Bars

This G-code can be pasted into the motion composer software and will run without any modifications.

The parameters for each bar can be input into the header (such as size, print speed etc...).

```
DVAR $xspace
DVAR $ylength
DVAR $numberofzlayers
DVAR $numberofxlayers
DVAR $plungerspeed
DVAR $tipdiameter
DVAR $syringediameter
DVAR $numberofbars
DVAR $xmove
DVAR $speed
DVAR $spacebetweenbars
DVAR $startparameter
$tipdiameter = 0.41 ;Diameter of the nozzle (mm)
$xspace = 0.34 ;Spacing between filaments. For dense bodies = (1/1.2) * nozzle diameter
$ylength = 35 ;Length of the bar
$numberofzlayers = 10 ;Must be even
$numberofxlayers = 10
$syringediameter = 9.54 ;9.54 for normal syringe, 15.6 big syringe
$numberofbars = 10
$speed = 10 ;Printing speed (mm/s)
$spacebetweenbars = 4
$startparameter = 0.2 ;The initial distance that the plunger moves to instigate flow
(mm)
$plungerspeed =
((( $tipdiameter * $tipdiameter ) / ( $syringediameter * $syringediameter )) * $speed
ENABLE X Y Z A
G1 A$startparameter
MOVEINC A 100 $plungerspeed

VELOCITY OFF

REPEAT $numberofbars ;number of bars to print
  G1 Y10 F$speed ;lead-in
  REPEAT ($numberofzlayers/2)
    REPEAT $numberofxlayers/2; layer 1
      G1 Y$ylength
      G1 X$xspace
      G1 Y-$ylength
      G1 X$xspace
    ENDREPEAT
    G1 Z$xspace ;move up layer
    G1 X-($xspace/2) ;Offset
    REPEAT $numberofxlayers/2; layer 2
      G1 Y$ylength
      G1 X-$xspace
      G1 Y-$ylength
      G1 X-$xspace
    ENDREPEAT
    G1 Z$xspace
    G1 X ($xspace/2)
  ENDREPEAT

  $xmove = ($xspace*$numberofxlayers)+$spacebetweenbars
  G1 Y-10 X$xmove Z(-$numberofzlayers*$xspace) F30 ;Move to next bar

ENDREPEAT
G1 A-$startparameter
DISABLE X Y Z A
```

Appendix IV – Correcting Weibull Modulus for Irregular Sized Samples

Volume correction for Weibull analysis

In Weibull statistics, the standard expression for probability of failure of a ceramic material where defects are found within a volume of the sample is generated by integrating over the volume where the stress is tensile, as given in “Ceramics Science and Technology- Set, Chapter 12- Fracture of Ceramics, 548-555”;

$$P_f = 1 - \exp\left(-\int \frac{dV}{V_{ref}} \left(\frac{\sigma_i}{\sigma_{o,ref}}\right)^m\right)$$

where P_f is probability of failure, V is sample volume, V_{ref} is the reference volume, σ_i is applied stress on sample i , $\sigma_{o,ref}$ is the reference stress, and m is the Weibull modulus. This can be combined with the expression for stress across a bar during 3 point bending;

$$\sigma = \frac{4\sigma_{max}xy}{lt}$$

where σ_{max} is the maximum stress in a bar in 3 point bending x is the distance along the length of the bar, y is the distance along the thickness of the bar, z is the distance along the width of the bar, l is the length of the bar, t is the thickness of the bar and w is the width of the bar.

These can be combined, and the integrals can be defined over the bottom half of the beam (the half in tension). The x integral can be defined over one half of the length for simplicity (due to the symmetry of the system) and the whole integral multiplied by 2 to account for this, giving:

$$P_f = 1 - \exp\left(-2 \int_{x=0}^{l/2} \int_{y=0}^{t/2} \int_{z=0}^w \frac{dx dy dz}{V_{ref}} \left(\frac{4\sigma_{max,i}xy}{lt\sigma_{o,ref}}\right)^m\right)$$

Upon integration:

$$P_f = 1 - \exp\left(-\left(\left(\frac{l_i w_i t_i}{2V_{ref}(m+1)^2}\right)^{1/m} \frac{\sigma_{max,i}}{\sigma_{o,ref}}\right)^m\right)$$

Comparing this expression to the standard Weibull expression:

$$P_f = 1 - \exp\left(-\left(\frac{\sigma_{i \text{ volume corrected}}}{\sigma_{o,ref}}\right)^m\right)$$

It is clear that the stresses, $\sigma_{i \text{ volume corrected}}$ calculated from the recorded failure strengths, $\sigma_{max,i}$ and the dimensions of the sample;

$$\sigma_{i \text{ volume corrected}} = \left(\frac{l_i w_i t_i}{2V_{ref}(m+1)^2}\right)^{1/m} \cdot \sigma_{max,i}$$

should follow a Weibull distribution with the same Weibull modulus as used to correct for the volume. Hence, to correct for varying sample dimensions: (i) guess a value for the Weibull modulus, (ii) calculate the volume corrected stress for each sample and determine the Weibull modulus for the $\sigma_{i \text{ volume corrected}}$ data set in the normal way, (iii) use this value of the Weibull modulus for the next iteration, i.e. to replace the guessed value of m . Convergence typically requires 2 to 3 iterations.

Area correction for Weibull analysis

In a similar manner, starting from the standard expression for probability of failure in Weibull statistics where only surface defects are across the surface area of the sample in tension cause failure, and the expression relating failure stress to maximum stress in a bending beam-

$$P_f = 1 - \exp\left(-\int \frac{dA}{A_{ref}} \left(\frac{\sigma}{\sigma_{o,ref}}\right)^m\right) \text{ and } \sigma = \frac{4\sigma_{max}xy}{Lt}$$

Where A is the area of the tensile face and A_{ref} is the reference area.

Combining these:

$$P_f = 1 - \exp\left(-2 \int_{x=0}^{l/2} \int_{z=0}^w \frac{dx dz}{A_{ref}} \left(\frac{4\sigma_{max,i}xy}{lt\sigma_{o,ref}}\right)^m\right)$$

Setting $y=t/2$ and integrating:

$$P_f = 1 - \exp\left(-\left(\left(\frac{l_i w_i}{A_{ref}(m+1)}\right)^{\frac{1}{m}} \sigma_{max,i}\right)^m\right)$$

Therefore:

$$\sigma_{i \text{ area corrected}} = \left(\frac{l_i w_i}{A_{ref}(m+1)}\right)^{1/m} \cdot \sigma_{max,i}$$

The same procedure described in the volume correction can then be used to find the corrected Weibull modulus.